Development of Patternable Conducting Polymers Based Organic Thin Film Transistors for Acoustic Sensor

Thesis submitted

in partial fulfilment of the requirements for the award of the degree of

Doctor of Philosophy

in the
Faculty of Science
Cochin University of Science and Technology
Kochi – 682 022

by

Shiny Nair

Naval Physical and Oceanographic Laboratory
Thrikkakara, Kochi – 682 021

December 2018

Development of Patternable Conducting Polymers Based Organic Thin Film Transistors for Acoustic Sensor

Ph.D. Thesis in the Field of Materials Science

Author

Shiny Nair
Research Scholar, Registration No. 4432
Naval Physical and Oceanographic Laboratory
Defence Research and Development Organisation
Thrikkakara, Kochi-682 021, India
email: shinynair_2006@yahoo.com

Supervising Guide

Dr. T. Mukundan
Scientist G, Group Director
Naval Physical and Oceanographic Laboratory
Defence Research and Development Organisation
Thrikkakara, Kochi-682 021, India
email: mukundant2013@gmail.com

Naval Physical and Oceanographic Laboratory (NPOL)
(Recognized Research Centre of
Cochin University of Science and Technology)
Kochi, India, 682 021

December 2018

Dedicated to

My Dear Parents

Thesis Certificate

This is to certify that the thesis titled, **'DEVELOPMENT OF PATTERNABLE CONDUCTING POLYMERS BASED ORGANIC THIN FILM TRANSISTORS FOR ACOUSTIC SENSOR'** is an authentic record of research work carried out by **Ms. Shiny Nair** (Reg. No. 4432) under my supervision and guidance at the Naval Physical and Oceanographic Laboratory, Thrikkakara, Kochi-682021, in partial fulfilment of the requirements for the award of the degree of Doctor of Philosophy under the Faculty of Science, Cochin University of Science and Technology, Kochi and further that no part of the work reported in this thesis has been submitted earlier for the award of any other degree from any other institution. The thesis has been modified to incorporate all the relevant corrections and modifications suggested by the audience and recommended by the Doctoral Committee during the pre-synopsis seminar.

Dr. T. Mukundan
Supervising Guide
Scientist G
Naval Physical and Oceanographic Laboratory
Kochi - 682021

Kochi - 682021
12 Dec 2018

Declaration

I hereby declare that the work presented in this thesis titled, **‘DEVELOPMENT OF PATTERNABLE CONDUCTING POLYMERS BASED ORGANIC THIN FILM TRANSISTORS FOR ACOUSTIC SENSOR’** is based on the original research work carried out by me under the supervision and guidance of **Dr. T. Mukundan**, Scientist G, Naval Physical and Oceanographic Laboratory, Kochi, for the award of the degree of Doctor of Philosophy of Cochin University of Science and Technology, Kochi. I further declare that the contents of this thesis, in full or in parts have not been submitted to any other University or Institute for the award of any degree or diploma.

Shiny Nair
Research Scholar
Naval Physical and Oceanographic Laboratory
Kochi- 682 021

Kochi - 682021
12 Dec 2018

Acknowledgements

All praise and thanks to God Almighty for all the blessings showered on me from time to time.

First and foremost, I owe my profound sense of gratitude to my supervisor and guide, Dr. T. Mukundan, Scientist 'G', NPOL, for his patience, enthusiasm, immense knowledge and relentless encouragement and endless support, which paved the way for the successful completion of my doctoral dissertation. I have been extremely fortunate to have a supervisor who cared so much about my work and I cherish the opulent experience of working with him.

I sincerely express my gratefulness to Shri S. Kedarnath Shenoy, Outstanding Scientist and Director, NPOL, for permitting me to complete the doctoral thesis and providing all the necessary facilities at NPOL. I am extremely thankful to Shri S. Ananthanarayanan, former Director of NPOL, for giving me an opportunity to pursue my Ph. D. research work at NPOL.

I feel extremely privileged to place on record my sincere gratitude and respect to Dr. P. V. Hareesh Kumar, Scientist 'G', Associate Director, Chairman, Doctoral Research Committee (DRC) of NPOL, for valuable suggestions, encouragement and constant support rendered during the period of research. I am deeply indebted to Dr. A. Unnikrishnan, Scientist 'H' (Retd.) and Dr. K. Sudarsan, Scientist 'G' (Retd.), who headed the Human Resource Development (HRD) Council of NPOL, for being instrumental in providing the opportunity to commence my doctoral programme at NPOL, a recognized research centre of Cochin University of Science and Technology (CUSAT), Kochi.

At this juncture, I would like to place on record my deepest sense of gratitude to Dr. V. Natarajan, Scientist 'G', Director, Research and Innovation Centre, Chennai and former Group Head, Material Science and Engineering, NPOL. He has played a pivotal role in establishing the clean room facilities at NPOL, where I have carried out major part of my research. I am indebted to his selfless support and proficient guidance during the course of my research.

I take this opportunity to thank the doctoral committee members, Dr. K. Sreekumar, Professor, Department of Applied chemistry, CUSAT, Dr. A. V. Ramesh Kumar, Scientist 'F', Dr. R. Ramesh, Scientist 'F', NPOL and Departmental Research Committee members, Dr. K.P.B. Moosad, Scientist 'G', Dr. Reji John, Scientist 'G', Dr. T. Santhanakrishnan, Scientist 'F' and Dr. P. Muralikrishna, Scientist 'F', NPOL, for sparing a lot of their valuable time and providing proper direction, suggestion, conducting examination and revision etc., without which, this thesis would not have taken this shape.

I sincerely express my heartfelt gratitude to Dr. N. Manoj, Associate Professor and Head, Department of Applied Chemistry, CUSAT, Kochi, for granting permission to complete two courses, as part of Ph.D course work at the Department of Applied Chemistry, CUSAT. I was fortunate to have the opportunity for attending the classes conducted by Dr. S. Prathapan, Professor, Department of Applied Chemistry, CUSAT, on 'Spectroscopy'. His interactive sessions during the course rekindled the classroom experiences, in addition to the benefits of the knowledge imparted by him through sincere and dedicated efforts.

I owe a lot to Shri M. Kathiresan, Scientist 'E', NPOL, a colleague who has helped in solving the problems related to functioning of equipments in the clean room, the proper functioning of the clean room and had helped me in the measurements of electrical properties of organic transistors. Without his timely support, the completion of the thesis would not have become a reality.

I feel happy to express heartfelt gratitude to my colleague Smt. R. Rajeswari, Technical Officer 'B', NPOL for her timely assistance in sample preparation and analysis that has aided in the smooth and successful completion of many experiments. I am indebted to Shri C. Sajith, Technical Assistant, NPOL for all his support in the maintenance of the clean room and the facilities in it, without which, the completion of the research for the doctoral thesis would not have been possible.

I am extremely privileged to have the of support of Dr. Raja Shunmugam, Associate Professor, Indian Institute of Science Education and Research, Kolkata and his student, Dr. Shivshankar Mane, for fruitful discussion and guidance for the synthesis of regioregular poly(3-hexylhiophene) and the copolymers.

Special thanks to Shri Srinivasan Pitchai, MosIC Solutions, Bangalore, for his help and guidance in the fabrication of wafer probing test jig and the measurement of amplifier characteristics of the flexible amplifiers.

I am extremely thankful to Dr. Partha Ghoshal, Scientist 'F' and Head, Electron Microscopy Division, Defence Metallurgical Research Laboratory, Hyderabad, for the help extended in the SEM and TEM analysis of conducting polymer samples.

The help extended by the staff of Sophisticated Test and Instrumentation Centre (STIC), CUSAT, is also acknowledged for the structural and morphological analysis of samples at various stages of my research.

I thank all my colleagues of Materials Science and Engineering Group of NPOL, for their support, guidance and help at different stages of my research.

I convey my sincere thanks to the HRD cell, administrative and library staff of NPOL, for their help and assistance.

My deep felt gratitude goes to all my teachers, who introduced me to the vast expanses of knowledge, throughout my education. Without their help, I would not have been able to accomplish my professional ambitions.

I dedicate this thesis to my Mummy and Daddy who have supported me all these years and given me the strength to fulfil my dreams. They have been always a source of inspiration, offering a helping hand with reassuring support in all situations that looked difficult to me.

Finally and most importantly, words are too short to express my deep sense of gratitude towards my beloved husband Shri M. Girish and my loving children Gayatri & Giridhar for their understanding, encouragement, patience and unwavering love. Without the unconditional love and emotional backing given by my family, I would never have been able to complete the research work.

Shiny Nair

PREFACE

‘Organic Electronics’ has witnessed unprecedented growth in the last few decades, driven by the ever increasing demand for flexible electronic devices. The development of the field of organic electronics rests on the π-conjugated organic semiconductors and conductors that form the active and conducting layers of the devices. Amongst the organic electronic devices, organic thin film transistors (OTFTs) have generated a high level of commercial interest as they are considered as basic building blocks of modern flexible electronic devices, for either amplifying signals or operating as on-off switches. Due to the less complex processes involved in their fabrication, compared to the conventional Si technology, OTFTs are actively researched for application in large area flexible sensors. Transistor based sensors normally have high sensitivity because of the combined functionality of signal transduction and amplification in the same device. For application in acoustic sensors, OTFT based electronics has the advantage of flexibility and integration in close proximity to the sensor.

In the domain of sensing of acoustic signals at low frequencies, OTFT based flexible interface circuits have great potential. Large area flexible acoustic sensors utilizing polymeric piezoelectric sensors inherently have low capacitance, that attenuate the input signal. The interface electronics between the sensor and signal conditioning electronics, if is at a larger distance, will further decay the signal owing to the large cable capacitance. In this context, flexible electronic interface circuits, having the dual advantage of flexibility and possibility of integrating in close proximity to the sensor, is highly significant. For the intended application of sensing at low frequencies, the limitation with respect to the low mobilities of the organic materials is also not a constraint. An intelligent choice of materials and processes are necessary for the fabrication of OTFTs to be employed as components in the interface circuits of sensors.

Suitably patterned conjugated polymers in their semiconducting and conducting form can enhance the performance of OTFTs to a great extent, widening the potential for applications in large area flexible sensors. The device performance in OTFTs is significantly limited by poor charge injection and therefore, a small enhancement in injection would lead to a considerable improvement of OTFT performance. Materials for source/drain electrodes in OTFT should possess a suitable work function to reduce the charge-carrier injection barrier and form an ohmic contact with organic layers. Substitution of metal electrodes with a conductive polymer, of suitable work function, is a significant step towards providing lower-energy barriers for hole carrier injection with the added advantage of reducing material cost and ease of fabrication on flexible substrates. An effective and scalable patterning technique of solution processable conducting polymers is vital for the low-cost fabrication of organic electronic devices with suitable polymer electrode.

Solution processable semiconducting polymers are also vital in OTFTs since the usual low temperature thermal evaporation processes, involving high vacuum, employed for the deposition of small molecule semiconductors are not suitable for the realization of large area flexible sensors based on OTFTs. One approach for solving this problem is to synthesize solution processable, semiconductors in copolymer structures with various polymer blocks that display desirable mechanical properties, leading to a variety of polymeric materials with improved functionalities.

Most of the best performing organic circuits to date have been realized by combining solution and vacuum processing with photolithographic steps. Photolithography allows fabrication of features of much higher resolution which is especially important for defining the source–drain gap (channel length, L) in TFTs. Solution processing of materials employed in the fabrication of TFT enables large area fabrication of OTFT based sensors and circuits. Hence, it is optimum to combine suitable solution processes with photolithography and vacuum processes for fabrication of different layers in an OTFT, depending on the nature and type of the layer material. Consistent functioning of organic circuits has also to be ensured by efficient passivation of the transistors for increasing their operational life. High performance organic electronic circuit for amplification of acoustic signal necessitates the availability of optimum fabrication techniques of OTFT, employing solution processable patterning methods of high performance semiconductors, conductors and effective passivation techniques.

The research for this doctoral thesis has been carried out at NPOL, a laboratory that comes under the naval cluster of Defence Research and Development Organization, Government of India. The laboratory has established self-reliance in the development of sensors and technologies for underwater surveillance. The recent requirement for underwater large area flexible acoustic sensors that operate at low frequencies led to the study on development of flexible interface circuits for acoustic sensors. As the basic building blocks for such applications for signal amplification are high performance OTFTs, studies were initiated for the development of materials and processes for realization of OTFTs that can be integrated into flexible circuits.

The thesis titled, "Development of Patternable Conducting Polymers based Organic Thin Film Transistors for Acoustic Sensor", has been divided into seven chapters and the contents of each chapter are briefly highlighted below.

Chapter 1 gives a general introduction to organic electronics; organic thin film transistors; application of OTFTs in sensors, analog & digital circuit regime and acoustic sensors; importance of conjugated semiconducting polymers and conducting polymers in organic electronics; patterning of conducting polymers, a brief introduction on polyaniline and the objectives of the thesis.

Chapter 2 deals with the various synthesis methods, resulting in polymeric nanostructures of polyaniline (PANi) used as conducting electrode and poly(3-hexylthiophene)-b-poly(t-butyl acrylate), used as the semiconducting channel material of OTFT. Theoretical aspects and details of all the experimental techniques used for material, device and organic circuit characterization in the present studies are also described. A brief discussion on the various general device fabrication steps, employed in this study, for the complete fabrication of an OTFT has also been included in this chapter.

Conducting polymer nanowires of PANi has been synthesized by both chemical and electrochemical methods. Dilute & interfacial polymerization by chemical methods and template & step galvanostatic method (SGM) by electrochemical method are employed for the synthesis of PANi nanofibers. To overcome the difficulties in processing PANi, water dispersible, nanostructured conductive polymer composite, poyaniline:polystyrene sulphonic acid (PANi-PSS) is synthesized by oxidative polymerization of aniline, templated with polystyrene sulphonic acid. For the formation of stable dispersion of PANi-PSS with desired conductivity, concentration of the precursor acid used in the synthesis is optimized. The conductivity of films thus obtained from a stable dispersion is increased by more than two orders of magnitude by secondary doping with dichloroacetic acid (DCA). Structural, morphological, thermal, electrochemical, wetting and electrical characterization of the synthesized PANi nanostructures are described and the experimental procedure is elaborated. Since solution processable semiconducting polymers are also vital as channel material in OTFT, poly(3-alkylthiophene) in copolymer structure with polymer block of t-butyl acrylate was synthesized. Poly(3-hexylthiophene)-b-poly(t-butyl acrylate) (PHT-b-PBA), thus synthesized via atom transfer radical polymerization (ATRP), is completely characterized and examined their film forming properties. The basic conventional techniques employed in the fabrication and characterization of OTFTs is also discussed.

Chapter 3 discusses the analysis results of the synthesized conducting and semiconducting polymer. Spectroscopic techniques confirmed the formation of emeraldine salt form of the PANi nanowires, synthesized by the different chemical and electrochemical routes. Morphology of the nanowires studied by scanning electron microscopy (SEM) and transmission electron microscopy (TEM) aided in the systematic analysis of the formation of nanostructures that depended on the concentration of monomer, dopant acid and method of synthesis. An acceptable correlation could be established between the results of conductivity, morphology and electrochemical analysis. PANi nanowires synthesized by SGM at lower concentration of monomer and dopant acid are found suitable amongst the nanowires to be employed for the formation of conducting electrode in OTFT.

Conductive polymer composite, PANi-PSS are systematically analyzed to study the effect of concentration of precursor acid and polystyrene sulphonic acid on structure, morphology and conductivity. One of the samples (PSN3-3), with an average particle size of 20 nm and sufficient conductivity is found optimum for device fabrication as it formed very stable dispersion (stability maintained even after storing for months). Analysis results of the synthesized PHT-b-PBA, pertaining to its structure, thermal properties, molecular weight and film forming capability are also presented.

Chapter 4 discusses different methods adopted for the fabrication of OTFT. For the initial optimization of parameters employed in the realization of simple OTFT, the fabrication is carried out on a thermally oxidized silicon wafer with pentacene as the semiconductor layer. The deposition time, thickness, etching time, etching rate, power required for etching in RIE, energy requirements in photolithographic processes, development time etc. are optimized prior to the fabrication of TFT on different substrates and employing different layer materials. The chapter brings about the novel approach of effective simultaneous passivation and patterning of OTFTs fabricated on flexible polyethylene naphthalate (PEN) substrate, highlighting the improved device performance of poly(p-xylylene) polymer (parylene C) passivated OTFTs when compared to the conventional poly(vinyl alcohol) (PVA) passivated OTFTs.

Fabrication of OTFT on PEN substrate with solution processable semiconducting and conducting polymers is also discussed. A novel, modified parylene lift-off process is studied to pattern nanostructured, PANi-PSS as electrode in OTFT. This patterning technique for conducting polymer electrode, without exposure to harmful solvents, resulted in a resolution of 5 μm, which is one among the highest reported in literature. Performance of the fabricated device with PANi-PSS electrode is compared with pentacene based OTFT with non-ohmic palladium electrode, which is a relatively low cost metal with matching work function for *p*-type pentacene. The shortcomings with non-ohmic nature of Pd metal electrode that leads to higher contact resistance, are overcome by the use of PANi-PSS conducting polymer electrode. Electrical characteristics of OTFT fabricated with solution processable, PHT-b-PBA semiconductor and PANi-PSS conducting polymer is also presented.

Chapter 5 discusses a computer-aided methodology for modelling of OTFTs using SILVACO's ATLAS software. Emphasis is given on two dimensional (2D) numerical simulation of OTFTs to fully understand the electrical characteristics of pentacene TFT with conducting polymer, PANi-PSS as electrodes. Effect of contact barrier, morphology dependent mobility and interface traps are step-wise incorporated to model the electrical characteristics of the device accurately and match the experimental data. A comparison of electrical characteristics of the pentacene TFT with conducting polymer electrode and Pd electrode is also presented. The microscopic and physical mechanisms are determined from the 2D numerical simulation which explains the difference in contact resistance in the two types of devices.

Chapter 6 discusses the method adopted for configuring the discrete TFTs fabricated on a 3″ flexible substrate as a single stage differntial amplifier. A wafer probing test jig designed to simultaneously measure the electrical characteristics of all the devices on a 3″ substrate could easily select the device of required aspect ratio in the configuration of the amplifier. Feasibility of real time sensing of acoustic signal generated by a standard piezoelectric sensor is tested with the fabricated single stage flexible differential amplifier. The gain and and frequency bandwidth of flexible amplifier consisting of OTFTs with solution processable conducting polymer electrode, patterned by the novel parylene lift-off method, is determined in the study.

Chapter 7 discusses the general conclusions and the scope for future work. Refernces and list of publications are included in the subsquent sections.

CONTENTS

Chapter 1

Chapter 2

Chapter 3

Development of Conjugated Polymers for Application in Organic Thin Film Transistor------------------------------------- 57- 92

Chapter 4

Fabrication Methodology of Organic Thin Film Transistor 93- 120

Chapter 5

Two Dimensional Numerical Simulation of Organic Thin Film Transistor-- 121- 142

Chapter 6

Organic Thin Film Transistor Amplifier for Acoustic Sensor---143-158

Chapter 7

GLOSSARY OF TERMS

A_{dB}	Amplifier gain in dB
AFM	Atomic Force Microscopy
APS	Ammonium peroxydisulphate
ATRP	Atom Transfer Radical Polymerization
9-BBN	9-Borabicyclo [3.3.1] nonane
BW	Bandwidth
$CHCl_3$	Chloroform
CMOS	Complementary metal oxide semiconductor
CP	Conducting polymer
CSA	Camphor 10-sulphonic acid
CuBr	Cuprous bromide
CVD	Chemical vapour deposition
CV	Cyclic voltammogram
DCA	Dichloroacetic acid
E-beam	Electron beam
EB	Emeraldine base form of polyaniline
E_f	Fermi energy
E_g	Energy band gap
ES	Emeraldine salt
f_c	Cut-off frequency
GBWP	Gain band width product
g_m	Transconductance
HCl	Hydrochloric acid
HMDS	Hexamethyldisilazane
HOMO	Highest occupied molecular orbital

H_3PO_4	Phosphoric acid
I_{ds}	Drain-source current
ICP	Inherently conducting polymers
I_{on}/I_{off}	Ratio of transistor on current and off current
IE	Ionization energy
IPA	Isopropyl alcohol
JFET	Junction field effect transistor
k	Relative permittivity
LUMO	Lowest unoccupied molecular orbital
MOSFET	Metal oxide semiconductor field effect transistor
MTR	Multiple trap and release
μ	Field effect mobility
μ_o	Zero field mobility
μ_i	Intrinsic mobility
N_c	Effective Conduction Band Density of states
N_V	Effective Valence Band Density of states
N_{TA}	Exponential trap density
NH_4OH	Ammonium hydroxide
N_{ic}	Interface charge
Ni(dppp)Cl	[1,3- Bis (diphenylphosphino) propane] Nickel (II) Chloride
NMP	N-methylpyrrolidinone
OLED	Organic light emitting diode
OPV	Organic photovoltaic
OSC	Organic semiconductor
OTFT	Organic thin film transistor
OTS	Octadecyltrichlorosilane

PANi	Polyaniline
PANi-PSS	Polyaniline-polstyrene sulphonic acid composite
PANi-CSA	Polyaniline doped with CSA
PANi-HCl	Polyaniline doped with HCl
Pd	Palladium
PEN	Poly(ethylene naphthalate)
PEDOT:PSS	Poly(3,4-ethylenedioxythiophene) polystyrene sulfonate
PMDETA	N,N,N',N",N", pentamethyl diethylene triamine
PVA	Poly(vinyl alcohol)
PVD	Physical vapour deposition
PVDF	Polyvinylidene fluoride
PHT	Polyhexylthiophene
P3HT	Poly(3-hexylthiophene)
PVP	Poly(4-vinyl phenol)
PSS-Na	Poly(sodium 4-styrenesulfonate)
PHT-b-PBA	Poly(3-hexylthiophene)-b-poly(t-butyl acrylate)
rr-P3HT	Regioregular poly(3-hexyl thiophene)
RIE	Reactive ion etching
R2R	Roll to roll
SEM	Scanning electron microscopy
SGM	Step galvanostatic method
Si	Silicon
SiO_2	Silicon dioxide
SONAR	SOund Navigation And Ranging
S_n	Subthreshold swing
TEM	Transmission electron microscopy

THF	Tetrahydrofuran
TFT	Thin film transistor
TLM	Transfer Line Method
VRH	Variable range hopping
V_{on}	Turn-on voltage
V_{ds}	Drain-source voltage
V_{gs}	Gate-source voltage
V_T	Threshold voltage
δ	Interfacial dipole
Δ	Zero field thermal activation energy
Φ_m	Work function of metal
Φ_{bh}	Charge injection barrier
χ_{pc}	Electron affinity
W/L	Width/Length
W_{TA}	Characteristic energy

LIST OF FIGURES

LIST OF TABLES

Chapter 1

INTRODUCTION

1.1 Organic Electronics

The last few decades have witnessed incredible developments in the field of organic electronics, driven by the demand for large scale displays, sensor arrays, lighting panels and photovoltaic modules [1]. The origin of organic electronics stems from the ability of a class of functional organic molecules known as π-conjugated organic semiconductors (OSCs) to actively absorb light, emit light or transport charge under appropriate conditions [2]. While this requirement can be satisfied by both inorganic and organic materials, the latter have attracted specific interest due to their exceptional film-forming capabilities and controllability of physical properties through conventional wet chemistry. The optical and electrical properties of OSCs have been studied since 1960. A renewal in interest in the field owes largely to the demonstration of organic light emitting diodes (OLEDs) based on a double layer structure of the organic thin films, tris(8-hydroxylquinoline) aluminium (Alq_3) and an aromatic diamine in 1987 [3] and the first successful demonstration of green-yellow polymer-based OLED using 100 nm thick film of poly(p-phenylene vinylene) as an active layer in 1990 [4].

Amongst the organic electronic devices, the technology of OLEDs is perhaps the most advanced organic device platform. An OLED device, in its simplest form, consists of two organic layers (electron and hole transport layer), sandwiched between two electrodes, a cathode and an anode. When a voltage is applied across the electrodes, the charges start moving in the device under the influence of the electric field. Electrons leave the cathode and holes move from the anode in opposite direction. These electrons and holes drift to the interface between the electron and hole transport layer under the applied cell potential; it is the recombination of electron-hole pairs that generates radiative emission. Thus, the electrical power applied to the electrodes is transformed into light [5-6]. The first commercial application of organic electronics, the displays, is based on OLEDs. Though OLED displays were first used in high–end mobile phones, it can now be seen in a variety of handsets and even in 77 inches televisions [7]. The present generation of OLED displays are driven by silicon transistor based back planes. In the longer term, the goal is to develop ultra-thin, flexible displays fabricated completely from organic components, including the backplanes.

Another organic device platform, organic photovoltaics (OPVs) are also emerging as a major area of interest, impelled both by favourable government policies for alternative energy and by the increasing commercial opportunities. OPVs operate on the reverse principle to OLEDs. OPVs consist of an electron donor and an electron acceptor, sandwiched between the anode and the cathode. Under illumination, electrons from the highest occupied molecular orbital (HOMO) of the donor are excited to the lowest unoccupied molecular orbital (LUMO) or some higher excited states, followed by transfer to the LUMO of the acceptor, resulting in separated charges and the power output [8]. Extensive research to achieve improvements in device efficiency by design of new materials that have electronic energy levels capable of generating larger cell voltages, absorbing more light, improving charge separation, avoiding losses from the recombination of generated charges and having optimal transport properties are being carried out. Although OPV technology is still at an early stage of its development, it is an important candidate of energy source for applications in most of the domestic energy needs (such as lighting) in remote rural places or off-grid urban communities [9].

In addition to OLEDs and OPVs, organic thin film organic transistor (OTFT) devices [10] are generating a high level of commercial interest. Many startup companies are leading the technology development with small monochrome electrophoretic display products that are driven by organic transistor backplanes. The following section discusses in detail, the principle, operation and application of OTFTs in sensors.

1.2 Organic Thin Film Transistors

Transistors are considered basic building blocks of modern electronic devices, either for amplifying signals or operating as on-off switches. Most organic transistors are organic field effect transistors (OFETs) made by depositing thin films of an active semiconductor layer, the dielectric layer and metallic contacts over a supporting (but non-conducting) substrate and hence the name, ‘Organic Thin Film Transistors’ (OTFTs) [11]. An OTFT is analogous to the metal oxide semiconductor field effect transistor (MOSFET), in basic design and function. It is a three-terminal device, in which, when a bias is applied to the gate electrode (V_{gs}), charges can accumulate capacitively at the organic semiconductor-dielectric interface. This in turn creates a channel in which the accumulated charges can transport between the source and drain electrodes in response to the applied drain-source (V_{ds}) voltage. A basic schematic of OTFT is shown in Fig. 1.1.

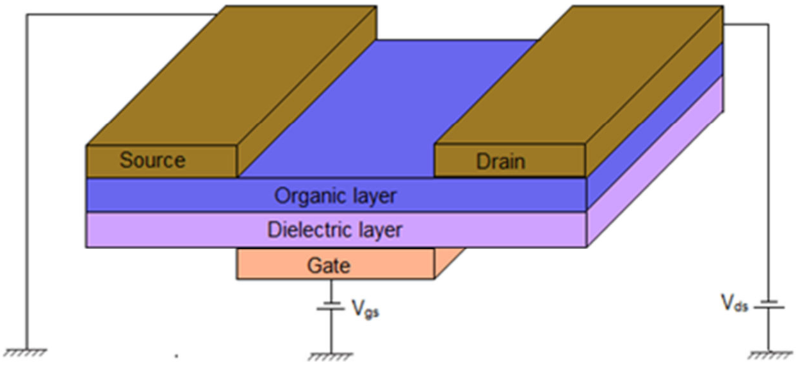

Fig. 1.1: Schematic of a thin film transistor.

OTFTs have gained importance due to the less complex processes involved in their fabrication compared with conventional Si technology, which involves high temperature and high vacuum deposition processes. In a conventional MOSFET, the semiconductor layer generally consists of lightly doped Si or combinations of Group III and V elements, such as GaAs. The applied gate voltage causes an accumulation of minority charge carriers and a resultant ‘inversion layer’ at the semiconductor-dielectric interface. In this channel, current flow results due to the carriers injected from the source and drain electrodes that pass through the channel [12]. However, in an OTFT, the active semiconductor layer consists of a thin film of highly conjugated small molecules or polymers. In stark contrast to MOSFETs, an inversion regime does not exist in organic transistors and majority carriers pass the current in them. This basic difference is correlated to the kind of charge transport in each of these semiconductors. In an ordered inorganic material, e.g. single-crystal Si, a band-type mode of transport results due to the delocalization of electrons over equivalent sites, with the charge carriers moving through a continuum of energy levels. In less ordered organic materials, the proposed mechanism of transport is hopping of charge carriers between discrete, localized states of individual molecules [2]. The presence of inconsistencies or impurities may result in traps that modify the relative energy levels and restrict the flow of charge carriers. The first OTFT was reported by Koezuka and co-workers, in 1986, on a structure based on electrochemically polymerized polythiophene [13]. Since then, there has been great progress in both the material performance and development of new fabrication techniques.

1.2.1 Operating Principle and Characteristic Parameters

To demonstrate the operating principle of the OTFTs, a simplified energy level diagram showing the position of the HOMO and LUMO of the OSC, relative to the Fermi levels of the source and drain contacts are shown in Fig. 1.2. If there is no gate voltage applied as in Fig. 1.2(a), the OSC which is intrinsically undoped will not show any charge carriers. Current flow in the OSC is established by only way of direct charge injection from the source/drain electrodes. Due to high resistance of the OSCs and large distance between the source and drain electrodes, such currents will be relatively small.

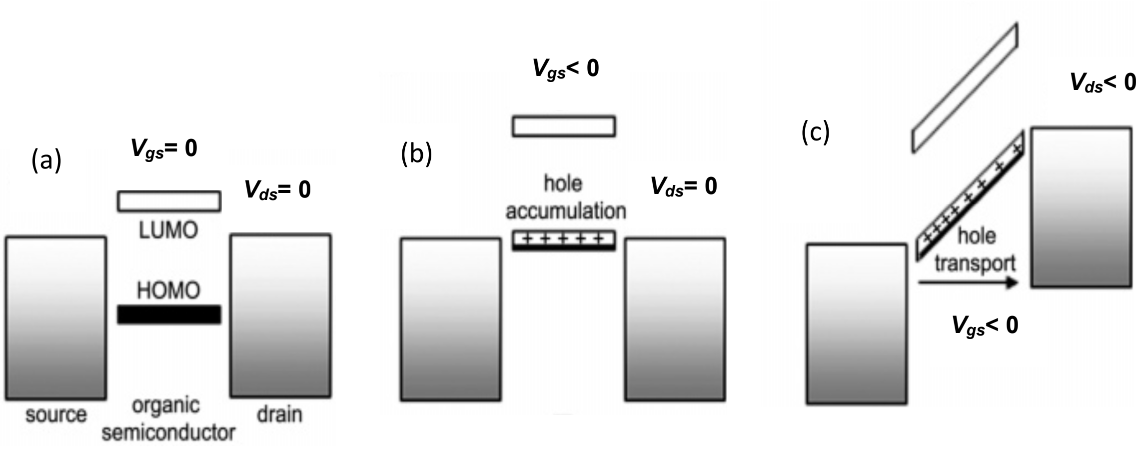

Fig. 1.2: Illustration of working principle of an OTFT with respect to applied gate voltage when (a) $V_{gs} = 0$ V, $V_{ds} = 0$ V (b) hole accumulation and (c) hole transport.

Ideally, when gate voltage is not applied, in the absence of mobile charge carriers, the conductance of the semiconductor film is enormously low i.e., the device is “off”. When the gate voltage is applied, mobile charges are induced and the transistor is “on”. Application of a negative gate voltage, in the case of a *p*-type semiconductor, produces a large electric field at the organic-insulator interface. This field causes the HOMO and LUMO levels in the semiconductor to shift up (increase in energy) such that the HOMO becomes resonant with the Fermi levels of the contacts and electrons spill out of the semiconductor into the contacts, leaving positively charged holes [Fig. 1.2(b)] [14]. These holes are now the mobile charges that move in response to an applied drain voltage as in Fig. 1.2(c). TFTs are typically characterized in one of the two ways, either by holding V_{gs} constant and sweeping V_{ds} (commonly referred to as I_{ds}-V_{ds} or output curves) or by holding V_{ds} constant and sweeping V_{gs} (commonly referred to as I_{ds}-V_{gs} or transfer curve) [15] (I_{ds} is referred to as the drain-source current). The performance of an OTFT is judged on the basis of the parameters given below.

- Mobility (μ): The mobility of a transistor is described as the average charge carrier drift velocity per unit electric field. It is a measure of how efficiently charge carriers can move along the conducting path [14]. This parameter can be extracted from current-voltage measurements and would ideally be as large as possible.
- Threshold voltage (V_T): Threshold voltage is the minimum gate voltage required for accumulating the charge carriers at the semiconductor-dielectric interface forming a conducting path between the source and the drain [15]. It determines the switching behaviour of a device and hence, needs to be controlled to ensure proper operation of the devices and thereby the circuits.
- I_{on}/I_{off} ratio: This parameter is the ratio of the maximum to minimum I_{ds}. It is known that a higher "on" current offers better driving capability, while a lower "off" current results in low leakage current [16]. Consequently, a higher ratio is preferable. It gives an idea about amplification capability of the device. It should be as high as possible. Typical values of I_{on}/I_{off} greater than 10^5 are desirable for high speed organic electronic devices [10].
- Turn-on voltage (V_{on}): Corresponds to the V_{gs} at which I_{ds} starts to increase. It can be determined from the log I_{ds}-V_{gs} graph.
- Subthreshold swing (S_n): This parameter indicates the V_{gs} required to increase I_{ds} by one decade and is evident in the subthreshold region [17]. It is defined in V/decade.

$$S_n = \left(\frac{d \log(I_{ds})}{d \log V_{gs}} \right)^{-1} \tag{1.1}$$

A smaller S_n is preferable, resulting in lower power consumption and higher speed. Both, I_{on}/I_{off} and S_n are dependent on the device geometry, operating conditions and measurement apparatus and thus, are only truly useful when cited along with this information or when used to compare devices tested under identical circumstances.

Mostly, the point at which mobile charge carriers are first introduced into the organic film does not correspond to $V_{gs} = 0$. For a *p*-channel semiconductor, a mismatch between the Fermi level of the metal and the organic HOMO leads to charge transfer between the metal and the organic, resulting in a dipole and band bending in the organic. This dictates the application of a nonzero V_{gs}, just to achieve the flat-band condition. Furthermore, if there are large numbers of deep traps present in the film, these will have to be filled before the channel can conduct. To handle these conditions, it is convenient to define a threshold gate voltage, V_T, necessary to induce mobile charges [15]. At low V_{ds}, I_{ds} increases linearly with V_{ds} (linear regime) and is approximately determined from the following Eqn.

$$I_{ds} = \frac{W}{L} C_i \mu \left(V_{gs} - V_T - \frac{V_{ds}}{2} \right) V_{ds} \tag{1.2}$$

where μ is field carrier mobility, W the channel width, L the channel length and C_i the capacitance per unit area of the insulator layer.

The mobility, μ, which describes how easily charge carriers can move within the semiconductor layer under the influence of an electric field, can be calculated in the linear regime from the transconductance,

$$g_m = \left. \frac{\partial I_{ds}}{\partial V_{gs}} \right|_{V_{ds}=\text{const.}} = \frac{WC_i}{L} \mu V_{ds} \tag{1.3}$$

by plotting I_{ds} versus V_{gs} at a constant low V_{ds}, with $-V_{ds} << -(V_{gs} - V_T)$ and equating the value of the slope of this plot to g_m. For $-V_{ds} > -(V_{gs} - V_T)$, I_{ds} tends to saturate (saturation regime) due to the pinch-off of the accumulation layer and is given by the Eqn.

$$I_{ds} = \frac{W}{2L} \mu C_i \left(V_{gs} - V_T \right)^2 \tag{1.4}$$

In the saturation regime, μ can be calculated from the slope of the plot of $|I_{ds}|^{½}$ versus V_{gs} [18].

1.2.2 Materials in Organic Thin Film Transistor

It is now well understood that the performances of OTFTs rely on the functional materials employed in the different layers: organic semiconductors, insulators and conducting materials. The semiconducting layer in Fig. 1.1 can be a small molecule organic material, usually deposited by vacuum deposition or a polymeric semiconductor deposited by solution processable methods such as spin coating or dip coating. Organic materials are characterized by lower field effect mobility in comparison to the conventional semiconductors. With continuous efforts, mobilities of conjugated small molecules have increased from less than 0.05 cm^2/Vs in 1993 [19], by several orders, now in excess of 43 cm^2/Vs for single crystal rubrene [20]. For conjugated polymers, a successful realization of high mobility conjugated polymer is regioregular poly(3-hexyl thiophene) (rr-P3HT), which has been the benchmark of polymeric semiconductors. The highest carrier mobility of 0.1 cm^2/Vs for polymeric semiconductors, with rr-P3HT was demonstrated in 1996 [21]. Amazingly, high mobility of over 10 cm^2/Vs [22] for polymeric semiconductor has also been achieved. With optimization of fabrication methods and synthesis of novel functional materials, the mobility can be undoubtedly increased further. The earliest organic semiconductors were *p*-channel materials (hole carriers), though remarkable progress has been made recently in designing *n*-channel (electron carriers) OSCs, in spite of their lower stabilities [23]. Discussion in detail, on different types of OSCs used in OTFTs is done in section 1.5.1.

The selection of the material for the insulator or gate dielectric layer is vital for the performance of the OTFT. The accumulation of charge carriers at the semiconductor-insulator interface on applying a V_{gs}, is strongly determined by the relative permittivity (*k*) and the thickness of the insulator. The insulator layer material should exhibit high *k* and high electrical resistance. Inorganic materials such as silicon dioxide, silicon nitride, zirconium oxide, aluminium oxide etc. [24] and polymeric insulators such as poly(4-vinyl phenol), poly(vinyl alcohol), poly(methyl methacrylate), etc. [25] are generally employed as the dielectric layer in an OTFT. High-*k* insulating materials, such as hafnium oxide, lanthanum oxide, polyvinylidene fluoride and its copolymers are beneficial in attaining a steep sub-threshold slope and low threshold voltage [26].

The selection of material for electrodes is of equal importance as that of semiconductor and dielectric material, to achieve high performance organic transistors. Electrode material for the source and drain electrodes should be selected in such a way that it does not produce a high contact resistance. The contact between electrode and OSC film determines the charge injection in organic device. Poor charge injection due to high contact resistance always limits the performance of devices. It indicates that the contact must possess a low interface barrier with the active semiconductor layer for aiding a large number of charge carrier injection [27]. Metals such as gold, palladium or platinum are often used in *p*-type OTFTs due to their high work function (~ 5 eV). The *p*-type OSCs exhibit their HOMO level near 5 eV and hence have close match with the work function of such metal electrodes [28].

A novel series of conducting polymers (CPs) are also employed for fabricating the electrodes, so as to achieve a completely flexible organic device. Conducting polymer, poly(3, 4-ethylenedioxythiophene): polystyrene sulfonic acid (PEDOT-PSS), polyaniline: polystyrene sulphonic acid (PANi-PSS), polyaniline doped with camphor sulphonic acid (PANi-CSA) show high work function, dispersibility and stability, which make them suitable for solution-processed flexible and transparent devices [29]. The material for gate electrode should have good patterning capabilities and adhesion with gate dielectric and substrate, respectively. Moreover, the work function of the gate metal should be comparable to that of semiconductor layer for attaining low threshold voltage. Such electrode materials include heavily doped silicon, aluminium, gold, palladium and indium tin oxide (ITO) [30]. Typical OTFT device structures are shown in Fig. 1.3. Source and drain electrodes are deposited on top of the OSC layer in a top contact geometry. Alternatively, OSCs can be deposited onto the already patterned source and drain electrodes to give bottom contact geometry [14].

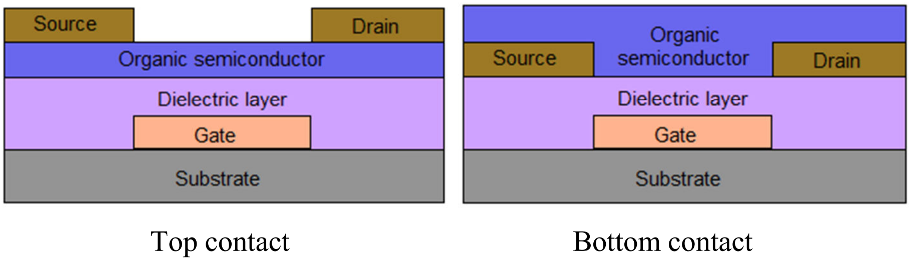

Fig. 1.3: Typical OTFT architectures.

1.3 Application of Organic Thin Film Transistor in Sensors

Transistor based sensors normally have high sensitivity because of the combined functionality of signal transduction and amplification in one device [31]. As flexibility and large area processes are the prerequisites for this application, organic electronics plays an important role in this field, allowing the fabrication of sensors on large and even non-planar surfaces at relatively low costs. To date, many OTFT based sensing elements have been successfully demonstrated for the sensitive detection of biological species, chemical compounds, temperature, pressure and light, illustrating the potential and rapid growth of this exciting research area [32]. Biological sensors sense analytes by incorporating biological molecules, such as antibody, DNA, bacteria, etc., as the biological elements whereas chemical sensors normally consist of a chemically sensitive layer along with a physical transducer and can give information on ambient environment [33].

Among the OTFT based mechanical sensors, tactile, temperature and pressure sensors are important. In this case, the sensed parameter is directly transduced and amplified by the transistor; as a result, current or voltage signals with high signal-to-noise ratios are directly available for the readout and conditioning electronics [34-35]. If a sensed parameter such as pressure results in deformation of the morphology of the OSC film, a marked variation of the output current can be detected, due to the alteration of charge transport mechanism, as recently demonstrated for several semiconductors and device architectures [36-38].

With regard to application in digital and analog electronic circuits for sensors, organic electronics has grown from the single unit fabrication into the circuit level integration [1]. The flatness and rigidity of silicon based electronics restrict its use in curvilinear objects. Conformable flexible electronics can accomplish real-time sensing on such objects, presenting better signal quality by being in close proximity to the site of interest. All-organic complementary logic circuit with combination of both *p* and *n*-type transistors would help realize the benefits of silicon-like logic circuits, in terms of ease of design, robust operation and low power dissipation [39]. However, *n*-type OSCs exhibit much lower mobilities than that of *p*-type ones, which leads to a high static power dissipation and low operational performance stability for the complementary circuits and thus has limited the development of organic circuits [40]. As a result, over the years, most researchers have resorted to the less desirable unipolar circuit options, utilizing only the single *p*-type semiconductor [41]. Three years after the major achievement in realizing organic integrated circuits [42], flexible organic circuits were demonstrated by Philips Research Laboratories for the first time in 1998 [43]. This was also the first organic integrated circuit with definite logic functions in reasonably large scales. Over the years, the fastest organic 5-stage ring oscillators were realized with a signal propagation delay of 5 µs/stage with voltage as low as 7 V [44].

In the analogue regime, the simplest organic analog circuit is a single-stage common-source (CS) amplifier which acts as a voltage or transconductance amplifier [12]. Flexible common-source amplifiers (as well as all other amplifier types) are usually designed in an unipolar configuration with an active *p*-type TFT and different pull-up loads [45-46]. Many amplifier topologies, from simple buffers to more complex differential amplifiers have been shown using unipolar *p*-channel OTFTs [47-49]. Marien et al. demonstrated differential amplifier with pentacene based transistors, optimizing basic differential pairs by following four different techniques. Their circuit showed a gain of 18 dB. After shelving for four months and stressing at 15 V for 10 days in ambient environment, DC output was not significantly altered and AC gain dropped only by 4 dB. Thus, it was demonstrated that even with pentacene, analog circuits could deliver satisfactory and acceptable performance [50]. Recently, Reuveny et al. demonstrated organic amplifiers based on small organic semiconductor, DNTT. They achieved voltage amplification of 13 dB with cut-off frequency 2.5 kHz. A high uniformity in the gain, among six amplifier circuits, 13.0 ± 1.2 dB over 4×4 cm^2 was also demonstrated. The open loop design gave gain bandwidth product of 45 kHz with operating voltage of 7 V [49].

1.4 Application of Organic Thin Film Transistor in Acoustic Sensor

OTFT possesses the dual functionality of transduction of pressure signal and also as read out circuits for application in acoustic sensors. The development of low cost and large area compatible pressure-sensing pixels with sufficient sensitivity is of fundamental importance to the realization of these applications. The first attempt to develop OTFT based pressure sensors relied on engineered exploration of organic transistors as transducers for conductive rubber based pressure-sensing elements [38, 51]. Static pressure sensing has also been demonstrated incorporating MOSFET technology [52]. However, the technology based on rigid Si substrate is difficult to implement on flexible substrate, costly due to the Si-manufacturing processes and provides lower sensitivity of pressure than that demonstrated for pressure sensors developed by microstructuring the dielectric layer of the OTFT [34, 53]. These flexible capacitive pressure sensors with microstructured polydimethylsiloxane (PDMS) dielectric layer had a pressure sensitivity of up to 8.4 kPa^{-1} [53] and response time in the milliseconds range in both air and water media. The direct dependence of the output current on the capacitance in OTFT enabled the sensing of an applied pressure. A broad range of sensors which can withstand harsh, murky and cluttered seawater environments, find application in underwater acoustic sensing. Since OTFTs have been demonstrated to operate stably underwater [54], such pressure sensors integrated with organic transistor based read out circuits or amplifiers will find application in ultrasensitive pressure detection, target detection and imaging.

Recently, a unique device geometry with flexible suspended gate organic thin film transistors (SGOTFTs) was adopted to provide a powerful strategy for the development of low-cost ultra-sensitive pressure sensors. The SGOTFT with sensitivity of 192 kPa^{-1}, featured a fast response time of < 10 ms and a low power consumption of < 100 nW when operated at a battery voltage of 6 V, enabling real-time response to acoustic vibrations [55]. In a transducer configuration, pressure sensor based on ferroelectric polymer composite functioned as a pressure transducer, a touch sensor, a pressure-activated switch and as a microphone, sensing pressure > 1 MPa [56]. Capacitive coupling of polymer ferroelectret actuators to the gate electrodes of OTFTs on flexible substrates is a promising route, which showed sensitivity to static pressure of loads ≥ 2 kPa [57].

In one of our papers [58], we have demonstrated a hybrid laminated polyvinylidene fluoride (PVDF)/OTFT structure on a sheet polymer foil which reduced the parasitic capacitance, traditionally seen coupling to silicon substrates, by fabricating the structure on an insulating plastic. The concept of using OTFTs monolithically integrated on freestanding PVDF sheets to sense strain, stress or pressure has also been demonstrated [59]. The transistors formed a transimpedance amplifier directly at each sensing site, allowing conversion of the piezoelectric charge signal into a current signal, which could be externally detected. The literature in the field of acoustic sensors fabricated with OTFTs is very scanty but recent progress made in the field of tailored functional materials, engineered fabrication methods of sensors and monolithic integration of electronic interface with sensors would pave the path to high sensitive OTFT based acoustic sensors.

1.5 Conjugated Materials for Organic Electronics

The serendipitous discovery of the conducting polymer, polyacetylene, by Shirakawa et al. in 1977 [60] was a major breakthrough that opened up many new and exciting applications of organic electronics. By the mid-1980s, several investigators were exploring π-conjugated small molecules and polymers to gain advantage of their unique semiconducting properties, paving the way to the emergence of the field of organic electronics [61-62].

1.5.1 Organic Semiconductors

Organic and polymeric semiconductors are the core materials for constructing OTFTs. The vital property that allows organic molecules to conduct electronic charge is molecular conjugation, i.e. the presence of alternating single and double bonds between covalently bound carbon atoms. The effect of conjugation is that, one of the four valence electrons of each carbon atom that participates in the conjugated system gets delocalized, resulting in efficient transport of electronic charge along a conjugated molecule [63]. Most of the high mobility values in OTFT reported so far have been achieved for *p*-type OSCs, which conduct holes in the channel. As discussed in section 1.3, for many electronic applications, *n*-channel OTFTs using *n*-type OSCs, which conduct electrons, are required to make complementary metal oxide semiconductor (CMOS)-like logic circuits together with the *p*-channel OTFTs. One significant reason for the lack of high performance *n*-type OSCs is the non-availability of sufficient electron withdrawing building blocks that can be used for making *n*-type semiconductors with stable electron transport properties. When an electron is injected to the OSC in an OTFT, it is similar to an electrochemical reduction process. If the OSC has a rather low electron affinity (or high LUMO energy), the injected electron in the LUMO of the semiconductor is at a high-energy state. Such an electron is susceptible to interact or react with some species such as the Si-OH groups on the SiO_2 dielectric surface, oxygen and water in ambient air and thus the injected electrons get trapped. Therefore, electron transport is inhibited or weakened [Fig. 1.4].

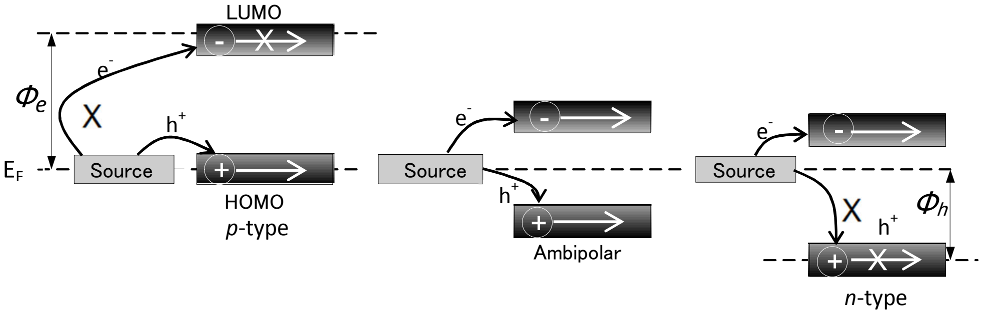

Fig. 1.4: Schematic showing the relationships among the HOMO and LUMO energies of the organic semiconductor, Fermi energy (E_F) of the source electrode and the polarity of the majority charge carriers of the OTFT device, ('X' denotes the inhibition of charge injection, 'Φ_e' and 'Φ_h' denote the electron and hole injection barrier heights, respectively).

Few polymers, in addition to having very high electron mobilities, also possess relatively high HOMO energies. As a consequence of this, in these semiconductors, insufficient hole injection barrier heights (Φ_h) is created that cannot block hole injections and hence, allow stable hole transport as shown in Fig. 1.4. These materials exhibit ambipolar (hole and electron) charge transport properties, which are not desirable for CMOS-like logic circuits because ambipolar OTFTs normally have high off current (I_{off}) and low I_{on}/I_{off} ratio [64].

Small molecule OSCs have been widely used and showed reasonable performance in various organic devices. Pentacene [Fig. 1.5] is one of the commonly studied semiconductors for OTFTs. Klauk et al. [65] reported μ of pentacene based OTFTs as high as 1 cm^2/Vs. A well-known derivative of pentacene is triisopropylsilylethynyl (TIPS)-pentacene, which has bis (TIPS) on the 6, 13 positions of the pentacene backbone [66]. μ as high as 4.6 cm^2/Vs has been observed in TIPS-pentacene OTFTs, constructed using solution based processes [67].

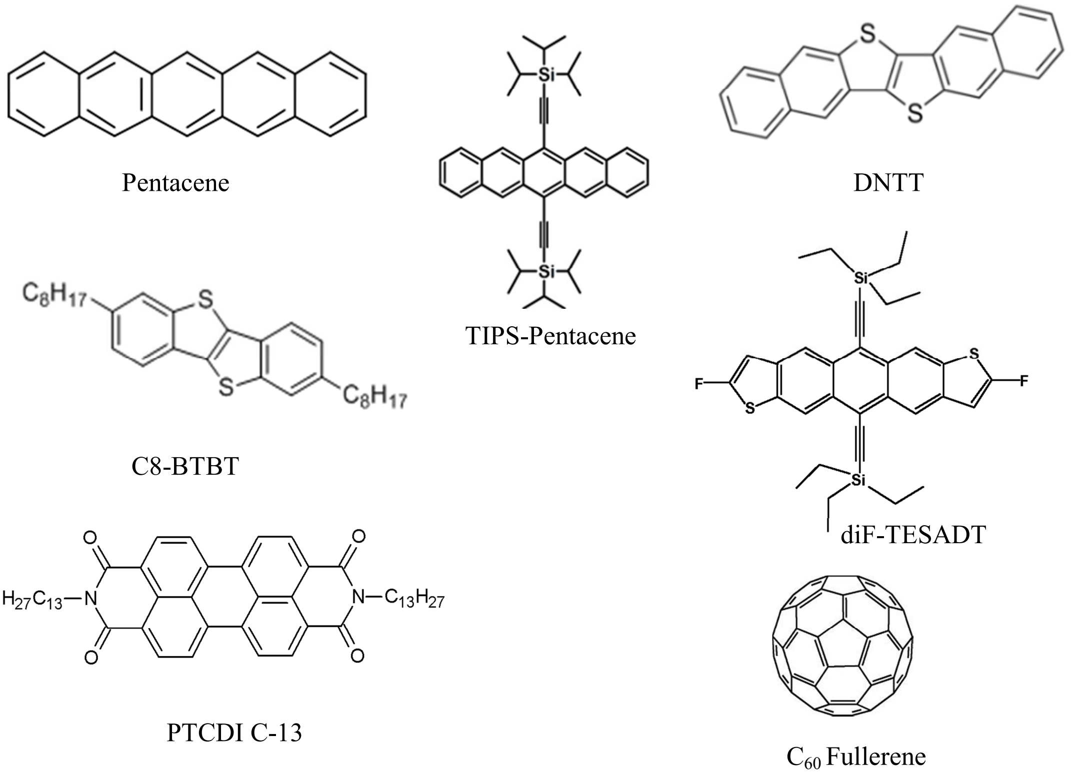

Pentacene

TIPS-Pentacene

DNTT

C8-BTBT

diF-TESADT

PTCDI C-13

C_{60} Fullerene

Fig. 1.5: Chemical structure of 'small molecule' organic semiconductors.

Currently, the standard mobility of pentacene and its derivative is 1–10 cm^2/Vs. Dinaphtho [2,3-b:2',3'-f] thieno [3,2-b] thiophene (DNTT), 2,7-dioctyl-[1] benzothieno [3, 2-b] benzothiophene (C8-BTBT) and 2,8-Difluoro-5,11-bis (triethylsilylethynyl) anthradithiophene (diF-TESADT), shown in Fig. 1.5, have also demonstrated great potential to achieve high μ. For example, C8-BTBT OTFTs with off-center spin coating showed μ > 40 cm^2/Vs [68]. Of the several *n*-type OSCs, C_{60} and its derivatives are the most commonly studied ones. OTFTs based on thermally evaporated C_{60} exhibited electron mobility of 0.08 cm^2/Vs [69]. N,N′-ditridecylperylene3′,4,9,10-tetracarboxylic diimide (PTCDI-C13) is a typical *n*-type material that has attracted attention since a high electron mobility of 2.1 cm^2/Vs in vacuum was reported [70].

Polymeric OSCs are lower in cost and mechanically flexible than small molecule semiconductors, making them ideal for flexible electronics. However, polymers are more complex systems and there are challenges balancing their performance and solubility. One of the most studied polymers for *p*-type OTFTs, poly(3-hexylthiophene) (P3HT), though exhibited high solubility in various solvents, the mobility was very low (10^{-5}–10^{-4} cm^2/Vs at room temperature) [71]. Significant efforts have been made to modify its molecular structure and to enhance the performance. Owing to the presence of only head-to-tail couplings in regioregular P3HT, formation of uniform microstructures is favoured and significant improvement in OTFT mobility [21, 72] is observed. Poly(2, 5-bis(3-tetradecyllthiophen-2-yl) thieno [3,2-b] thiophene) (PBTTT) has potential for giving high performance OTFTs due to its ability to form highly organized microstructures on annealing. Mobility of 1.3 cm^2/Vs were achieved with annealed PBTTT based OTFTs [73]. Chemical structure of a few polymeric semiconductors is shown in Fig. 1.6.

Donor- acceptor (D-A) copolymers that are recently more commonly studied, show higher mobility than the conventional semiconducting polymers for both *n* and *p*-type. In one of the D-A copolymers, diketopyrrolopyrrolethieno[3,2-b]thiophene (DPPT-TT), based OTFTs, due to the small bandgap of the material, show substantial ambipolar characteristics. Chen et al. [74] reported that DPPT-TT OTFTs exhibited well-balanced ambipolar transport, with both electron and hole mobilities exceeding 1 cm^2/Vs. In another example, electron withdrawing properties of the benzothiadiazole (BT) group in the conjugated polymer poly(9,9-di-n-octylfluorene-alt-benzothiadiazole) (F8BT), make it a good candidate for electron transport in OTFTs [75]. Sirringhaus's group has demonstrated increase in crystallinity of semiconducting polymer film of indacenodithiophene-co-BT (IDT-BT) by annealing process, that resulted in a nearly disorder-free polymer, exhibiting $\mu \approx 2$ cm^2/Vs in amorphous phase [76]. High performance of OSCs depend both on the molecular structure and processes adopted in device fabrication.

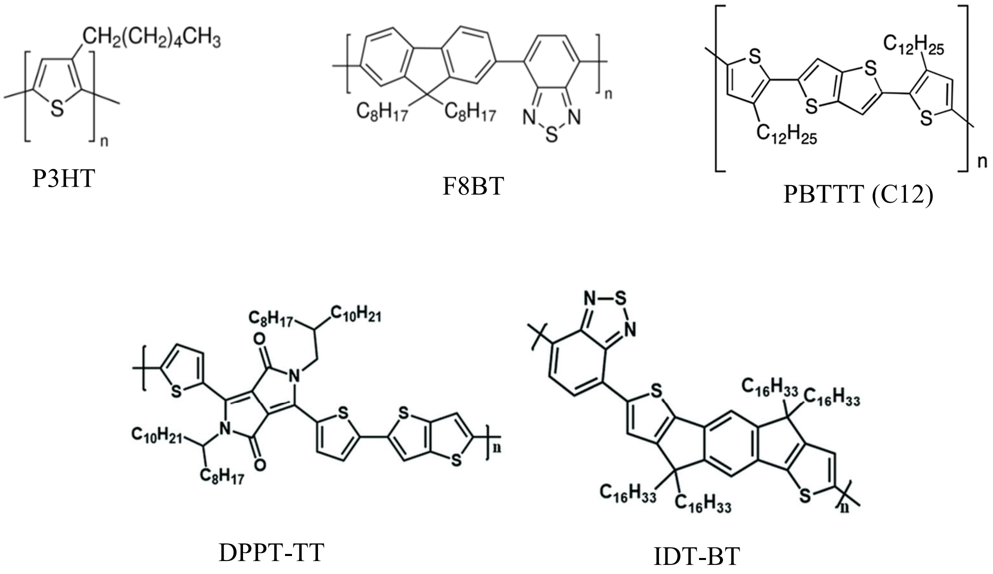

P3HT F8BT PBTTT (C12)

DPPT-TT IDT-BT

Fig. 1.6: Chemical structure of 'polymeric' organic semiconductors.

1.5.2 Charge Carrier Transport in Organic Semiconductors

The phenomenon of charge transport in the amorphous and organic semiconductors is different from the conventional semiconductors and metals. In the former, it is phonon assisted, whereas in the latter, phonon scattering limits the transport efficiency. Till date, different theories on microscopic charge transport mechanisms have been proposed [77-78]. Theories of charge transport can be roughly classified based on the structural disorder or crystallinity of the semiconductors.

1.5.2.1 Band transport

For disorder-free OSCs, which are mainly single crystalline materials [79-80] or certain conjugated polymers with extremely low torsions of chains [76], classic band-like transport is expected. Atoms combine to form molecules, which creates molecular orbitals. The highest molecular orbital filled with electrons is denoted as HOMO and the lowest molecular orbital devoid of electrons as LUMO. HOMO and LUMO in OSCs are used synonymous to the opposing edges of the valence and conduction bands in traditional semiconductors. They are separated by an energy gap. Generally, the electronic properties of a semiconductor are strongly influenced by the positions and distances of the opposing edges of the valence and conduction band. Charge transport of holes in the valence band and of electrons in the conduction band is limited by scattering of the charge carriers at lattice vibrations or impurities. The mobility of charge carriers decreases with elevated temperature because lattice vibrations are less pronounced at lower temperatures [81]. In these semiconductors, charge carriers move as highly delocalized plane waves in wide bands and have a very high mobility ($\mu >> 1$ cm^2/Vs).

1.5.2.2 Hopping transport

In general, OSCs are considered as disordered systems where band like transport between different molecules does not seem appropriate. Here, hopping transport provides a better explanation of the charge transport [82]. In this model, free movement of charge carriers is not possible. Instead, they hop between neighbouring hopping sites. When a charge carrier hops to a near-by site, a local deformation in the polymer is created due to its presence. The pair of charge carrier and deformation is called polaron and is considered as a single quasi-particle. In order to move between sites, the polaron has to overcome an energy barrier. The probability of crossing this energy barrier and hopping between sites increases with elevated temperatures [83]. The prominent among the hopping mobility models is the Variable-range Hopping mobility (VRH) model [78]. According to the VRH model, charge carriers hop between localized electronic states by quantum-mechanical tunnelling through energy barriers. The probability of a hopping event depends on the hopping distance and the energy distribution of the localized states. Specifically, charge carriers either hop over short distances with large activation energies or over long distances with small activation energies. As hopping is thermally activated, the mobility increases with increase in temperature. On increasing gate voltage, charge carriers accumulated in the channel fill the states that are lower in energy, thereby reducing the activation energy and increasing the mobility [83].The VRH model is usually discussed in the context of amorphous or highly disordered semiconductor films with room-temperature mobilities below 10^{-2} cm^2/Vs

Many small-molecule OSCs that have a strong tendency to form polycrystalline films, with low extent of structural disorder than single crystalline materials, the mobility edge model is applicable and it is similar to the multiple trap and release (MTR) model [84]. As a result of the regular molecular arrangement, the delocalized orbitals of nearby molecules overlap partially, thereby enabling more effective charge-carrier transfer and carrier mobilities that are much larger than in amorphous semiconductor films, usually well above 10^{-2} cm^2/Vs. Such large mobilities are not easily explained with the VRH model.

1.5.3 Conducting Polymers

In order to exploit the potential of OTFTs completely, the adopted process technology has to be augmented for low-cost fabrication techniques. The most suitable approach would be to use all-organic layers for interconnects and electrodes based on simple patterning techniques. The technology for fabrication of all-polymer circuits demand the requirement for CPs with suitable work functions that can be patterned by solution processable techniques such as spin coating. Soon after the discovery of a ninefold increase in conductivity of polyacetylene after doping with AsF_5 [60], a series of stable CPs, including polypyrrole (PPy), polyaniline (PANi) and polythiophene (PTh) were reported by the end of the 1970s to the beginning of the 1980s with promising applications in electronic equipment, antistatic formulations, corrosion protection, light emitting devices, light weight batteries, transistors, photodiodes and sensors [85].

Oxidative coupling of monomers is the basis for synthesis of the CPs. The first step in the synthesis, the oxidation of the monomer can be by any one of the three initiation routes, chemical, electrochemical or photo-induced. In the chemical route, chemical oxidants (such as ammonium persulphate or ferric chloride) are employed to oxidize the monomer [86]. In the electrochemical route, the monomers are oxidized electrochemically [87] and in the photo-induced method, light oxidizes the monomer with a photo initiator [88]. The advantage of the chemical method is that it provides various possible routes to synthesize variety of CPs, along with the possibility of large-scale production, which is currently not possible with electrochemical route. Electrochemical polymerization can produce very thin film of CPs, whereas very thick films or powders are usually produced by the chemical method. As compared to the chemical route, polymerization by photochemical method is of more benefit because irradiation results in the radical formation through hydrogen abstraction, which is generally more efficient than direct fragmentation via a thermal reaction. From a thermodynamic viewpoint, photochemical polymerization can resolve the problem of large activation barriers for the reaction, which is the limitation of chemical polymerization [89]. The selection of the synthesis route generally depends on the application intended for. The structures of some of the CPs are given below in Fig. 1.7.

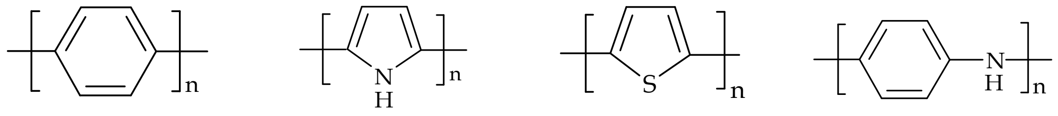

Poly(para-phenylene) Poly(pyrrole) Poly(thiophene) Polyaniline

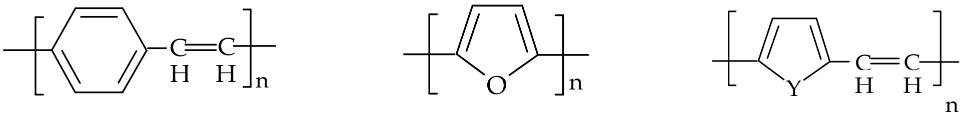

Poly(phenylene vinylene) Poly(furan) Poly(hetero aromatic vinylenes)

Fig. 1.7: Structures of some conducting polymers.

Conjugated organic polymers are either electrical insulators or semiconductors. The concentration of free carriers in these materials is very low at normal temperatures owing to the relatively large band gaps. Therefore, in spite of having backbone structures well suited to conduction (i.e. high carrier mobilities), the low carrier concentration results in negligible conductivity in conjugated polymers. Semiconducting conjugated polymer are made conducting by reacting or doping them with a reducing or oxidizing agent or a protonic acid, resulting in highly delocalized polycations or polyanions [90]. The extended π-systems of conjugated polymer are highly prone to chemical and electrochemical oxidation and reduction. The concept of doping is the central, unique, fundamental factor, which differentiates CPs from all other types of polymers. During the doping process, an organic polymer, either a semiconductor or insulator, having a small conductivity, typically in the range of 10^{-10} to 10^{-5} S/cm, is converted to a polymer, which is in the metallic conducting regime (nearly 1 to 10^4 S/cm) [91]. The controlled addition of usually small (≤ 10%), non-stoichiometric quantities of known chemical species (such as low molecular weight acids) results in dramatic changes in the electrical, electronic, optical, magnetic and structural properties of the polymer. The significant physical size of the dopant and also the extensive charge transfer that takes place between the polymer chain and the dopant perturbs the polymer extensively. This causes both the dopant and polymer to become ionic and leading to alterations in the geometry of the chain. The process of doping is reversible and produces the original polymer with no or little degradation of the polymer backbone. Both doping and dedoping processes, involving dopant counter ions which stabilize the doped state can be carried out either chemically or electrochemically.

Though highly conductive (> 100 S⁄cm), doped CPs are insoluble in common solvents, restricting their use in proposed applications of OLEDs and OTFTs. To overcome the intractability of CPs, polymeric acids, instead of small-molecule acids have been used as counterions to maintain charge neutrality in doped poly(ethylene dioxythiophene), or as proton sources for doping PANi, effectively rendering these materials water dispersible [92]. But, such improvement in processability comes at the cost of electrical conductivity, apparently due to additional structural disorder introduced by the polymeric acid during polymerization. CPs templated with polymeric acid dopants, thus frequently have electrical conductivities (< 1 S/cm) that are one to two order lower than those of small-molecule acid doped systems. When these CPs are incorporated as electrodes in OTFTs or as anodes in organic solar cells and OLEDs, the bulk resistance of the CPs severely limits device performance [93]. Exposing doped CPs to certain selective reagents can enhance electrical conductivities through a process of secondary doping [94]. Secondary doped processable CPs with required conductivity are highly essential for the development of all polymer organic electronic circuits for large area sensors.

1.6 Patterning of Conducting Polymers

Doped forms of conjugated polymers are potential alternatives to metallic electrodes, conducting channels and connecting wires since their conductivity and work function can be tailored over a wide range by changing the doping level. Various techniques have been developed for the formation of patterned microstructures of CPs. Polyaniline and polythiophenes represent two examples of organic conductors that are widely studied. The non-conducting (undoped) form of PANi is soluble in some common organic solvents, whereas the doped PANi is typically insoluble. Direct photopatterning of conducting PANi can take advantage of this solubility difference [95]. UV or electron-beam exposure of PANi mixed with onium salts through a mask initiates decomposition of the onium salts and generates acid. The acid converts the exposed PANi into insoluble conductive form, with onium salts as the dopant, whereas the unexposed (undoped and nonconductive) PANi that is soluble can be removed by washing with N-methylpyrrolidinone (NMP) [43]. Photolithography, which is the conventional technique in inorganic semiconductor industry, has been explored for patterning polymer electrodes. Halik et al. fabricated all-organic pentacene TFTs on polymeric substrates, with photolithography-patterned PEDOT-PSS contacts [96]. A similar photo-induced patterning method, called photochemical patterning was developed by Gelinck et al. They demonstrated all-polymer integrated circuits fabricated by fully-solution-processed methods with conducting PANi electrodes, defined by photochemical conversion through a shadow mask [97].

Though the process of photolithography is adequately mature and capable of patterning with high resolution, its application in patterning layers of OTFTs is rather limited due to degradation of OSCs upon exposure to the etching chemicals. Screen printing, which is much cheaper and suitable for large scale production than photolithography, has been employed in OTFTs much earlier than photolithography. The first all-organic TFTs were demonstrated way back in 1994 by Garnier et al., of which the electrodes were all screen-printed from a graphite based ink, while the small molecular semiconductor was thermally evaporated [98]. Most recently, photolithography-patterned silicon sheet was used as the stencil to improve the resolution of screen printing by Hyun et al. [99] in an all-solution processed, electrolyte gated transistors.

Microcontact printing, a non-photolithographic technique, which transfers patterns from stamps, can achieve a resolution as high as that of photolithography while retaining low cost. An electron-transfer blocking layer was patterned by Parashkov et al., by this method on a gold plate to realize selective electro-polymerization of PEDOT-PSS as source and drain electrode with final channel length as small as 10 µm [100]. The electrodes were then transferred onto a polyimide substrate where polyvinyl alcohol and pentacene were deposited as the dielectric and semiconductor layer. Another cost-effective and simple patterning technique is inkjet printing. The advantages of its fully additive feature, flexibility in pattern design and low material consumption, make inkjet printing an attractive deposition technique in OTFT fabrication. The patterning resolution of the process, however, is generally tens of micrometers, attributed to the difficulty in controlling the size of droplet and ink-spreading on substrates. To overcome the resolution limitation, methods have been demonstrated by depositing the functional ink onto a substrate containing a predefined surface-energy pattern. The deposited ink droplets could be split to form a narrow gap [101] on the substrate and sub-micrometer channel length was achieved by inkjet printing of PEDOT-PSS ink. To further exploit the direct-writing capability by inkjet printing, a lithography free nanopatterning method was developed in which a self-assembled surface layer induced the dewetting of PEDOT-PSS, resulting in channels of sub-micrometer size [102]. A direct-writing patterning technique to pattern organic electrodes with 2 µm resolution by inkjet printing was developed by modifying the surface wettability of the polyethylene terephthalate (PET) surface with PVA, achieving high resolution by direct inkjet printing [103].

The method of selective patterning of various types of biological materials with parylene lift-off process have recently been employed to pattern CP electrodes [104]. Patterning resolution of 20 µm with PEDOT-PSS was achieved by this method. OTFTs with conductive polymer composite, PANi-PSS electrodes were fabricated in the present study and reported for the first time a resolution as high as 5 µm, by a simple modified parylene lift-off process. The functionality of the conducting and semiconducting material is not affected by this technique and it is fully amenable for patterning on a flexible substrate [105].

1.7 Polyaniline

Among the CPs, polyaniline (PANi) has received considerable interest because of the ease of synthesis, solubility, high chemical and thermal stability of both its doped (conducting) and undoped (insulating) forms. The wide range of electrical, optical and electrochemical properties makes PANi attractive as an electronic material. PANi differs from other inherently conducting polymers (ICPs) such as polythiophenes and polypyrroles, in that, it possesses three readily accessible oxidation states [Fig. 1.8] with the half oxidized state (emeraldine) being highly conductive in its protonated state. PANi also differs from polypyrroles and polythiophenes in that the nitrogen atom participates directly in the polymerization process and also in the conjugation (of the conducting form of the polymer) to a larger extent than the N and S heteroatoms of polythiophene and polypyrrole. In addition, the possibility of rapid conversion between the salt and base forms of PANi, by treatment with acid or base, makes it unique among ICPs [106]. PANi is not charge conjugation symmetric i.e. the valence and conduction bands are asymmetric to a great extent. A partial oxidation of PANi results in an increase in electrical conductivity owing to the reorganization of bonds. The physico-chemical properties of PANi are strongly dependent on the ratio of quinone imine and aryl amine units present.

Protonic acid doping in PANi occurs by proton addition to the polymer chain rather than by partial oxidation or reduction of the polymer π-system. Consequently, doping in PANi involves no change in the number of electrons associated with the polymer backbone. The doping of the base form of PANi was the first example of non-redox doping of an organic polymer to a highly conducting one by a process of this type [90]. Protonation of the partially oxidized, emeraldine base (EB) form gives the conductive form of PANi called the emeraldine salt (ES), as given in Fig. 1.9. Only the imine nitrogen atoms in the polymer backbone can be protonated in whole or in part to get the corresponding salts. Complete protonation of imine nitrogen atoms in the emeraldine base form of PANi results in a delocalised poly-semiquinone radical cation. The extent of protonation depends on the EB oxidation state and the pH value of the aqueous acid medium in which the polymerization is carried out. De-protonation of the ES form leads to the formation of EB form of PANi [106].

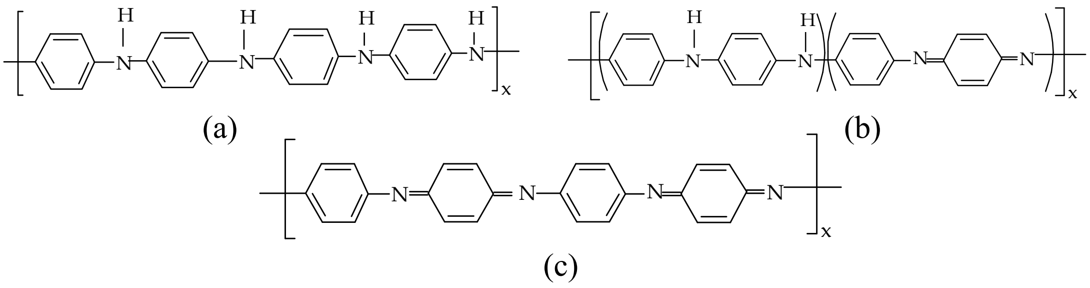

Fig. 1.8: Different oxidation states of PANi (a) Leucoemeraldine base (fully reduced) (b) Emeraldine base (half oxidized/reduced) and (c) Perigraniline base (fully oxidised).

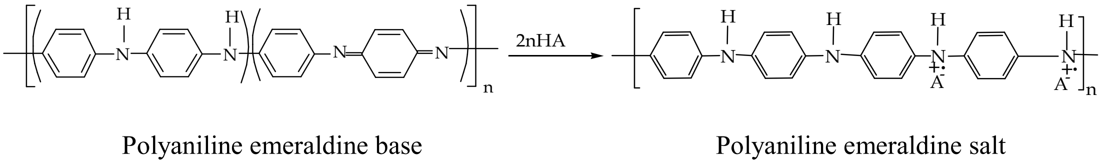

Fig. 1.9: Scheme representing proton doping in PANi.

PANi and its composites can be synthesized by a large number of synthetic routes with a variety of dopants. Among them, chemical synthesis, electrochemical oxidation of the monomers and polycondensation are the most popular ones, but many other uncommon approaches such as, photochemically initiated polymerisation and enzyme-catalyzed polymerisation are also investigated [107]. Due to their exceptional properties, PANi and its composites have been identified for a variety of applications including sensors, conductive coatings, electromagnetic shielding devices, electrostatic charge dissipation systems, supercapacitors, organic and polymer light emitting diodes, organic photovoltaic devices and rechargeable batteries [108]. Although specific conductivity and the temperature dependence of its conductivity are semi-metallic, all other properties, e.g. its thermopower must be classified as clearly metallic. PANi in its non-conducting or dedoped form exhibits a conductivity of ~ 10^{-8} S/cm. On a laboratory scale, it is possible to achieve considerably higher conductivities of PANi under certain conditions, e.g. 800-1000 S/cm [109]. PANi polymer blends may be developed with conductivity between 10^{-9} and 10^{2} S/cm. In the conductive state, it is green and may change its colour and its conductivity on exposure to a variety of media [110].

The use of PANi in various areas of electronics and engineering is restricted owing to its limited solubility. For application in organic electronic devices, dispersions of PANi that can form smooth patternable films are required. Nanostructured PANi that form stable dispersion in certain solvents have been synthesized employing various techniques [108, 111]. PANi dispersions can be efficiently patterned as hole injection layers (HIL) for passive and active matrix display and as electrodes in TFT applications. In order for OSCs to perform efficiently in an OTFT, proper energy band alignment between the metal and HOMO of the semiconductor is essential. This ensures a low voltage drop for injection of charge carriers in such systems. Work function of PANi can be tuned efficiently to achieve a proper alignment with the adjacent layers by controlling the concentration of the dopant acid or precursor acid during the synthesis of PANi [112].

1.8 Objectives of the Present Work

Flexible large area piezoelectric sensors for sensing acoustic signals are finding increased attention in advanced technologies such as SOunnd NAvigation and Ranging (SONAR). Polymeric large area piezo sensor arrays based on polyvinyledene fluoride have inherent low capacitance which results in attenuation of sensed acoustic signal. Large cable lengths employed for signal transfer to remote electronics further decay the signal due to the parasitic cable capacitance. Therefore, need for the interface electronic circuit to be in close proximity to the sensor is highly essential. Transistors are integral part of amplifier circuits used for amplifying signal output from any sensor. MOSFETs or junction field effect transistors (JFETs) are commonly used in such circuits. Amplifier circuits based on OTFTs can replace the MOSFETs or JFETs for on-site signal amplification. OTFTs, being flexible can also be monolithically integrated with the flexible piezo sensors to achieve lower signal attenuation, which is not possible with conventional silicon based electronics. Though, the performance of OTFTs is limited by their lower field effect mobilities, for low frequency applications of acoustic sensing, the reported values are sufficient. Hence, functional flexible amplifier circuits based on OTFTs are ideal for integrated acoustic sensor- amplifier system for operation at low frequencies. Main objective of this thesis is to develop materials and processes for the fabrication of high performance OTFTs. The OTFTs thus developed would be configured as amplifier circuit to demonstrate the proof of concept of signal amplification for low frequency applications.

For the fabrication of high performance OTFTs, for application in flexible amplifier circuits, suitable solution processable conjugated polymers in semiconducting and conducting forms have to be developed. Such polymers should also be amenable to conventional fabrication techniques (such as UV-photolithography and vacuum processing) and specialized techniques for their patterning. These polymers also have to be patternable as thin films on flexible substrates as the active or electrode layer of OTFT. A combination of solution processing, vacuum processing and photolithography is essential for the development of OTFTs for flexible electronic circuits. Once the materials with optimum properties are identified for different layers of OTFT, suitable patterning techniques have to be developed. Solution processable patterning techniques have the advantage of accessibility to large area substrates. Nevertheless, the solvents and other chemicals employed in the patterning processes should not affect the other layers of OTFTs.

Patternable conducting polymers reduce the charge injection barrier between the electrode and the semiconductor. Developing suitable solution processable patterning techniques for conducting polymers is a challenge, owing to their limited solubility in any common solvents. PANi, in its conducting form is a suitable polymer to be patterned as conducting electrodes of OTFTs. The conductivity of PANi can also be increased by two orders with a process of secondary doping with certain solvents such as *m*-cresol or dichloroacetic acid. To overcome the difficulty with solubilizing PANi, it can be synthesized in a dispersion form by templating with polymeric acid dopants such as poly(2-acrylamido-2-methyl-1-propane sulphonic acid) or polystyrene sulphonic acid. The PANi dispersions with nanostructured particles can be patterned as smooth films on flexible substrates. Patterning techniques by modifying the parylene lift-off method can be adopted, to pattern the conducting polymers as electrodes in the fabrication of OTFT. Novel patterning methods can bring about a technological revolution in the field of all-organic transistors, enhancing the potential for applications in large area flexible sensors.

Passivation of the channel material of the organic TFTs is extremely important to inhibit their degradation due to contact with moisture or oxygen. Compared to inorganic passivating materials that require high temperature deposition processes, passivation by organic barrier coatings with parylene are more effective. Parylene is a material that can be subjected to conventional photolithographic and dry etching processes. A patterning method that can simultaneously passivate and pattern the active semiconductor layer can be developed that could improve the OTFT performance to a great extent. A better understanding of the microscopic mechanisms that control the charge transport properties in OTFTs can lead to better organic electronic devices for specialized application. In this respect, physics based two dimensional numerical simulation can model various interface effects and obtain an advance idea of the electrical characteristics of the device of given dimensions, which otherwise requires tedious 'trial and error' fabrication processes. Suitably passivated organic TFTs, fabricated by dedicated processes for patterning of solution processable semiconducting and conducting polymers, can be used in the realization of flexible organic amplifiers. A flexible amplifier with required gain and frequency response can thus be realized with OTFTs fabricated by adopting optimized processes for different layers. Passivating layer of the semiconductor will ensure consistent operation of the amplifier for a much longer duration. In addition, real time sensing on any curved surface is also possible, opening the path for various applications requiring sensing of acoustic signal. The flexible amplifiers realized in the present study are intended to be used for amplification of low voltage signals generated by large area flexible acoustic sensors.

Taking into consideration, all these aspects, the objectives of the present work can be summarized as follows:

1. To synthesize solution processable polyaniline and its composites using different chemical and electrochemical routes, to be employed as conducting organic electrode in OTFT.

2. To synthesize solution processable regioregular poly(3-hexyl thiophene) and its copolymer with acrylates, to be employed as semiconducting channel layer in OTFT.
3. To develop efficient passivation and patterning methods using parylene C to protect the semiconducting channel layer in OTFT from moisture, oxygen and other environmental entities present in ambient conditions.
4. To develop novel solution processable patterning techniques to realize conducting polymer electrodes as charge injecting source and drain electrodes of OTFT.
5. To systematically analyse, by way of two dimensional numerical simulation, the microscopic mechanisms of charge injection in an OTFT, with metal and conducting polymer electrodes.
6. To compare the electrical characteristics and contact resistance in OTFTs fabricated with metal and conducting polymer source and drain electrodes.
7. To realize a single stage differential amplifier circuit with OTFTs, fabricated by optimized processes and materials, for the intended application of amplifying acoustic signals.

Chapter 2

EXPERIMENTAL TECHNIQUES

The materials used in the synthesis of conjugated polymers, fabrication of OTFT, experimental techniques employed for characterisation of synthesized polymers and device fabrication are discussed in this chapter.

2.1 Materials

2.1.1 Synthesis of Conjugated Polymers

Aniline (99.9%); ammonium peroxydisulphate (APS) (> 98%); poly(sodium 4-styrenesulfonate) (PSS-Na), M_w ~ 70,000; dichloroacetic acid (DCA) (99%); camphor-10-sulphonic acid (CSA) (98%); platinum foil, 0.05 mm thick (99.99%;) hydrochloric acid (HCl) (35-37%); ammonium hydroxide (NH_4OH) (28-30% ammonia basis); *m*-cresol (99%); chloroform ($CHCl_3$) ($\geq$ 99%); phosphoric acid (H_3PO_4) (85 wt% in water), were purchased from Sigma–Aldrich Chemicals, USA and used as such, except aniline, which was double distilled under reduced pressure and stored at 0 ºC. APS was dried over molecular sieves and under vacuum overnight. Whatman Nuclepore gold coated track-etched polycarbonate membrane filter, diameter: 1.3 cm, pore size: 0.8 µm, was used for the electrochemical template synthesis of PANi.

2,5- dibromo-3-hexylthiophene (97%); butyl magnesium chloride (2 M in diethyl ether); [1,3-Bis (diphenylphosphino) propane] Nickel (II) Chloride, (Ni(dppp)Cl); vinyl magnesium bromide (1 M in THF); 9 Borabicyclo[3.3.1]nonane solution, (9-BBN); sodium hydroxide pellets (98%), anhydrous; triethylamine, (99.5%); 2-bromopropionyl bromide (97%); t-butyl acrylate, (98%); methyl acrylate, (99%); cuprous bromide, (CuBr), (98%); N,N,N',N'',N''-pentamethyl diethylene triamine, (PMDETA) (99%); tetrahydro furan (anhydrous); methanol, anhydrous, (99.8%); chloroform, anhydrous, (99%); 1, 2-dichlorobenzene (anhydrous), (99%); sodium metal; benzophenone (99%); 4A molecular sieves, beads, 4-8 mesh; p- dimethoxy benzene (99%); toluene, (99.8%) were also purchased from Sigma–Aldrich Chemicals, USA.

2.1.2 Device Fabrication

Si (100) substrate and thermally oxidised Si wafer (2000 Å SiO_2) were purchased from Nova Electronic Materials, USA; Palldium metal (Pd) (99.95%) was purchased from Vacuum Engineering and Materials, USA. Shipley MICROPOSIT S1813 photoresist, MICROPOSIT MF 319 developer, MICROPOSIT remover 1165 and LOR 10A lift-off resist were purchased from Microchem Corp., USA. Semiconductor grade acetone and isopropyl alcohol (IPA) were purchased from Sigma-Aldrich Chemicals. Biaxially oriented, poly(ethylene naphthalate) (PEN) and polyimide film of thickness 50 µm (Goodfellow, UK) were used after cleaning with acteone, IPA and deionized water. Poly(4-vinyl phenol) (PVP), M_w 20000; Polyvinyl alcohol (PVA), (87-89% hydrolysed), M_w 85000-124000; Poly(melamine-co-formaldehyde) methylated (84 wt.% in 1-butanol), Propylene glycol methyl ether acetate (>99.5%); Pentacene (99%); hexamethyldisilazane (HMDS) (≥99%); ammonium dichromate (99%); acetone (>99.9%); 2-Propanol (99.9 %); were purchased from Sigma-Aldrich Chemicals, USA. Octadecyltrichlorosilane (≥ 85%), Fluka was used only inside glove box. Parylene C dimer was purchased from SCS Inc., USA.

2.2 Synthesis of Nanostructured Conducting Polyaniline

2.2.1 Chemical Oxidative Polymerization

PANi in the salt form was synthesized by chemical oxidation of the monomer, aniline with APS as oxidant in 1 M HCl solution [106]. Aniline (10 mL, 0.107 mol) was dissolved in 600 mL of 1 M HCl and the mixture was precooled to below 5 ºC in an ice bath. 200 mL of APS solution containing 5.6 g (0.025 mol) in 1 M HCl was added to the aniline solution drop wise over a period of 15-20 min with vigorous stirring. After 2 h, the precipitate was collected on a Buchner funnel and washed with four portions of 100 mL 1 M HCl. The precipitate was then transferred into a beaker containing 400 mL, 1 M HCl. The resulting mixture was stirred at room temperature for nearly 4 h, followed by filtration. HCl-doped PANi was obtained as a green powder after drying under dynamic vacuum at room temperature for 24 h. Scheme of synthesis of PANi by chemical oxidative polymerization is shown in Fig. 2.1. Part of the PANi in the salt form, as synthesized above was converted into the base form by stirring nearly 3 g of the polymer powder in an excess amount (500 mL) of 0.1 M NH_4OH at room temperature for 3 h. The resultant base form of PANi (EB) was filtered and dried under dynamic vacuum for 24 h. PANi in its base form was redoped with CSA to improve the processability. CSA and EB in 2:1 ratio (of CSA to EB repeat unit) were ground together in a mortar and pestle to obtain a completely protonated polymer of EB-CSA (PANi-CSA).

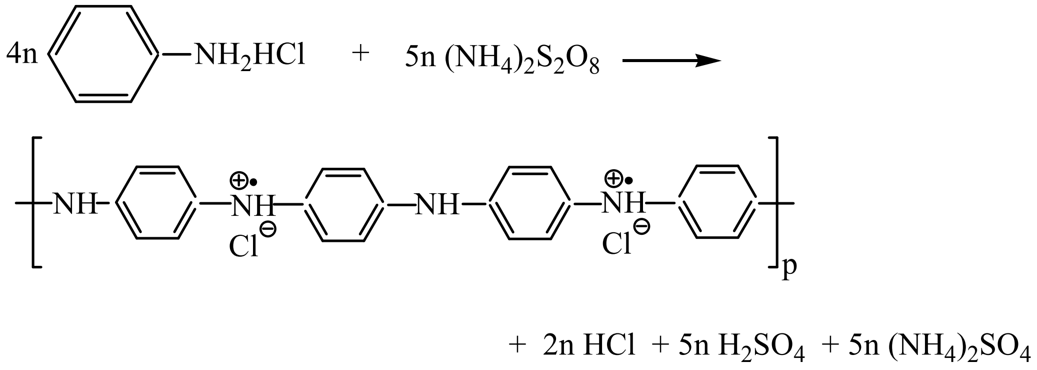

Fig. 2.1: Oxidation of aniline with ammonium peroxydisulphate.

PANi nanofibres were also synthesized using dilute polymerization with reduced concentrations of both monomer and oxidant. A typical dilute polymerization was carried out with 0.01 M concentration of monomer in 1 M HCl, with the ratio of monomer / APS maintained at 1.5. Rapid addition of APS and thorough mixing of the reaction mixture (before the initiation of polymerization) was done to inhibit the secondary growth on PANI nanofibers. Other concentrations of monomer such as 0.0075 M and 0.005 M were also used for synthesis. Nanostructured PANi was also synthesized with the monomer/APS ratio of 0.15. The filtered HCl-doped PANi was dried under dynamic vacuum at room temperature for 24 h, to obtain as green powder samples. The designations of the samples prepared with different concentrations of monomer and dopant is given in Table 2.1

Table 2.1: Designation of nanofiber samples synthesized by dilute polymerization method.

Sample designation	Concentration of monomer (aniline)	Molar ratio of monomer to oxidant
ALN1	0.01 M	1.5
ALN2	0.0075 M	1.5
ALN3	0.005 M	1.5
ALN4	0.01 M	0.15

2.2.2 Interfacial Polymerization

Chemical synthesis of the PANi nanofibers was carried out, employing the method of interfacial synthesis using APS in 1 M aqueous acid solution. In a typical synthesis, aniline was dissolved in 50 mL $CHCl_3$. Interfacial polymerization was carried out by adding the monomer solution to 50 mL of dopant acid solution mixed with APS, in a vial. HCl or CSA was used as the dopant acid. The molar ratio of the monomer to oxidant was always kept 4:1. The samples synthesized with 0.3, 0.2 and 0.1 M concentration of monomer were designated as INT1, INT2 and INT3, respectively. An overnight reaction time was sufficient for the completion of the reaction. After 24 h, the entire aqueous phase was filled homogeneously with dark green PANi, while the organic layer appeared red orange, probably due to the formation of aniline oligomers. The product was collected and purified through filtration and dried at 50 ºC. Sample was then powdered well. The yield was almost quantitative. Dedoped nanofibers were obtained by stirring with excess of 0.1 M NH_4OH.

Fig. 2.2 shows the interfacial polymerization of aniline in a water- $CHCl_3$ system. From (a) to (c), the reaction times are 1.5, 5 and 10 min, respectively. The top layer is an aqueous solution of 1 M HCl and APS; the bottom layer is aniline dissolved in the organic solvent $CHCl_3$ (the dark particles are the nanofibers).

(a) 1.5 min (b) 5 min (c) 10 min

Fig. 2.2: Interfacial polymerization - progress of reaction.

2.2.3 Electrochemical Template Polymerization

Template synthesis was used as one of the methods to synthesize PANi nanofibers electrochemically [108]. Gold coated track-etched polycarbonate membrane was used as the working electrode, Pt foil as the counter electrode and silver/silver chloride (Ag/AgCl), as the reference electrode. The polymerization reaction was carried out in 200 mL, 1.0 M HCl solution with 0.3, 0.2 and 0.1 M aniline monomer with electrode potentials swept continuously between – 0.2 to 1.0 V at a scan rate of 0.001 V/s, at room temperature. The samples synthesized with 0.3, 0.2 and 0.1 M concentration of monomer were designated as TMP1, TMP2 and TMP3, respectively. An Autolab PGSTAT 30 (Netherlands) instrument was used to perform the electrochemical synthesis and analysis of the samples. Number of scans given was 2. PANi was obtained inside the pores of the nanoporous membrane. The template membrane was then dissolved in methylene chloride and the PANi nanofibers were collected and used for further characterization and device fabrication. In the discussion, in following chapters, PANi base, PANi doped with HCl and PANi doped with CSA are designated as EB, PANi-HCl and PANi-CSA, respectively.

2.2.4 Electrochemical Step Galvanostatic Method

Another method for the synthesis of PANi was by using a three-step, electrochemical step galvanostatic method (SGM) [113]. In a typical synthesis, for a 0.3 M monomer case, 5.58 g of aniline was added to 200 mL of HCl. The volume of the electrolyte was maintained at 200 mL in each synthesis. Ag/AgCl was used as the reference electrode. A platinum strip and titanium strip were used as counter and working electrodes, respectively. In the three-step method, PANi was polymerized on the surface of titanium by polymerization of aniline using a programmed stepped constant-current method, designed to control the nucleation and growth rate. The optimized procedure was arrived at as 0.08 mA cm^{-2} for 0.5 h, followed by application of 0.04 mA cm^{-2} for 3 h and 0.02 mA cm^{-2} for another 3 h. By passing constant current density to the electrochemical cell, dark green PANi was deposited on the working electrode. After completion of the process, the electrode was allowed to dry at room temperature. The product, which was a smooth film of deposited conducting polymer, was collected and powdered well for analysis. Dedoped PANi, emeraldine base (EB) form was obtained by stirring the salt form of PANi in 1.0 M NH_4OH solution for 4 h.

Table 2.2: Designation of samples synthesized by electrochemical SGM.

Sample designation	Concentration of monomer (aniline)	Concentration of acid (HCl)
NP1	0.3 M	1M
NP2	0.1 M	1M
NP3	0.0125 M	1 M
NP4	0.0125 M	0.25M

By varying the concentration of the monomer and the dopant acid, a series of PANi nanowires were obtained. To compare the morphology, samples prepared as per the details shown in Table 2.2 were studied. The initial growth and formation of nanowires were investigated by electrochemically depositing the polymer at an interval of 5 min for a period of half an hour at all concentrations.

2.2.5 Polymer Acid Template Assisted Chemical Polymerization

Conductive polymer composite, poyaniline:polystyrene sulphonic acid (PANi-PSS) was obtained by oxidative polymerization of aniline in aqueous PSS medium using APS as initiator. For the synthesis of PSS doped PANi in the ratio 1:1, 0.03 mole (based on -C_6H_4NH- repeat unit) aniline was added to 60 mL, 1 M HCl. Separately, 0.03 mole PSS-Na (based on acidic repeat unit) was dissolved in 40 mL, 1 M HCl. 0.01 mole APS was added to acidified PSS-Na solution and stirred for 1 h. PSS-Na was turned to PSS by sodium-hydrogen ion exchange due to solution acidity. The solution was brown in colour. APS–PSS solution was added dropwise to aniline solution and stirred for 24 h at 0 ºC. The solution turned green upon stirring. The doped PANi was washed with deionized water and the precipitate separated by a centrifuge. The synthesized sample was designated PSN4. PSS doped PANi samples with composition PANi:PSS, 1:2, 1:1.5, 1:1.25, 1:0.75, 1:0.25, 1:0.1 and 1:0.05 were synthesized and designated as PSN1, PSN2, PSN3, PSN5, PSN6, PSN7 and PSN8, respectively [105].

In the oxidative reaction to produce PANi or PANi–PSS composites, acids assist in the polymerization. HCl was chosen as the precursor acid in all syntheses. Since PSN3 gave the highest conductivity, the ratio of PANi:PSS, 1:1.25 was selected for studying the effect of concentration of precursor acid, HCl, on the stability of the synthesized dispersion and to obtain optimum conductivity for the thin film in the fabrication of organic transistor. The concentration of the precursor acid, HCl was varied from 0.1 mM to 2.0 M in the synthesis of PANi-PSS. The polymers with the PANi:PSS ratio, 1: 1.25 were designated as PSN3-1, PSN3-2 (same as PSN3), PSN3-3, PSN3-4, PSN3-5, PSN3-6 and PSN3-7, synthesized with the precursor acid concentration, 2 M, 1 M, 0.5 M, 0.1 M, 0.01 M, 0.001 M and 0.1 mM, respectively. The scheme of synthesis of PANi-PSS composite in the presence of precursor acid HCl is depicted in Fig. 2.3.

After the synthesis and purification of PANi-PSS, to obtain thin films, its 3 wt% aqueous dispersions were prepared. PSN3-3 was chosen for film formation and device fabrication as PSN3-3 gave a stable dispersion with optimum conductivity (discussed in section 3.4.1). PSN3-3 films were spin cast on glass slide and Si/SiO_2 wafer for further characterization. Secondary doping with DCA was done by soaking the film in preheated DCA at 95 ºC for five minutes. The samples were baked at 95 ºC for 1 h to drive away the residual DCA. The films were further exposed to a vacuum of 10^{-7} Torr for 4 h to expel any traces of DCA in the sample.

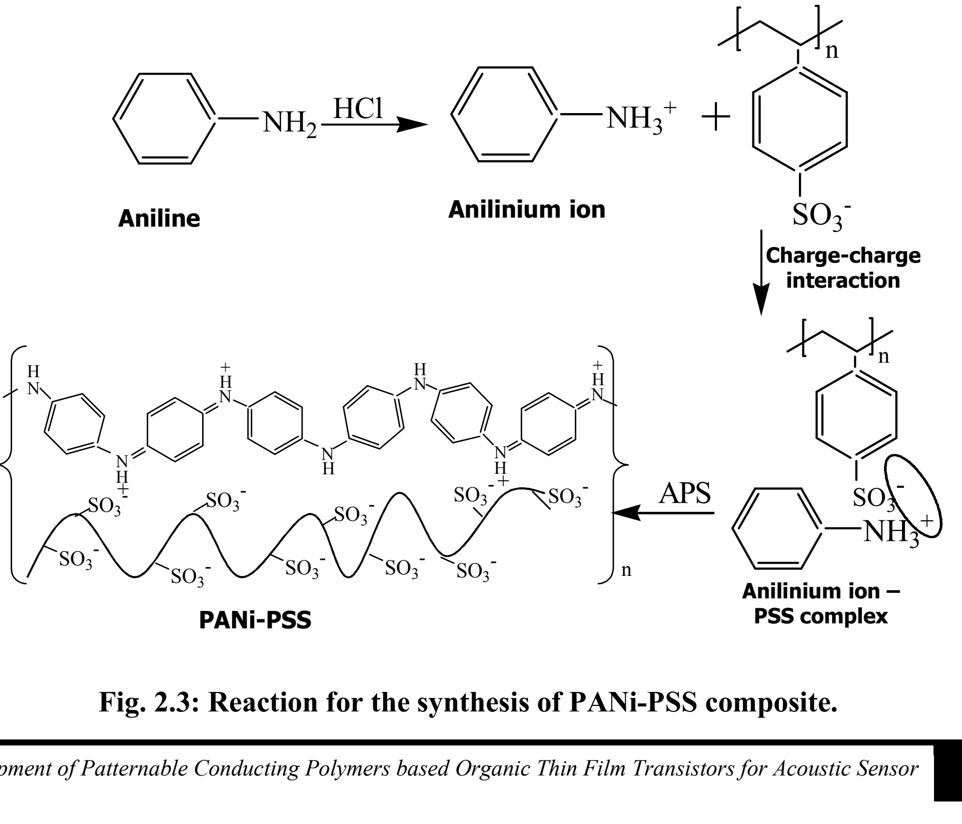

Fig. 2.3: Reaction for the synthesis of PANi-PSS composite.

2.3 Synthesis of Regioregular Poly(3-hexyl thiophene) and Copolymers

a. Synthesis of vinyl terminated poly(3-hexyl thiophene) (PHT):

The synthesis was carried out following the procedure reported in literature [114]. 2, 5- dibromo-3-hexylthiophene (4.9 g) and anhydrous THF (150 mL) was taken in a dry 100 mL three-neck flask, flushed with N_2. To this mixture, 2 M solution of butyl magnesium chloride (7.5 mL) in diethyl ether was added and the reaction mixture was refluxed for 3 hr. The reaction mixture was allowed to cool down to 40-50 ºC, at this time, $Ni(dppp)Cl_2$ (0.15 g,) was added to the reaction mixture. The polymerization was allowed to proceed for 12 h at room temperature followed by the addition of a 1 M solution of vinyl magnesium bromide (3 mL). The reaction mixture was stirred for 30 min followed by quenching in methanol. The mixture was filtered and packed in a filter paper and finally kept in a Soxhlet thimble. Soxhlet extractions were performed with methanol (to remove monomer and salts) for 48 h, hexane (to remove catalyst and oligomers) for 48-72 h and chloroform for 24 h. The chloroform fraction was reduced and dried in vacuum to yield the vinyl terminated PHT polymer (**1** in Fig. 2.4) as a violet solid.

b. Hydroboration/oxidation of vinyl terminated PHT:

Vinyl terminated PHT, from above; (0.2 g) was dissolved in anhydrous THF (10 mL) under N_2. To this reaction mixture, a 0.5 M solution of 9-BBN (0.4 mL) in anhydrous THF was added using a syringe. The reaction mixture was stirred for 24 h at 40 ºC. After completion of 24 h, a 6 M solution of NaOH (0.2 mL) was added to the reaction flask. The reaction mixture was stirred for another 15 min. After the reaction mixture was cooled to room temperature, a 0.2 mL, 33% aqueous solution of hydrogen peroxide was added and the reaction continued for additional 24 h at 40 ºC. The hydroxy terminated PHT (**2** in Fig. 2.4) was isolated by precipitation in a methanol-water (1:1) mixture followed by filtration.

c. Synthesis of PHT macroinitiator:

Hydroxy terminated PHT (0.1 g) was dissolved in anhydrous THF (100 mL) under N_2. The reaction mixture was stirred at 40 ºC for 15 min. At this point, 0.9 mL triethylamine was added followed by a drop-wise addition of 0.75 mL, 2-bromopropionyl bromide. The reaction was continued with stirring for 24 h at 40 ºC. The resulting PHT macroinitiator (**3** in Fig. 2.4) was precipitated in methanol and extracted with methanol.

d. Synthesis of block copolymer of t-butyl acrylate using PHT macroinitiator:

ATRP of t-butyl acrylate was performed using CuBr–PMDETA, in 1, 2-dichlorobenzene (50 vol%) at 80 ºC. The molar ratio was $[M]_0$:$[PHT\text{-}MI]_0$:$[CuBr]_0$:$[PMDETA]_0$=300:1:1:2. In a dry Schlenk flask, PHT macroinitiator (0.1 g,), t-butyl acrylate (2.7 mL) and CuBr (0.014 g) were added. After the reaction mixture was immersed in a thermostated oil bath at 90 ºC, PMDETA (0.04 mL) was added to the reaction mixture using a syringe (deoxygenated) and an initial sample was withdrawn. Samples were periodically removed from the reaction mixture and polymerization quenched (after 24 h) by using diethyl ether to follow the conversion and the molecular weight. The polymer was isolated by precipitation with ethanol [115]. The scheme for the synthesis of poly(3-hexylthiophene)-b-poly(t-butyl acrylate) (**4** in Fig. 2.4) is shown in Fig. 2.4.

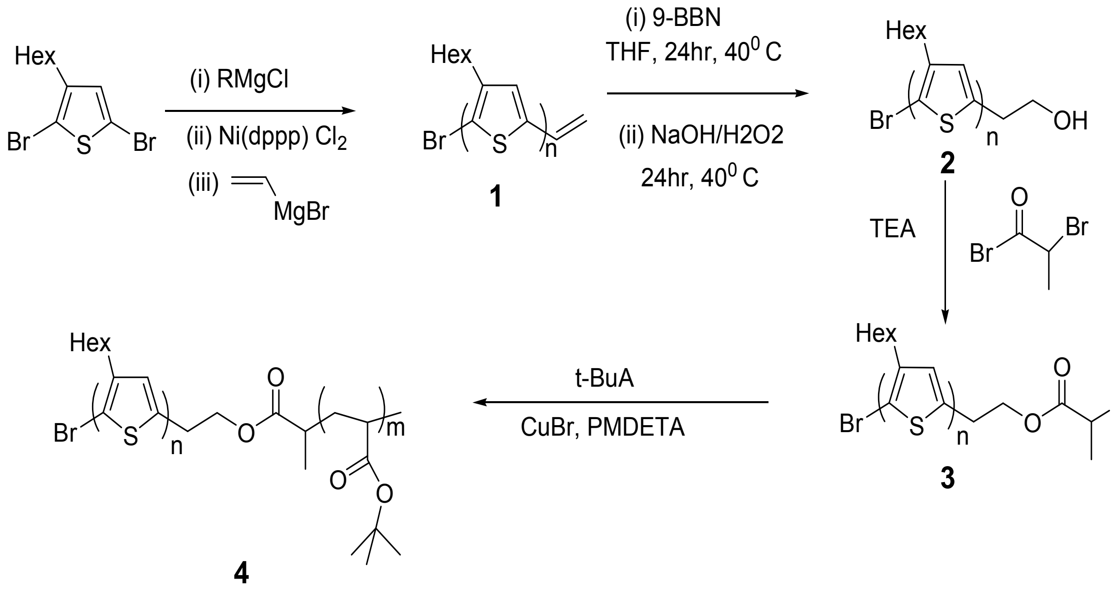

Fig. 2.4: Synthesis of poly(3-hexylthiophene)-b-poly(t-butyl acrylate).

2.4 Structural Characterization

2.4.1 Fourier Transform Infrared Spectroscopy

Fourier transform infrared spectroscopy (FTIR) refers to the technique used to obtain an absorption or emission infrared spectrum of a solid, liquid or gas in the infrared wavelength range of 400-5000 cm^{-1}. Compared to a dispersive spectrometer, an FTIR can simultaneously collect data of high resolution over a wide spectral range [116]. The spectroscopic technique is useful in identifying the functional groups in a compound that absorb IR radiation at characteristic wavelength. In the present study, FT-IR analysis was done by Thermo Nicolet, Avatar 370 instrument. The IR spectral studies have been utilized in confirming the extent of doping in PANi and conformation of formation of para-coupled dimers during the initial stages of synthesis of PANi.

2.4.2 UV-vis-NIR Spectroscopy

Ultraviolet–visible (UV-Vis) spectroscopy refers to the absorption or reflectance spectroscopy in which sample absorbs radiation in the ultraviolet to near-infrared (190-2500 nm) region, resulting in electronic transitions within the sample. The nature of chemical groups present in the sample determines the absorption of light in this region. UV-Vis spectroscopy is able to provide information about the π-conjugation along the polymer backbone and hence conduction electron mobility, allowing the conducting and non-conducting forms of conducting polymers to be easily distinguished [117]. The effect of doping on the electronic structure of the materials can also be understood from the UV-Vis absorption spectrum [118]. UV-vis-NIR spectroscopy of the synthesized conducting polymers in this study were performed by Varian, Cary 5000, spectrophotometer.

2.4.3 Nuclear Magnetic Resonance Spectroscopy

Nuclear magnetic resonance (NMR) spectroscopy is a non-destructive analytical technique that allows detecting magnetic properties of atomic nuclei and giving information on what sort of environment they are within their molecule [119]. NMR spectroscopy has been used in this study to determine the extent of regioregularity in synthesized poly(3-hexyl thiophene) and its copolymers. NMR study is useful in distinguishing the different trimeric sequences and their extent, which can arise in a synthesized P3HT, therby predicting the percentage of regioregularity.

2.4.4 X-ray Diffraction

X-ray diffraction (XRD analysis) is a method used for determination of crystallinity of a compound, including atomic arrangement, crystallite size and imperfections. XRD analysis is based on constructive interference of monochomatic X-rays and a crystalline sample [120]. It is an independent and non-destructive analytical approach to evaluate the amount of crystalline content present in polymers, especially the conducting polymers [121]. Polymers are blends of crystalline and amorphous matrix. The degree of crystallinity of the material can be determined by measuring the width of the peaks on the integrated diffractogram (diffraction pattern). X-ray diffraction analysis of conducting polymer samples in the present study were done using Bruker AXS D8 Advance diffractometer with Cu-Kα radiation of wavelength, 1.542 Å.

2.5 Thermal Analysis

2.5.1 Thermogravimetric Analysis

Thermogravimetric analysis (TGA) is a branch of thermal analysis that measures the mass change of a material as a function of increasing temperature over time, in a controlled atmosphere of nitrogen, air, helium, other gas, or in vacuum. The analysis determines weight change and temperature of decomposition reactions, which allows quantitative composition analysis [122]. The thermal stability of samples in the present study was determined using Q-500, TA Instruments (USA), Thermo Gravimetric Analyzer, under nitrogen atmosphere at a heating rate of 10 ºC/min.

2.5.2 Differential Scanning Calorimetry Analysis

Differential scanning calorimetry (DSC) is a method of thermal analysis which measures the amount of energy absorbed or released by a sample when it is heated or cooled [123]. The method gives information on qualitative and quantitative data on exothermic (heat evolution) and endothermic (heat absorption) processes [124]. DSC analyses of the samples in the present study were done by Q-2000, TA Instruments (USA), Differntial Scanning Calorimeter.

2.6 Morphology Characterization

2.6.1 Scanning Electron Microscopy

A Scanning Electron Microscope (SEM) is a powerful magnification tool to obtain information on morphology of samples. The high-resolution, thee-dimensional images obtained from SEM provide, morphological, topographical and compositional information [125]. The samples, in the present study were analyzed using the SEM, LEO 440i, JEOL Model JSM - 6390LV and Carl Zeiss EVO-18. SEM analysis has been extensively used in this study to understand the morphology of nanostructured conducting polymers, device architecture of OTFTs and morphology of interfaces in OTFT.

2.6.2 Transmission Electron Microscopy

Transmission Electron Microscope (TEM), with magnification as high as 1 nanometer, are the most powerful microscopes. TEM utilizes energetic electrons to provide compositional, morphological and crystallographic information of samples. TEMs produce high-resolution, two-dimensional black and white images from the interaction of high energy electrons in the vacuum chamber and the prepared samples [126]. Analysis in the present study were done using the TEM, JEOL-JEM 2100F. Few of the samples were also analysed by FEI Tecnai G2, TEM.

2.6.3 Atomic Force Microscopy

The atomic force microscopy (AFM), a kind of scanning probe microscopy, is one of the most versatile and powerful method of microscopy, for studying samples at nanoscale, requiring minimal sample preparation. The microscopic technique can generate images on the order of fractions of a nanometer, with height information at angstrom scale resolution [127]. In the present study, Park XE-100 AFM, from Park

Systems, in non-contact mode was employed for the analysis of topography of polymer and semiconductor samples. The AFM has been mostly employed in the present study to obtain the grain size of semiconductor grown on the dielectric in an OTFT.

2.7 Contact Angle Measurement

Contact angle measurements are used to assess the effects of surface treatments and surface cleanliness, developed as a part of fundamental research. The contact angle is the angle measured through the liquid, where a liquid-vapour interface meets a solid surface. Adhesive forces are experienced by a drop of pure liquid on a plane surface. These forces acting between the liquid and the surface favour spreading, whereas, the cohesive forces within the liquid oppose spreading. The balance between these two forces determine the contact angle, θ. Young's equation [Eqn. (2.1)] describes this balance and relates θ to the surface free energies of a system containing solid (S), liquid (L) and vapour (V) phases.

$$\gamma^{SV} - \gamma^{SL} = \gamma^{LV} \cos\theta \qquad (2.1)$$

where γ^{SV} is the solid-surface free energy, γ^{LV} is the liquid-surface free energy (surface tension) and γ^{SL} is the solid-liquid interfacial free energy. A drop spreads on the solid surface if the surface energy is higher than the surface tension of the liquid drop. The solid surface in such case undergoes complete wetting so that adhesiveness dominates and contact angle is 0^{o}. If the solid surface has a relatively high surface energy, but lower than the liquid's surface tension, the liquid wets the surface and the resulting contact angle is $0^{o} < \theta < 90^{o}$. If the surface energy of the solid surface is low enough, it will have poor adhesiveness and poor wetting of the drop, resulting in a larger contact angle. A liquid drop that has a contact angle $> 90^{o}$ is considered as non-wetting and the surface is characterized to be hydrophobic [128].

Contact angle measurements on surface in this study were done by OCA-20 contact angle tester, DataPhysics Instruments. The measurements have been carried out to determine the wettability or non-wettabilty of different surfaces during the fabrication of OTFT. Measurements were also done on dielectrics such as SiO_2 and PVP, that had been treated with OTS solution prior to the deposition of semiconductor.

2.8 Electrochemical Characterization

The most common electrochemical method employed for characterization is cyclic voltammetry (CV). This involves the application of a potential gradient in forward and backward direction to the polymer as an electrode in solution. The current flow as a function of this potential variation is measured. This current flow is a result of oxidation/reduction processes and the concomitant ion flow that occurs. Cyclic voltammteric conditions were maintained using Autolab PGSTAT30 potentiostat-galvanostat. Cyclic voltammetry studies of the films synthesized were performed in a monomer free 1.0 M HCl aqueous solution. Platinum was used as the working and counter electrodes and Ag/AgCl as the reference electrode. The potential was swept continuously between – 0.2 to 1.0 V at a scan rate of 0.001 V/s. The experiments were conducted on nanowires synthesized by interfacial, template and SGM method, with 0.1 M concentration of aniline in 1 M acid. Samples of equal weight were used for the analysis. NP1, NP3 and NP4 samples synthesized by SGM, of equal weight were also analyzed for their CV response.

Electrochemical analysis was also used for the determination of the work functions of the conducting materials (metal and conducting polymer) and semiconducting materials from the measured equilibrium electrochemical potentials. The electrochemical equilibrium potential (E_{eq}) correlates to Fermi level (E_f) or the work function (Φ_w) of the conducting materials. Generally, a simple offset of 4.5 eV is assumed to exist between electrochemical potentials and distinct energy levels such as the work function [129]. A simple way to measure the equilibrium electrochemical potential of a material is to measure its open circuit potential [130-131] in an electrolyte solution versus a standard reference electrode such as an Ag/AgCl electrode. Once the electrochemical potential is measured, the work function was calculated from Eqn. 2.2:

$$\text{Work Function (eV)} = E_{eq} \text{ vs Ag/AgCl} + 4.5 \text{ eV} \qquad (2.2)$$

For the measurement of E_{eq}, the material (metal, conducting polymer or semiconductor) was deposited on an insulating material, PEN film of size 10 × 5 mm. A three electrode cell was constructed consisting of a 50 mL beaker filled with 1 M

H_3PO_4, an Ag/AgCl reference electrode, platinum counter electrode and the working electrode of freshly prepared test material. The open circuit potential experiments were performed with the poentiostat-galvanostat, adopting the method of potentimetry (zero current) under the option chronoamperometry. The potential was measured as a function of time for at least one hour. If the potential was not observed to reach a steady state, additional time was given to allow the potential to stabilize.

2.9 DC Electrical Conductivity by Four-Point Probe Method

Conductivity of samples can be measured by two probe or four probe method. When conductivity (or resistance) is measured with a two probe, the resistance of the cables leading to the sample and any resistance at the contacts is measured along with the resistance of the sample. The four-point probe set up consists of four equally spaced metal electrode tips with finite radius. Each electrode is supported by springs on the top to minimize damage to sample during probing. The four metal electrodes are part of an auto mechanical stage which can move up and down during the measurement of conducivity. A current source of high impedance is used to supply current though the outer two probes, a voltmeter measures the voltage across the inner two probes to determine the sample resistivity. Typical probe spacing is ~ 1 mm. The inner probes draw no current because of the high input impedance voltmeter in the circuit. Thus, unwanted voltage drop at the inner probes caused by contact resistance between sample and probes is eliminated from the potential measurements [132]. Since these contact resistances are very sensitive to pressure and to surface condition, error with conventional two-electrode technique (in which potential-measuring contact passes a current) can be quite large.

The volume resistivity by four-point probe method is calculated by Eqn. 2.3

$$\rho = \frac{\pi}{\ln 2} \times \frac{V}{I} \times t \times k \qquad (2.3)$$

where ρ = volume resistivity (Ω-cm), V = the measured voltage (volts), I = the source current (A), t = the sample thickness (cm) and k = a correction factor based on the ratio of the probe to wafer diameter and on the ratio of wafer thickness to probe separation.

In the present study, S 302-4 model probe heads mounted on a resistivity stand from Signatone Corp., USA and interfaced with Keithley SCS-4200 semiconductor characterization system [Fig. 2.5] were used to measure the conductivity of thin film and powdered pressed pellet samples. PANi nanowires samples were dedoped in NH_4OH, redoped with CSA and 3 wt% of the doped polymer were secondary doped with *m*-cresol and drop-cast as thin films for conductivity measurement.

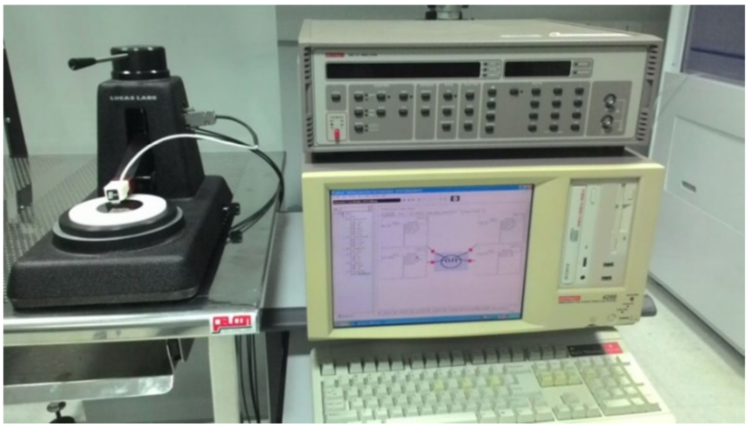

Fig. 2.5: Photograph of four-probe conductivity measuring unit interfaced with semiconductor characterization system.

2.10 Processes in Device Fabrication

2.10.1 Wafer Cleaning

Silicon and oxidised silicon wafers are prone to contaminants simply by exposure to air which contains high degree of organic contaminants. These contaminants strongly bond to the wafer surface due to strong electrostatic force. In order to function properly and for ease of lamination of flexible substrates to the wafer, it must be completely free of any contaminants. Since in the present study, wafers have been used only as the handling substrates for fabrication of OTFT, solvent clean method was employed for the purpose of cleaning [133]. The procedure involved is rinsing the wafer for 3 minutes each in acetone and IPA in an ultrasonic bath. Once the rinsing in the solvents was completed, the wafer was rinsed with deionized water and blown dry with nitrogen for further processing. Fig. 2.6 shows the Branson 2510 (USA), ultrasonicator used for rinsing the wafer in acetone and IPA solvents.

Fig. 2.6: Photograph of Branson-2510 ultrasonicator.

2.10.2 Differential Pressure Lamination

Differential Pressure Lamination is a process used to adhere a flexible material to another flexible or rigid material of varying thickness. Vacuum evacuation, heat and pressure are combined in a single process to provide an environment free of air, where complete adhesion happens. OPTEK make DPL-24, USA, was used in the present study for the lamination of flexible substrate to a rigid substrate like silicon wafer used in OTFT. A rigid support to the flexible substrate makes the handling of flexible substrate easier. The alignment of patterns in photo lithography is also made easier with a laminated flexible substrate. In a typical lamination process, a cleaned Si substrate was placed on the platen of the laminator, mounted in its sliding drawer. A silicone gel film, with adhesive on both surfaces (top surface covered with a plastic sheet) was carefully placed over the Si wafer. The substrate along with the gel film was exposed to 'Vacuum Dwell' for a time determined by a precision digital timer. At the end of the 'Vacuum Dwell', a preheated silicone rubber diaphragm descended onto the work-substrate and drove the spring-mounted drawer mechanism into intimate contact with the lower heater platen. The temperatures of both the upper and lower heat platens were controlled independently by digital 'Temperature Controllers'. A positive pressure of up to 10 psi was applied by the equipment to the top of the diaphragm to bring the combined differential to nearly 25 psi. The 'Pressure Dwell' was also adjusted by a precision digital timer identical to that employed in the 'Vacuum Dwell'. Upon completion of a cycle, the drawer mechanism was retracted and gel film laminated Si wafer was taken out to remove the plastic sheet over the top surface [134]. Cleaned PEN or polyimide film was then placed over gel film laminated Si wafer (that had exposed adhesive layer on the top) on the platen of the laminator. The process of lamination was repeated as described above. Fig. 2.7 shows the DPL-24 laminator with the inset showing the polyimide film laminated silicon wafer.

Fig. 2.7: Photograph of DPL-24 differential pressure laminator with the inset showing the polyimide film laminated silicon wafer.

2.10.3 Spin Coating

Spin coating is a technique that is used to deposit uniform thin films on substrates with thickness of the order of nanometers to micrometers. In a typical process, a small puddle of the fluid to be coated is applied onto the centre of a substrate and allowed to spin at high speed (typically around 3000 rpm). Centripetal acceleration causes the fluid to spread on and eventually off the substrate, leaving a thin film of the fluid on the substrate. Final film thickness and quality of the film depend on the nature of the fluid (viscosity, solid percentage, surface tension, drying rate etc.) and the parameters chosen for the spin process. Factors such as acceleration, final rotational speed and fume exhaust define the properties of the coated films. The spin coating of photoresist typically runs at 1000 to 5000 rpm for 30 to 60 seconds and produces a layer between 0.5 and 2.5 micrometres thick. The spin coating process results in a uniform thin layer, usually with uniformity of within 5 to 10 nanometres [135]. In the present study, Brewer Science (USA) make, Cee-200 spin coater was used for the spin coating of resists, dielectrics etc. on the substrate during the microfabrication process of OTFT. Fig. 2.8 shows the photograph of the spin coater used in the study.

Fig. 2.8: Photograph of Cee-200 spin coater.

2.10.4 Electron-Beam Evaporation

Electron-beam (E-beam) evaporation is a physical vapour deposition (PVD) method in which an intense, electron beam is generated from a filament and steered via electric and magnetic fields to strike source material (e.g. pellets of metal) and vaporize it within a vacuum environment. As the source material is heated via this energy transfer, at some point its surface atoms have sufficient energy to leave the surface. They then traverse the vacuum chamber and get coated on a substrate positioned above the evaporating material. Since thermal energy is very low, the pressure in the chamber is maintained below the point where the mean free path is longer than the distance between the electron beam source and the substrate (the mean free path is the average distance an atom or molecule can travel in a vacuum chamber between successive collisions, which disturbs its direction or energy to some degree). This is typically around 3.0×10^{-4} Torr or lower [136]. In the present study, Hind High Vacuum Company's (India), BC-300 model, box coater was used for the deposition of metal, Pd that was most commonly used as the electrode in OTFT fabrication. The deposition was carried out at a rate of 0.8 – 1.0 Å/s at a vacuum < 1×10^{-5} mbar. Fig. 2.9 shows the E-beam evaporation unit used in the study.

Fig. 2.9: Photograph of E-beam evaporation unit.

2.10.5 UV-Photolithography

UV-photolithography refers to the series of steps that establish the shapes, location and dimensions of the various components in microfabrication. For lithography processing, a hard copy of the pattern is first generated. This is called a photomask. For transferring the design on the photomask to the substrate, a viscous, liquid fluid of photoresist is coated on the substrate by spin coating. The photoresist coated substrate is then softbaked to drive off excess photoresist solvent, typically at 90 to 110 °C for 60 to 90 seconds on a hotplate. After the soft bake, the photoresist is exposed to UV light. The exposure to light causes a chemical change that allows some of the photoresist to be removed by a solution called developer. Positive photoresist, which is the most common type, becomes soluble in the developer when exposed; while with negative photoresist, unexposed regions are soluble in the developer [137]. The wafer is then ‘hard-baked’, typically at 100 to 120 °C for 5 to 10 minutes. The hard bake hardens the photoresist that is left behind, to make a more robust protective layer for, wet chemical etching, or etching by plasma. Schematic of UV-photolithography with a positive photoresist is shown in Fig. 2.10(a). All photolithographic processes in the present study were done using ABM 6 mask aligner, USA, shown in Fig. 2.10(b).

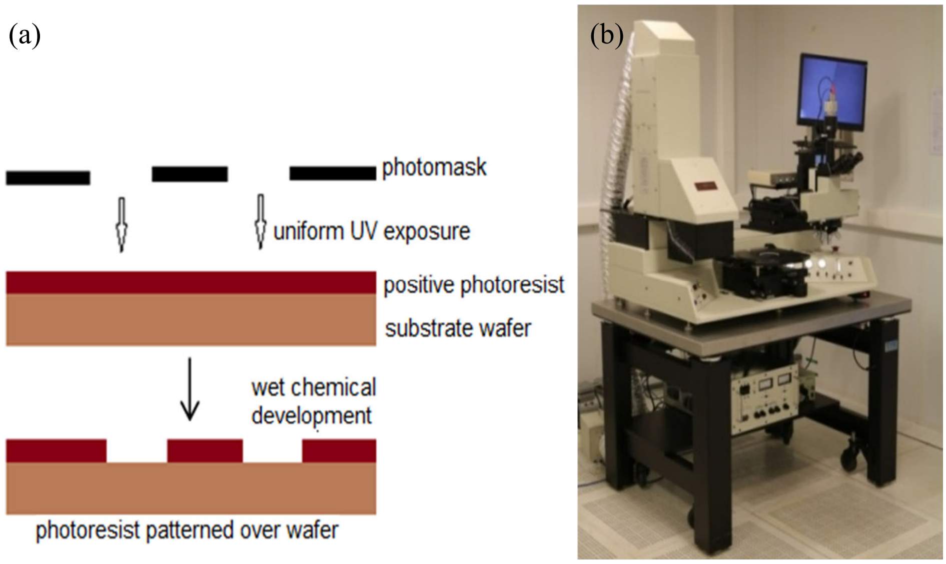

Fig. 2.10: (a) Schematic of photolithography with positive photoresist and (b) photograph of ABM-6 mask aligner.

2.10.6 Patterning of Metal by UV-Photolithography

Metal used as electrodes in OTFT in the present study are patterned by either of the two techniques, wet chemical etching or the lift-off.

2.10.6.1 Wet chemical etching

Etching is the process of chemically removing of layers from the surface of a substrate during microfabrication. In the present study, Pd metal has been mostly employed as electrodes in OTFT. Positive photoresist was used as the masking layer during photolithography, which protected the electrode part, without being attacked by the chemical etchant [138]. KI/I_2 solution in the ratio, KI : I_2 : H_2O, 4 g : 1 g : 40 mL was used for etching. During Pd etching with KI/I_2, Pd and iodine formed palladium iodide via

$$Pd + I_2 \longrightarrow PdI_2$$

The solubility of PdI_2 was improved by adding KI to the solution. In the above mentioned mixing ratio, at room temperature, etch rate of 0.5 µm/min Pd was achieved. Schematic of a typical wet etching process used in the study is shown in Fig. 2.11.

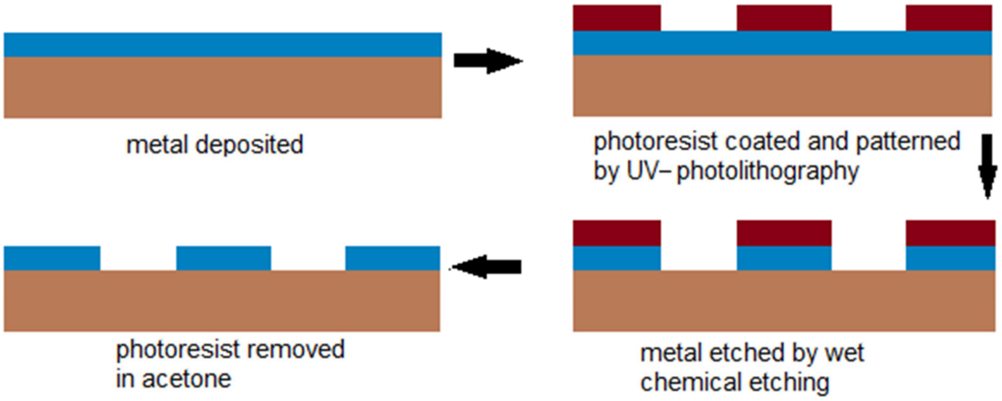

Fig. 2.11: Schematic of wet chemical etching.

2.10.6.2 Metal lift-off

Lift-off process for pattering is a method of creating patterns on a substrate surface using a sacrificial layer such as photoresist. It is an additive technique, unlike subtractive technique like etching [139]. An inverse pattern is first created on the substrate with the sacrificial photoresist layer. The target material (metal) is then deposited; it gets deposited over the whole of the wafer, but reaches the surface of the substrate, only where the final pattern is to be created. The metal stays on top of the sacrificial layer in the regions where it was not previously developed in a developer. When the photoresist is then removed in acetone, the metal on top of the resist is also lifted off. After the lift-off, the metal layer remains only in the region where it had direct contact with the substrate as shown in the schematic in Fig. 2.12(a). In the present study positive photo resist (MICROPOSIT S1813) along with a lift-off resist (LOR 10 A) was employed as the sacrificial layer for patterning metal on flexible substrates.

By using two different types of resist on top of each other, it was possible to precisely pattern the top resist and then undercut the bottom resist to form a very clean lift-off profile. The use of an additional lift-off resist was very essential to overcome the difficulty in patterning metal on a flexible substrate. The soft-bake time for the photoresist and development time after UV exposure was accordingly increased to get an optimum developed pattern of the photoresist. Figs. 2.12(b) and 2.12(c) show an improper and a better lift-off (assisted by a lift-off resist), respectively.

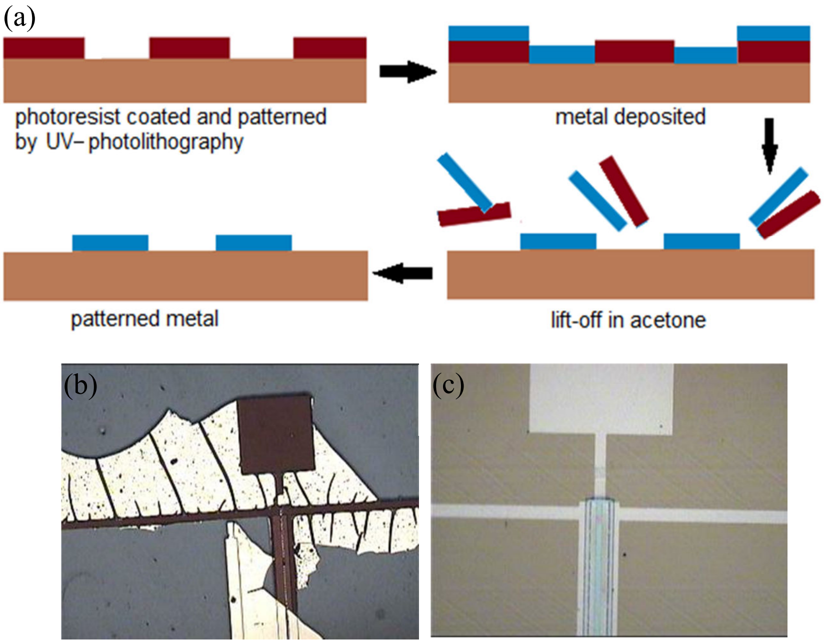

Fig. 2.12: (a) Schematic of metal lift-off process (b) micrograph of an improper lift-off and (c) micrograph of lift-off assisted by a lift-off resist.

2.10.7 Thermal Evaporation

Thermal evaporation is also a method of PVD. In this simplest form of PVD, a resistive heat source is used to evaporate a solid material in a vacuum environment to form a thin film. The material is heated in a high vacuum chamber until vapour pressure is produced. The evaporated material traverses the vacuum chamber with thermal energy and coats the substrate. Low temperature evaporation (LTE) is ideal for deposition of high vapour pressure materials such as those used in organic electronics technology. Like conventional thermal evaporation, LTE involves heating materials to a temperature at which it evaporates or sublimes. However, LTE sources are configured to allow for fine control over temperature and heating power due to the much lower melting points of the compounds involved (compared with, metals). This enables fine control over deposition rate and the thickness of films formed on substrates [121]. In the present study, PVD-75, Kurt J. Lesker Company, USA, with LTE source was used for the deposition of pentacene. The material was deposited at a pressure of $< 5\times10^{-8}$ Torr, at a rate of 0.1 Å/s and substrate temperature, 80 ºC. The unit used in the study is shown in Fig. 2.13.

Fig. 2.13: Photograph of PVD-75 physical vapour deposition unit for the low temperature evaporation of pentacene.

2.10.8 Thin Film Thickness Measurement

Thin films are deposited during the fabrication of OTFT by different processes such as spin coating, dip coating, thermal evaporation and other vacuum deposition techniques. For optimum performance of the fabricated devices, required thickness of the films after deposition and during optimization process of etching are very important. In the present study, since opaque films have been used mostly, stylus based thickness measurement mode has been resorted to. The stylus instrument measures thickness and roughness by monitoring the deflections of a fine-tipped stylus as it is dragged along the surface of the film. This method of thickness measurement requires a step in the film to measure thickness [140]. In the present study, AMBIOS, XP-200 profilometer, USA, [Fig.2.14] has been used to measure the thickness of metal, organic, dielectric and thin films used for passivating the fabricated OTFTs.

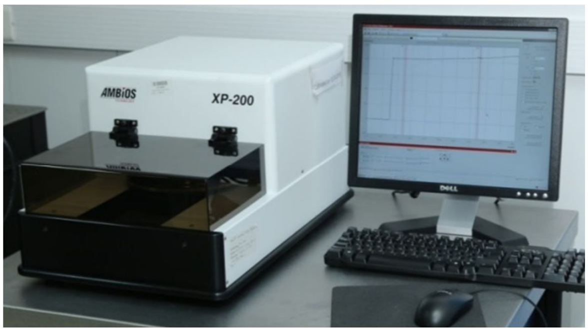

Fig. 2.14: Photograph of AMBIOS-200 stylus profilometer.

2.10.9 Reactive Ion Etching

Reactive ion etching, unlike chemical etching is a method of dry etching in which, a chemically reactive plasma is used to remove undesired part of deposited material from the substrate. The plasma is produced in the system, under vacuum by applying a strong radio frequency electromagnetic field to the wafer platter at 13.56 MHz, at varying power. Plasma is created by the oscillating electric field by ionizing the gas molecules and stripping them of electrons. High energy ions from the plasma, attack the material on the substrate surface, react with it leading to the etch. While RIE provides a much stronger as well as directional etch. The plasma etches in a downward direction with almost no sideways etching. In a typical RIE system, wafer platter is located at the bottom portion of cylindrical vacuum chamber, isolated from the rest of the chamber. Gas entry is controlled by control valves, through inlet tubes, chamber is evacuated and residual gases exit to the vacuum pump. The types and amount of gas depend on the film being etched [141]. RIE system from Torr International, Corp., USA, shown in Fig. 2.15(a), was utilized for etching organic materials, dielectrics and passivating layers in oxygen plasma, for fabrication of OTFT in the present study.

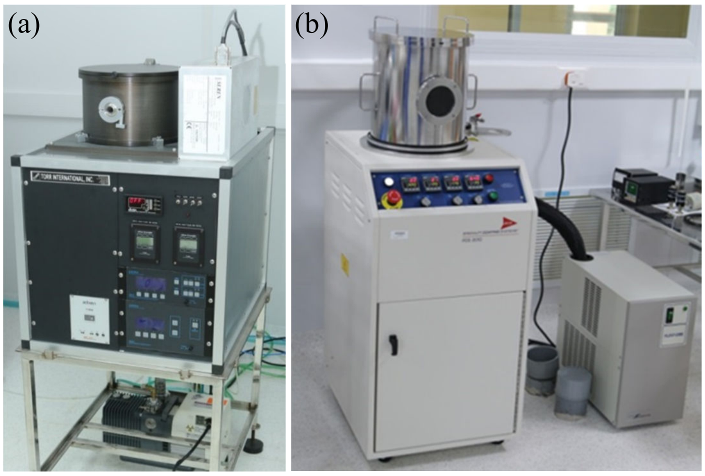

Fig. 2.15: Photograph of (a) reactive ion etching and (b) parylene deposition unit.

2.10.10 Parylene Deposition

Poly(p-xylylene) polymer (parylene C) is a polymer that can be deposited by chemical vapour deposition (CVD) as a conformal barrier layer for application in sensors and electronic circuits. Deposition of parylene is unique among conformal coatings, done with specialized vacuum equipment. Solid granular raw material, a dimer is heated under vacuum and vaporized into a dimeric gas in the first step. The gas is then pyrolized to the monomeric form, which is subsequently deposited on all surfaces as a thin transparent polymer film at room temperature. The vacuum pump with the equipment plays an important role in disposing of waste vapour. As the parylene gas exits the deposition chamber, the pump pulls it though a cold trap. That trap is usually cooled to subzero temperatures, causes the parylene in exhaust to solidify and be disposed off [142]. In the present study, Specialty Coating System's, PDS-2010, USA, make parylene deposition unit was utilized, the photograph of which is shown in Fig. 2.15(b). Parylene, in coating applications, can be applied on chemically sensitive materials (organics) without deteriorating them. The polymer is also used as dielectric and passivation layer in OTFTs. The schematic of parylene deposition process is shown in Fig. 2.16.

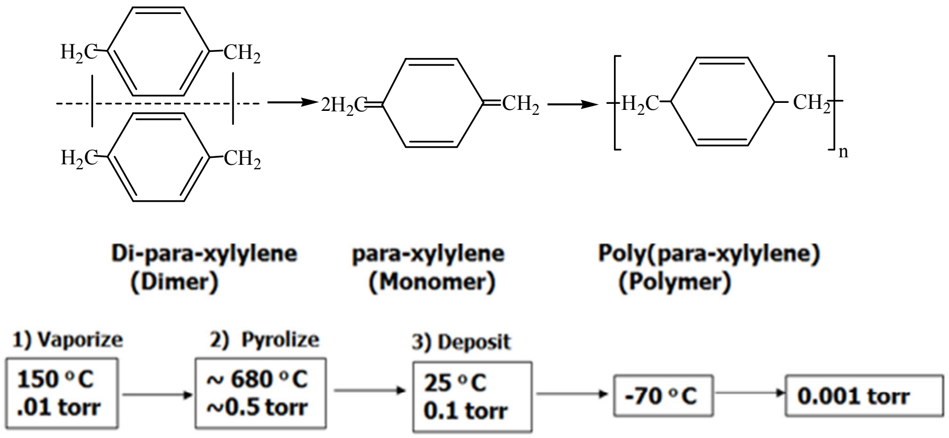

Fig. 2.16: Schematic of chemical vapour deposition of parylene.

2.11 Device Characterization

2.11.1 I-V Characterization: Semiconductor Parameter Analyzer

A mechanical probe station is used to electrically characterize semiconductor devices. The probe station is usually equipped with micromanipulators, which allow the positioning of thin and sharp tip needles on the surface of probing pads of semiconductor devices. If the device is electrically stimulated, the signal is acquired by the mechanical probe and is displayed on a source measurement unit (SMU) or oscilloscope. The probe system is usually interfaced with a semiconductor parameter analyser, a test instrument that integrates multiple measurement and analysis capabilities to perform current-voltage (IV) and capacitance-voltage measurements (CV). In the present study, electrical and transfer characteristics of fabricated OTFTs were characterized by Signatone make, S - 725- SRM model probe station. The probe station is interfaced with Keithley SCS-4200, semiconductor parameter analyzer. The photograph of probe station, interfaced with Keithley SCS-4200 is shown in Fig. 2.17. Testing of flexible TFTs were done as per IEEE standard 1620-2008.

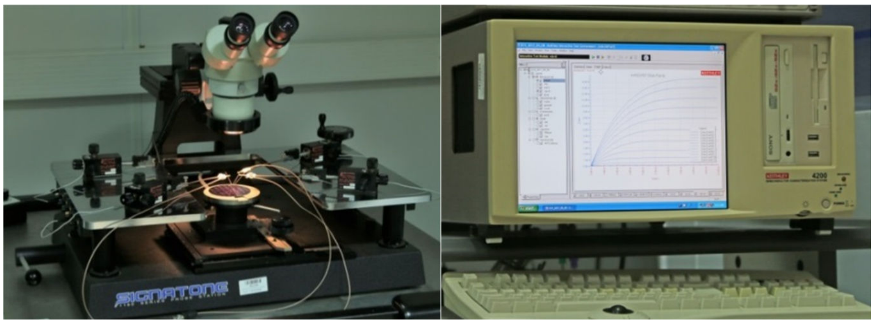

Fig. 2.17: Photograph of probe station interfaced with semiconductor parameter analyser.

2.11.2 Testing of Circuits: Wafer Probing Test Jig

The batch fabrication of OTFT was done on a 3″ Si substrate or flexible substrate. The design consisted of 37 number of OTFT (different W/L ratio) with the source, drain and gate of the devices connected to metal contact pad of dimension 500 x 500 µm. To avoid the complications involved in taking connections from each contact pad, a wafer probing test jig was in-house designed and fabricated for the purpose of testing the devices and configuring them as amplifiers for acoustic sensors. The wafer probing assembly could probe the 500 x 500 µm metal pad terminals of all the devices on a wafer and connect to configurable matrix of switchable jumpers. The wafer probing test jig could work with maximum of 100 V DC voltage, hence the components used in this test jig had sufficient voltage rating. The wafer probing test jig was designed to have scalability to accommodate different aspect ratio for different devices, in totally independent manner by shunting multiple devices together. The performance of the amplifier topology could be checked for multiple wafers by just inserting the wafer on the jig. To account for a low noise amplifier design realization on the test jig, shielded BNC connectors (Keithley) were used for feeding the input signal to the input devices of amplifier. Similarly the output of the amplifier was also routed through BNC connectors. Shielded coaxial cables were provided for monitoring the signal. A guide card was fabricated as per the mask design of contact pads and lay out of OTFTs, which could guide all the probe pins of test jig to correctly align and connect to the metal pads on the wafer. Pins used in the jig were special type of spring loaded POGO pins. The electrical connections were not permanent, but could be replaced with ease. The photograph of the wafer probing test jig is shown in Fig. 2.18.

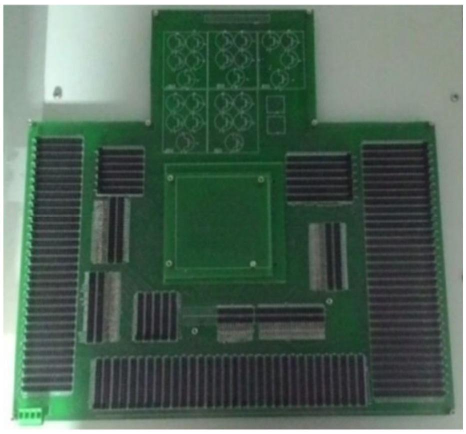

Fig. 2.18: Photograph of the wafer probing test jig.

Chapter 3

DEVELOPMENT OF CONJUGATED POLYMERS FOR APPLICATION IN ORGANIC THIN FILM TRANSISTOR

3.1 Introduction

Conjugated polymers in its semiconducting or conducting form, patterned as the active layer or electrode layer in an OTFT can bring technological revolution in the field of all-organic transistors paving the way for applications in large area flexible sensors. High performance OTFTs demand the availability of solution processable conjugated polymers with adequate conductivity and work function to be employed as the electrode layer in such devices. These polymer electrodes are ideal for replacing the conventional metal electrodes in OTFTs. Molecular order and crystallinity are the main concerns in the case of solution processable semiconducting polymers for use in OTFTs. However, the device performance in OTFTs is significantly limited by poor charge injection and therefore, a small enhancement in charge injection would lead to a considerable improvement of OTFT performance. Materials for source/drain electrodes in OTFT should have a suitable work function to reduce the charge-carrier injection barrier and should form an ohmic contact with organic layers. When the semi-conducting layer consists of a *p*-type material, the work function of source/drain electrode materials matches or is close to the HOMO level of the semiconductor [27]. Hence, metals with a high work function, such as gold, platinum and palladium are usually preferred for the source/drain electrodes. Gold and platinum, which form good ohmic contacts and usually used in OTFTs, are not economical for use in commercial large area sensors. Palladium is a cheaper electrode material, but has been reported to have relatively high contact resistance due to the non-ohmic nature of contacts [28, 143]. Substitution of metal electrodes with a conductive polymer, of suitable work function [144-145], is a significant step towards providing lower-energy barriers for hole carrier injection. It has the added advantage of reducing material cost and fabrication cost on flexible substrates. Promising materials for flexible electrodes to match with organic active layers are poly(3, 4-ethylenedioxythiophene), polypyrrole or polyaniline [146-147]. These materials have relatively high electrical conductivity, flexibility, ease of synthesis and environmental stability. Further, an effective and scalable patterning technique of solution processable conducting polymers is also critical for the low-cost fabrication of organic electronic devices with suitable polymer electrode.

Solution processable semiconducting polymers are vital since the usual low temperature thermal evaporation processes involving high vacuum, employed for the deposition of small molecule semiconductors are not suitable for the realization of large area flexible sensors based on OTFTs. The synthesis and study of rr-P3HT has provided conjugated polymers that has furthered the use of these materials in the aforementioned applications [148]. However, despite their high conductivity and good solubility, regioregular polythiophenes have poor mechanical and process properties relative to the typical flexible polymers. One approach to solving this problem is to synthesize poly(3-alkylthiophene) in copolymer structures with various polymer blocks that display desirable mechanical properties, leading to a variety of polymeric materials with improved functionalities [149].

In this chapter, discussion on the structural, thermal, electrochemical, morphological and electrical properties of the conducting polymers synthesized with suitable dopants by various chemical and electrochemical methods is made and their suitability to be used as conducting electrode in OTFTs is presented. Discussion on the properties of the synthesized block copolymers of regioregular P3HT, employed as the channel material in OTFT, is also done.

3.2 Doped Polyaniline Nanowires

One dimensional polyaniline nanowire structures that have diameter between 1 and 100 nm and possess high aspect ratios, have main advantages of high surface-to-volume ratio leading to fast reaction speed, in the case where they are used as active materials and high sensitivity, when used as an electrically conducting path in sensors. In addition, this aspect also leads to ease of miniaturization, minimum power consumption and low cost as a result of the small volume of required reagents [150]. It has been reported that polyaniline has an intrinsic nature to grow 1-dimensionally [151] which is not the case for other types of conducting polymers such as polypyrrole or polythiophene. In this study, polyaniline was synthesized by both chemical and electrochemical methods, as described in Chapter 2, to obtain polyaniline nanostructures. The polymers were characterized for their structural, morphological, electrical and electrochemical characteristics. The conventional method of polymerization of aniline, commonly referred to as bulk polymerization, resulted in irregularly shaped agglomerates containing nanofibers and particulates. Electrochemical methods, with the aid of templates and SGM resulted in uniform nanostructures of polyaniline.

PANi synthesized by all methods resulted in the emeraldine salt form, which on treatment with NH_4OH, was converted to the emeraldine base form. To improve the processability of synthesized PANi, it was redoped with CSA and treated with secondary dopant, *m*-cresol. Spectroscopic studies confirmed the formation of the emeraldine form PANi, synthesized by all methods. Spectroscopic results, morphology, electrochemical and conductivity analysis are discussed in the following sections.

3.2.1 UV-vis-NIR spectra

UV-Vis spectroscopy is able to provide information about the π-conjugation along the polymer backbone and hence conduction electron mobility, allowing the conducting and non-conducting forms of polyaniline be easily distinguished. One of the major limitations of conducting polymers is that they are characterized by very low solubility in common organic solvents. A typical UV-Vis specimen was prepared dissolving a minimal amount of EB in chloroform resulting in a blue solution. The doped form, PANi-CSA was dissolved in both chloroform and *m*-cresol to record the UV-vis spectrum. There were two sharp and well defined absorption peaks around 326 and 624 nm in the UV-vis spectrum of EB, which were ascribed to the π– π^* transition of the aminebenzenoid rings and the exciton absorption of the iminequinoid rings, respectively [152], as shown in Fig. 3.1.

In a doped form of PANi, when the imine groups are protonated by acids, it is expected that the nitrogen atom and its neighbouring iminequinoid ring become a semiquinoid radical cation (Fig. 1.9 in Chapter 1) and the intensity of exciton absorption band decreases. For fully protonated imine groups, the exciton absorption band of the PANi tends to disappear [153]. In this study, for PANi-CSA in chloroform, two new absorption bands at 410 nm and 800 nm were observed at the same time due to the excitation of corresponding polaron band, the former is a shoulder band and the latter a broad one. Hence, the spectrum of conducting PANi dissolved in chloroform showed three distinctive peaks at 360, 410 and 800nm, corresponding to π-π* transition of benzenoid, polaron-π* and bipolaron transitions, respectively. On the other hand electronic spectra of PANi-CSA in *m*-cresol gave only one absorption peak at about 440 nm and a steadily increasing “free carrier tail”. The absorption peak at 440 nm and the free carrier tail for the sample in *m*-cresol are consistent with an expanded coil-like conformation and a delocalized polaron structure (longer conjugation length). The spectra confirm the effect of secondary doping of PANi-CSA with *m*-cresol [154].

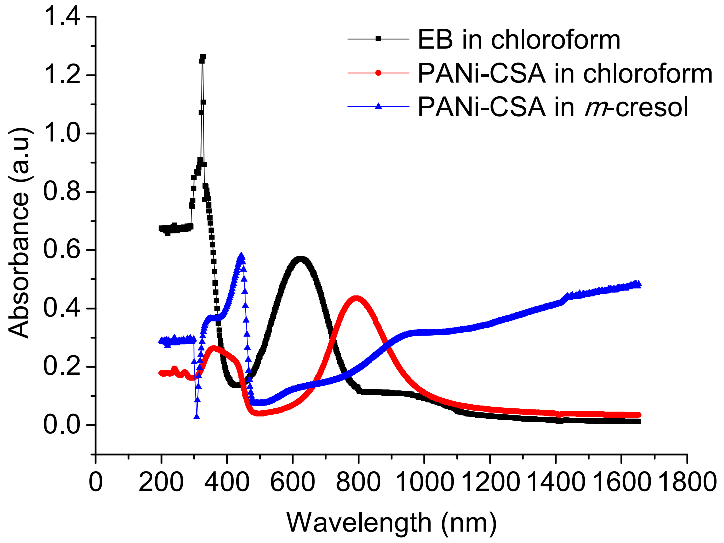

Fig. 3.1: UV-vis-NIR spectra of base and doped forms of PANi.

3.2.2 FTIR Spectra

Fig. 3.2 shows the FT-IR spectra of undoped and doped nanofibers of PANi. For the emeraldine base (EB) form of the nano and the bulk synthesized PANi, the peak for C=C stretching of quinoid ring appears at 1598 cm^{-1} and the band of C=C stretching of benzenoid ring appears at 1490 cm^{-1}. The band of C–N stretching vibration of secondary aromatic amine appears at 1307 cm^{-1}. A strong characteristic band appears at 1160 cm^{-1}, which has been explained as an electronic band [155] or a vibrational band of nitrogen quinine. The C–H out-of-plane bending mode has been used to identify the type of substituted benzene [156]. For EB, this mode was observed as a single band at

825 cm^{-1}, which is found in the range of 800–860 cm^{-1}, predicted for a 1,4-disubstituted benzene. A band attributable to other types of substituted benzenes was not observed. Thus, the FTIR spectrum gives evidence of the formation of EB form of PANi with very low degrees of branching and/or crosslinking. The vibration bands situated around 507 cm^{-1} was attributed to the benzenoid ring's 1,4 disubstituted N-H out of plane bending.

For the HCl doped EB (PANi-HCl), the bands at 1562 cm^{-1} and 1483 cm^{-1} correspond to the stretching vibrations of quinoid and benzenoid rings, respectively, indicative of the oxidation state of emeraldine salt (ES) of polyaniline. As commonly observed for ES polyaniline, the quinoid band is less intense than that of the benzenoid band. The strong band at 1150 cm^{-1} (N=Q=N, Q representing the quinoid ring, related to the protonated form) was described by MacDiarmid et al. [157] as the "electronic-like band". It is considered to be a measure of the degree of delocalization of electrons and thus a characteristic peak of conducting PANi. The peak at 1294 cm^{-1} can be assigned to the stretching vibration of C–N for conducting PANi, associated to the oxidation or protonation states. For the CSA doped nano and bulk forms (PANi-CSA), the band of C=O stretching vibration appears at 1743 cm^{-1} and the peak corresponding to C–O stretching vibration appears at 1164 cm^{-1}. The spectra obtained for the base and salt form of PANi are in good agreement with that reported in literature [156].

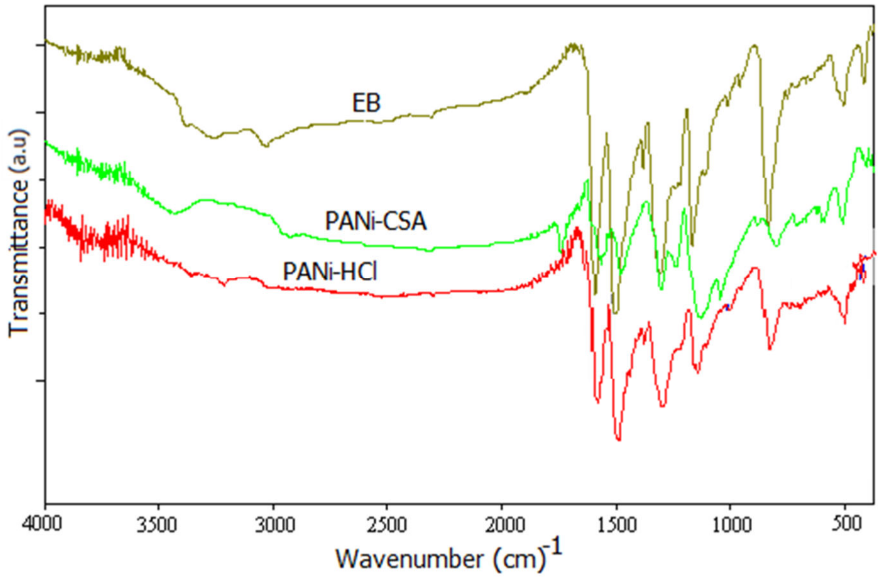

Fig. 3.2: FTIR spectra of base (EB) and salt form of PANi, PANi-CSA and PANi-HCl.

3.2.3 Morphology of PANi Nanowires

Since it is reported [111] that synthesis by conventional oxidative polymerization reaction also results in nanostructured PANi, the morphological evolution of PANi during synthesis by conventional method was studied. Samples were withdrawn as soon as the green colour of PANi became visible, after 30 min and after the complete reaction of 2 h. The SEM image of samples of PANi, during the course of the reaction and after completion of reaction are shown in Figs. 3.3(a)-3.3(c). Polyaniline nanofibers start forming at an early stage of reaction as evident in Fig. 3.3(a). These nanofibers have an average diameter of 80-85 nm. As more APS was fed into the reaction mixture, the nanofibers became scaffolds for secondary growth of polyaniline [Fig. 3.3(b)] and finally turned into irregularly shaped agglomerates containing nanofibers and particulates [Fig. 3.3(c)]

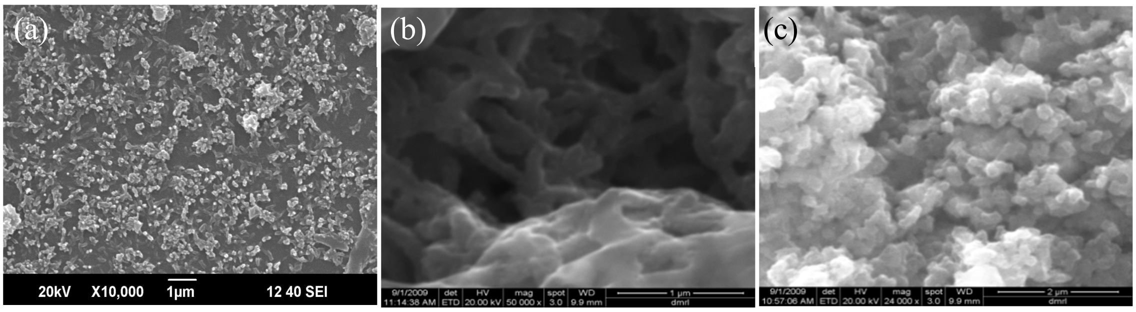

Fig. 3.3: SEM images (a-c) showing the morphological evolution of PANi during chemical oxidative polymerization in 1 M HCl at about 0 ºC. The samples were extracted: a) as soon as the green color of PANi became visible b) after 30 min and c) after 2 h.

It was thus inferred that if secondary growth could be suppressed by employing lower concentrations of monomer and APS or by template polymerization, nanostructured PANi could be obtained. The SEM images of PANi synthesized by dilute polymerization are shown in Figs. 3.4(a) and 3.4(b). As discussed in the experimental section, various concentrations of monomer and the molar ratio of aniline/APS were used for the synthesis. For ALN1, ALN2 and ALN3, the obtained nanofibers had more or less similar morphology. Significant difference in morphology was observed only when the molar ratio of aniline to oxidant was reduced to 1/10. As shown in Fig. 3.4(a), at a higher molar ratio of aniline:APS (ALN1), short and non-uniform nanofibers with diameter ranging from 500 nm to 1μm was obtained. Reducing the molar ratio of aniline/oxidant to 0.15 from 1.5, resulted in nanofiber growth of smaller diameter, but the sample was observed to be highly agglomerated as shown in Fig. 3.4(b), for ALN4.

To avoid secondary growth on PANi nanostructures, the method of interfacial polymerization was also attempted. Since the monomer, aniline and the initiator, APS were separated by the boundary between the organic and the aqueous phase, polymerization occurred only at this interface where all the components needed for polymerization came together [158]. Due to the hydrophilic nature of the doped PANi nanofibers formed, they could move away to the aqueous layer, thus inhibiting secondary growth. New nanofibers could then be allowed to form at the interface. The SEM image of PANi nanofibers formed by interfacial polymerization is shown in Fig. 3.5(a). Though nanofibers of 200-300 nm were obtained by interfacial polymerization, the uniformity of the obtained nanofibers was poor and the agglomeration also could not be avoided.

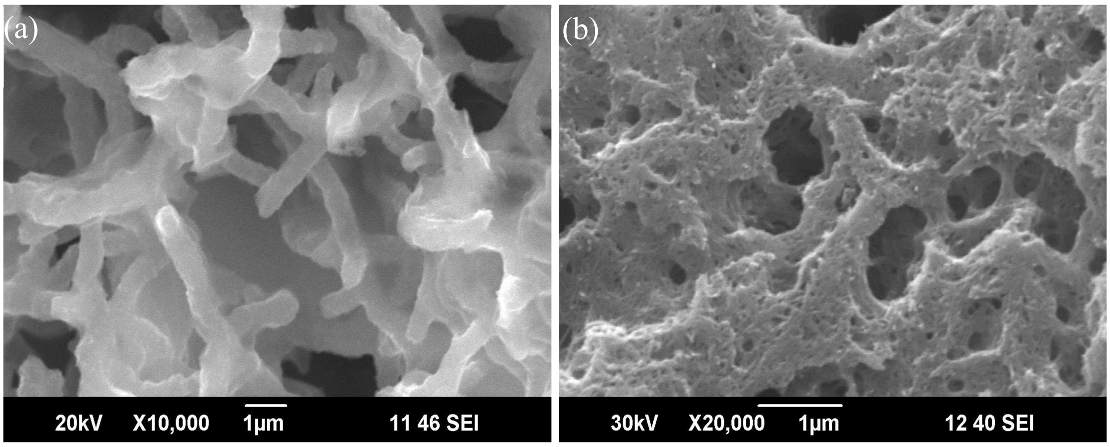

Fig. 3.4: SEM image of PANi nanofibers synthesized with very low concentration of aniline monomer (0.01 M) (a) ALN1 with aniline/APS ratio of 1.5 and (b) ALN4 with aniline/APS ratio of 0.15.

Uniform morphology of nanofibers could not be obtained by the chemical methods of polymerization employed for synthesis. In order to control the morphology of the synthesized nanofibers, electrochemical template polymerization using track etched membrane and SGM methods were employed. The diameter of the nanowires depend on the diameter of the pores of the track etched membrane. The SEM image of a representative template synthesized nanofibers is shown in Fig. 3.5(b). Using a track etched membrane of 800 nm pore size, uniform nanofibers of ~ 400 nm were obtained. The disadvantage of the method was the difficulty in retrieving the formed polymer from the gold coated polycarbonate membrane. The template when dissolved in methylene chloride, the nanofibers could be isolated only along with gold film, the separation of which was very difficult.

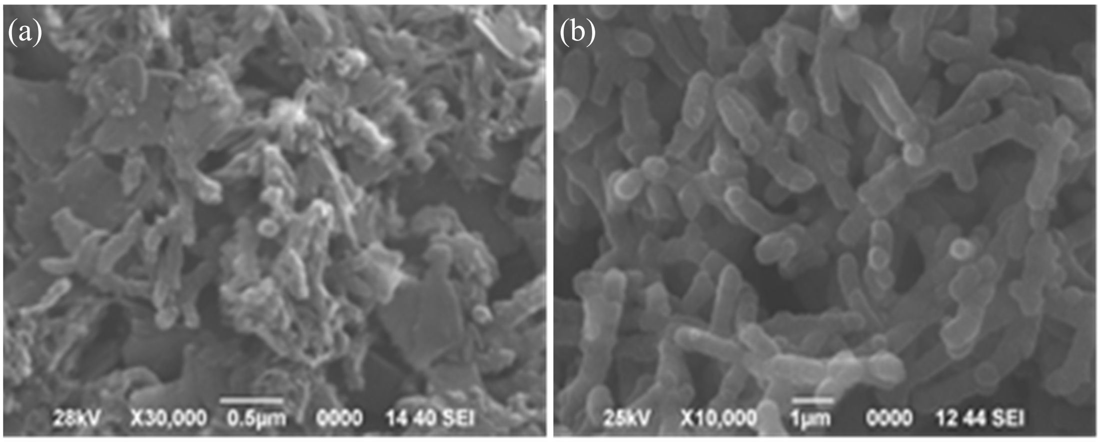

Fig. 3.5: SEM of nanofibers synthesized by (a) interfacial polymerization and (b) template polymerization.

SGM method of synthesis yielded more uniform nanowires, with controlled morphology, depending on the concentration of the monomer and acid used for synthesis. A detailed study was done to understand the evolution of nanofiber formation. The highest concentration of the monomer used for the study was 0.3 M. At concentrations higher than 0.3 M, uniform films could not be obtained and the deposits were porous in nature and were of non-uniform morphology. The formation of nanowire with increase in reaction time was studied for the case of 0.3 M of monomer in 1 M HCl (designated as NP1). After completion of 6.5 h of deposition, morphology characterization revealed formation of short rods (4 to 5 µm length) of diameter ~ 500 nm as the primary structure. At this concentration of the monomer, the SEM picture revealed a super structure like secondary growth on the rods [Figs. 3.6(a) & 3.6(b)]. The primary and the secondary structures were further analyzed by TEM. The primary nanostructure was revealed to be nanorods on which the secondary superstructure nanotubes of ~ 50 nm diameter, protruding out. Figs. 3.7(a) and 3.7(b) show the TEM of the primary structure with the secondary superstructure growth over them. Fig. 3.7(c) shows the TEM of a single nanotube over the primary nanorod.

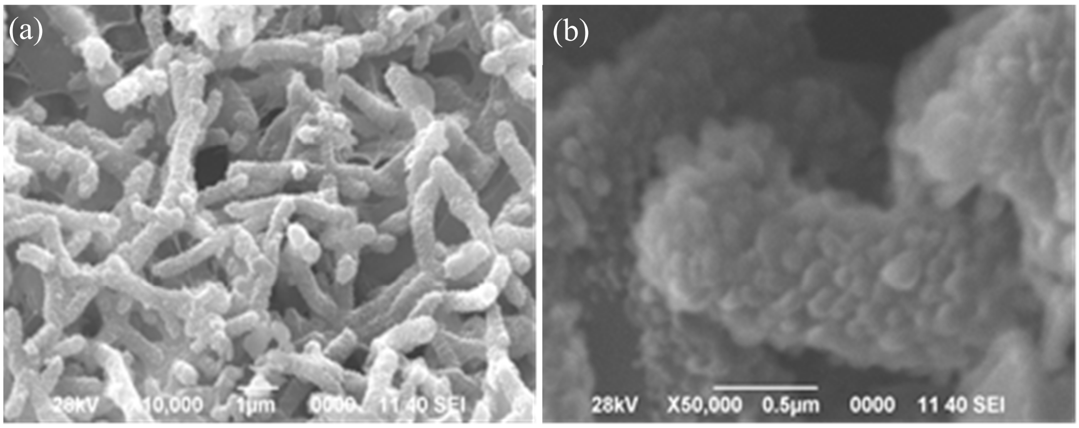

Fig. 3.6: SEM of (a) NP1 at lower magnification and (b) NP1 superstructure at higher magnification.

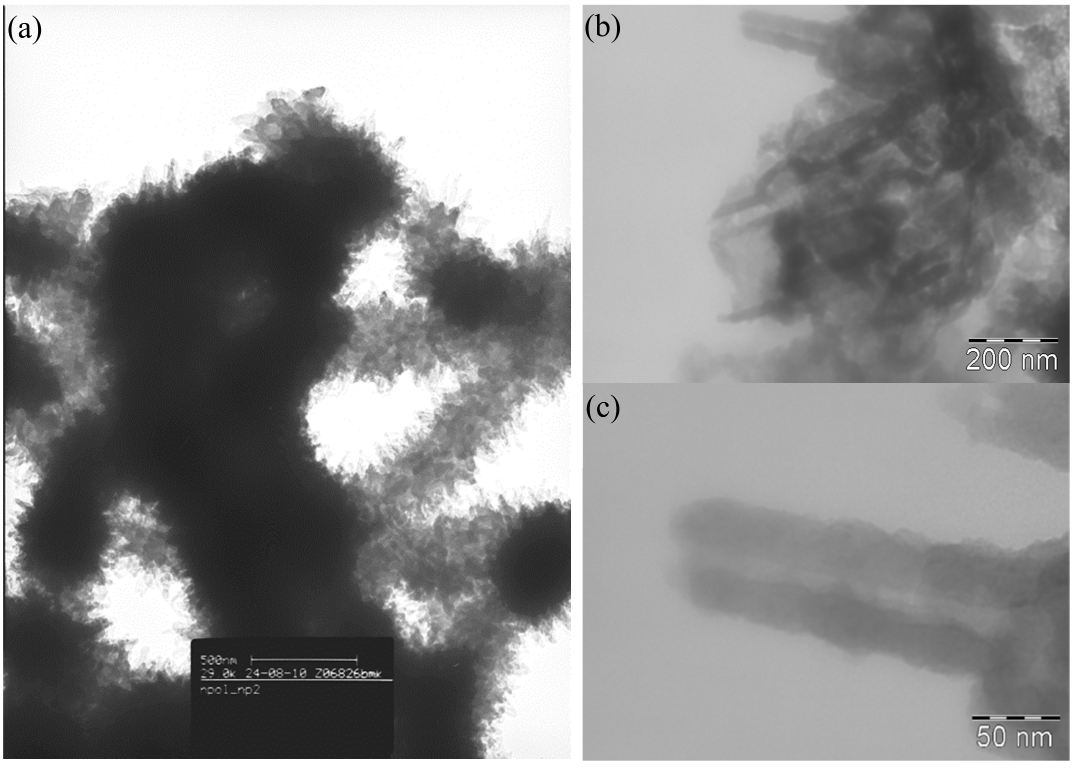

Fig. 3.7: TEM of NP1 showing (a) the primary structure (b) at higher magnification showing the secondary superstructure and (c) an individual nanotube.

Morphology of the nanowires, NP1, synthesized was studied in detail by SEM at definite time intervals during the initial stage of synthesis. The SEM micrographs were obtained at 5, 10, 20 and 30 min from initiation of synthesis. In Figs. 3.8(a) and 3.8(b), the diameter of the wires do not show much variation and was around 170 nm. But the yield of the wire at 10 min is seen to be higher when compared to 5 min of deposition. The diameter of the wires at 20 min and 30 min is 200 nm and 310 nm, respectively [Figs. 3.8(c) & 3.8(d)]. The increase in density of the wire deposited with time reveal that all the nucleation centres are not formed at the start of the deposition, but also during the course of the deposition process. Unlike the reported growth on the gold and platinum substrates, the morphology on titanium substrate after 5 min of synthesis, which is the length of time at which initial growth of polymer becomes discernible in the SEM, did not show any circular deposits as nucleation centres. Instead, nanowires of lower diameter are deposited [Fig. 3.8(a)] which grow in density as well as in size (diameter) with time. It was further noted that unlike on platinum or gold substrates [159], no oriented nanowires were obtained on the titanium substrate. An extension of growth in the vertical direction was not observed. The difference in morphology on gold/platinum and titanium may be due to the difference in lattice structure of the metals [160]. With increase in time, the deposition seemed to occur radially, increasing the diameter of the nanowire. Figs. 3.8(a)-3.8(d) also reveal that the length of the deposited wire tends to reduce as a function of time. Thus, it can be seen in Figs. 3.8(c) & 3.8(d) that there are bright white spots at the tip of about 50% of the wires. In comparison, in Figs. 3.8(a) & 3.8(b) there are no such bright spots. These bright spots are attributed to be the breakage points on the nanowire. It is inferred that as a function of time, when more and more material gets deposited, increasing the diameter of the nanowire, a tendency for breakage sets in. The thickness of the deposited film of NP1 was measured by placing wire deposited on titanium vertically on the SEM sample stage. Fig. 3.8(e) shows the thickness of nanowire deposited on the electrode surface as ~ 30 μm.

As the binary structured nanorods are not suitable for electronic applications, where 1-D nanostructres are the potential candidates, synthesis of the nanowires were attempted by varying the concentration of the monomer and the acid downwards. The morphology of the nanowires thus synthesized, NP2, NP3 and NP4 are shown in Figs. 3.9(a), 3.9(b) & 3.9(c), respectively.

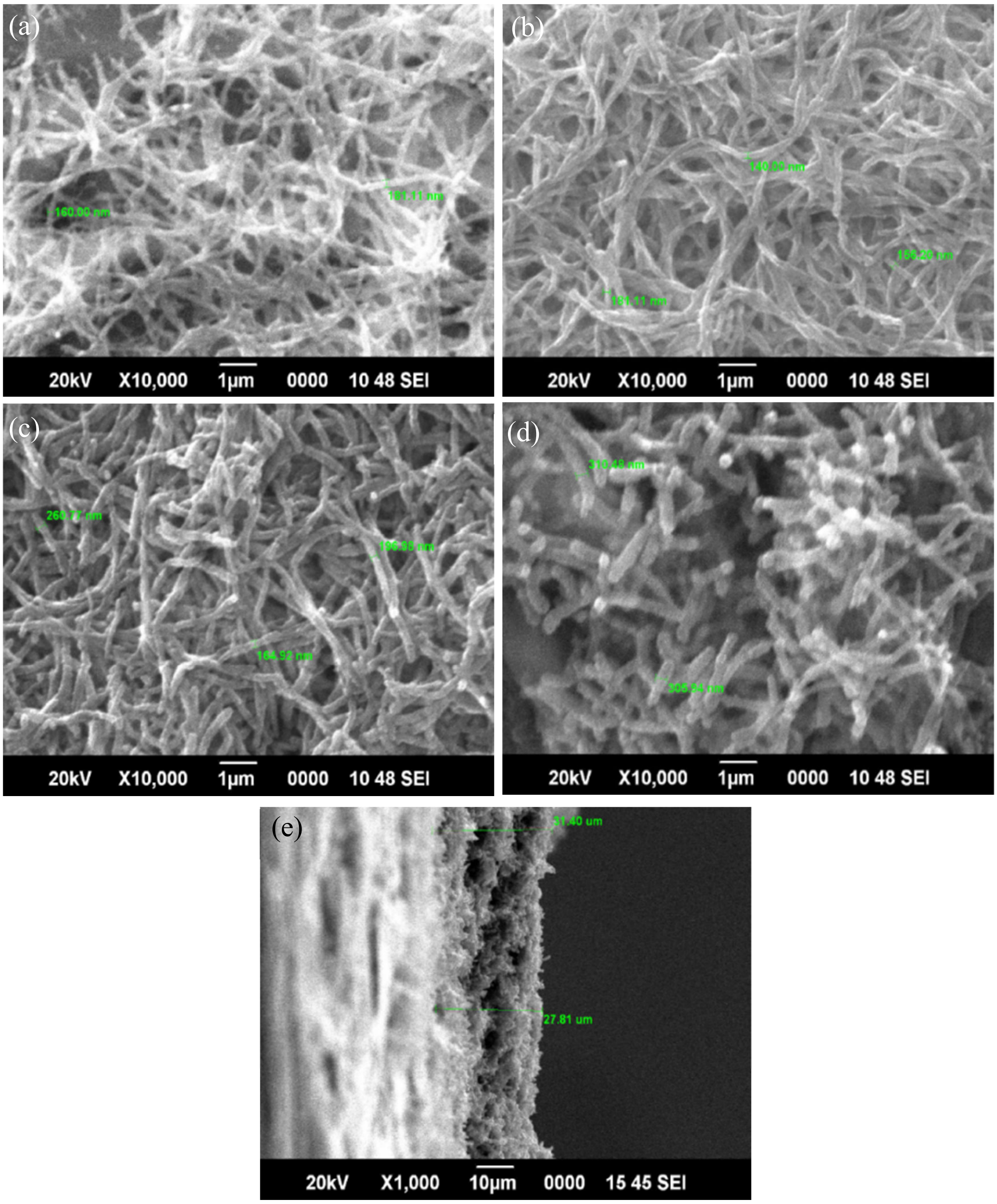

Fig. 3.8: SEM of (a) NP1 at 5 min (b) NP1 at 10 min (c) NP1 at 20 min (d) NP1 at 30 min; (e) SEM showing thickness of NP1.

The SEM micrographs of these nanowires obtained after 6.5 h of synthesis reveal that the conditions of electrochemical synthesis involving variation in acid and monomer concentrations do affect the morphology of the nanowires. On reducing the concentration of the monomer from 0.3 M to 0.1 M, the diameter of the wires was found to decrease from 400 nm to 375 nm. The length of the nanowire was found to increase with decrease in monomer concentration. The diameter is further reduced to 150 nm with further reduction in monomer concentration to 0.0125 M. A slight reduction is again observed by reducing the acid concentration to 0.25 M [Fig. 3.9(c)]. The diameter of the wires is lowest, (~ 80 nm) at the lowest concentrations of the monomer and the acid used (NP4).

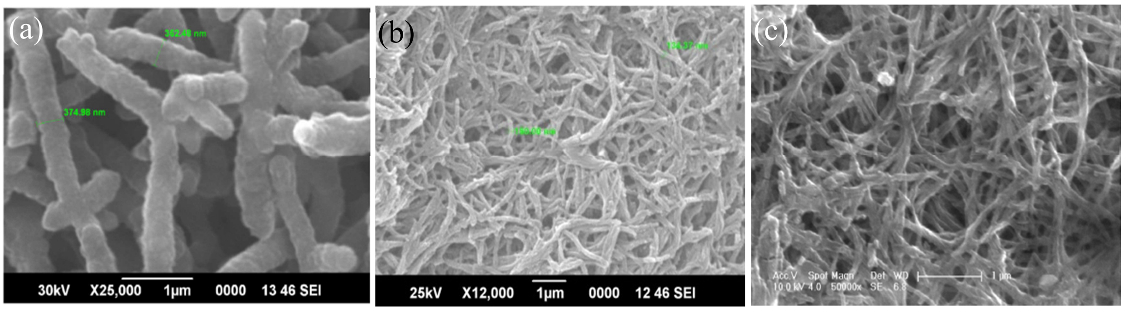

Fig. 3.9: SEM of (a) NP2 (b) NP3 and (c) NP4.

Compared to the nanowire growth on platinum and gold substrate, the growth on titanium is disordered with fibril growth at higher concentration. The fibril growth is reduced on gradually decreasing the concentration of the monomer and becomes nill for the lowest concentration of the monomer (NP4). The reduction in the occurrence of superstructure growth is clear from the TEM micrographs of NP2 as revealed in Fig. 3.10(a). The nanorods show very less amount of growth of the secondary superstructure. At the lowest concentration of the monomer, exclusively nanowires were obtained with no superstructure growth. Further reducing the monomer and acid concentrations did not yield nanowires that form smooth films of the conducting polymer. In this case, the polymer yield was also very less. Morphology could thus be controlled by varying the monomer and acid concentration. The thickness of the film of NP4, after the complete 6.5 h of deposition was found to be ~ 1.5 µm [Fig. 3.10(b)].

Morphology of NP2 nanowires were also studied in detail by SEM at definite intervals during the initial stage of synthesis. The SEM was recorded after 5, 10, 15, 20, 25 & 30 min from initiation of synthesis [Figs. 3.11(a)–3.11(d)]. In these cases also, the diameter of the wires increased with increase in time. However, it was observed that at lower concentrations of the monomer, diameter of the synthesized wire gets reduced.

The wires deposited at 5 min and 10 min were of diameter ~ 85 nm. As in the case of NP1, there is not much variation in the diameter of the NP2 wires in the first 5 and 10 min, except that the density of the deposited nanowire is more at 10 min. At 20 min of deposition, the diameter increased to an average of 120 nm and it is further increased to 160 -170 nm at 30 min of deposition.

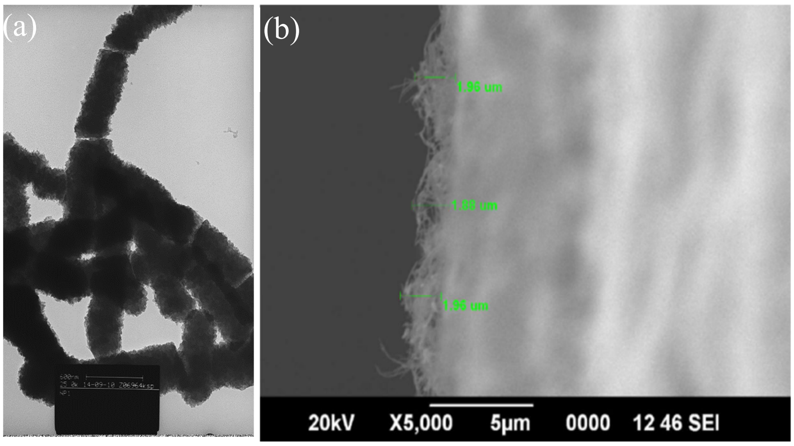

Fig. 3.10: (a) TEM of NP2 and (b) SEM showing thickness of NP4.

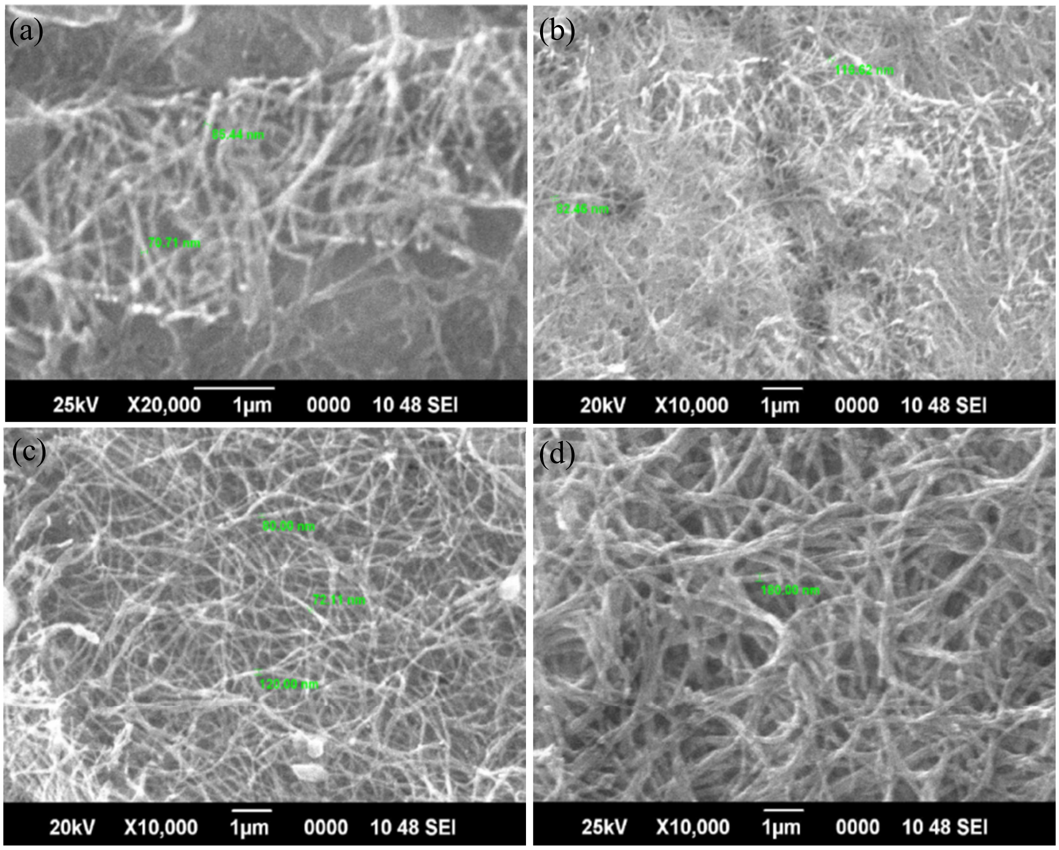

Fig. 3.11 SEM of NP2 at (a) 5 min (b) 10 min (c) 20 min and (d) 30 min

In the case of NP3 and NP4 there was no appreciable amount of deposition for the first 30 min of synthesis as revealed in SEM. At the lower concentrations, the minimum time required for occurrence of initial stages of growth was about half an hour, when a resolvable SEM micrograph could be obtained. The SEM of NP4 after 30 min of synthesis is shown in Fig. 3.12. Here too, no initial nucleation centres are discernible, instead very low density deposition was observed. This indicates that at lower concentrations, an induction period exists for the initiation of nucleation and growth. Interestingly, for NP4, the diameter of the wires did not change even after the completion of synthesis at 6.5 h.

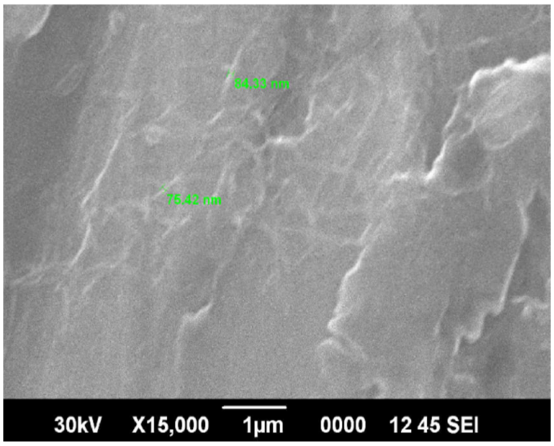

Fig. 3.12: SEM of NP4 after 30 min of synthesis.

From the morphological analysis on the growth of nanowires at times ranging from 5 min to 6.5 h, it is observed that it is difficult to detect the formation of any nucleation centres as circular deposits at the initial stages of deposition at any of the concentration of the monomer studied. Instead, even at the start of the deposition (after 5 min), long nanowires are formed, which increase in number and diameter with time. Also, none of the SEM images reveal a 2D growth at the initial or later stages; the growth is exclusively one dimensional. This type of technologically important 'one dimensional growth' is not observed on other substrates such as platinum and gold [159], which is crucial for electronic applications. At lower concentrations of the monomer, the density of the wires formed per unit deposition area was found to be higher, which indicates that at higher concentration, the tendency of the polymer is to get deposited over the already existing nanowire thereby leading to the secondary superstructure growth. At lower concentrations, the growth is lengthwise; also, more number of wires are formed.

3.2.4 Electrochemical Analysis

Investigations on the electrochemical stability of PANi nanofibers were carried out for samples synthesized by the three different methods, interfacial, electrochemical template and SGM polymerization. These experiments were performed by means of a potentiodynamic procedure involving repetitive oxidation and reduction in HCl media. It was established that SGM and template synthesized PANi are much more stable than interfacially synthesized ones. The cyclic voltammogram is characterized by a first oxidation wave, corresponding to the interconversion between the fully reduced and the semiquinone form at about 0.25 V and a second main wave at about 0.75 V related to the interconversion between the semiquinone and the fully oxidized form of polyaniline [91]. With respect to the reversibility of the electrochemical reaction during the cycles, the voltammetric behaviour remained almost unaffected for 75 cycles [Fig. 3.13 and Fig. 3.14] for the electrochemically synthesized samples.

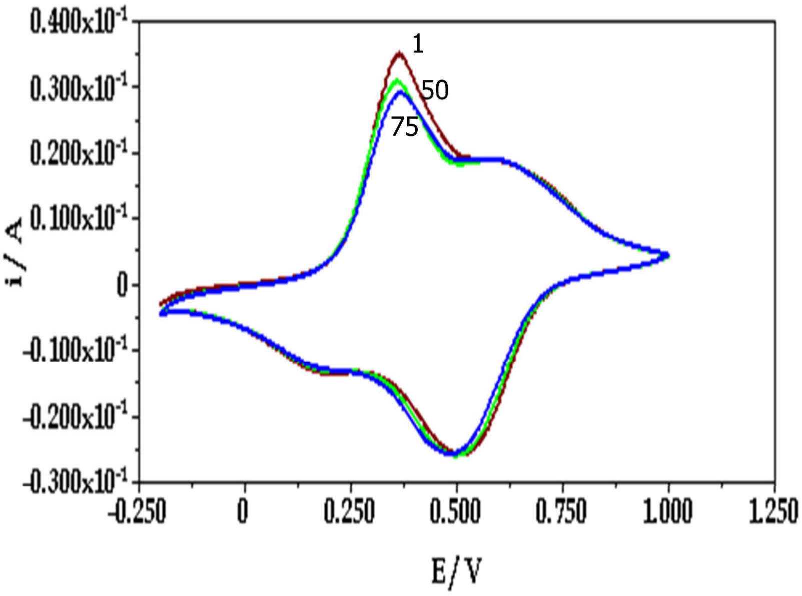

Fig. 3.13: Cyclic voltammetry analysis of nanofibers synthesized by SGM.

The interfacially synthesized PANi, however, showed a significant alteration in the voltammetric curves as shown in Fig. 3.15. This is attributed to the more uniform structures of the nanowires synthesized by the electrochemical method. Higher redox current [Fig. 3.16] was observed for the SGM synthesized nanofibers than the interfacial and template polymerized nanofibers revealing higher surface area for the SGM nanofibers, which is of advantage for current conduction, when used as electrode in OTFT.

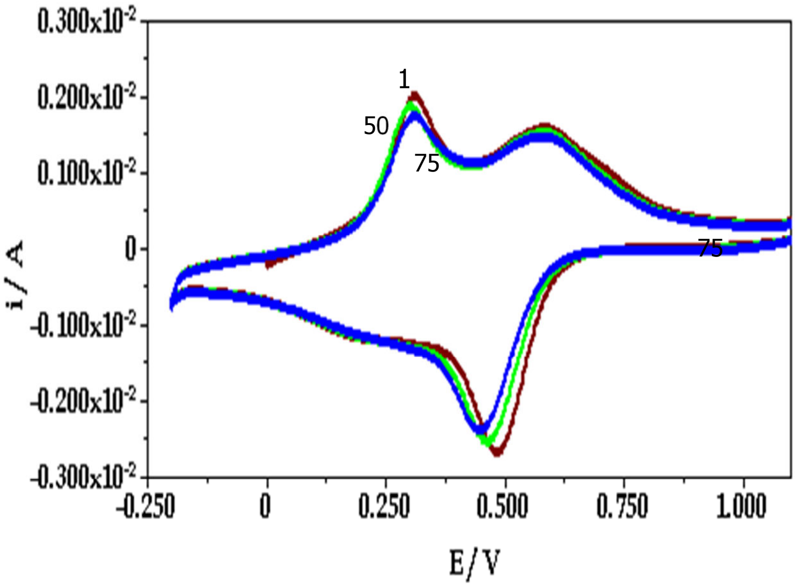

Fig. 3.14: **Cyclic voltammetry analysis of nanofibers synthesized by template polymerization.**

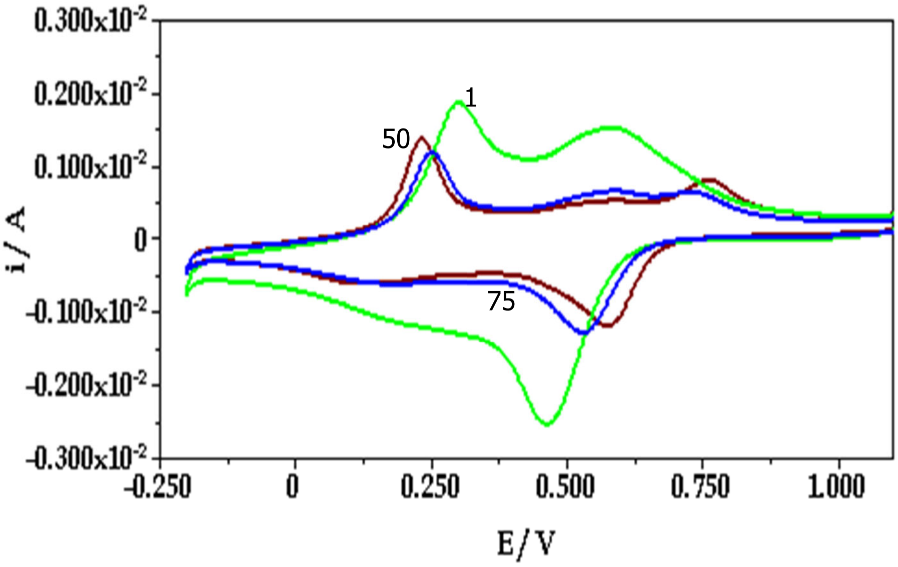

Fig. 3.15: **Cyclic voltammetry analysis of nanofibers synthesized by interfacial polymerization.**

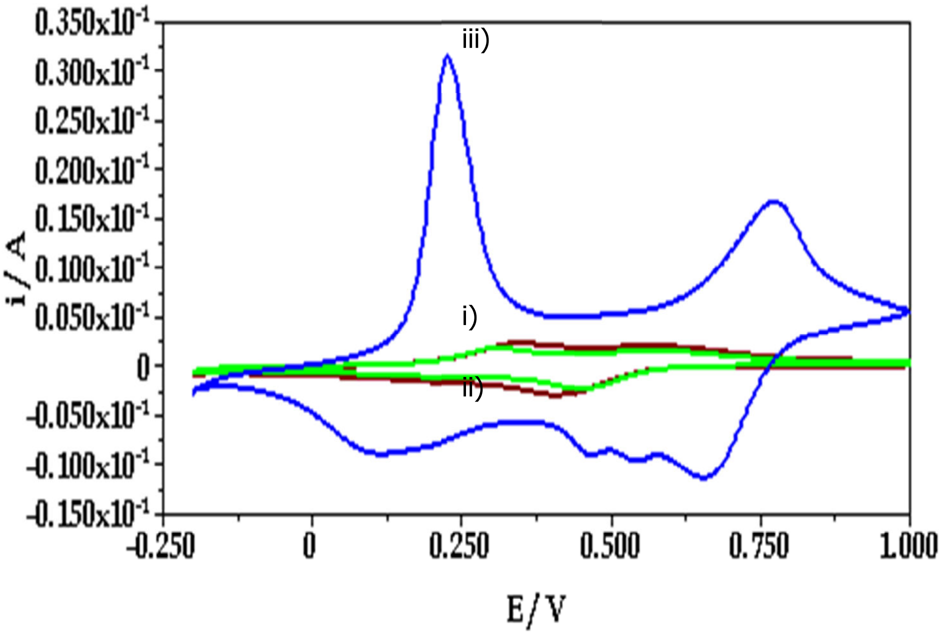

Fig. 3.16: Cyclic voltammetry analysis of nanofibers synthesized by i) template polymerization ii) interfacial polymerization and iii) SGM.

Results of comparison of CVs of NP1 an NP4 synthesized by SGM, are shown in Figs. 3.17 and 3.18, respectively. As evident from the figures, the redox current is higher for NP4, compared to NP1. This is attributed to higher surface area and aspect ratio of NP4, compared to NP1. Hence, NP4, when dispersed in suitable solvent is more appropriate to be used as electrode in OTFT than other nanofibers with lower aspect ratio.

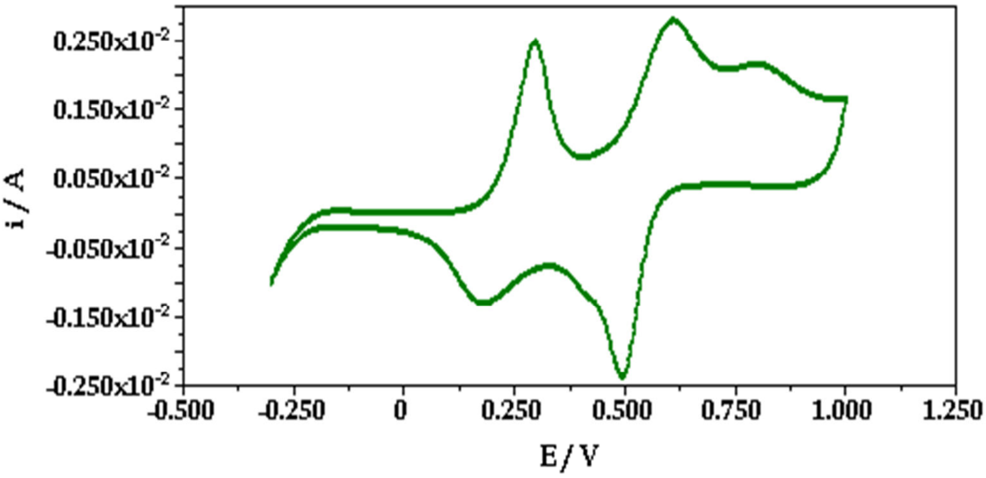

3.17: Cyclic voltammetry analysis of NP1.

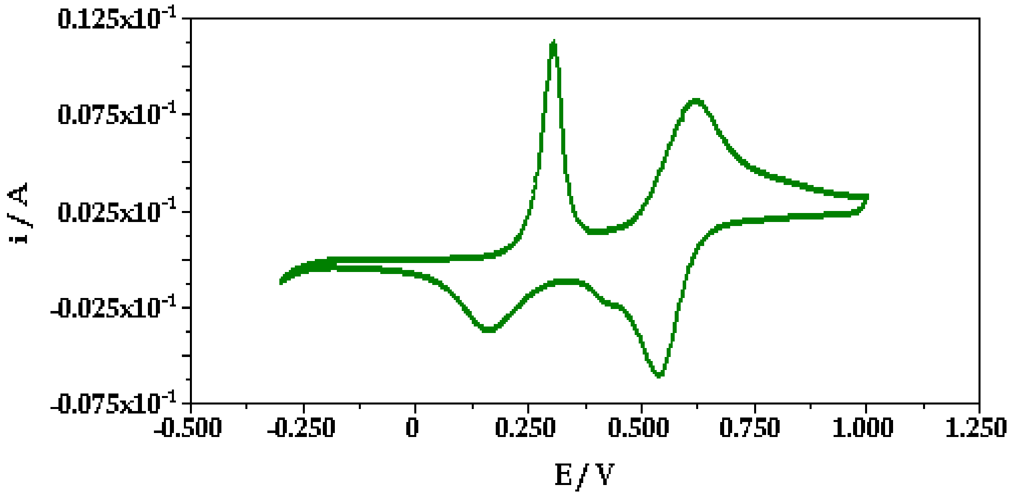

Fig. 3.18: Cyclic voltammetry analysis of NP4.

3.2.5 Conductivity Studies

The conductivity results of the powder pressed pellets and films of synthesized PANi samples are as shown in Table 3.1.

Table 3.1: Conductivity of synthesized PANi nanowires.

S. No.	Sample Designation	Conductivity (S/cm)	
		HCl doped pellet	CSA redoped, film from *m*-cresol
1.	Bulk synthesized PANi	4×10^{-1}	123
2.	ALN series (dilute polymerization)	$2 \times 10^{-1} - 6 \times 10^{-1}$	~ 235
3.	INT series (interfacial polymerization)	$3 \times 10^{-1} - 5 \times 10^{-1}$	~ 185
4.	TMP series (template polymerization)	$4 \times 10^{-1} - 9 \times 10^{-1}$	~ 210
5.	NP1, NP2, NP3 (SGM)	$7 \times 10^{-1} - 9 \times 10^{-1}$	~ 350
6.	NP4 (SGM)	$5 \times 10^{-2} - 7 \times 10^{-2}$	~ 80

PANi nanowires synthesized from 1 M acid yielded polymers with almost similar conductivity, revealing a fully protonated form of emeraldine salt. Pellets of NP4, synthesized from 0.25 M acid had relatively lower conductivity, probably due to insufficient protonation of the imine nitrogen of emeraldine base. For the synthesis of completely doped emeraldine salt, synthesis in strong acid environment is highly essential, which initiates the formation of para-coupled structures [161] of aniline-oligomers at the initial stages of polymerization. Secondary doped NP4 exhibited a conductivity of only 80 S/cm, which was one order less than the other secondary doped samples. The lower conductivity of secondary doped NP4 may be due to the initial formation of branched or cross-linked polymers in a medium of low acidity (0.25 M HCl), which eventually reduced the effective conjugation and hence the resultant conductivity. Redoping with CSA and subsequent secondary doping could not increase the conductivity to the level of other NP series secondary doped films, due to the undesired crosslinking and branching in the polymer structure [161].

The PANi synthesized by different methods were examined for their film forming capability. Dedoped samples of PANi nanowires were redoped with CSA; 3 wt% of the doped polymer were secondary doped with *m*-cresol and drop cast as thin films. Figs. 3.19(a)-3.19(c) show the microscopic images of films cast from ALN4, INT3 and NP4 samples. As is evident from the micrographs, NP4 nanowires formed a more uniform dispersion in *m*-cresol solvent and hence, utilized as conducting electrodes in the fabrication of OTFTs, in spite of its lower conductivity when compared to other conducting polymer nanowires synthesized. The higher uniformity of the film was attributed to the less agglomerated nanostructure of NP4 when compared to ALN4 and INT3.

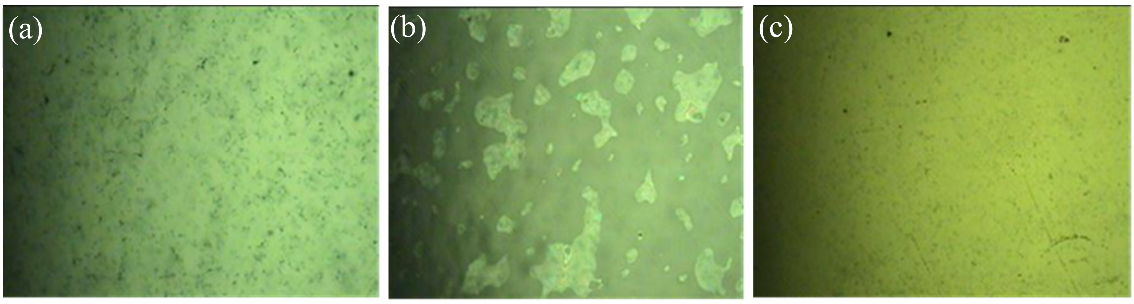

Fig. 3.19: Microscope image of films of CSA doped samples, casted from *m*-cresol solvent of (a) ALN4 (b) INT3 and (c) NP4.

3.3 Patternable Water Dispersible Polyaniline Nanoparticles

Most of the PANi synthesis methods result in powders, which are difficult to process and solubilize. Obtaining a polymer soluble in water and/or in polar solvents is strongly related to the dopant employed in the synthesis process. As discussed in Chapter 2, section 2.2.5 nanostructured PANi, templated with polystyrene sulphonic acid (PANi-PSS) has been synthesized and its conductivity enhanced by more than two orders of magnitude by secondary doping with DCA. This material is readily processed from solution and hence makes excellent alternative to costly metals and metal oxide conductors in organic electronics. The analysis results of water dispersible PANi nanoparticles is discussed in following sections.

3.3.1 UV-vis-NIR Spectra

The UV-vis-NIR spectra of PANi-PSS samples are shown as a function of aniline to acid molar ratio in Fig. 3.20. The peaks corresponding to π-π^* transition of benzenoid at 360 nm, polaron-π^* at 410 nm and bipolaron transition at 785-865 nm [162-164] were observed in the spectra, which confirmed the formation of conductive polyaniline [165-166]. As the PSS content is increased in PANi-PSS, the polaron interband transition (bipolaron transition) of PANi-PSS is red shifted (PSN8 to PSN3). The polaron interband transition is blue shifted again with further increase in PSS content in PANi-PSS (PSN3 to PSN1). The position of polaron interband transition peak (λ_{max}) is quantified in Fig. 3.21. The shift of λ_{max} to higher wavelengths typically indicated an increase in conjugation length of the material [117]. As the content of sulfonic acid group increases, it is expected to increase the number of sites for doping PANi. The conjugation length of PANi therefore increases with increasing amount of PSS. However, PSS is inherently insulating. Excess PSS can thus hinder macroscopic conduction and charge hopping. Therefore, the conjugation length of PANi-PSS decreases with further increasing the PSS content. PSN3 with PANi:PSS ratio 1:1.25 has the highest λ_{max} indicating the maximum doping at this composition.

Fig. 3.22 shows the effect of concentration of precursor acid, HCl, on the UV-vis-NIR spectra. PSN3, which has the highest doping level (PANi:PSS ratio, 1:1.25) in the PSN series, was selected for the study. As the concentration of the acid is decreased, the λ_{max} is blue shifted, indicating insufficient doping of the imine nitrogen of polyaniline during synthesis. On decreasing the acid concentration from 2.0 M to 0.1 mM, the peak at 410 nm almost disappears indicating the formation of insufficiently doped polyaniline. At very low concentration of 0.1 mM, the spectrum is similar to that of emeraldine base (undoped form of polyaniline) with the π–π* transition of benzenoid rings at 334 nm and exciton absorption of the quinoid rings at 632 nm [167-168]. Due to the very low concentration of precursor acid, mixed ortho-para coupling of aniline radicals occurs at the initial stages, leading to the formation of short chain length conjugated polymer and hence the peak at 334 nm is not properly resolved. In a strong acidic environment, the formation of a para-coupled structure is favoured. The subsequent polymerization processes result in emeraldine salt (ES) PANi [161, 169].

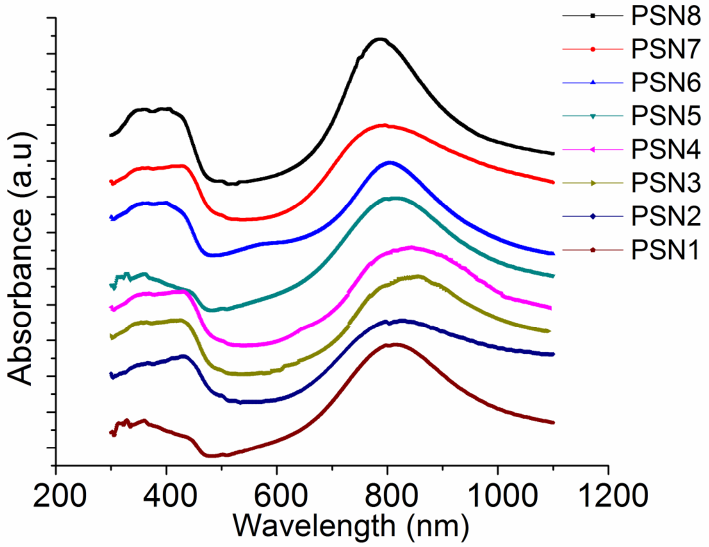

Fig. 3.20: UV-vis-NIR spectra of PANi-PSS samples as a function of aniline to acid molar ratio.

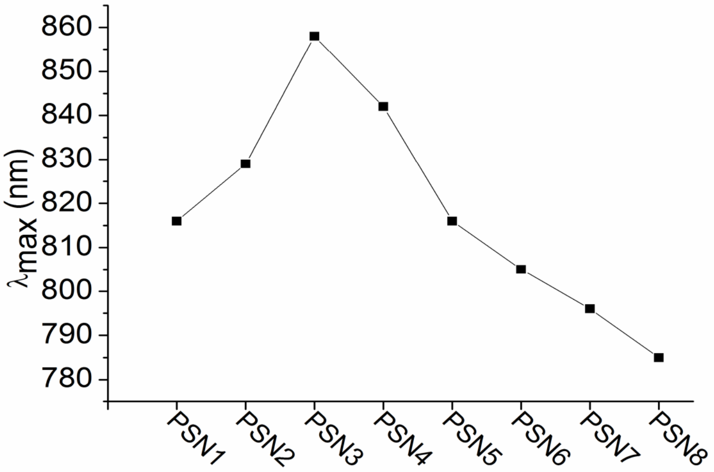

Fig. 3.21: Position of λ_{max} for polaron interband transition for PSN1 to PSN8.

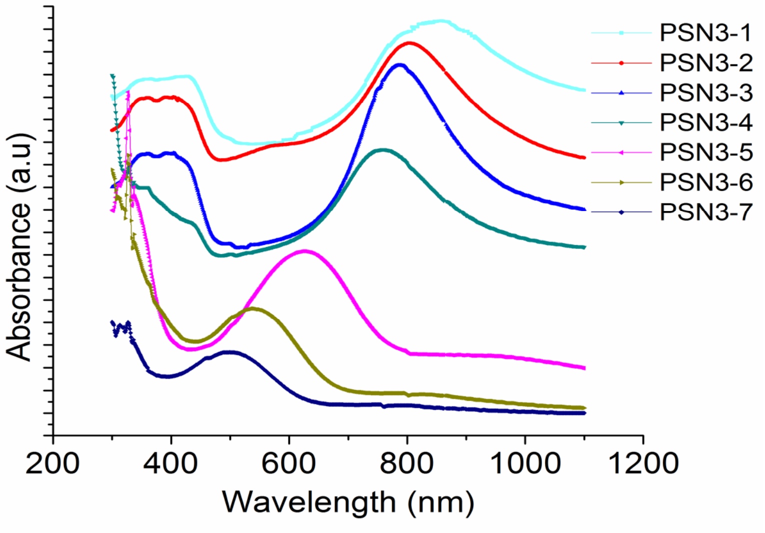

Fig. 3.22: Effect of concentration of precursor acid, HCl on the UV-vis-NIR spectra of PANi-PSS composite.

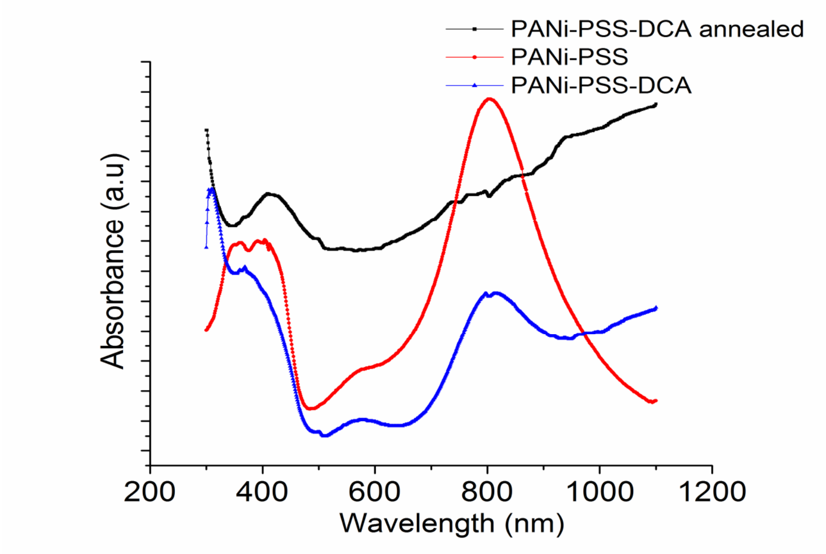

Fig. 3.23: UV-*vis*-NIR spectra of PANi-PSS film (untreated), DCA treated and DCA treated & annealed.

Fig. 3.23 compares the UV-vis-NIR spectra of PANi- PSS films, secondary doped with DCA. PSN3-3 was selected for the study due to its optimum conductivity and morphology for the formation of a stable dispersion (discussed in section 3.3.2). For the film, secondary doped and annealed at 95 ºC, there is an absorption peak at ~ 414 nm and a steadily increasing free carrier tail starting from ~ 1000 nm to the NIR region. The free carrier tail is characteristic of metallic conductive materials. The spectra confirm the effect of secondary doping of PANi-PSS with DCA. The secondary doped PANi-

PSS films have an expanded coil conformation, without any twist defects between aromatic rings. The absorption peak at ~ 800 nm is replaced by interband transitions between half-filled polaron bands [153]. Fig. 3.23 also shows the spectra of DCA treated, unannealed sample where the effect of secondary doping is not complete, as seen from the peak at 809 nm along with the free carrier tail. In the fully annealed samples, the peak due to π-π^* transition also becomes very weak and eventually disappears.

3.3.2 Conductivity Studies

Fig. 3.24(a) shows the structure-conductivity relationships of PANi-PSS (PSN series) as a function of aniline to polystyrene sulphonic acid ratio. As the sulfonic acid group content increases, relative to that of aniline, the conductivity of PANi-PSS increases by approximately 260 times. PANi-PSS at PANi:PSS ratio of 1:1.25 has the highest conductivity of 1.3 S/cm observed in this series of polymers. This conductivity is comparatively higher than the reported values for polymer acid doped PANi [170-171]. Since the polymerization is done in strong acidic environment, which is highly essential for the initial formation of para-coupled structures [172] of aniline-oligomers, it resulted in the completely doped emeradine salt of PANi. Further increasing the PSS content, however, results in a decrease in the conductivity of PANi-PSS. Conductivity of PSN3 further confirms that the maximum doping of imine nitrogen of polyaniline occurs at PANi:PSS ratio, 1:1.25.

Fig. 3.24(b) shows the effect of concentration of precursor acid, HCl on the conductivity of PANi-PSS film (PSN3 series). On decreasing the concentration of HCl from 2 M to 0.1 mM, the conductivity of the films falls by 4 orders of magnitude. For both PSN and PSN3 series, samples with highest λ_{max}, corresponding to the bipolaron transition, in Fig. 3.20 and 3.22 show maximum conductivity in Fig. 3.24(a) and 3.24(b), respectively, which is indicative of the maximum doping levels. The trend is followed for all samples in the two series. Conductivity measurements performed on DCA annealed samples of PSN3-3 exhibited a conductivity of 54 ± 6.0 S/cm. This two order increase in conductivity is due to the effect of secondary doping with DCA [173], which is also substantiated by the appearance of a free carrier tail in the NIR region of the UV-*vis*-NIR spectra [153]. Conductivity results are thus well correlated with the structure of the polymer evidenced by the UV-*vis*-NIR results. The observed conductivity was maintained for several months, as compared to PANi doped with small-molecule acid such as HCl. This is probably due to the lower volatility of polymeric acid that preserves the electrical conductivity of PANi-PSS conducting polymer. The electrochemical stability could not be established by cyclic voltammetric analysis due to the difficulty in resolving the redox peaks in the voltammogram.

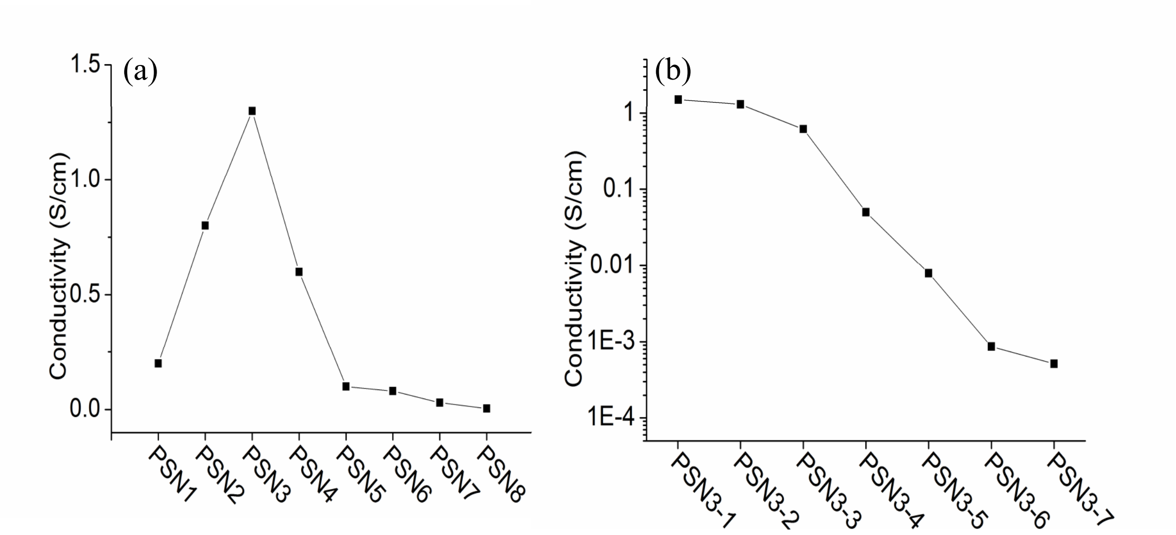

Fig. 3.24: (a) Conductivity of PANi-PSS as a function of aniline to polystyrene sulphonic acid ratio and (b) Effect of precursor acid, HCl, on the conductivity of PANi-PSS film.

3.3.3 X-ray Diffraction

Due to uncertainty in polymeric chains, polymers exhibit different XRD patterns, which arise as a result of the selected synthetic route, ionization state, solvent etc. Fig. 3.25(a) shows the X-ray diffraction plots of the three compositions of PSN series. The three samples have peaks with 2θ around 16°, 20.5° and 25° corresponding to (010), (100) and (110) plane of PANi, which are characteristic of conductive PANi [174]. The peaks are indicative of crystalline regions dispersed in an amorphous medium. The (110) plane corresponding to the crystalline peak appears at almost the same 2θ value of 25° and is observed in all PANi-PSS samples, without any obvious peak shift. This peak is associated with the ionic association between aniline and sulfonic acid groups [171]. The peak of PANi-PSS at 25° of PSN3 is sharper than that of PSN1 and PSN5, indicative of higher crystallinity in PSN3, which is also consistent with the results of conductivity and UV-*vis*-NIR studies.

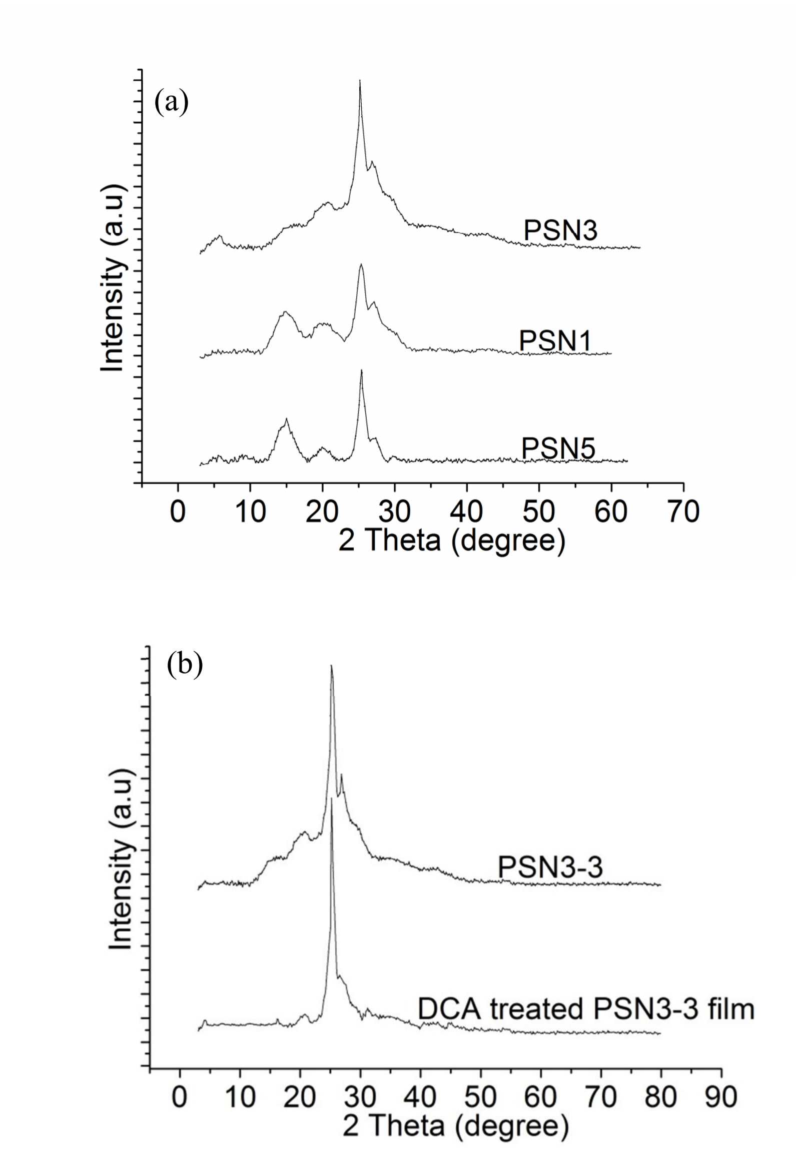

Fig. 3.25: XRD plots of (a) PANi-PSS with three different compositions and (b) DCA treated and untreated, optimum PANi- PSS film, used for device fabrication.

It has been reported that in highly conducting polyaniline, the peak corresponding to (110) plane is prominent and those of (100) and (010) are less intense or absent [175]. In the present study also, the peaks at 16° and 20.5° are more intense for PSN1 and PSN5 and gradually disappear for PSN3, which has higher crystallinity than PSN1 and PSN5. Fig. 3.25(b) shows the XRD plot of PSN3-3 and DCA treated PSN3-3. For the DCA treated sample, the broad background is decreased and the peaks corresponding to

(100) and (010) are absent, which is indicative of a metal like conductivity and very high crystallinity. This is attributed to the improved molecular structure of DCA treated PANi-PSS, reducing the twist defects between aromatic rings due to compact coil conformation of untreated PANi-PSS samples. These observations suggest a straightening of PANi-PSS chains, ultimately resulting in an increase in conductivity by increasing electron delocalization along the PANi backbone.

3.3.4 Morphology

Fig. 3.26(a) shows the image of as prepared PANi-PSS nanocomposite dispersions synthesized with varying concentrations of precursor acid, HCl. The ratio of the PANi:PSS was maintained at 1:1.25 in all the samples (as in PSN3). The colour of the dispersion changes from green to olive to brown from PSN3-1 to PSN3-7, indicating the formation of not fully protonated emeraldine salt of PANi-PSS. SEM micrographs of PSN3-1, PSN3-2, PSN3-3 and PSN3-5 are shown in Figs. 3.27(a)-3.27(d), respectively. The SEM images show that precursor acid concentration plays an important role on the yield and size of the PANi-PSS nanoparticles formed. With the increase of the acid concentration, large diameters and higher yields of nanoparticles were obtained. Synthesis of PANi-PSS at 2 M precursor acid concentration resulted in short length nanofibers that have secondary growth or overgrowth of irregular particles on primary nanostructures [Fig. 3.27(a)].

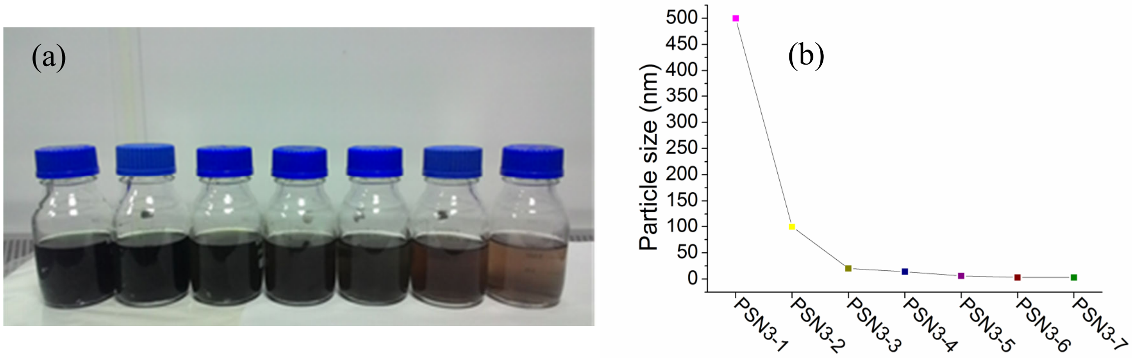

Fig. 3.26: (a) Photograph of PANi-PSS nanocomposite dispersions synthesized with varying concentrations of precursor acid, HCl (PSN3-1 to PSN3-7, from left to right) and (b) the corresponding particle size of nanoparticles.

The PSN3-1 dispersion in water was unstable and settled within 2-3 days. Decreasing the concentration of the precursor acid in the synthesis of PANi-PSS resulted in nanoparticles with much lower dimension than PSN3-1. Fig. 3.26(b) illustrates the size of nanoparticles formed on varying the concentration of precursor acid for the PSN3 series. At very low concentration of the acid, the size of the particles is not resolvable from the SEM images as they remain as agglomerates of very small particles resulting from polymerization. PSN3-3 with an average particle size of 20 nm is optimum for device fabrication as it forms very stable dispersion (stability maintained even after storing for months) and has a conductivity of 0.62 ± 0.05 S/cm, which is further increased to 54 ± 6.0 S/cm on secondary doping with DCA.

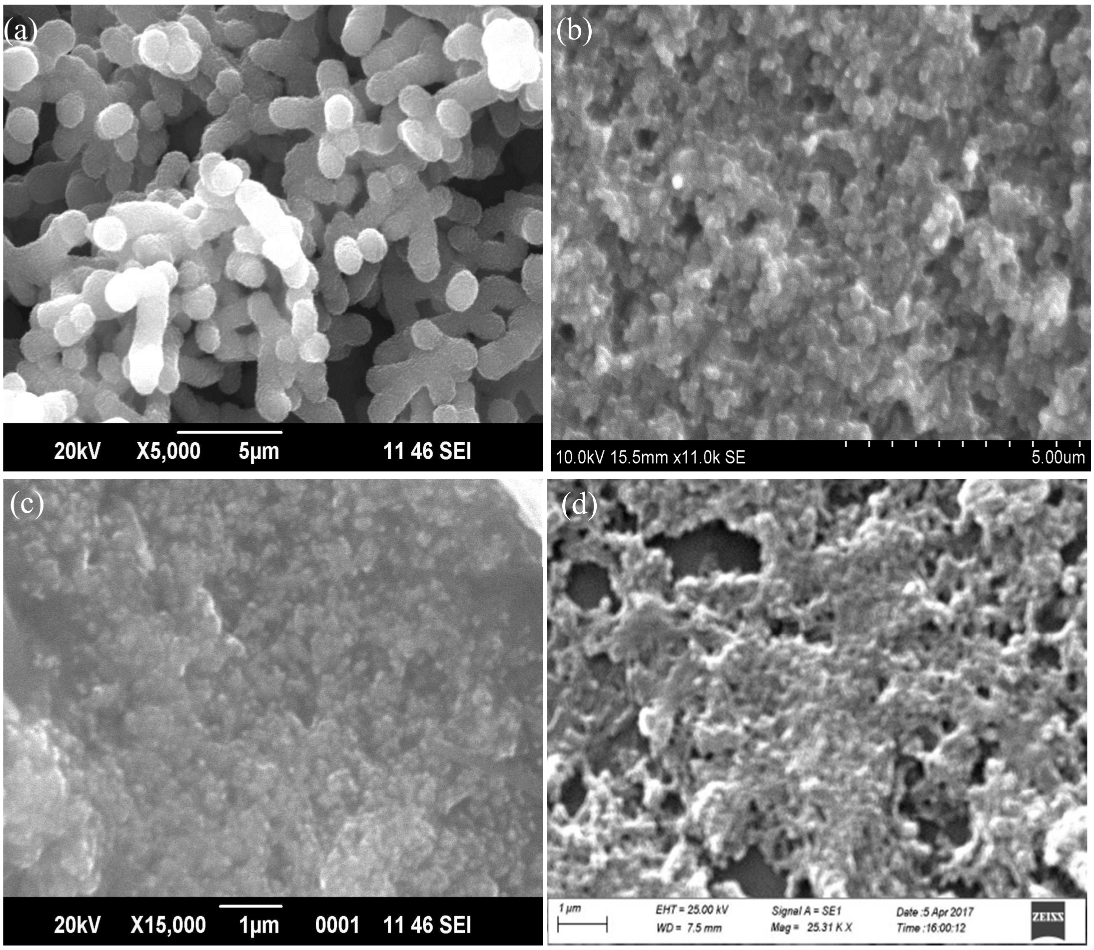

Fig. 3.27: SEM micrographs of (a) PSN3-1, (b) PSN3-2, (c) PSN3-3 and (d) PSN3-5.

Figs. 3.28(a)-3.28(e) show the TEM images of PSN3-1, PSN3-2, PSN3-3, PSN3-4 and PSN3-6, respectively. Short fibre structure of PSN3-1 is evident in the image, with secondary growth over the primary structure. The reduction in particle size with the decrease in the concentration of precursor acid is well evident in the images. The reduction in particle size is achieved at the cost of decrease in conductivity on using lower precursor acid concentration during synthesis.

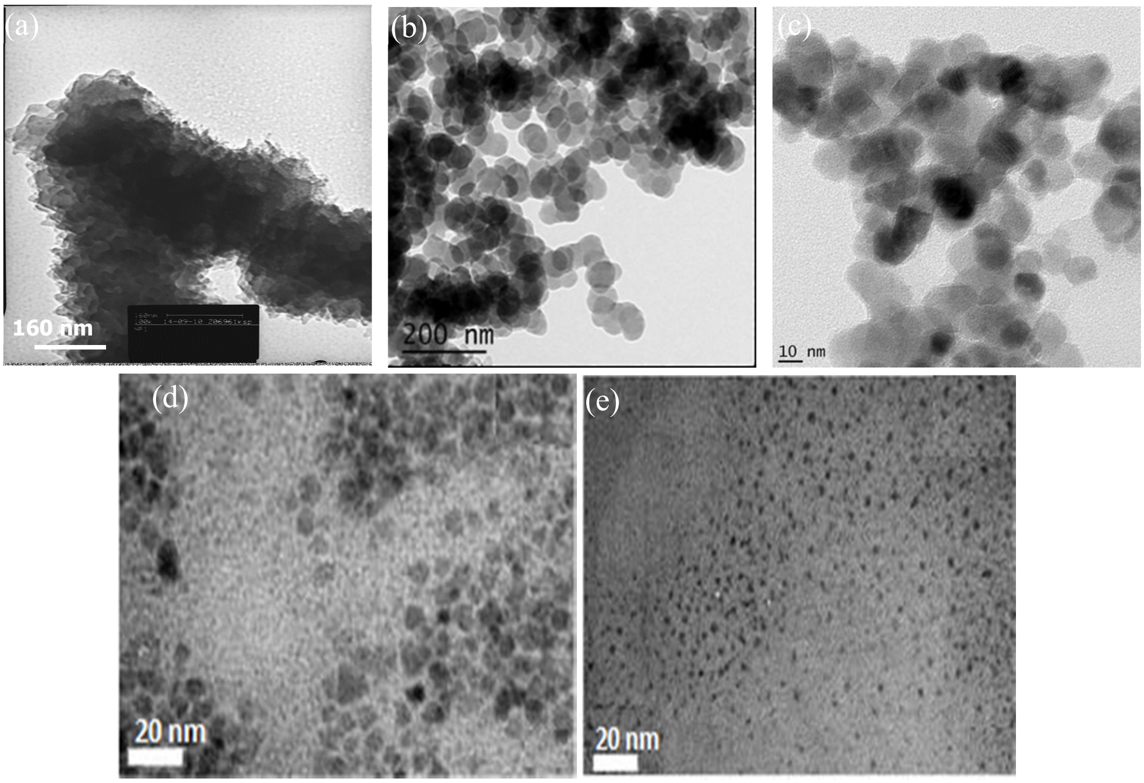

Fig. 3.28: TEM image of (a) PSN3-1, (b) PSN3-2, (c) PSN3-3, (d) PSN3-4 and (e) PSN3-6.

3.4 Electrochemical Work Function of Conducting Electrode Materials

Nanostrutured PANi was synthesized with an aim to use it as the conducting electrode material in OTFT. For a conducting polymer to be employed as the electrode for charge injection in an OTFT, its work function should have a close match to the HOMO energy of the semiconductor used in the channel. This ensures efficient charge injection from the electrode to the channel of the OTFT. In the present study, work function of the synthesised polymers and the metal used in the fabricated OTFT were calculated from electrochemical equilibrium potential determined by the measurement of electrochemical open circuit potential using equation 2.1. A summary of the results is shown in Table 3.2. Jinsung et al. have demonstrated that the work function of PANi nanoparticles decreases with increase in the HCl concentration [176]. Polk et al. have also investigated the effect of some strong protonic acids, such as triflic acid, on the work function of PANi and showed that the relative work function decreases with increasing acid concentration. The phenomenon was attributed to the formation of localized states after protonation that could cause the work function to decrease [177]. As can be seen, the results are in good agreement with literature values [112] and the highest work function has been obtained for PANi synthesized with relatively lower concentration of precursor acid. From the results, the work function of NP4 and PSN3-3 have a close match to the HOMO of pentacene (~ 5.0 eV). NP4 and PSN3-3 also form better dispersion and hence, form high quality films, which are ideal for the fabrication of electrodes in OTFT.

Table 3.2: Work function of conducting electrode materials.

S. No.	Sample designation	Work function (eV)
1.	Bulk PANi	4.43
2.	ALN1	4.52
3.	ALN4	4.85
4.	INT3	4.89
5.	TMP1	4.93
6.	NP1	4.90
7.	NP4	5.07
8.	PSN3-1	4.85
9.	PSN3-3	5.01
10.	Pd metal	5.04

3.5 Semiconducting Regioregular Poly(3-hexyl thiophene) and Block Copolymers

The method adopted for the synthesis of poly(3-hexylthiophene) di-block copolymers with acrylates used vinyl terminated PHT as precursor as shown in Fig.2.4. Hydroxyethyl end group was obtained by the conversion of the vinyl end group. Bromoester terminated PHT was formed by the reaction of hydroxyethyl end group of hydroxyl terminated PHT with 2-bromopropionyl bromide. The bromoester terminated PHT was then used as macroinitiator for Atom Transfer Radical Polymerization (ATRP) of acrylates. ATRP is a versatile controlled living chain polymerization that can be performed at different temperature ranges and is unaffected by many functional groups present in monomers. PHT-b-PBA synthesized via ATRP was characterized and their film forming properties were examined.

3.5.1 Proton NMR Analysis

^{1}H NMR spectrum of vinyl terminated PHT, compound **1** (all the compunds discussed in this section are with reference to Fig. 2.4) indicated the presence of vinyl protons at δ 5.05 ppm and δ 6.8 ppm in Fig. 3.29.

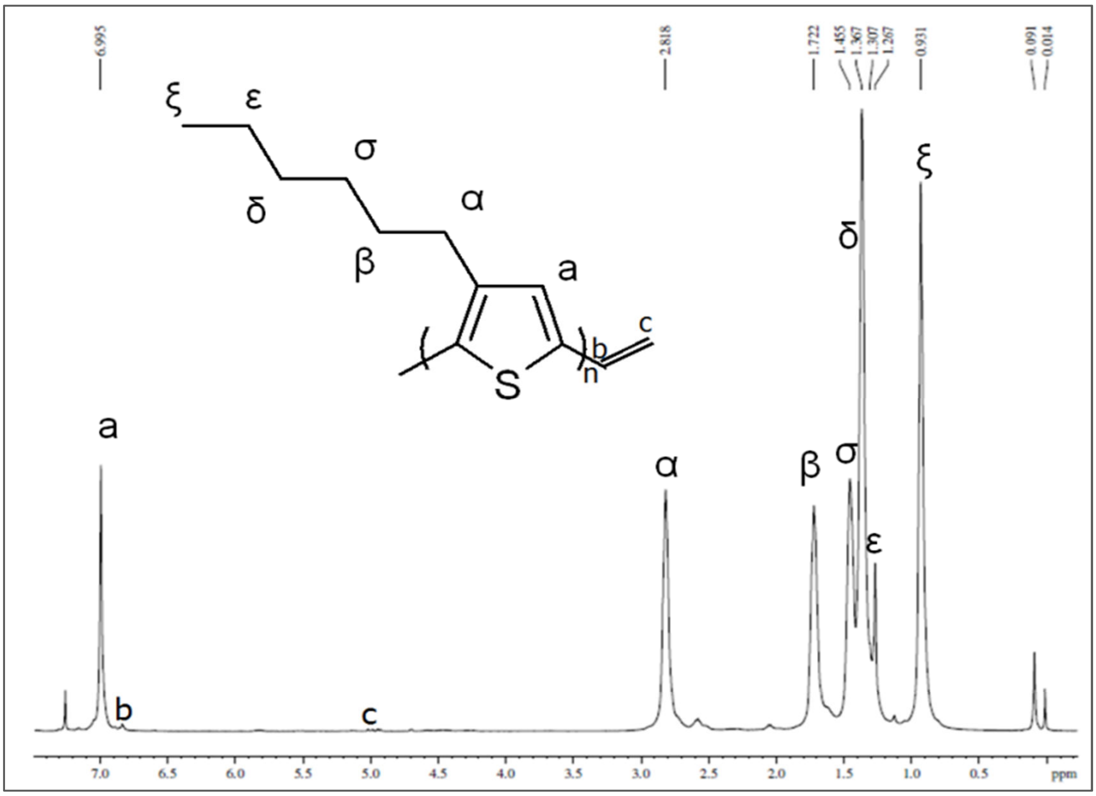

Fig. 3.29: ^{1}H NMR spectrum of vinyl terminated PHT.

The formation of compound **2** was confirmed by the disappearance of vinyl proton signal and appearance of new signal at δ 3.0 and δ 4.0 ppm (due to methylene protons) as shown in Fig. 3.30. The formation of PHT macro initiator (compound **3**) was confirmed from the new signal at δ 4.5 ppm and δ 1.8 ppm along with δ 3.0 ppm and δ 4.0 ppm in Fig. 3.31. The ^{1}H NMR spectrum confirmed the formation of compound **4** where the new signal in aliphatic region at δ 0.5 ppm to δ 3.4 ppm was observed due to acrylate functionality in Fig. 3.32. The high degree of regioregularity can be deduced by the appearance of only one singlet in the aromatic region as well as a clean triplet in the methylene region of the ^{1}H NMR spectrum in Fig. 3.29. These observed values are in good agreement with that reported in literature [178] and thus confirms the regioregularity of compound **1**.

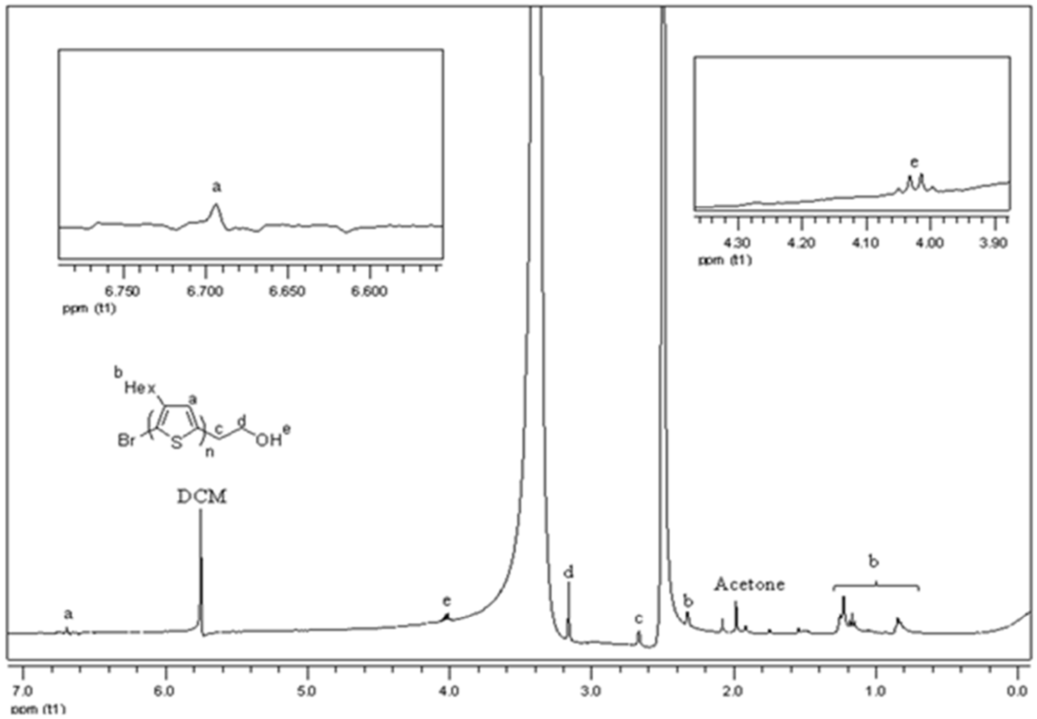

Fig. 3.30: ^{1}H NMR spectrum of hydroxy terminated PHT.

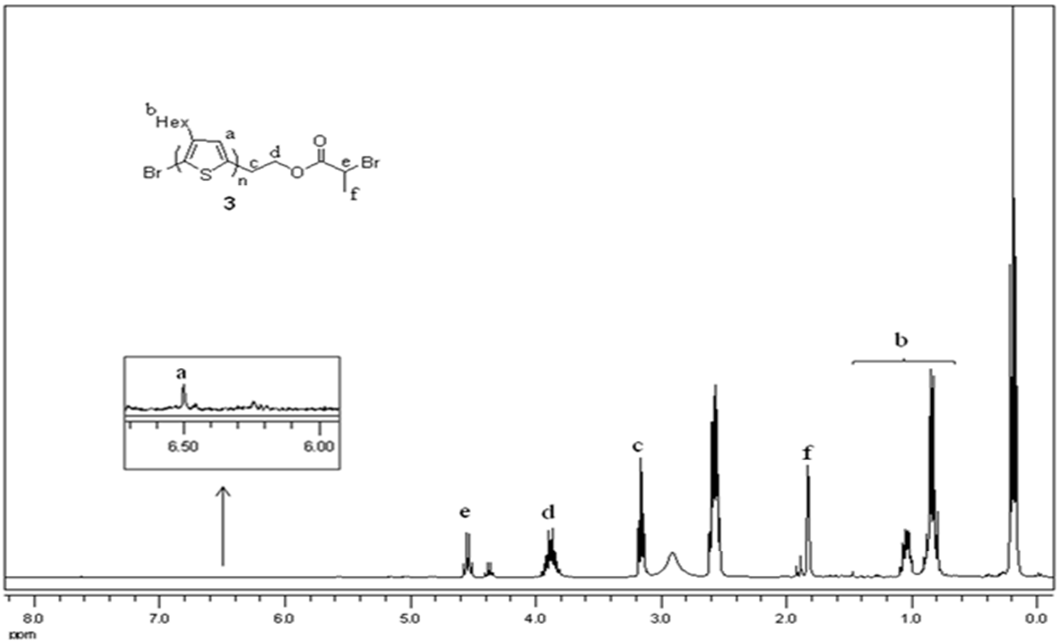

Fig. 3.31: ^{1}H NMR spectrum of PHT macroinitiator.

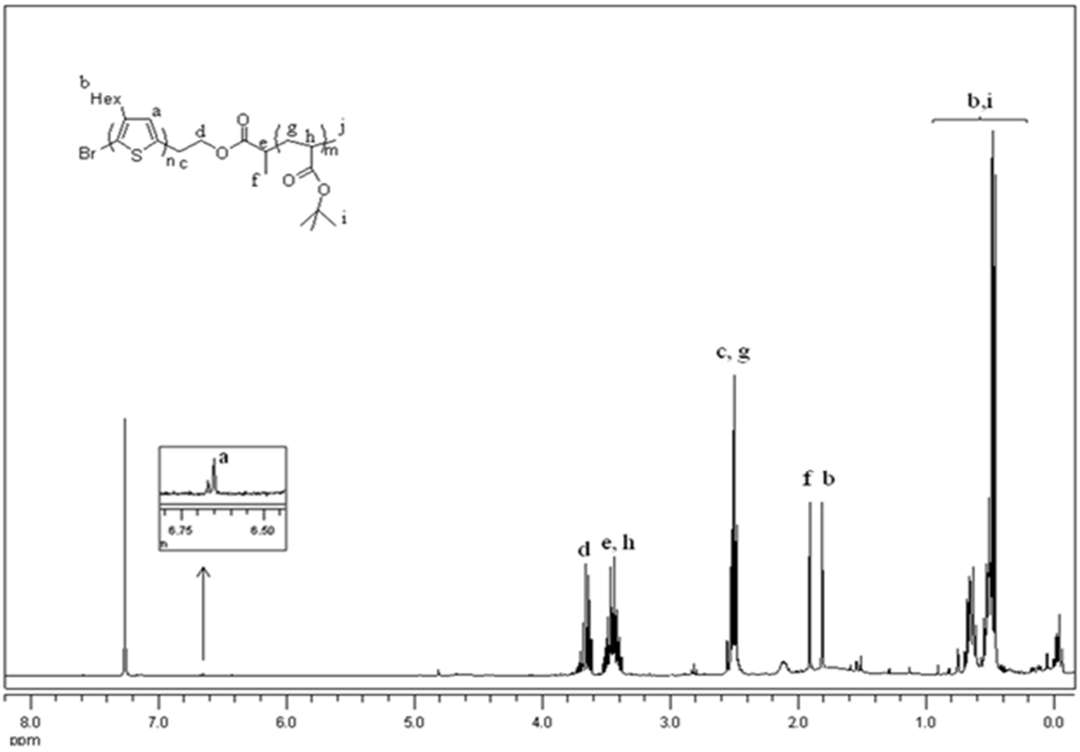

Fig. 3.32: ^{1}H NMR spectrum PHT-b-PBA.

3.5.2 Molecular Weight Analysis

The molecular weight of compound **1** and **4** of Fig. 2.4 were determined by Gel Permeation Chromotography (GPC). The molecular weights were obtained using THF as eluent. The obtained molecular weight of compound **1** and **4** is 5200 and 7100 Da, respectively with narrow polydispersity index (PDI) as shown in Fig. 3.33. Degree of polymerization (DP) of vinyl terminated PHT was estimated from the GPC as DP = 40.

3.5.3 Thermal Analysis

Thermal analysis of vinyl terminated PHT and PHT-b-PBA was carried out to study the thermal stability and crystallinity of the synthesized semiconductor.

3.5.3.1 Thermogravimetric analysis

Figs. 3.34 and 3.35 show the results of thermogravimetric analysis of compound **1**, vinyl terminated PHT and compound **4**, PHT-b-PBA. The TGA and the DTG curve were recorded for the compounds, **1** and **4**. Both the compounds were thermally stable beyond the maximum processing temperature of 180 °C and hence, the regioregular polymers are suitable to be employed as the channel material in the fabrication of OTFT.

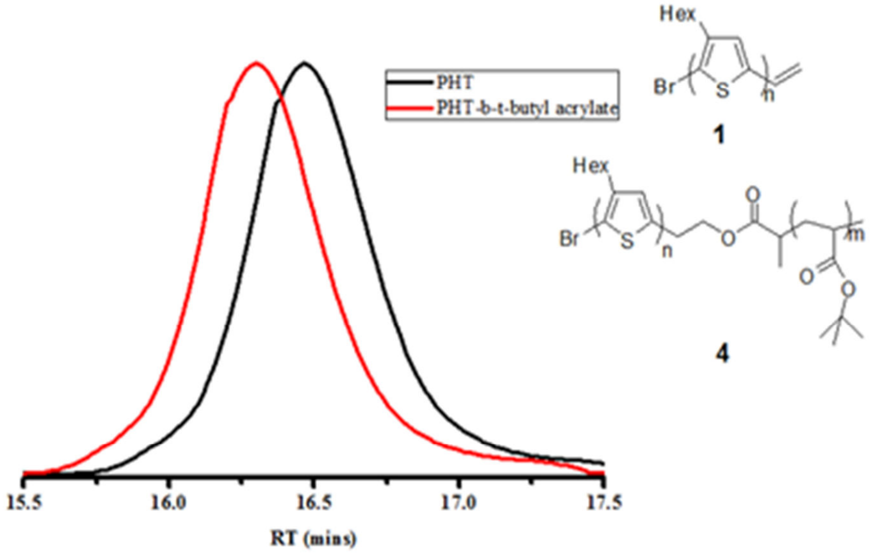

Name	M_n by GPC	PDI
Compound 1	5200	1.03
Compound 4	7100	1.04

Fig. 3.33: Molecular weight analysis of vinyl terminated PHT and PHT-b-PBA.

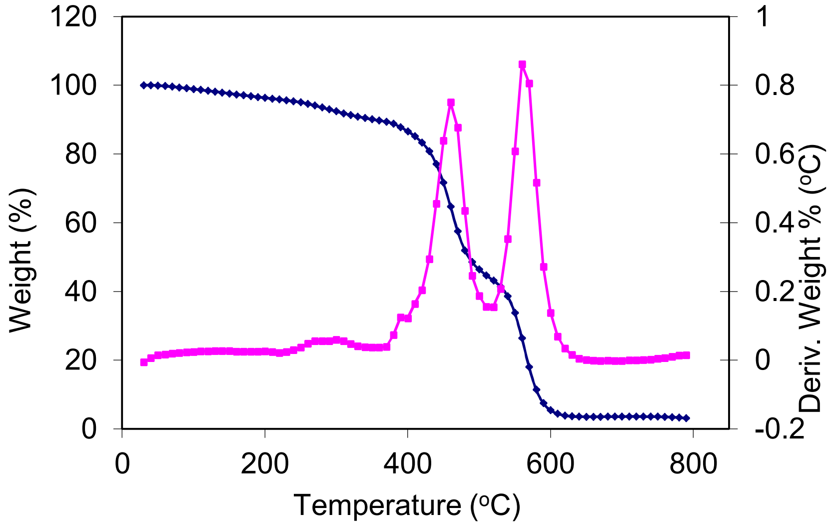

Fig. 3.34: TGA and DTG curve of vinyl terminated PHT.

It is clear from Fig. 3.34 that that vinyl terminated PHT is very stable against thermal decomposition. It is observed that the mass loss takes place in a two-step mechanism. The differential thermal analysis consists of two maxima at temperatures around 460 °C and 560 °C indicating two different components of similar oxidation behaviour. The beginning of the mass loss might be due to the loss of an alkyl side group attached to the aromatic thiophene backbone (hexyl group), resulting in almost 54% loss of weight. As the temperature increases above 500 ºC, the oxidation is accelerated and the pyrolysis of the aromatic backbone of polymer chains is ignited, which resulted in the loss of the remaining polymer sample. PHT-b-PBA exhibited an additional weight loss step, probably due to the loss of acrylate side chain, with a weight loss of 22% [Fig. 3.35], initiating at 260 ºC.

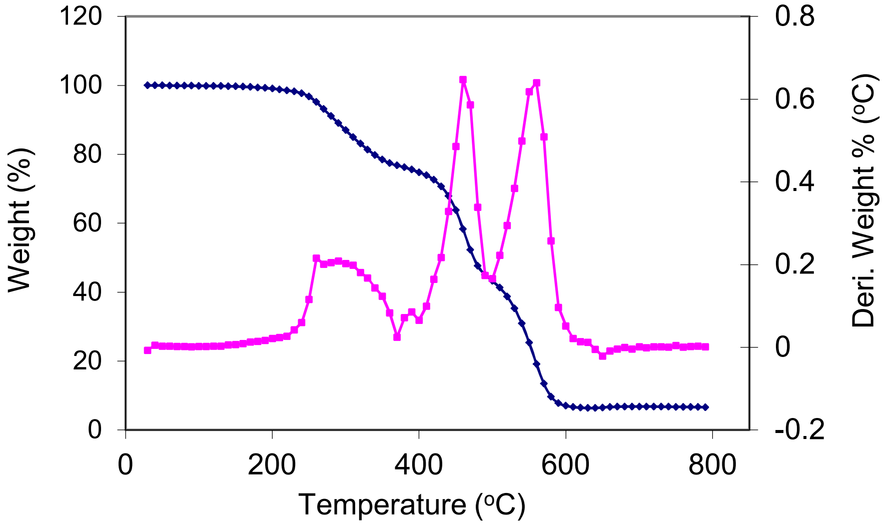

Fig. 3.35: TGA and DTG curve of PHT-b-PBA.

3.5.3.2 Differential scanning calorimetric analysis

For the DSC analysis of compound **1** and **4,** samples were first heated to 250 ºC and 240 ºC respectively, for 10 min and then cooled rapidly (cooling rate, 50 $^{\circ}\mathrm{Cmin}^{-1}$). The cycle was repeated five times, to remove any thermal history from the sample. Subsequently, the samples were reheated at a slower scan rate, 10 $^{\circ}\mathrm{Cmin}^{-1}$. For compound **1**, analysis was performed to 250 ºC and for compound **4**, to 240 ºC and cooled at 10 ºC min^{-1} for both the cases. Compound **1** and **4** exhibited a broad endothermic peak at around 224 ºC and 210 ºC, respectively, showing the crystal melting. The exothermic peak for crystal formation shifts to lower temperature, 177 ºC for compound **4**, when compared to 184 ºC for compound **1** under the similar experimental conditions. The heat of melting in both the cases is higher than the heat of crystallization, revealing that the initial structure is highly amorphous. From the comparatively higher values of heat of crystallization of compound **1**, it is concluded that due to the amorphous nature of t-butyl acrylate, the extent of crystallinity is less in compound **4** than that of compound **1**. Nevertheless, compound **4** is employed in the studies as semiconducting layer in OTFT, due to its better solution processability and better film forming capability. Figs. 3.36(a) and 3.36(b) show the DSC analysis of vinyl terminated PHT and PHT-b-PBA, respectively.

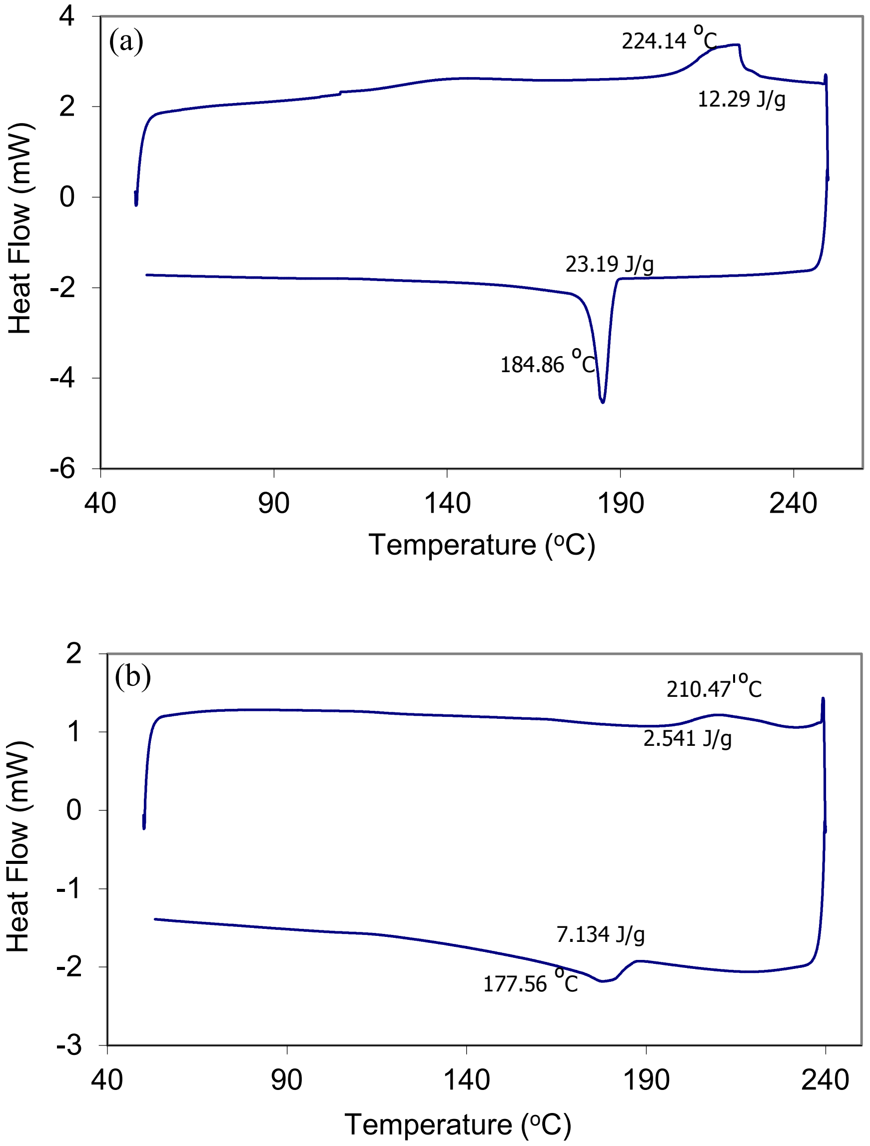

Fig. 3.36: DSC analysis of (a) vinyl terminated PHT and (b) PHT-b-PBA.

Conducting polymers synthesized in-house and characterized for optimum conductivity, work function and possessing good film forming properties were selected to be employed as the source and drain electrode in OTFT. The fabrication methods and the evaluation results are given in detail in the next chapter. Synthesized PHT-b-PBA was also investigated as the semiconducting channel material.

3.6 Conclusions

The methods employed for the synthesis of various conjugated polymers to be used in the fabrication of OTFT has been discussed in this chapter. The synthesized polymers were characterized for their structural, morphological, electrical and thermal properties. Among the conducting polymers, PANi was synthesised in nanostructured morphology by both chemical and electrochemical polymerization. Polymerization by chemical route, dilute polymerization and the interfacial method, resulted in nanofiber growth, but the uniformity and prevention of agglomeration could not be controlled. Electrochemical template polymerization resulted in uniform nanofibers but the retrieval of the synthesized polymer after the separation of gold of the track etched-membrane of the template was difficult. The structure of the nanofibers could be controlled with the SGM method. At a reduced concentration of both monomer and dopant acid, the sample NP4, with diameter less than 80 nm could be synthesized. CSA doped NP4 also resulted in smooth film when casted from the secondary dopant and solvent, *m*-cresol.

Water dispersible nanostructured conducting PANi-PSS composite for patterning as electrodes of OTFT was synthesized by bulk polymerization of aniline templated with polystyrene sulphonic acid. The PANi:PSS ratio and concentration of precursor acid during the synthesis were controlled so as to obtain conducting polymer samples with optimum conductivity and film forming capability. The conductivity of synthesized PANi was enhanced by more than two orders by secondary doping with DCA. Solution processable PHT-b-PBA, semiconductor was also synthesized and characterized to be employed as the active layer of the OTFT. The results on the fabricated OTFTs are discussed in Chapter 4.

Chapter 4

FABRICATION METHODOLOGY OF ORGANIC THIN FILM TRANSISTOR

4.1 Introduction

The most commonly accepted methods for roll to roll (R2R) large area fabrication of organic electronic devices are usually based on solution processing such as inkjet, screen, flexo or gravure printing. However, employing solution processable techniques leads to poor yield as a result of various reasons such as open or short circuited electrodes, defective gate insulating layer etc. The fabrication constraints are even more severe when device dimension reduces or production speed increases. Most of the best performing organic circuits to date, however, have been achieved by combining solution and vacuum processing with photolithographic steps [179-180]. Photolithography allows fabrication of features of much higher resolution which is especially important for defining the source–drain gap (channel length, *L*) in TFTs. Given these problems and limitations, adopting only solution processable methods may not yield high performance OTFTs for commercial applications. In this context, it is usually argued that the capital cost is prohibitive, yet commercial equipments are available for high resolution metal patterns on plastic substrate in R2R fabrication by high vacuum processes [181]. Hence, it is optimum to combine suitable solution processes with pholithographic methods and vacuum processes for fabrication of different layers in an OTFT, depending on the nature and type of the layer material.

Stability of OTFT in exposed environments has recently been viewed as an increasingly important issue of concern. The environmental instability of OTFTs has been attributed to molecular structure, ionization potential, broken conjugation, chemical impurities, light exposure, water and oxygen [182]. Organic semiconductor materials such as the oligomer, pentacene, when used as the active layer of OTFTs in high mobility field effect transistors [183], are susceptible to environmental stimuli present in ambient conditions. As a result, conventional OTFTs with unpassivated pentacene as active layer exhibit a relatively short lifetime. The field effect characteristics of pentacene thin film transistors suffer degradation from contact with humidity, oxygen and UV light. Theoretical studies have revealed the formation of a compound pentacenequinone [184] as a result of reaction in which oxygen forms a stable chemical bond with the middle ring of pentacene. This molecule, which is embedded in crystalline pentacene film, serves as a scattering centre for charge carriers in the OTFT channel [185] and affects the electrical performance of the device, i.e. reduce the on-current, shift the threshold voltage in positive direction and decrease the I_{on}/I_{off} ratio [186]. Moisture gets usually trapped in the organic layer from ambient environment while the transistor is in operation. The voltages at the electrodes induce electric fields that dissociate the water molecules, attaching them to the dielectric interface and grain boundaries of pentacene [185]. This results in a decrease in charge carrier mobility due to the generation of trapping states and disturbing potential walls at the grain boundaries.

In order to guarantee secure and consistent functioning of the organic circuits, operational lifetime of organic transistors should survive a period of several months. A few studies have been reported on encapsulated OTFTs that maintain the electric characteristics for a long time [187-189]. Ultrathin inorganic or organic/inorganic hybrid encapsulation layers when used as passivation can deteriorate the underlying semiconducting layer with the physicochemically active species (such as solvents, plasma and chemical precursors) [190-192]. Organic materials, due to their flexibility and compatibility with the underlying organic semiconducting surfaces, are seemingly the most suitable for the encapsulation of OTFTs. Nevertheless, structural weakness of organic passivating layers (e.g., high permeation of H_2O/O_2 and low solvent resistance) prevents these materials from becoming encapsulation candidates [193].

This chapter discusses the different fabrication methods adopted during the study for the fabrication of OTFT. For the initial optimization of parameters employed in the realization of simple OTFT, the fabrication was carried out on a thermally oxidized silicon wafer. The deposition time, thickness, etching time, etching rate, power required for etching in RIE, energy requirements in photolithographic processes, development time etc. were optimized prior to the fabrication of TFT on different substrates by employing different layers of materials. Due to the sensitivity of most organic thin films to the chemicals/solvents used in standard photolithographic process, special consideration must be given while developing a compatible fabrication process for organic electronic devices. An unpatterned semiconductor layer is inadequate for creating highly integrated devices [194] and robust circuits. Patterning of the organic semiconductor active layer is crucial to fulfil various performance, functionality and integration objectives. The chapter brings out the novel approach of effective simultaneous passivation and patterning of OTFTs, highlighting the improved device performance of poly(p-xylylene) polymer (parylene C) passivated OTFTs when compared to the conventional poly(vinyl alcohol) (PVA) passivated OTFTs [195].

Parylene is a material that can be deposited by chemical vapour deposition (CVD) as a conformal barrier layer in medical devices and electronic circuits. Parylene, in coating applications, is deposited around room temperature leading to conformal coatings that can be applied on chemically sensitive materials (organics) without degrading them. The performance of unpassivated and unpatterned device is compared with organic transistor passivated with polyvinyl alcohol and parylene C. The decay in the performance with time of the unpassivated transistor and those passivated with PVA and parylene C have been studied. Fabrication of OTFT on PEN substrate with solution processable semiconducting and conducting polymers is also discussed with an emphasis on novel parylene lift-off process for patterning conducting polymer electrode.

4.2 OTFT on Silicon Substrate

For the fabrication, a simplified TFT structure [Fig. 4.1] was employed in which a heavily doped 3 inch *n*-type silicon wafer (As doped; (100); surface resistivity- 0.005 ohm-cm; 525±25 µm thickness) was used as the substrate and gate electrode, with a layer of thermally grown silicon dioxide (200 nm) serving as the gate dielectric. The schematic of the complete fabrication process is depicted in Fig. 4.2.

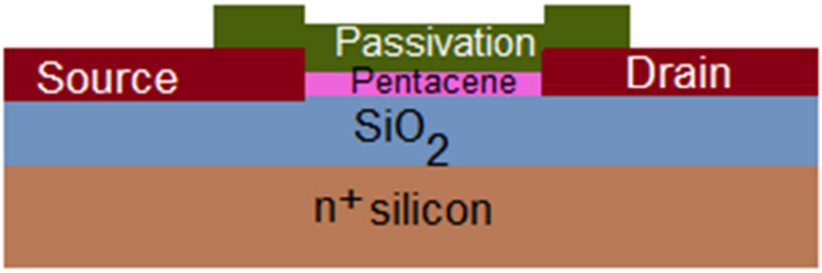

Fig. 4.1: Schematic of OTFT on Si substrate.

The metal electrode, palladium (Pd) was deposited by E-beam evaporation and patterned by wet chemical etching as source and drain electrode. The optimized thickness, measured using thickness profilometer, of metal deposited by E-beam evaporation is shown in Fig. 4.3(a) and microscopic image of patterned source and drain electrode is shown in Fig. 4.3(b). The dielectric, SiO_2 was solution treated with octadecyltrichlorosilane (OTS), prior to semiconductor layer deposition, to achieve 2D semiconductor film growth [19]. The active semiconductor material, pentacene was then deposited by thermal evaporation at a pressure of 10^{-8} Torr. The AFM image, showing the grain size of pentacene deposited on OTS treated SiO_2 is shown in Fig. 4.4. The dendritic structure and uniform grain size is evident in the AFM image. Pentacene was patterned and passivated with parylene C. The output characteristics of OTFT fabricated on Si substrate, designated as D1 are shown in Figs. 4.5(a) and 4.5(b). Mobility of 1.15 x 10^{-2} is achieved for the OTFT fabricated on Si wafer. Due to bias stress effects, the saturation current at all V_{gs} values commenced at very close V_{ds} values.

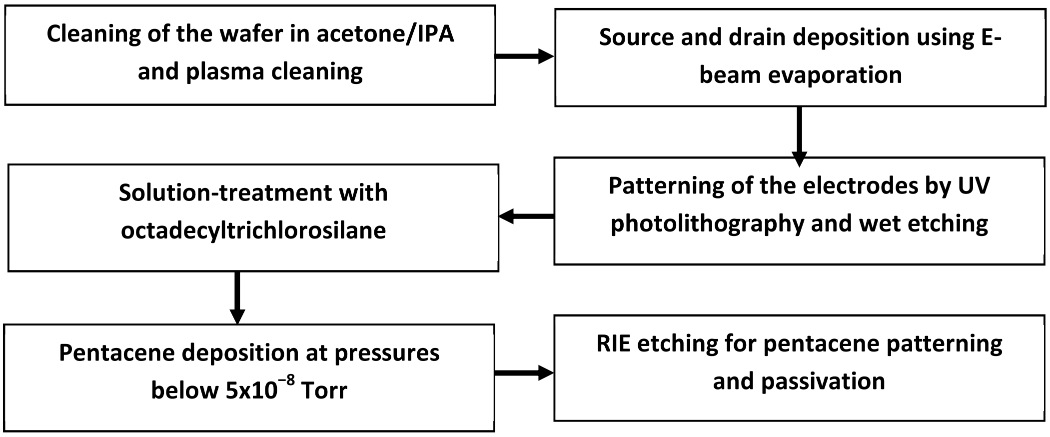

Fig. 4.2: Schematic of fabrication of TFT on Si substrate.

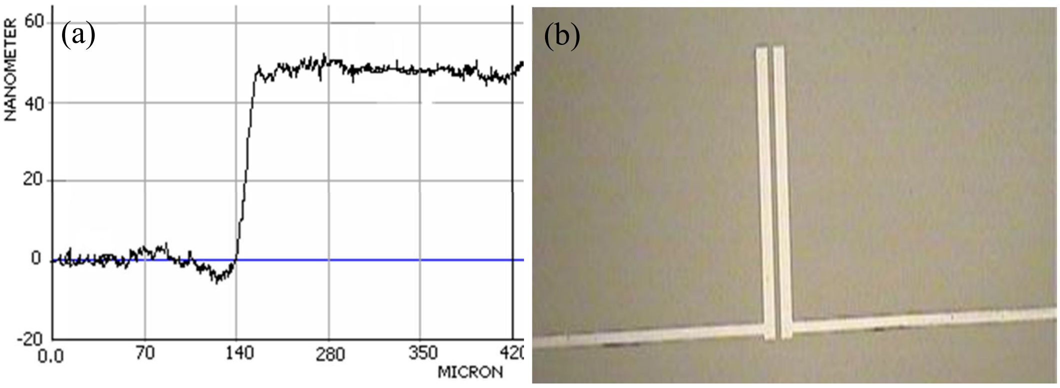

Fig. 4.3: (a) Thickness profile of metal deposited by E-beam evaporation and (b) microscopic image of patterned source and drain Pd electrode.

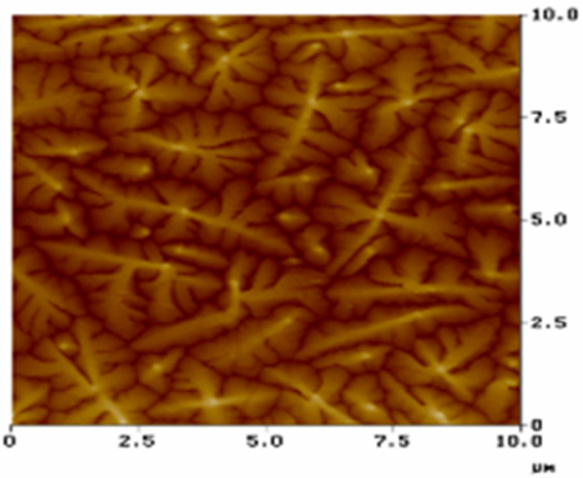

Fig. 4.4: AFM image of pentacene grown on SiO_2 dielectric.

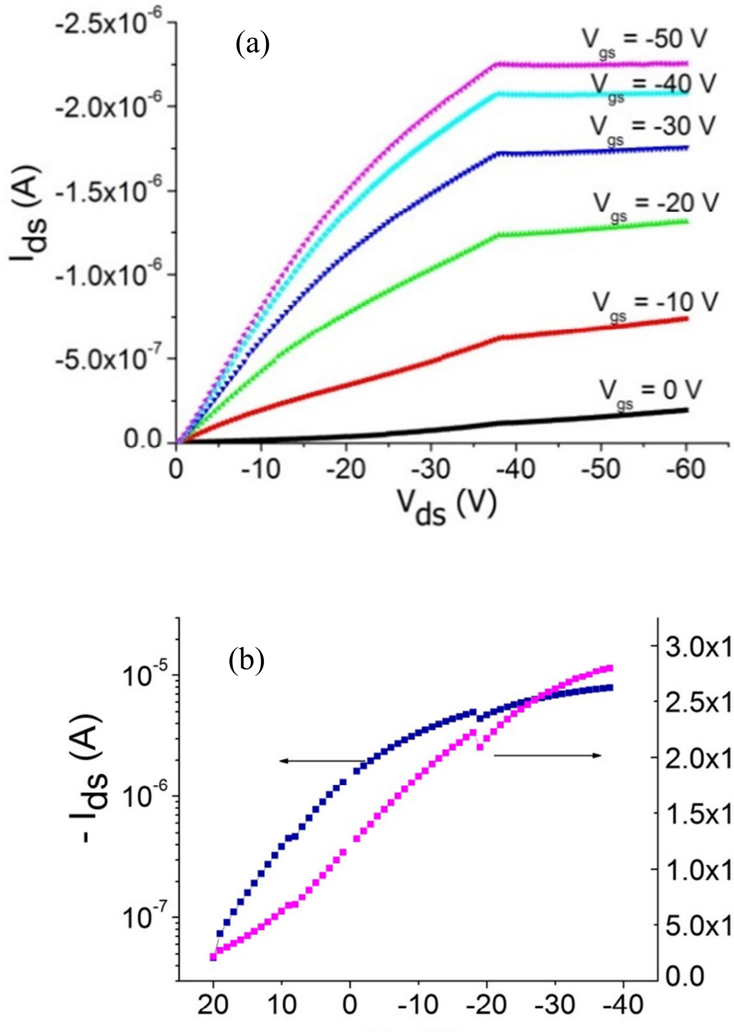

Fig. 4.5: (a) I_{ds}- V_{ds} characteristics, (b) transfer characteristics of OTFT on Si substrate.

4.3 OTFT on Flexible Substrate

4.3.1 Device Fabrication Methodology

A clean silicon wafer was laminated with (PEN) film. Prior to device processing, the PEN was preshrunk at 165 °C in an oven to improve its dimensional stability. To define the gate, a 70 nm thick palladium metal layer was defined using photolithography and lift-off process. The optimization of lithographic patterning on PEN substrate is an involved process. The intensity of UV light of mask aligner was measured to be 60 mW/cm^2, the time of exposure for 1.23 μm thick film of the S1813 photoresist, that required energy of 150 mJ/cm^2, was determined. The theoretical calculation, however, resulted in overexposed pattern [Fig. 4.6(a)]. Optimized condition of 2.1 s resulted in well patterned photoresist and subsequent metal electrode pattern. Figs. 4.6(b) and 4.6(c), respectively, show the microscopic image of optimized photoresist and metal electrode pattern after a lift off process on flexible substrate.

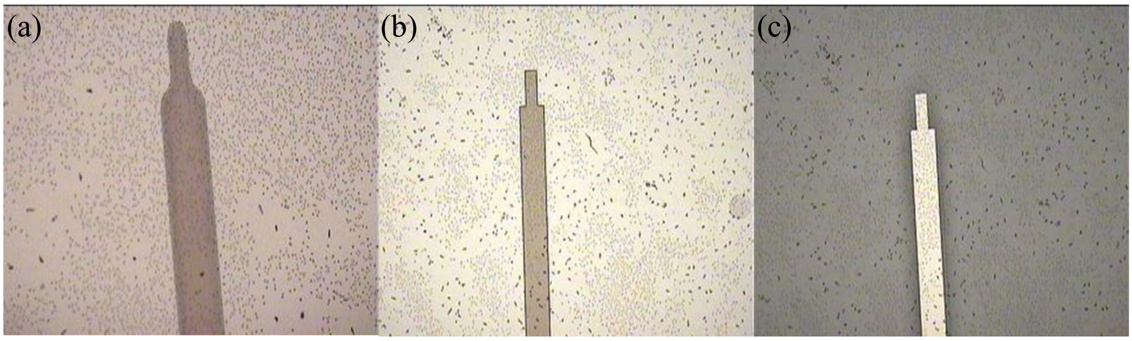

Fig. 4.6: Microscopic image of (a) Overexposed photoresist pattern (b) patterned photosresist with optimized time of exposure and (c) patterned metal electrode.

For the gate dielectric layer, PVP solution was prepared by dissolving PVP (12 wt% of solvent) and methylated poly(melamine-co-formaldehyde) (3 wt% of solvent) as cross-linking agent in propylene glycol methyl ether acetate solvent. The thickness of the dielectric was measured to be 650 nm after a three step spin coating process at 3000 rpm. The PVP insulator layer was patterned using photolithography and O_2 plasma etching. 70 nm thick palladium was defined as the source and drain metal layer using photolithography and the lift-off process. The channel length (L) was 20 μm and width (W), 1000 μm. The dielectric, PVP was solution-treated with OTS before the deposition of pentacene to improve ordering of the organic semiconductor. The surface energy studies on the OTS treated substrates were carried out by contact angle measurements. The contact angle on the PVP film was 62.7°, which improved to 106.9° on surface treatment with OTS [Figs. 4.7 (a) & 4.7(b)]. The shift of contact angle to 106.9° (hydrophobic side) favoured the 2D growth of pentacene on the PVP dielectric.

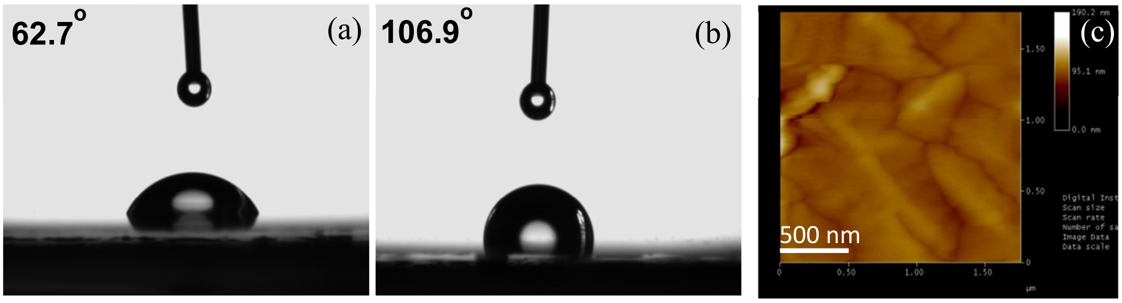

Fig. 4.7: Contact angle measured on (a) PVP dielectric (b) OTS treated PVP; (c) AFM image of pentacene deposited on PVP dielectric.

Pentacene film of 50 nm thickness was deposited by thermal evaporation at the rate of 0.1- 0.3 Å/s at a substrate temperature of 80 ºC. The AFM image of pentacene deposited on PVP substrate is shown in Fig. 4.7(c). Peak to valley roughness of 2.7-3.0 nm is revealed in the AFM image, with an average grain size of 1 µm. The device was then passivated and patterned to complete the fabrication process. The schematic of the processes involved in the device fabrication on PEN substrate is shown in Fig. 4.8.

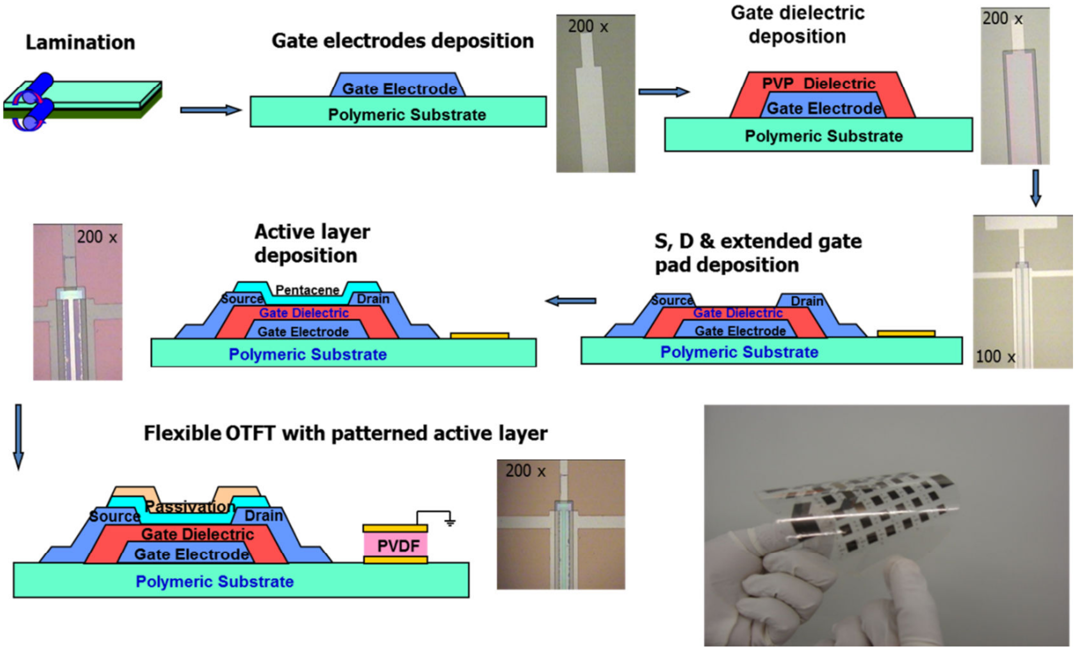

Fig. 4.8: Schematic for the fabrication of OTFT on PEN substrate, with respective microscopic images at each stage of fabrication.

4.3.2 Passivation of Semiconductor Layer

Two types of passivation layers were attempted to study the effect of passivation on the transistor characteristics as a function of time. For patterning the semiconductor pentacene, with PVA, the following method was adopted. A channel guard layer was formed on pentacene by spin-coating a water-based solution of PVA photosensitized with ammonium dichromate followed by exposing it to UV light through a mask (photolithography) [195], developing in water and baking in a vacuum oven at 80 ºC for 10 minutes. Reactive Ion Etching (RIE) confined the pentacene layer to the channel region using oxygen plasma, with the photosensitized PVA as the protective mask. The device is designated as D2. The schematic of PVA patterning is shown in Fig. 4.9(a).

A subtractive patterning approach was adopted to passivate the pentacene transistor with parylene. The schematic of the fabrication sequence is shown in Fig. 4.9(b) and the device is designated as D3. The stages given in Fig. 4.9(b) were fabricated as follows: After the deposition of a pentacene layer by thermal evaporation, parylene was deposited by chemical vapour deposition, with the substrate held at room temperature. The parylene layer was 1.3 μm thick. S1813 positive photoresist was spin coated on the substrate and was baked in a convection oven, (at 50 ºC) below the glass transition temperature of parylene. The patterns were then exposed on mask aligner and developed using MF319 developer. The process was optimized beforehand to yield near vertical sidewalls. The unprotected regions of parylene and underlying pentacene was anisotropically etched in oxygen plasma using RIE. The etch rate was in the range of 110–140 nm/min. The transistor characteristics were measured using Semiconductor Parameter Analyzer in nitrogen atmosphere at room temperature. The passivated transistors were stored in ambient conditions during the period of study.

The parylene coatings developed in the study are pinhole-free, for films [Fig. 4.10(a)] of sufficient thickness (typically > 500 nm thick). Once deposited, nearly inert parylene films resist strong acids, bases and solvents. Moreover, the process of deposition is compatible with conventional photolithography. The photoresist, once developed (which is positive tone as indicated in Fig. 4.9(b)), serves as a mask for a dry etch step for patterning the organic film below. The microscopic images of pentacene

TFT passivated with PVA and parylene are shown in Figs. 4.10(b) and 4.10(c), respectively. It is evident from the micrographs that the edges of PVA passivated device do not give a perfect protection to the underlying semiconductor layer when compared to that passivated with parylene C. This leads to slow permeation of moisture through the edges of passivating PVA layer (2 µm thick) leading to the eventual deterioration of the electrical properties with time. The photographs of 37 devices fabricated in a batch fabrication on Si substrate supported PEN film and the devices on PEN without the support wafer are shown in Figs. 4.11(a) and 4.11(c), respectively. The optical micrograph of a completed device with measurement pads is shown in Fig. 4.11(b).

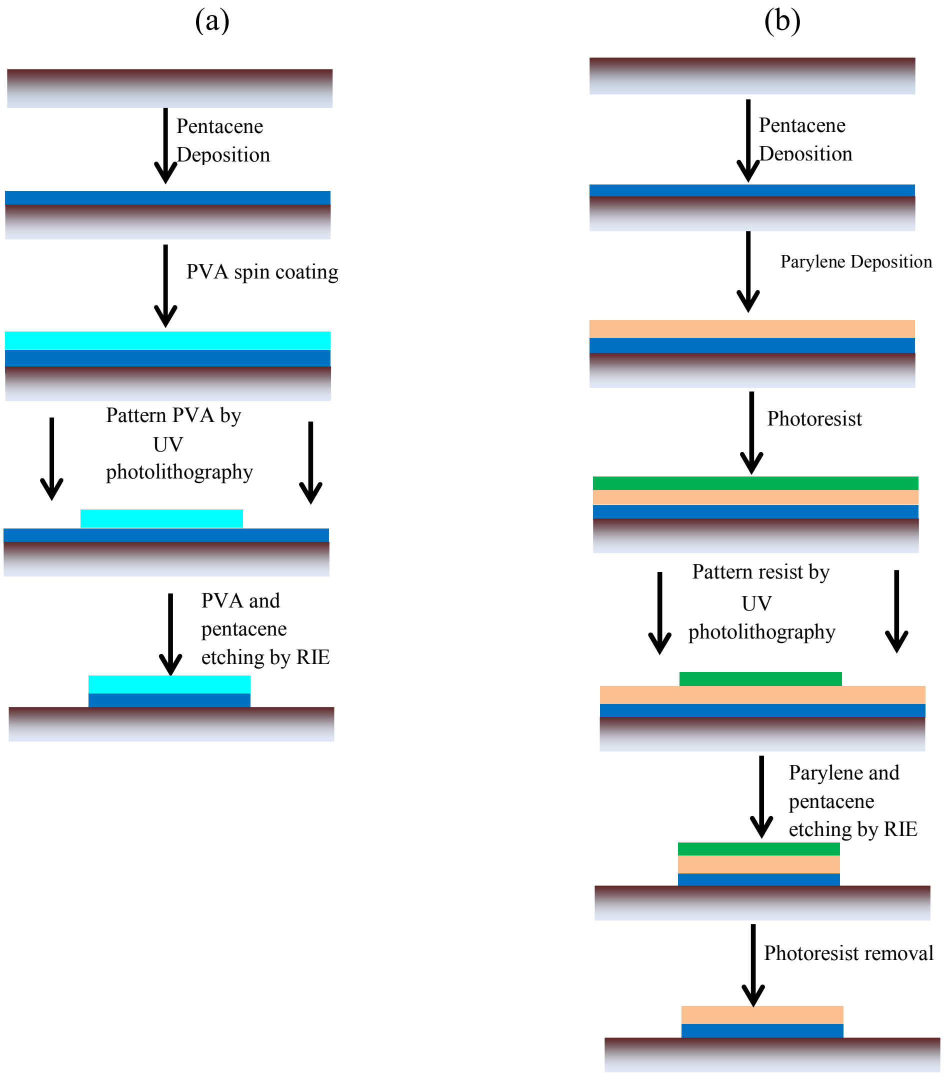

Fig. 4.9: Schematic for the passivation of pentacene TFT with (a) PVA and (b) parylene C.

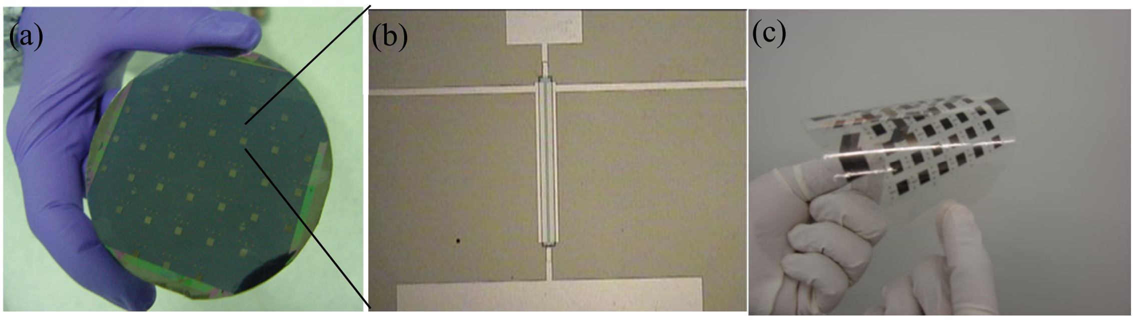

Fig. 4.10: **(a) Photograph of OTFT fabricated on 3″ PEN substrate laminated on a Si wafer; (b) optical micrograph of a single completed device and (c) photograph of flexible TFTs on PEN substrate.**

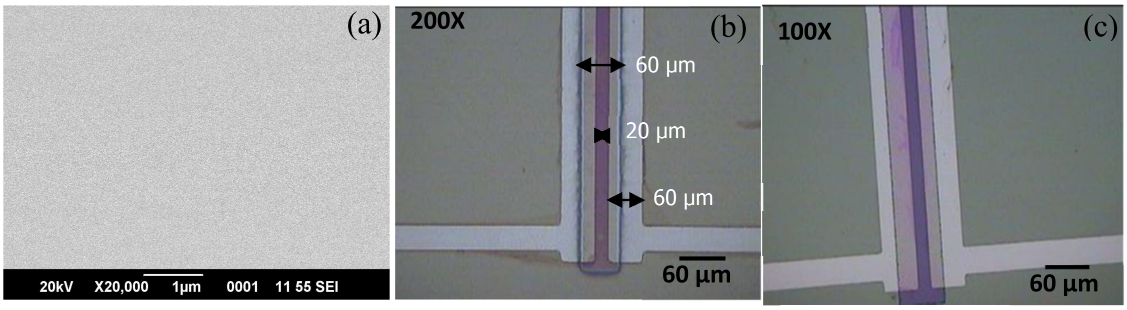

Fig. 4.11: **(a) SEM image of pin hole free parylene layer; optical micrographs of pentacene active layer passivated (b) with PVA and (c) with parylene C.**

4.3.3 Electrical characteristics of Unpassivated and Passivated OTFTs

4.3.3.1 Output characteristics of unpassivated and passivated OTFTs

The output characteristics of unpassivated (D2) and parylene C passivated (D3) pentacene OTFT in ambient atmosphere is shown in Figs. 4.12(a) & 4.12(b), respectively. The unpatterned and unpassivated pentacene TFT has shown high leakage current as revealed from the output characteristics. This leakage arises due to the cross talk and parasitic leakage between individual transistors. Since an OTFT operates by accumulation and there is no reverse biased junction to isolate the source and drain when the device is turned off, a leakage current always flows between source and drain through the semiconductor bulk and thus OTFTs are liable to higher off-currents and parasitic leakages. Since in an unpatterned OTFT, the organic semiconductor is not confined to the active channel region to isolate each transistor from neighbouring devices, the leakage and increase in off-current is more pronounced.

Fig. 4.13 shows the output characteristics measured on the same device (L = 20 µm) immediately after passivation and after 120 days. The I_{ds}-V_{ds} characteristics of the device do not show any perceptible change just after parylene passivation (0 days) and after 120 days. The passivation with parylene also simultaneously patterns the pentacene layer of individual transistors. By removing the semiconductor from the non-active transistor area, non-gated current carrying pathways (which contribute to constant leakage current) are removed; this decreases the off-current while making no significant changes to the on current.

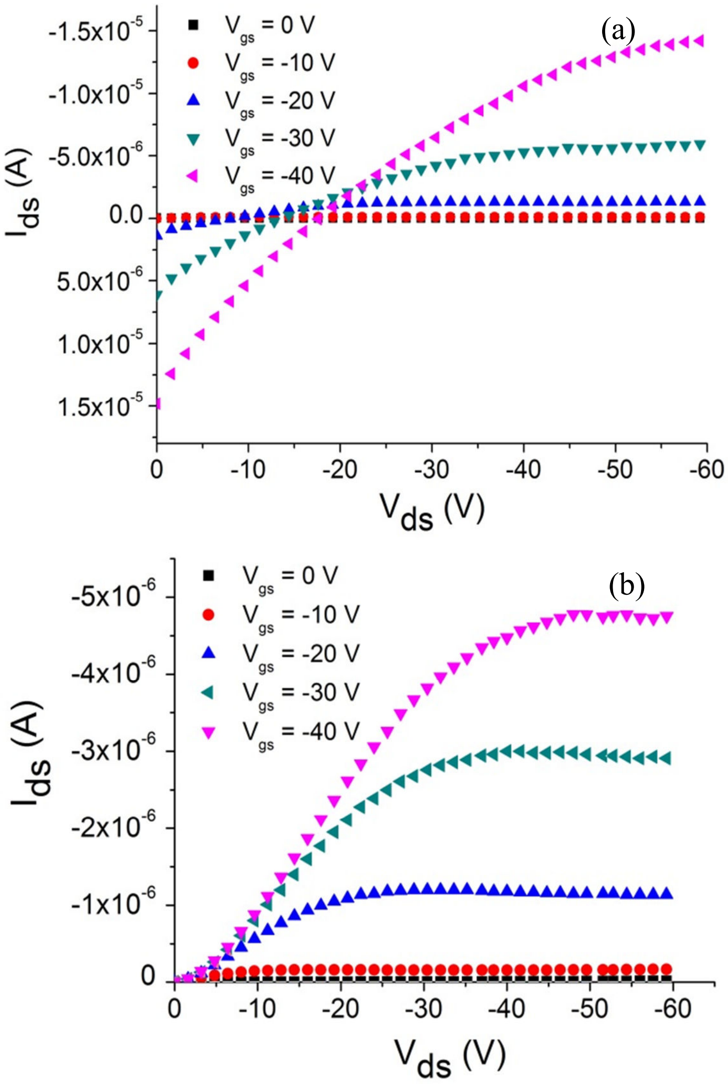

Fig. 4.12: **I_{ds}- V_{ds} characteristics of (a) unpatterned & unpassivated and (b) parylene C passivated pentacene OTFT.**

Fig. 4.14 shows the output characteristics of PVA passivated device just after passivation. Since the devices were fabricated under identical conditions except for the passivation process, the lower levels of drain current indicate the beginning of migration of PVA solution through pentacene. Moreover, PVA solution is water based and hence, the time elapsed between the spin coating of PVA and UV exposure for crosslinking PVA is highly significant. The water present in PVA solution starts deteriorating the underlying pentacene layer till the time taken for mask alignment and UV exposure for photolithography. The deterioration of the device is further revealed in the device characteristics measured on the same device 60 days and 120 days [Figs. 4.15(a) & 4.15(b)] after PVA passivation.

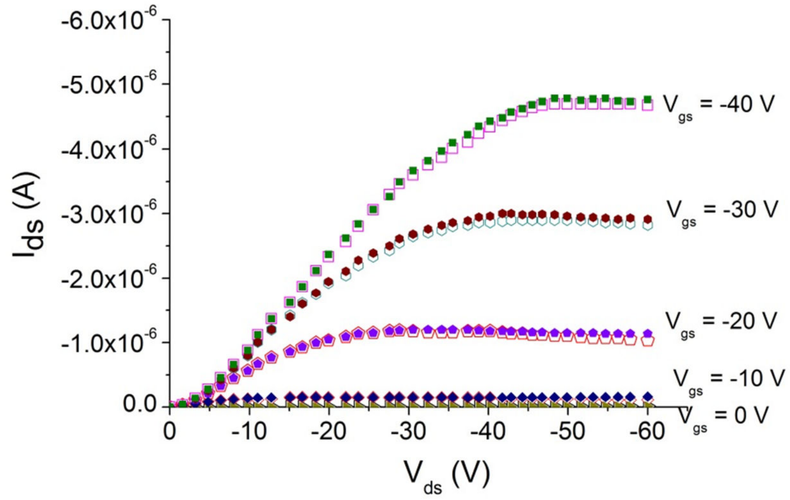

Fig. 4.13: I_{ds}- V_{ds} characteristics of parylene passivated OTFT, 0 days & 120 days (Closed symbols: 0 days and open symbols: 120 days).

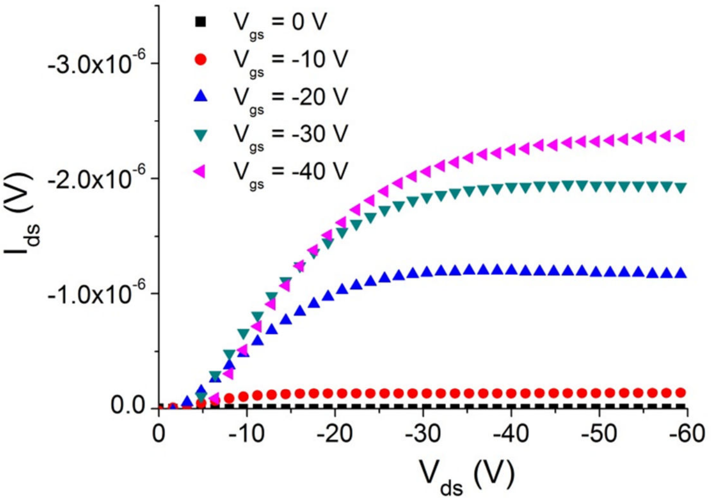

Fig. 4.14: I_{ds}- V_{ds} characteristics of PVA passivated OTFT, 0 days.

4.3.3.2 Transfer characteristics of unpassivated and passivated OTFTs

The transfer characteristics of unpatterned and parylene passivated TFT are shown in Figs. 4.16(a) & 4.16(b), respectively. The pentacene TFT passivated with parylene C showed a field effect mobility, μ=3.0x10^{-2} cm^2/Vs and remained constant during the period of study of four months. The mobility values were not affected even after six months. The mobility of PVA passivated TFT, [from Eqn. 1.4] was 2.5x 10^{-2} cm^2/Vs. For the TFT passivated with PVA, the output characteristics continually degraded with time. During the study on degradation for a period of four months, a two order decrease in mobility was observed for transistor with PVA passivation.

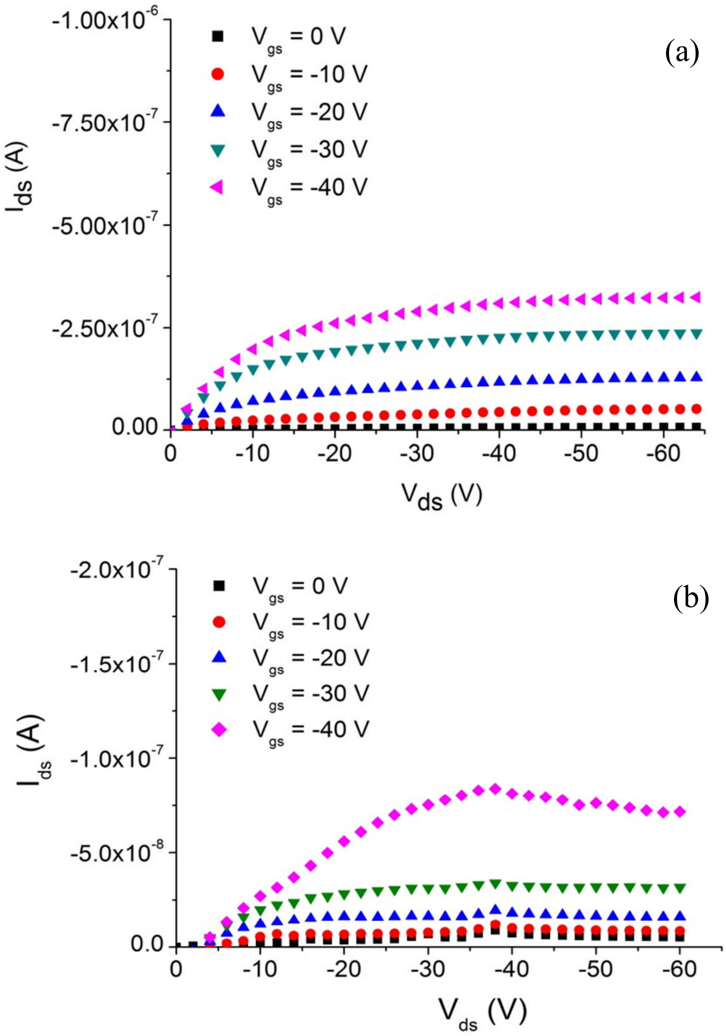

Fig. 4.15: *I_{ds}*- *V_{ds}* characteristics of (a) PVA passivated OTFT, 60 days and (b) PVA passivated OTFT, 120 days.

The output characteristics of unpassivated and unpatterned TFT were beyond the measurable ranges even after 60 days. The instability of PVA passivated TFT may be due to moisture and oxygen ingress with time, of the water based PVA layer. Though PVA is crosslinked during photolithography, water molecules already entrapped in pentacene leads to further deterioration with time. The PVA passivated device does not show any field effect characteristics when measured after 180 days. However, the pin hole free photolithographically patterned and parylene C passivated pentacene TFT is quite stable and characteristics of the OTFT is not affected the with time.

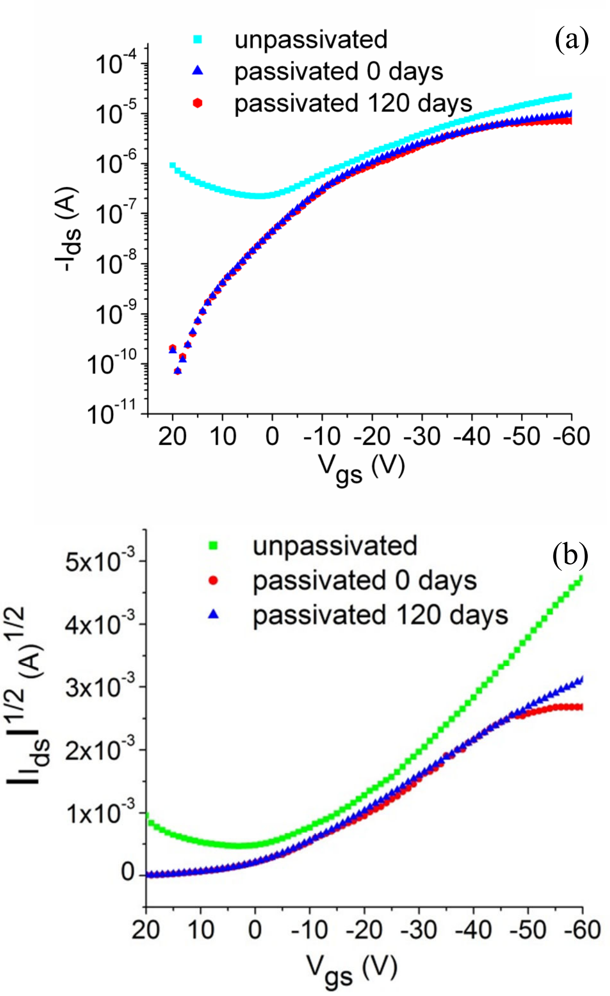

Fig. 4.16: Time dependent (a) $I_{ds} - V_{gs}$ transfer and (b) $|I_{ds}|^{1/2}$ - V_{gs} curves of bottom contact, unpassivated and parylene passivated OTFT in ambient air.

The susceptibility of OTFTs to environment induced degradation cause their output characteristics to change drastically. In the absence of a passivating layer, the channel material pentacene can undergo photooxidation, oxygen doping, degradation due to charge trapping by moisture and moisture induced doping. A poor passivation such as that with PVA, oxygen and moisture induced doping and charge trapping by moisture, are major contributors to device degradation. In the presence of oxygen and light, oxidation products such as transannular endoperoxide and dimeric peroxide are formed [196], deteriorating the semiconductor characteristics of the channel material. In the presence of absorbed oxygen, electrons are extracted from pentacene, generating holes. Oxygen doping contributes to increase in off-current and a positive shift in threshold voltage (V_T) as revealed in Figs. 4.17(a) and 4.17(b), respectively.

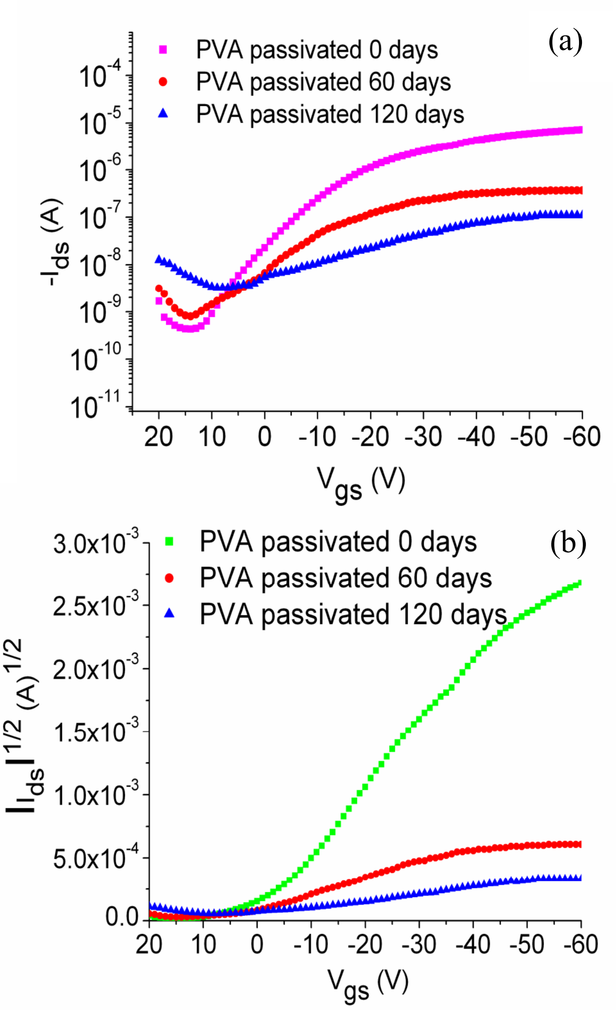

Fig. 4.17: Time dependent (a) $I_{ds} - V_{gs}$ and (b) $|I_{ds}|^{½}$ - V_{gs} transfer curves of bottom contact PVA passivated OTFT in ambient air.

The continuous degradation of the electrical performance of the unpassivated and PVA passivated OTFTs is also attributed to the charge trapping by the moisture present in atmosphere as well as that present in water based PVA solution in the case of PVA passivation. The water molecules residing at the grain boundaries can attract holes through charge dipole interactions, increasing energy barrier for inter grain charge transport and screen the electric field at the channel to reduce gate induced carriers. Besides impeding charge transport and trapping charges, the strong dipoles of polar water molecule can also induce holes in pentacene, causing the off-current to increase and shifting the V_T toward large positive value. The combination of increased off-current by doping and reduced on current by charge trapping results in significant lowering of the I_{on}/I_{off} ratio of the OTFT, upon getting exposed to moisture. In addition to meeting the upper limits on oxygen and moisture transmission rates, parylene passivating material does not cause degradation during encapsulation process. Vacuum deposition of parylene has the advantage of cleanliness of vacuum process, low deposition temperatures; non interaction of parylene with underlying pentacene and the process does not involve the use of harmful solvents affecting the underlying layers.

4.3.3.3 I_{on}/I_{off} ratio of unpassivated and passivated OTFTs

Fig. 4.18 shows the trend of the I_{on}/I_{off} ratio of the unpassivated, parylene C passivated and PVA passivated OTFT in ambient air, respectively. Parylene passivation, being a dry process, does not degrade the semiconductor layer, unlike permeation of water molecules present in PVA solution. The off-current is reduced by about two orders of magnitude in the parylene C passivated devices thereby increasing the I_{on}/I_{off} ratio. An I_{on}/I_{off} ratio of 10^5 is consistently maintained in the parylene passivated device even after four months. The method employed for passivation also effectively patterns the semiconductor layer of different device configuration on the substrate. Patterning the active layer reduces cross-talk between adjacent devices, reduces parasitic capacitance and limits leakage current (off-current). As a result, the devices have better performance characteristics.

Many technologies are used to encapsulate or passivate organic electronic devices. Vitex multilayer technology adopted by Samsung SDC with variation in the deposition techniques is currently used in the development and production of foldable displays and is expected to hold for the next generation [197]. However, up to now, because of high investment and low throughput, no mature product by thin film encapsulation technology is in the market. Recently, organic devices have been encapsulated by an alternative technology called Atomic Layer Deposition (ALD) [198]. However, due to their long growth time, they may not find application in industries in near future. Fumagalli et al. have used an architecture comprised of three-layers: aluminium oxide deposited by ALD and two layers of polyvinyl phenol [199] for passivation of OTFTs. The devices could operate with an I_{on}/I_{off} ratio only 10^3 during the study period of 100 days when compared to I_{on}/I_{off} ratio 10^5 with the single step parylene C passivation method, reported in this study. Moreover, physicochemically active species (such as solvents, plasma and chemical precursors) and the high thermal energy produced by the deposition of the encapsulation layer can severely break the semiconducting film morphologies, which lead to the deterioration of organic electronic circuits.

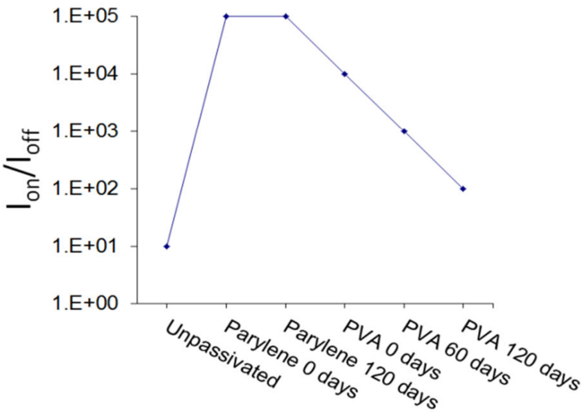

Fig. 4.18: Trend of the I_{on}/I_{off} ratio of bottom contact unpassivated, parylene passivated and PVA passivated OTFT in ambient air.

4.4 Fabrication of OTFT with Solution Processable Semiconducting and Conducting Polymers

One of the difficulties in patterning conducting polymers as electrodes in OTFT is that the conducting polymer itself is not easy to process with conventional microfabrication techniques, such as photolithography and etching. Conducting polymer films are easily diluted in the water-based developer used in lithography and can disintegrate in solvents that remove photoresist [200]. The PANi nanofibers, NP4, synthesized by electrochemical step galvanostatic method and PSN3-3 synthesized by polymer acid template assisted chemical polymerization were studied to be patterned as source and drain electrodes in OTFT by solution processable methods.

4.4.1 Electrochemically Deposited Polyaniline as Electrodes in OTFT

CSA doped PANi nanofibers, NP4, synthesized by electrochemical step galvanostatic method, formed smooth film when cast from *m*-cresol solvent [Fig. 3.16] and hence was found suitable to be used as source and drain electrodes in TFT. To optimize the process of fabrication with PANi nanofibers, a photomask was in house fabricated by simple laser printing on a flexible PEN film, with relatively higher channel lengths of 1 mm to 5 mm. A thermally oxidised silicon wafer with 200 nm thick SiO_2 was used as the substrate for fabrication. On a cleaned substrate, 3 wt% solution of PANi doped with CSA of NP4 was spin coated at an optimized speed of 4000 rpm. Sufficient time was given for the evaporation of the solvent from the substrate. The film was further dried at 60 ºC in a vacuum oven for 24 h to completely expel the solvent. The conducting film of PANi was photolithographically patterned with the help of the in house developed photomask and etched by RIE at a power of 20 Watts and etch rate of 11 Å/s. The fabricated device is designated as D4. The mask design and the fabricated TFT with NP4 film as the source and drain electrode is shown in Figs. 4.19(a) and 4.19(b), respectively. After the process optimization, the devices were fabricated with chrome photomask, with pentacene as the active layer of the TFTs. The fabricated device is shown in Fig. 4.19(c). Since the power required for etching the NP4 film is very close to that required for etching S1813, the edges of the fabricated NP4 electrodes were not sharp as that achieved with metal electrodes.

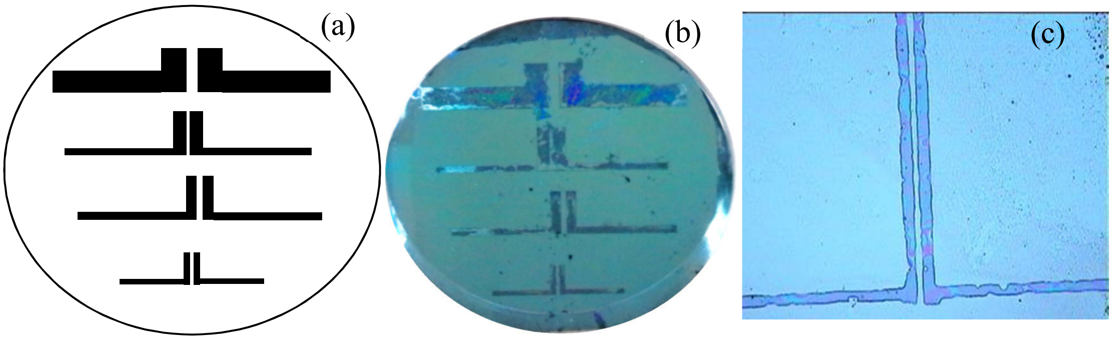

Fig. 4.19: (a) Design of the photomask printed on PEN substrate; TFTs fabricated on 3″ thermally oxidized wafer with NP4 film as source/drain electrode with channel length (b) 1 mm- 5 mm (photograph) and (c) 20 µm (micrograph).

The I_{ds} - V_{ds} characteristics of the fabricated TFT, D4 is shown in Fig. 4.20(a) and transfer characteristics shown in Fig. 4.20(b). The fabricated device exhibited a field effect mobility of 4.3 x 10^{-3} cm^2/Vs with relatively high leakage current due to the imperfections in the electrodes during fabrication.

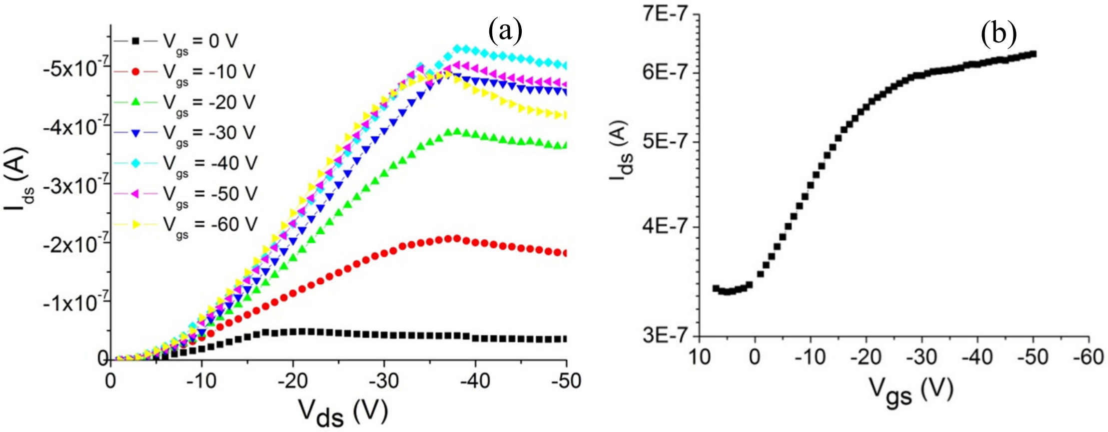

Fig. 4.20: (a) I_{ds}- V_{ds} characteristics and (b) transfer characteristics of TFT fabricated with NP4 electrodes.

4.4.2 Fabrication by the Parylene Lift-off Process

Parylene lift-off process has been used in recent years for patterning electrodes, dielectrics, proteins etc. for several applications [104, 201-202]. A novel, modified parylene lift-off process was studied to pattern nanostructured PANi, templated with polystyrene sulphonic acid (PANi-PSS) as electrode in organic TFT. Performance of the fabricated device was compared with pentacene-based OTFT with non-ohmic palladium electrode, which is a relatively low cost metal with matching work function for *p*-type pentacene. The contact resistance of the fabricated devices were extracted by Transfer Line Method (TLM).

OTFT fabrication in bottom contact configuration on PEN substrate, with palladium as source and drain electrode on flexible substrate, was carried out as previously described in section 4.3 and the device was designated as D5. For the fabrication of OTFT with PANi-PSS source and drain electrode, as for D5, PEN film laminated Si wafer was taken as the substrate. 70 nm thick Pd metal was patterned as gate electrode by lithography and lift-off process. PVP dielectric (850 nm, same as that in D5) was patterned over the gate metal by lithography and oxygen plasma etching. A modified parylene lift-off method was then adopted for patterning the solution processable electrodes of PANi-PSS as summarized in Fig. 4.21.

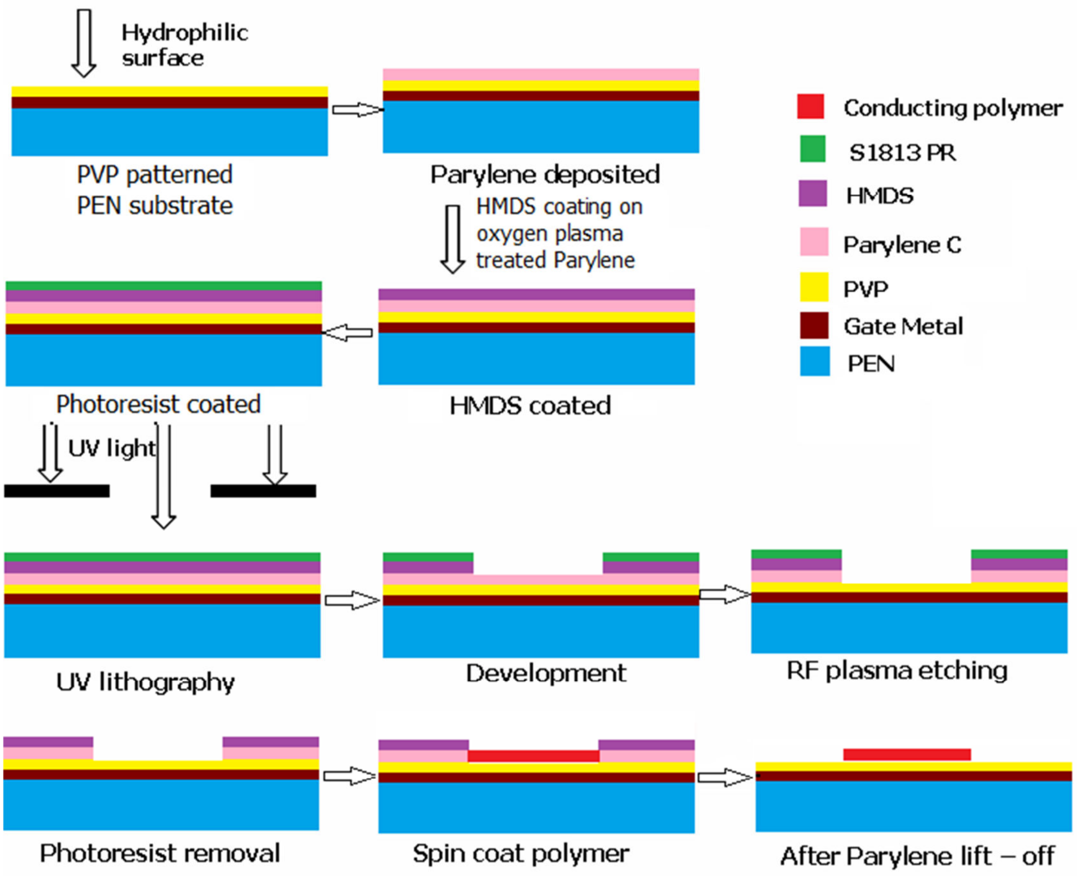

Fig. 4.21: Parylene lift-off process for the patterning of conducting PANi-PSS electrode.

Parylene C was coated over the gate dielectric patterned substrate. To create a smooth hydrophobic pattern that repels PANi-PSS, hexamethyldisilazane (HMDS) was spin coated over oxygen plasma treated parylene, followed by the deposition of the photoresist, Shipley S1813. The contact angle measured on PVP surface was 62.7º, on plasma treated parylene, almost 0º (hydrophilic) and on HMDS coated plasma treated parylene, 84º (hydrophobic) as shown in Figs. 4.22(a)-4.22(c). After exposure (with source and drain pattern), the substrate was immersed in a developer (MF319). The developer not only stripped the exposed photoresist, but also the underlying HMDS. Parylene was then etched in oxygen plasma. The etched region also became hydrophilic due to exposure to plasma. Photoresist was then removed in acetone. Since acetone does not remove adsorbed HMDS, this region remained hydrophobic.

Fig. 4.22: Contact angle measured on the surface of (a) PVP (b) plasma treated parylene and (c) HMDS coated plasma treated parylene.

Following this pattern definition, a 3 wt% PANi-PSS (PSN3-1 and PSN3-3 were studied for comparison) was spin coated on the molecular template. Since PANi-PSS selectively gets coated over the hydrophilic region, conductive PANi-PSS features in the predefined geometry of source and drain electrodes were created immediately after spin coating. Parylene was then lifted off which removed any undesirable layer of PANi-PSS from non-electrode region. Samples without the parylene deposition step and parylene lift-off were also studied for comparison. The fabricated electrodes were soaked in preheated DCA (95 ºC) for five minutes and annealed for 1 h at 95 ºC, to improve the conductivity by secondary doping. 50 nm thick organic semiconductor, pentacene was deposited by thermal evaporation and patterned to realize the organic transistor in bottom contact configuration and the device was designated as D6. OTFT with different channel lengths (10-50 µm) were fabricated to extract the device contact resistance.

4.4.2.1 Parylene lift-off

Fig. 4.23(a) shows the image of the process of lifting-off of parylene film after the patterning of PANi-PSS electrode. The lifted and unlifted region is evident in Fig. 4.23(b). Figs. 4.24(a)-4.24(d) show the optical micrographs of patterned PANi-PSS electrodes (with PSN3-1 and PSN3-3, 3 wt% solution) fabricated after patterning gate metal and gate dielectric. With both the dispersions, images, with and without the parylene layer is shown. Creation of selectively wetted and nonwetted regions on the substrate with the use of HMDS facilitates in high resolution patterning. Parylene lift-off assists in better resolution (5 µm) for the patterned electrodes without the undesired deposits on non-device regions. Though the electrodes with PSN3-1 have high resolution with parylene lift-off, uniform film is not formed due to higher particle size of PANi-PSS in the dispersion. A clean and smooth channel region (without undesired deposits) is essential for obtaining higher performance for the fabricated OTFT, which in this case is formed with PSN3-3 assisted with parylene lift-off process. Fig. 4.25(a) shows the optical micrograph of the completely fabricated polymer electrode based device on PEN substrate with the inset showing the corresponding SEM image. Fig. 4.25(b) shows the SEM image of the device of 5 μm resolution with PSN3-3 source and drain electrodes.

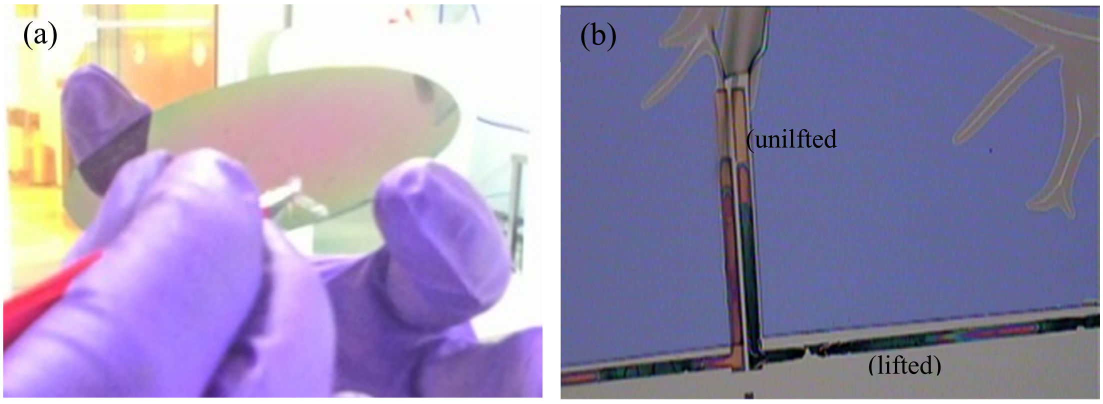

Fig. 4.23: (a) Photograph of lifting off of parylene film after deposition of PANi-PSS electrode and (b) micrograph of parylene lifted and unlifted region on the wafer with the patterned electrode.

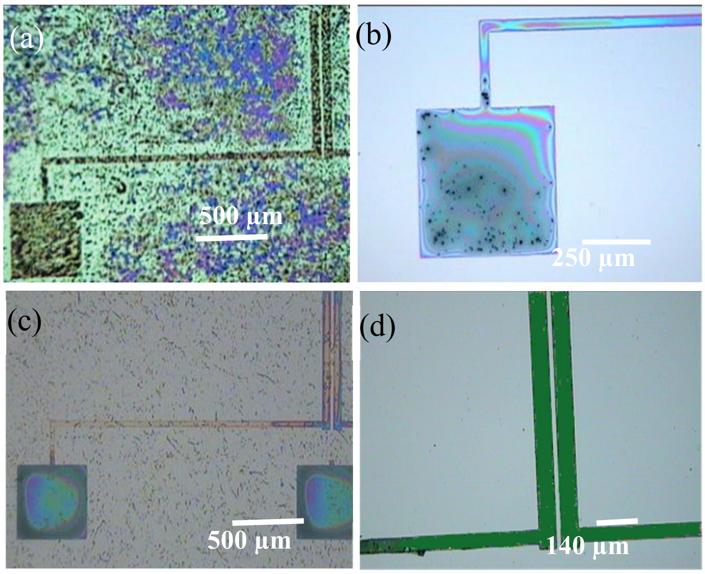

Fig. 4.24: Patterning of (a) PSN3-1 without parylene lift-off (b) PSN3-1 with parylene lift-off (c) PSN3-3 without parylene lift-off and (d) PSN3-3 with parylene lift-off.

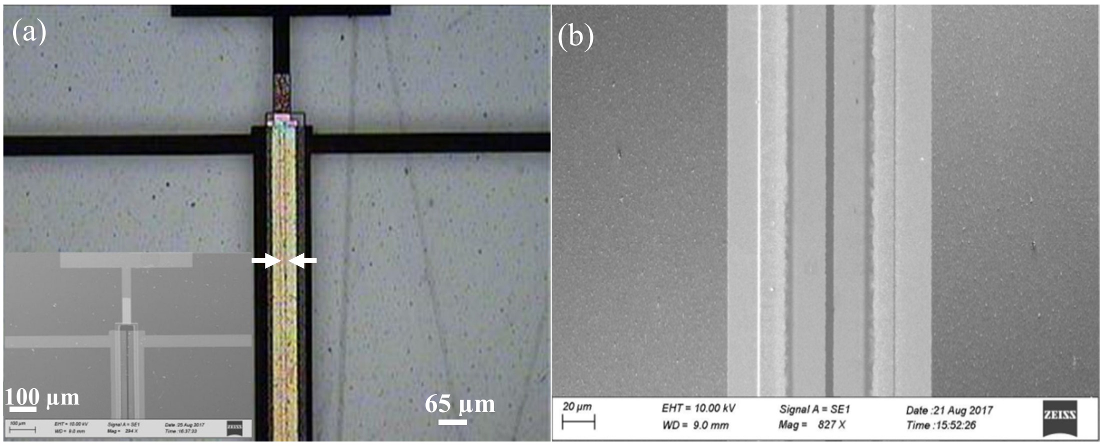

Fig. 4.25: (a) Optical micrograph of polymer electrode based OTFT fabricated on flexible substrate (inset shows the SEM image) and (b) SEM image of device of 5 µm resolution with PSN3-3 source and drain electrode.

4.4.2.2 Device characterization

I_{ds}-V_{ds} characteristics of device D5 and D6 are shown in Figs. 4.26(a) and 4.26(b), respectively. At lower V_{ds} values (circled portion), Fig. 4.26(a) depicts the presence of non-linearity, which is a direct consequence of the higher contact resistance in D5, due to the metal used as the electrode in OTFT. This non-linearity is absent in the case of D6, which employed PANi-PSS as the conducting electrode for hole injection. The characteristics of these devices are consistent with contacts that have an ideal ohmic character. Though the maximum I_{ds} values for both the devices are similar, the higher barrier to charge injection, due to non-ohmic contacts contributes in shifting the threshold voltage to a greater extent. It has been reported that hole injection barrier at interface between pentacene and conducting polymer electrode is smaller compared to that with metal electrode [29]. Adsorbed molecules on metal electrode contribute in lowering of the metal work function, leading to a large hole injection barrier than that is present with the use of conducting polymer (PANi-PSS) electrode.

TLM was employed to determine the contact resistance [203] in the devices with Pd and PSN3-3 as the electrode material. The total resistance, R is related to R_{ch}, channel length dependent resistance and R_c, channel length independent contact resistance that are associated with the contacts. R for different channel lengths was obtained from the inverse slope of the linear I_{ds}-V_{ds} curves. If RW is plotted as a function of channel length, where *W* is the width of the channel, it is seen that, at a constant V_{gs} (gate source voltage), the set of *RW* values of various transistors exhibit a linear variation. The contact resistance, R_c, was obtained from the *L*=0 intersection of the measured device resistance, *R*, as a function of channel length [203]. At different V_{gs}, that intercept varies with V_{gs}, thus providing the gate voltage dependent contact resistance.

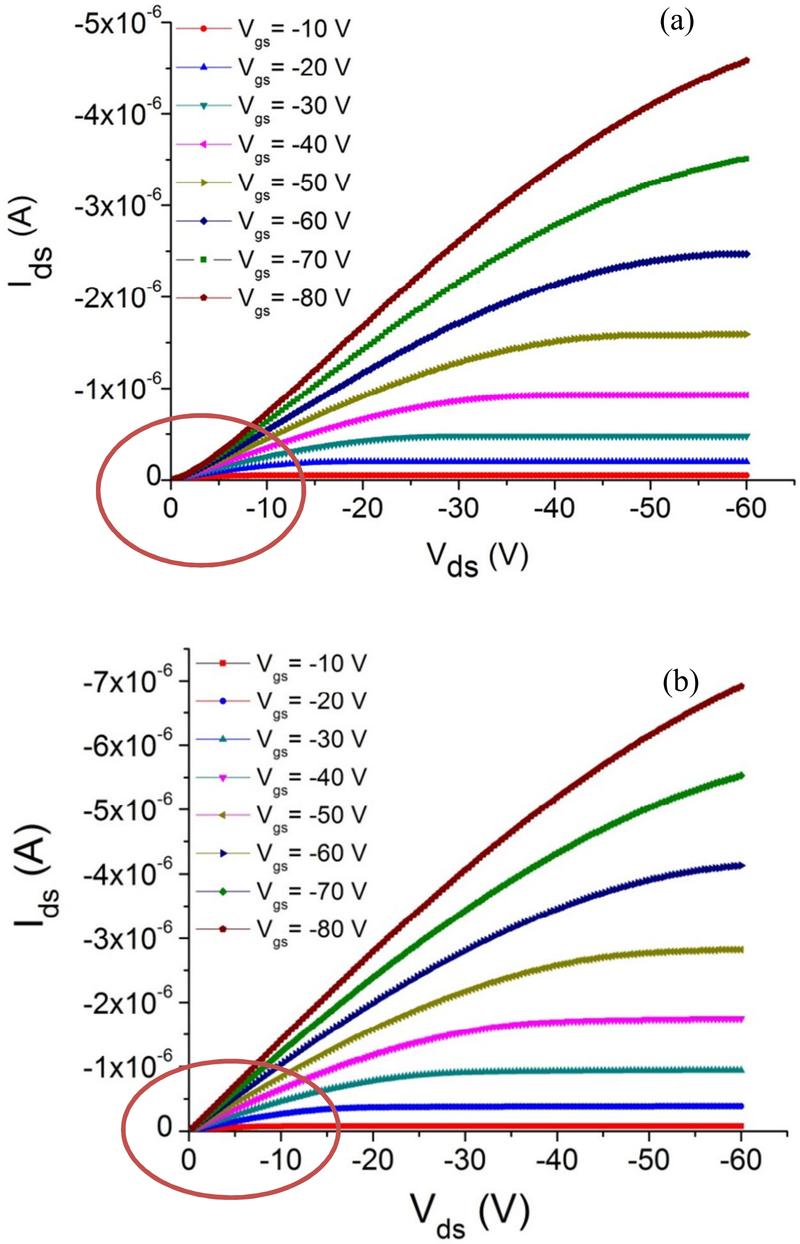

Fig. 4.26: I_{ds}-V_{ds} characteristics of OTFT fabricated with (a) Pd as the source and drain electrode and (b) 3 wt% solution of PSN3-3 as source and drain electrode.

Analysis of contact resistance from pentacene transistors with Pd and PANi-PSS conducting polymer source/drain electrode is shown in Fig. 4.27 and 4.28. Figs. 4.27(a) and 4.27(b) show the width normalized total resistance (R) as a function of channel length within the usually reported range of gate voltages from -30 to -80 V [204], with Pd and PANi-PSS employed as source and drain electrode, respectively. The transistor width in all cases is 1 mm. This plot has information about both the intrinsic channel resistance (R_{ch}) and contact resistance (R_c). The contact resistance as a function of gate voltage for Pd and PANi-PSS electrode are shown in Figs. 4.28(a) and 4.28(b), respectively. It is very evident that gate voltage modulates the contact resistance. The results show that R_c decreases with increasing gate voltage. The determined field effect mobility with PANi-PSS electrode is 0.54 cm^2/Vs and threshold voltage, 3.2 V, whereas with Pd electrode, the calculated mobility is 0.9 cm^2/Vs and threshold voltage, 7.4 V.

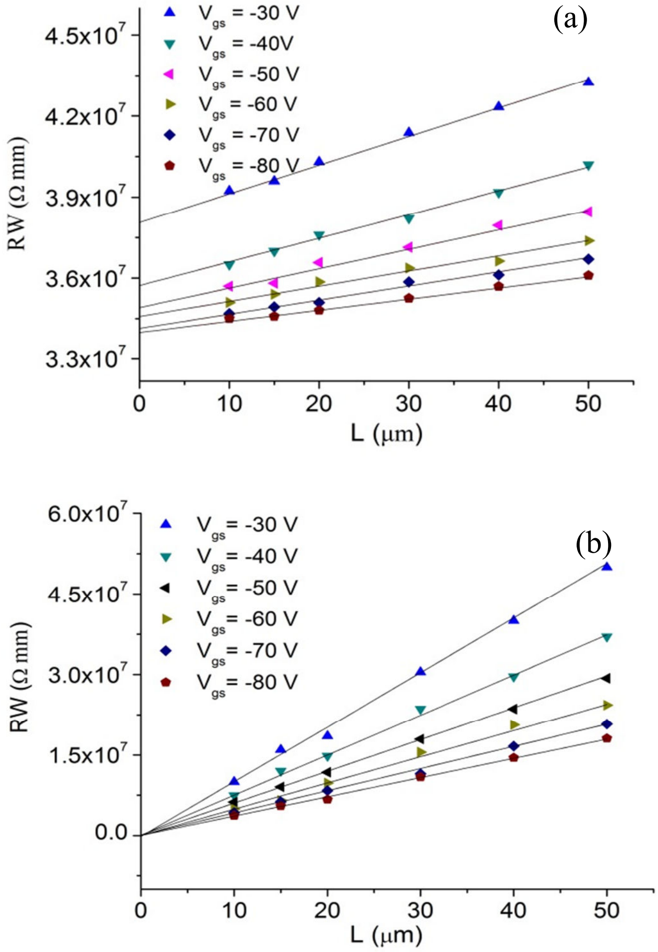

Fig. 4.27: Width normalized total resistance (R) as a function of channel length at gate voltages, -30 to -80 V with source and drain electrode (a) Pd and (b) PANi-PSS.

As shown in Figs. 4.27(a) and 4.27(b), the normalized resistance curve merges at a channel length L_o, which is independent of gate voltage. L_o is the additional channel length, introduced by the presence of the contacts. While L_o is ~ 0 for PANi-PSS electrode, it reaches more than 20 μm with Pd electrode. This may be one of the reasons for the observed higher threshold voltage with Pd electrode. The shortcomings with non-ohmic nature of Pd metal electrode have been overcome by the use of PANi-PSS conducting polymer electrode. The microscopic mechanism that explains the observed difference in the contact resistance with metal and conducting polymer electrode is explained in Chapter 5. The effects of roughness of dielectric layer, improvement upon reducing the trap states and other processing conditions have to be extensively studied to get further improvement upon the output characteristics of PANi-PSS electrode based TFTs.

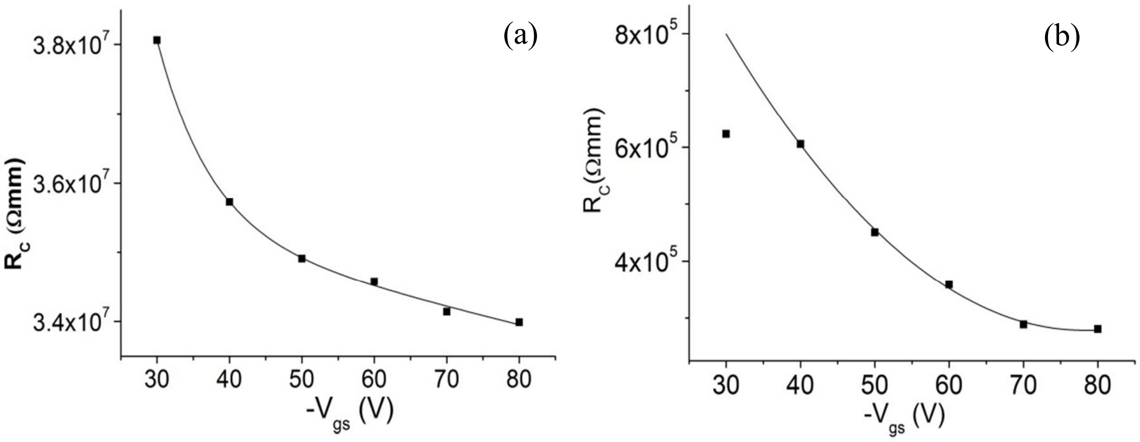

Fig. 4.28: The contact resistance as a function of gate voltage for pentacene OTFT with source and drain electrode (a) Pd and (b) PANi-PSS.

4.4.3 Fabrication of OTFT with Solution Processable Semiconducting Polymer

For the fabrication of the OTFT with solution processable semiconducting polymer as the active layer, the fabrication steps till the patterning of PANi-PSS electrode was followed as described in section 4.4.2. The dielectric surface was treated with OTS to obtain a hydrophobic surface. PHT-b-PBA in chloroform solvent was spin coated on the dielectric patterned substrate. A three step spin coating process at maximum rpm of 3000, was employed to achieve the required thickness (50 nm) of the semiconductor film. The film was allowed to dry completely in between the spin coating steps. The semiconductor film was annealed at 130 ºC to achieve the preferred orientation of grains. The patterning and passivation of the semiconducting active layer was done with parylene C as described in section 4.3. The device was designated as D7. The I_{ds}-V_{ds} characteristics and transfer characteristics of D7 are shown in Figs. 4.29(a) and 4.29(b), respectively. Saturation field effect mobility of 4.82 x 10^{-2} cm^2/Vs is achieved with the solution processable semiconductor, which is one order less than that achieved with vacuum evaporated pentacene for flexible TFTs. Hence, the choice of material and processes in the fabrication of organic TFTs, should consider the application it is intended for and best possible combination of vacuum and solution processes should be employed in order to achieve maximum possible performance.

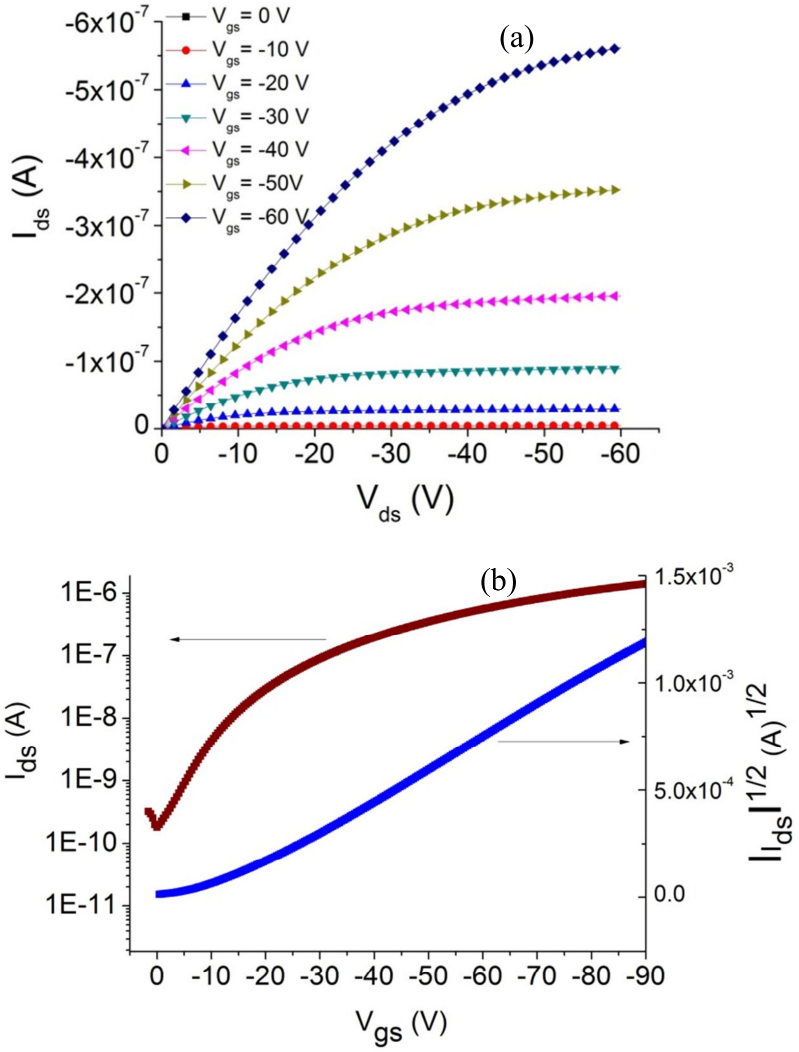

Fig. 4.29: (a) I_{ds}- V_{ds} characteristics and (b) transfer characteristics of TFT fabricated with PSN3-3 electrodes and PHT-b-PBA as semiconducting layer.

4.5 Conclusions

The studies on different electrode materials such as metal Pd; doped PANi nanofibers; dispersible PANi-PSS nanoparticles, secondary doped with DCA and semiconducting materials such as pentacene and PHT-b-PBA revealed that a combination of solution processable deposition of PANi-PSS by parylene lift-off process and deposition of pentacene by thermal evaporation at high vacuum were comparatively the best in this study, that led to optimum field effect mobility, I_{on}/I_{off} ratio, contact resistance and gate leakage currents in the devices. An effective method for simultaneous passivation and patterning of the semiconducting layer with photopatterned parylene C, reduced the off-current by about two orders, thereby increasing the I_{on}/I_{off} ratio. Other combinations of solution processable and vacuum deposited conducting-semiconducting materials with suitable work function and HOMO energies will be studied in future, to achieve best possible performance in organic TFTs.

Chapter 5

TWO DIMENSIONAL NUMERICAL SIMULATION OF ORGANIC THIN FILM TRANSISTOR

5.1 Introduction

OTFTs have shown remarkable improvement in performance in the recent years. However, progressive research is still necessary to catapult these devices to be suitable for commercial applications and to be competing with traditional inorganic-based transistors. It is now well understood that further scope for improvement lies in understanding the physical properties (morphology) of organic semiconductors and the interfaces. Any inhomogeneity or defect in the semiconducting film or at the interface, not only has critical effect on the device performance, but also impedes the evaluation of intrinsic properties of the organic semiconductor correctly [205].

The microscopic mechanisms of charge injection, carrier transport and traps pertaining to any new electrode material or organic semiconductor and their interaction with the other layers of the device have very high influence on the performance of the organic transistor. An understanding of these mechanisms is essential to improve the device performance by various engineering routes. Simple analysis of the experimental data through one dimensional analytical models that predict the overall device behaviour alone is not sufficient to understand the complexity involved in the actual physical mechanisms. In this regard, physics based two dimensional numerical simulation [206] has become utmost important in understanding the detailed microscopic processes in the interior of the devices in order to maximize their performances. Such investigations lead to the analysis of the cause of the non-ideal performance of device behaviour with the use of certain materials and can also be of help in explaining enhanced performance with the use of certain new conducting/semiconducting materials.

In this chapter, a computer-aided methodology for modelling of OTFTs using SILVACO's ATLAS software is presented. ATLAS provides general capabilities for physics based two dimensional (2D) and three dimensional (3D) simulation of semiconductor devices. The simulator functions by incorporating the physics that govern charge carrier transport and applies it to the dimensions of the device under study. From the simulation of organic TFTs, it is also possible to obtain an advance idea of the electrical characteristics of a device of given dimensions. Thus, devices with optimal dimensions can be realized, which otherwise requires tedious 'trial and error' fabrication processes, without having an idea of how a device of given dimensions would behave, straining the vital resources [207-208].

The simulator predicts the electrical characteristics of a given structure at applied bias conditions based on the application of a set of fundamental device equations [209]. Two basic bottom contact structures are considered for simulation; one which has nonflexible, inorganic, heavily doped silicon acting as a substrate as well as gate, along with its most widely used inorganic silicon dioxide dielectric; and the other which is a flexible device consisting of an organic, PEN film as substrate along with organic PVP dielectric. The basic parameters like interface charge density, low mobility layers around the already laid down contacts, acceptor like trap states are studied for their effect on the device performance. The later part of this chapter discusses the 2D numerical simulation techniques, to fully understand the electrical characteristics of pentacene TFT with the conducting polymer, nanostructured polyaniline, templated with polystyrene sulphonic acid (PANi-PSS) as electrodes.

5.2 Simulation of non-Flexible Devices

5.2.1 Finite Element Modelling Using ATLAS

There are a variety of options for giving input to ATLAS for simulation as depicted in Fig 5.1. Deck Build window was used to program the necessary device analysis using the standard syntax specific to the simulator. For simulating the device of interest using ATLAS, a standard set of specifications were required as inputs. It is as follows

1. Structure specification
2. Material models specification
3. Numerical method specification
4. Solution specification
5. Result specification

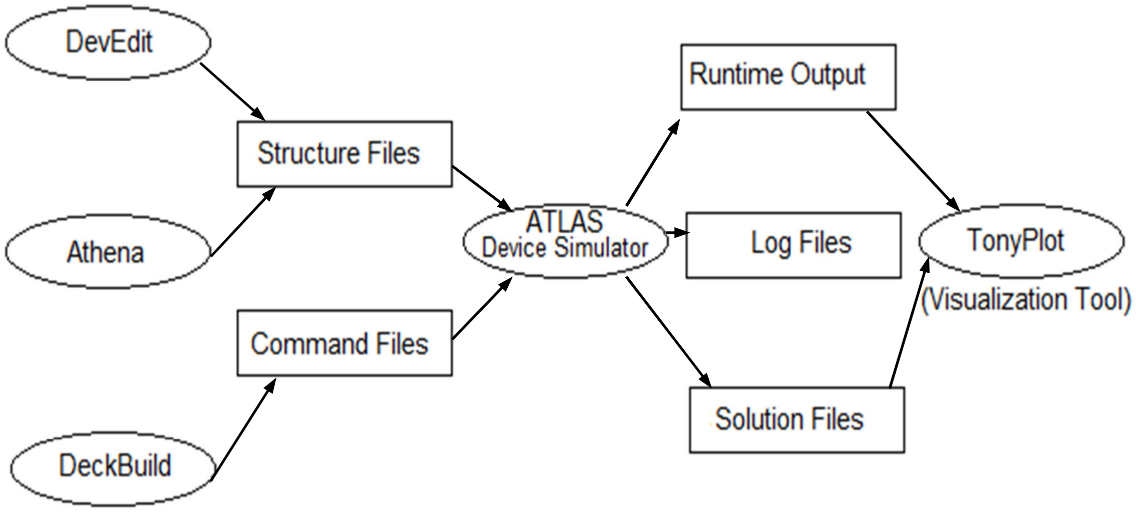

Fig. 5.1: Illustration of various ways of inputting and outputting the data to ATLAS.

5.2.2 Structure and Mesh Specification

To begin a simulation, the physical structure and dimensions of the device is to be defined, including the locations of the electrical contacts as per the structure shown in Fig. 5.2. Shown in Fig. 5.3 is the cross section of a bottom contact pentacene based OTFT, a close-up of the channel region. Once the main features, materials and dimensions are described, the internal regions are broken down into a mesh. The mesh comprises a complex grid of triangles where the simulation entails the calculations of the results at each node (triangle corner). The density of the triangles depend on the complexity of the physics of the region of the device being studied. For instance, the oxide-semiconductor boundary is a common place for carrier accumulation and transport to occur. Therefore, the density of the mesh is made quite high at this location compared to others. The bulk region of the substrate is a low activity area and therefore, consists of a lower density mesh. Mesh definition is a function of the program which needs to be optimized. A poorly defined mesh can give inaccurate results, while a mesh which is too dense will increase the run time of the simulation. Furthermore, there is an upper limit to the amount of mesh points which can be defined for the simulation to run. Zoomed view of the meshing done in the channel region of the bottom contact OTFT is shown in Fig. 5.4.

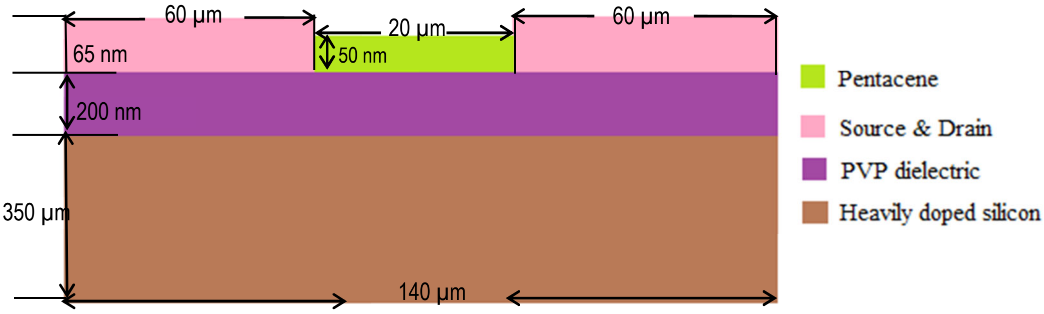

Fig. 5.2: Schematic of OTFT on Si substrate.

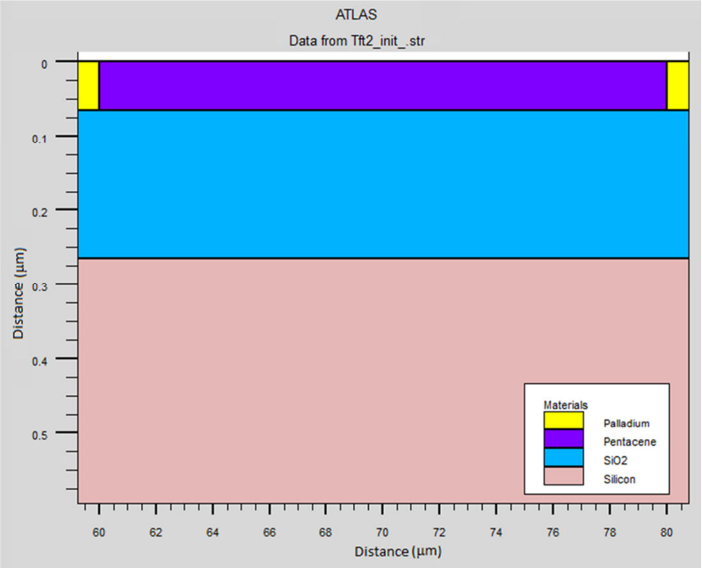

Fig. 5.3: Structure file of the bottom contact device (a zoomed view using Tonyplot).

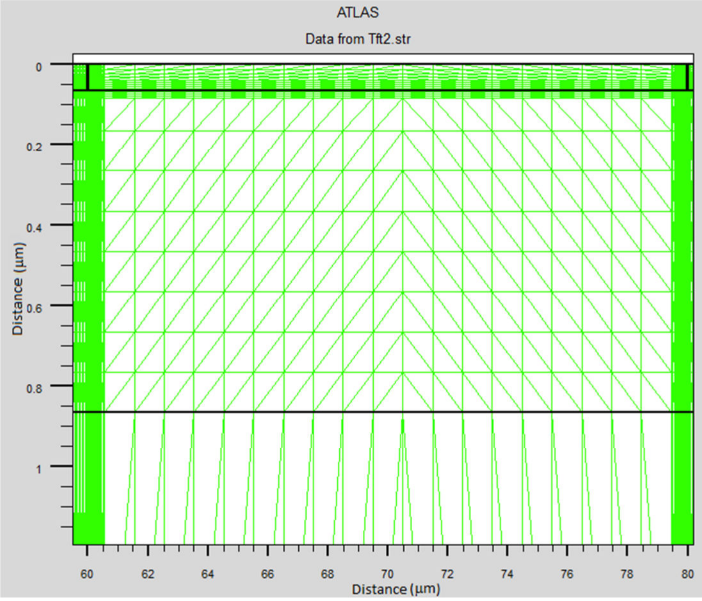

Fig. 5.4: Zoomed view of the meshing in bottom contact organic TFT.

5.2.3 Device Physics Equations

The mesh density in the internal regions of the OTFT structure to be studied is important because it defines where the charge carrier densities within the device will be calculated. These charge carrier densities are figured by simultaneously solving the fundamental device equations including, Poisson's equation, continuity equations for electrons and holes, charge transport equations and defect density equations [209]. These equations are the default equations which ATLAS uses to determine the device's electrical characteristics.

5.2.3.1 Poisson's equation

Poisson's equation relates the electrostatic potential to the space charge density, which is given as follows:

$$div(\varepsilon\nabla\Psi) = -\rho \qquad (5.1)$$

where Ψ is the electrostatic potential, ρ is the local space charge density and ε is the local permittivity.

5.2.3.2 Carrier-continuity equation

The continuity and the transport equations describe the way that the electron and hole densities evolve as a result of transport processes, generation processes and recombination processes. The continuity equations for electrons and holes are defined by Eqn.

$$\frac{\partial n}{\partial t} = \frac{1}{q} div\vec{J}_n + G_n - R_n \qquad (5.2)$$

$$\frac{\partial p}{\partial t} = -\frac{1}{q} div\vec{J}_p + G_p - R_p \qquad (5.3)$$

where, n and p are the electron and hole concentration, $\vec{J}_p$ and $\vec{J}_n$ are the electron and hole current densities, G_n and G_p are the generation rates for electrons and holes, R_n and

R_p are the recombination rates for electrons and holes respectively and q is the magnitude of the charge on an electron.

5.2.3.3 Transportation equation

A third important set of equation for describing the device physics are the charge carrier transport given by:

$$\vec{J}_\mathrm{n} = qn\mu_n\vec{E}_n + qD_n.\nabla n \tag{5.4}$$

$$\vec{J}_\mathrm{p} = qp\mu_p\vec{E}_p - qD_p.\nabla p \tag{5.5}$$

which contain both drift and diffusion components. These equations determine the current density of the charge carriers based on the mobility of the carrier (μ), the electric field (E), the carrier densities (n, p) and the diffusion lengths of the carriers (D).

ATLAS software hence, simultaneously and self consistently solves Poisson's equation, the continuity equations and the current density equations at each node in the two dimensional mesh for the given device structure, subject to the boundary conditions. The voltages applied at the contacts at each node is also taken into consideration during the simulation. Included in the solution is the electron and hole concentrations and the potential at each node. From these, the electric field distribution, electron and hole current densities and the terminal currents at the electrodes are calculated at each node. Discretization of the above equations is also performed so that they can be applied to the finite element grid used to represent the simulation domain.

5.2.4 Drift Diffusion Model

The device simulation was initially carried out using the conventional and a primitive, drift diffusion mobility model [210-211]. For the pentacene employed in the OTFTs studied here, the material parameters used in the simulation are summarized in Table 5.1. The transportation equations, taking this model into consideration are given by Eqns. (5.4) and (5.5) and the resultant device characteristics are as shown in the Fig. 5.5. The extracted device parameters from the simulation are given in Table 5.2. The simulated results cannot be correlated with experimental results of section 4.2 and exhibit large mismatch. Hence, for the simulation of devices based on organic semiconductors such as organic TFTs, taking into account the specific characteristics of organic semiconductors, the drift-diffusion model cannot be used without modifications. An important modification is to use a charge carrier mobility model which depends on the electric field and the temperature instead of a constant mobility model (Poole-Frenkel model, discussed in section 5.3).

Table 5.1: Summary of parameters used in the simulation by drift diffusion model.

Parameter	Material	Parameter	Reference
Energy band gap (E_g) (eV)	Pentacene	2.25	212, 213
Electron affinity (eV)	Pentacene	2.49	212, 214
Intrinsic *p*-type doping (cm^{-3})	Pentacene	$3x10^{16}$	215
Effective valence band density of states (N_V) (cm^{-3})	Pentacene	$2.88x10^{21}$	216
Effective conduction band density of states (N_c) (cm^{-3})	Pentacene	$2.88x10^{21}$	217
Relative permittivity	Pentacene	4	212, 214
	SiO_2	3.9	218
Work Function (eV)	Palladium	5.0	219

Since the focus of this thesis is to study the OTFTs fabricated on flexible substrate in detail, further 2D simulation studies were performed on devices fabricated on polymeric substrate, with PVP dielectric. For the simulation, both metal and conducting polymer electrodes were considered, taking into account, a field dependent mobility model, instead of the primitive drift diffusion model. A few other parameters, such as low mobility layers at electrode-semiconductor interface, charges trapped at the semiconductor-insulator interface, the interfacial and bulk traps etc. that are prerequisite for simulation, were also incorporated along with the field dependent mobility model.

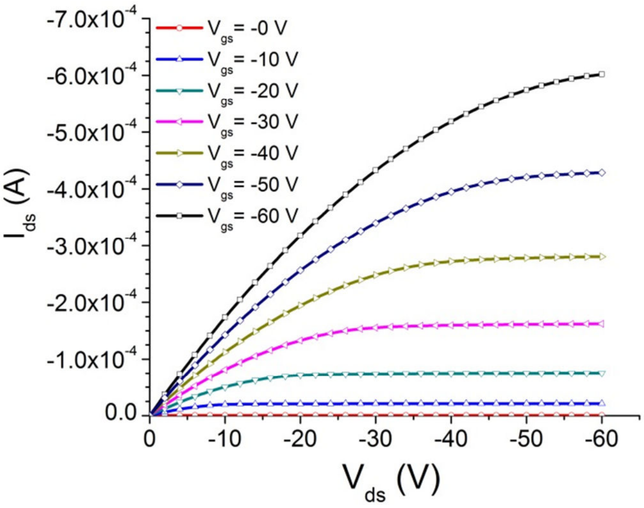

Fig. 5.5: I_{ds}-V_{ds} characteristics of OTFT on Si substrate, modelled by drift diffusion model.

Table 5.2: Electrical parameters of the device simulated by drift diffusion mobility model.

Parameter	**Mobility (cm^2 /Vs)**	**Threshold Voltage (V)**	**I_{on}/I_{off}**	**Sub-Threshold Swing (V/dec)**
Value	3.73	1.4	4.26x10^6	1.12

5.3 Simulation of Flexible Devices

As stated in section 5.2.4., drift diffusion model is not sufficient to model the organic TFTs. Hence, field dependent, Poole-Frenkel mobility model for charge transport was studied in detail, to simulate the device characteristics of flexible TFTs. Effect of contact barrier, by incorporating low mobility layer at the electrode-semiconductor interface, morphology dependent mobility, trap distribution in pentacene film and trapped charge at the semiconductor-insulator interface were step-wise incorporated to model the electrical characteristics of the device accurately. Devices with metal electrode, Pd and conducting polymer electrode, PANi-PSS, were simulated to match the experimental results and understand the physical mechanism of charge transport. An explanation for the observed difference in contact resistance with metal and conducting polymer electrode is also given.

5.3.1 Poole-Frenkel Mobility Model

Poole-Frenkel mobility was first theorized in 1938 by Frenkel [220] to explain the increase in conductivity in insulators and semiconductors when high fields were applied. In disordered organic semiconductors, charge transport occurs mainly by hopping between nearby localized states, which are induced by disorder. In a transistor, the physical effect of the source-drain electric field is then to effectively reduce the hopping barrier. The hopping probability and the mobility will have a dependence on electrical field which follows a Poole-Frenkel law and the mobility model for holes is given by, Eqn. (5.6).

$$\mu(E) = \mu_0 \exp\left(\gamma\sqrt{\mathrm{E}}\right) \qquad (5.6)$$

where $\mu(E)$ is the field-dependent mobility, E is the electric field, μ_o is the zero field mobility, γ is a prefactor which depends on the material and is generally inverse in proportion to temperature.

For the simulation, the bandgap of pentacene (E_g) was taken as 2.2 eV [212-213], electron affinity (χ_{pc}) as 2.8 eV [212, 214], density of both conduction and valance band states (N_c and N_v) as 10^{21} cm^{-3} [216-217] and relative permittivity as 4.0 [212, 214]. The acceptor doping concentration was taken as 3 x 10^{16} cm^{-3} [215]; the work function (Φ_m) of the source, drain and gate electrode was assumed to be 5.0 eV for both Pd and conducting polymer electrode based on literature values [105, 147]. Relative permittivity of PVP was taken as 3.8 [221]. γ=4.37 x 10^{-3} (cm/V)$^{1/2}$ with Pd electrode and 5.72 x 10^{-3} (cm/V)$^{1/2}$ with PANi-PSS electrode; μ_o = 8.3 x 10^{-3} cm^2/Vs with Pd electrode and 2.1 x 10^{-3} cm^2/Vs with PANi-PSS electrode for pentacene semiconductor [222] were used in the simulation, within the ranges reported in literature.

5.3.2 Device Fabrication

Pentacene based OTFT fabrication in bottom contact configuration with Pd as source-drain electrode, PVP as gate dielectric and Pd as gate electrode, on flexible PEN substrate, was carried out as previously described in section 4.3 and the device was designated as D8. For the fabrication of OTFT with conducting polymer as source-drain electrode, the modified parylene lift-off method was adopted for patterning the solution processable electrodes of PANi-PSS as described in section 4.4.2. The transistor in bottom contact configuration was designated as D9. The thickness and dimensions of layers in D8 and D9 were maintained identical for the purpose of comparison of experimental and simulation results. OTFT with different channel lengths (10-50 µm) were fabricated to extract the device contact resistance. The schematic of the fabricated OTFT of 20 µm channel length, with thickness and dimension of each layer is given in Fig. 5.6.

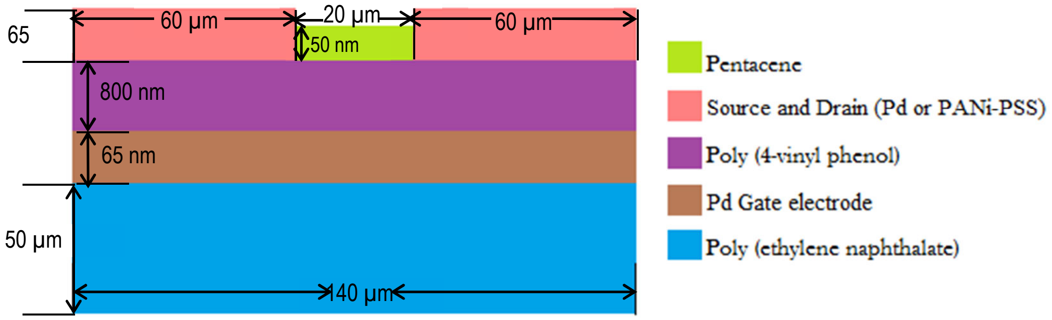

Fig. 5.6: Schematic of organic TFT with dimensions of each layer.

5.3.3 Discussion on the Experimental and Simulation Results

Solid lines in Figs. 5.7(a) and 5.7(b) show the experimental I_{ds}-V_{ds} characteristics of the device D8 and D9, respectively. Though the maximum I_{ds} values for both the devices are similar, there is significant difference in the nature of the curves at lower V_{ds} values. Fig. 5.8(a) depicts the presence of non-linearity, at lower V_{ds} values, which is a direct consequence of the higher contact resistance in D8, due to the metal used as electrode in OTFT [143]. This non-linearity is less or nearly absent in the case of D9, [Fig. 5.8(b)] which employed PANi-PSS as the conducting electrode for hole injection. The characteristics of these devices are consistent with that of other contacts that have ideal ohmic character.

To model the observed electrical characteristics of the devices, modelling parameters were systematically incorporated in ATLAS, to match the observed experimental results of Figs. 5.7(a) and 5.7(b). In an organic transistor, there exists a charge injection barrier between the electrode and the organic semiconductor interface.

This charge injection barrier (Φ_{bh}) interpreted as the energy barrier for injection of charge through the electrode-semiconductor interface can be defined as the energy difference between the ionization energy (*IE*) of the organic semiconductor and the work function of the electrode (Φ_m) as represented by Eqn. (5.7).

$$\Phi_{bh} = IE - \Phi_m \tag{5.7}$$

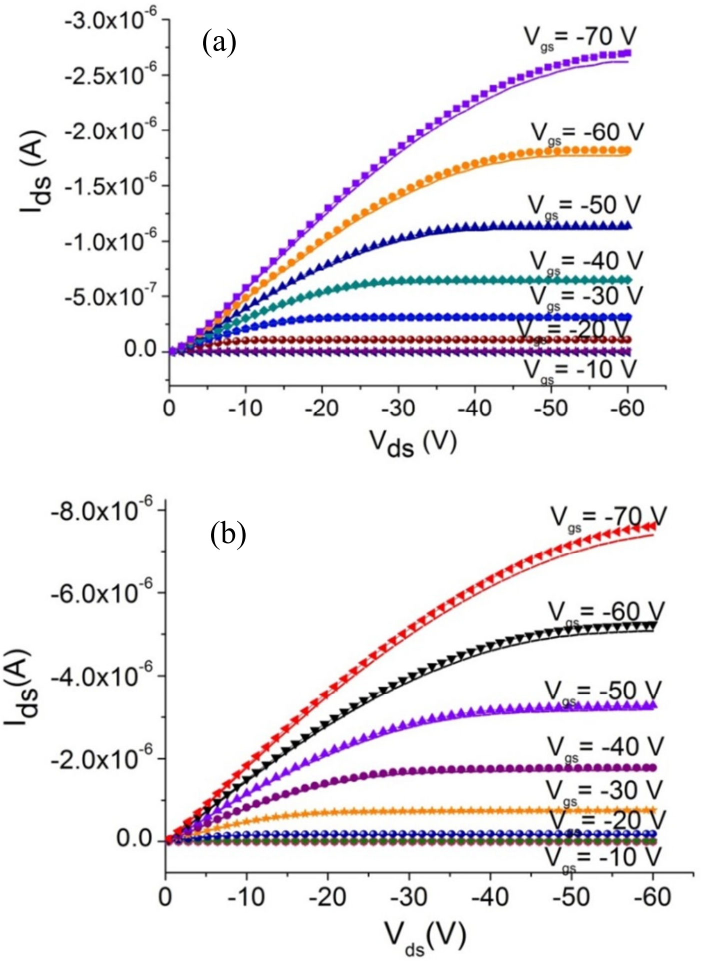

Fig. 5.7: I_{ds}-V_{ds} characteristics of experimental (solid lines) and numerical simulation (dashed lines) of OTFT fabricated with (a) Pd and (b) PANi-PSS, as source and drain electrode.

A large Φ_{bh} thus suggests that charge transfer is difficult from the electrode to the organic semiconductor. Fig. 5.9(a) shows the electronic band structure of the electrode-semiconductor interface in an ideal condition. The barrier height (Φ_{bh}) can also be written in terms of energy band gap (E_g) and electron affinity of pentacene (χ_{pc}) as in Eqn. (5.8).

$\Phi_{bh}=E_g+\chi_{pc}-\Phi_m$ (5.8)

In the present study, the electrode materials (both Pd and PANi-PSS) were selected in such a way that Φ_m of the electrode and HOMO level of pentacene have a close match in energy. But in actual conditions, in spite of this match in energy, an interfacial dipole (δ) exists between the organic semiconductor and the electrode as shown in Fig. 5.9(b). Then Φ_{bh} becomes higher and can be written as in Eqn. (5.9).

$\Phi_{bh}=(E_g+\chi_{pc}-\Phi_m)+\delta$ (5.9)

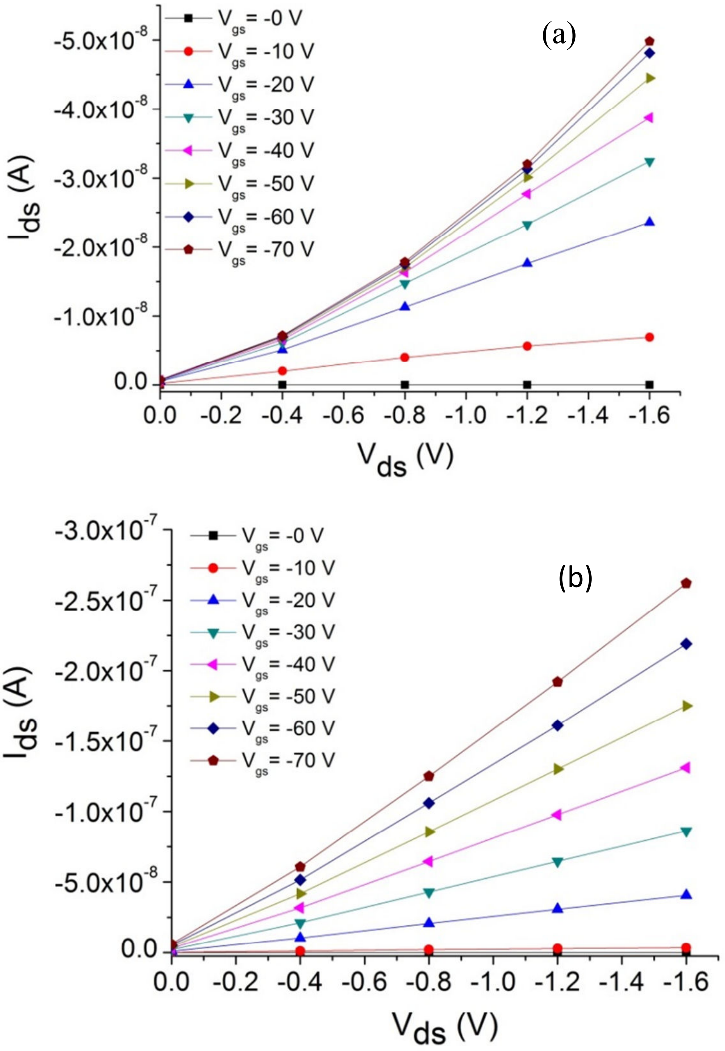

Fig. 5.8: I_{ds}-V_{ds} characteristics in the lower V_{ds} region of (a) D8 and (b) D9.

To account for the observed experimental results, interface phenomena discussed in following sections are considered.

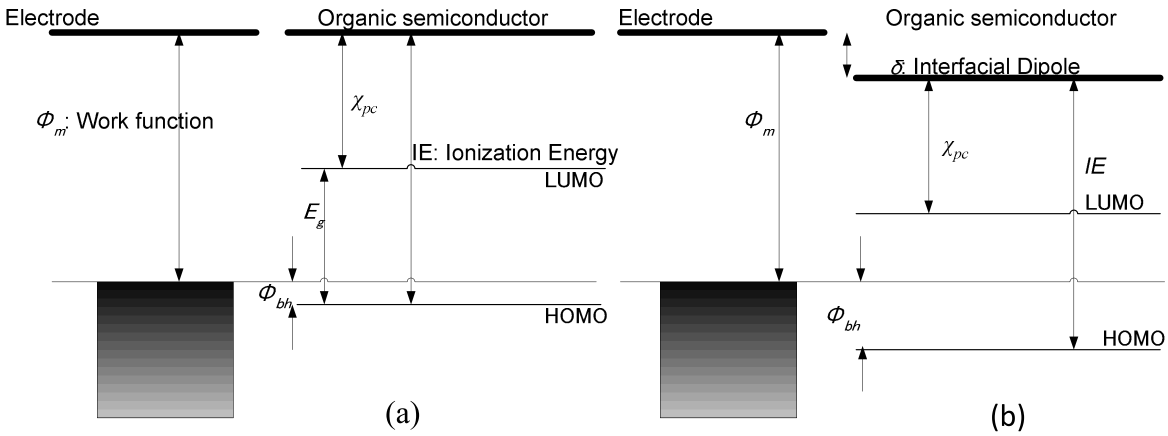

Fig. 5.9: Schematic of energy level diagrams of the interface between organic semiconductor and electrode when (a) interfacial dipole (δ) is absent and (b) interfacial dipole exists between the organic semiconductor and the electrode.

5.3.3.1 Low mobility interface layer: Inclusion of shifted electron affinity and reduced zero field mobility in simulation

To study the effect of grain size at the metal semiconductor interface, 1 nm thick pentacene was deposited on prepatterned Pd (D8) and PANi-PSS (D9) electrode that had PVP as the dielectric layer. From the SEM images in Figs. 5.10(a) and 5.10(b), the morphology of the pentacene at the interface and in the bulk (for device D8 and D9) are different for both pentacene-Pd and pentacene-PANi-PSS. The size of the grain at the semiconductor-electrode interface is lower for pentacene-Pd than that in pentacene-PANi-PSS.

In ATLAS, E_g, χ_{pc} and Φ_m can be incorporated to model the charge injection barrier and obtain the electrical characteristics. δ cannot be directly introduced in the simulation, but however, to interpret the observed experimental characteristics, a 10 nm wide interface layer at electrode-semiconductor interface was incorporated in the simulation where the morphology of pentacene and grain size was different. In the simulation, in this interface region, the electron affinity value was increased, that in turn introduced a vacuum level shift and hence, there was a relative change in the δ value at the interface and in bulk, which could model the electrode-semiconductor interface and the bulk pentacene. Fig. 5.11 shows the band energy diagram of pentacene-electrode interface with 10 nm wide interface pentacene layer and bulk pentacene with relative shift in δ value. The inherent band bending for approaching equilibrium is not included in this schematic representation.

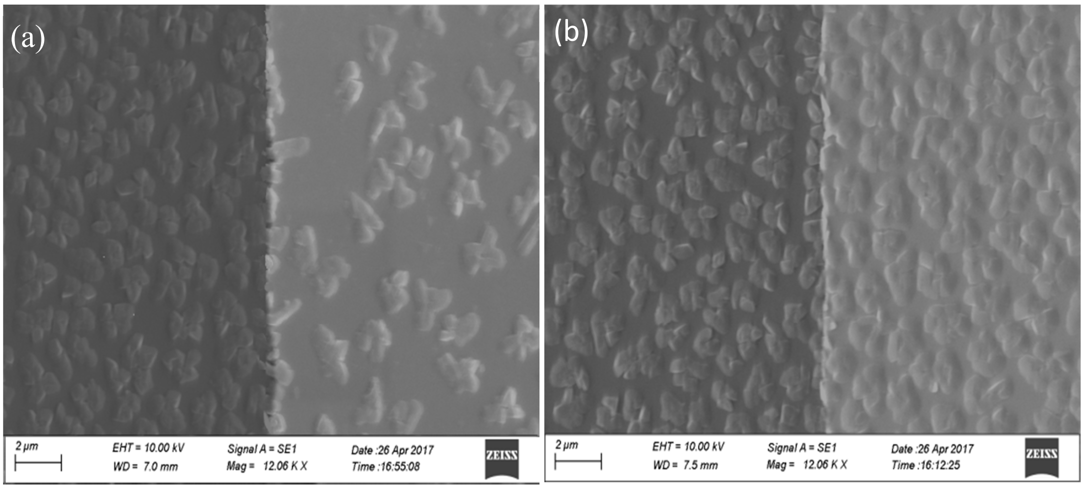

Fig. 5.10: SEM image of 1 nm thick pentacene deposited on prepatterned (a) Pd and (b) PANi-PSS, on PVP dielectric.

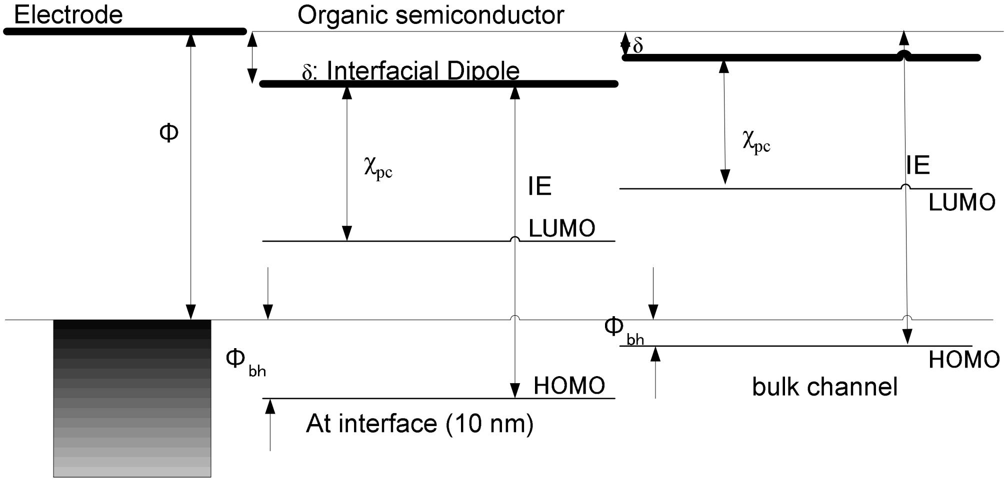

Fig. 5.11: Schematic energy level diagram of the interface between organic semiconductor and electrode with 10 nm pentacene at interface and bulk pentacene in the channel.

To satisfy the conditions of lower grain size at the interface, in the 10 nm wide interface region, grain size dependent low mobility region was introduced in the Poole-Frenkel model. To model the non-linear nature of the I_{ds}-V_{ds} curves, at lower V_{ds} values, μ_o and χ_{pc} were systematically introduced and optimum values to match with the experimental results were incorporated. Hence μ_o and χ_{pc} in the 10 nm region for D8 and

D9, respectively, used in the simulation were, 6.8 x 10^{-4} cm^2/Vs; 3.0 eV and 1.5 x 10^{-3} cm^2/Vs; 2.9 eV.

5.3.3.2 Inclusion of reduced intrinsic mobility and increased thermal activation energy

In the Poole-Frenkel mobility model, the zero field mobility is given by Eqn. (5.10).

$$\mu_o = \mu_i \exp\left(\frac{-\Delta}{kT}\right) \tag{5.10}$$

where μ_i is the intrinsic mobility at zero hopping barrier and Δ is the zero field thermal activation energy. Hence, according to Eqn. (5.6), the mobility increases with the temperature for typical values of the electric field strength ($E \approx 10^7$ Vm^{-1}) and the activation energy ($\Delta \approx$ 0.1 eV…0.5 eV) [208]. Fig. 5.12(a) shows the graph of simulation with Δ = 0.16 in the entire channel (dotted lines) and the experimental results (solid lines) for D8 (similar results for D9, not shown here).To get a good match between the experimental and simulation data in the entire range of the applied gate voltages, varied values of Δ were introduced in the simulation. Both for D8 and D9, Δ=0.16 and 0.3, was respectively used in the bulk and 10 nm interface region. μ_i for D8 and D9 in the 10 nm interface region was calculated from zero field mobility values and zero field thermal activation energy values, to be incorporated in the simulation. Due to the difference in morphology at the interface and bulk, μ_o and μ_i differ, in the two regions [213].

5.3.3.3 Acceptor traps with exponential distribution and trapped charges at the dielectric-semiconductor interface

To account for the deviation in the subthreshold region, which arises due to the presence of traps at dielectric-semiconductor interface or structural defects in the channel region, pentacene acceptor traps with an exponential distribution were considered [223] as follows in Eqn. (5.11).

$$g_{TA}(E) = N_{TA} \exp\left(\frac{E - E_c}{W_{TA}}\right) \tag{5.11}$$

where E refers to the energy measured from the valence band edge, N_{TA} and W_{TA} refer to the coefficient and the characteristic energy width of the exponential trap distribution, respectively. E_C represents the energy level of conduction band minimum. To account for any moisture, oxygen or mobile charges trapped in the dielectric, an additional interface trapped charge N_{ic} [224] has been included in the simulation. To account for the higher subthreshold swing observed in the experimental results, the values, $N_{TA} = 10^{16}$ cm^{-3}eV^{-1}, $W_{TA} = 0.55$ eV and $N_{ic} = 2\text{x}10^{11}$ cm^{-2}; $N_{TA} = 10^{18}$ cm^{-3}eV^{-1}, $W_{TA} = 0.55$ eV and $N_{ic} = 8\text{x}10^{11}$ cm^{-2} were used for OTFT simulation with Pd and PANi-PSS, electrode, respectively. All the parameters used for the simulation for trap energy level and pentacene trap concentration have close match to the values reported in literature [225-226]. In the transfer characteristics of D9 (and D8, not shown here) shown in Fig. 5.12 (b), at $V_{ds} = -50$ V, the simulation results without the inclusion of traps has lower subthreshold swing when compared to the experimental and simulation curve with the inclusion of trap parameters. All the parameters used for simulation are summarized in Table 5.3.

The simulated curves of the pentacene TFT, after incorporating all the optimized parameters are shown in Figs. 5.7(a) and 5.7(b) for Pd and PANi-PSS electrode, respectively, with dashed lines. The simulation results show a good agreement with experimental output characteristics. TLM was employed to determine the contact resistance [203] in the devices with Pd and PANi-PSS as the electrode material as was described for D5 and D6, in Chapter 4. The contact resistance (R_c) as a function of gate voltage with Pd was two order high in D8 than with PANi-PSS electrode in D9. The determined field effect mobility with PANi-PSS electrode is 0.5 cm^2/Vs and threshold voltage, 3.2 V, whereas with Pd electrode, the calculated mobility is 0.9 cm^2/Vs and threshold voltage, 7.4 V.

Charge concentration and potential profile was studied to explain the observed lower contact resistance in the OTFT with PANi-PSS and Pd electrode. Figs. 5.13(a) and 5.13(b) show the colour coded snapshot of the charge concentration in the 20 μm channel of D8 and D9, respectively, at V_{ds}= -30 V and V_{gs}= -20 V. Fig. 5.14(a) shows plots of the charge concentration profile, taken from a horizontal line cut 2 nm above the pentacene-PVP interface, running along the bottom of the channel for the two cases D8 and D9. From the extracted charge concentration values, it is evident that with the inclusion of parameters to meet the experimental results, the concentration of the charges at the electrode-semiconductor interface is comparatively higher in OTFT with PANi-PSS electrode than with Pd electrode, which is also consistent with the SEM images in Figs. 5.10(a) and 5.10(b). This high concentration of charges at a particular bias condition leads to good electrical contact between source/drain and the channel. This ultimately resulted in a lower charge injection barrier and hence, lower contact resistance in D9 than in D8.

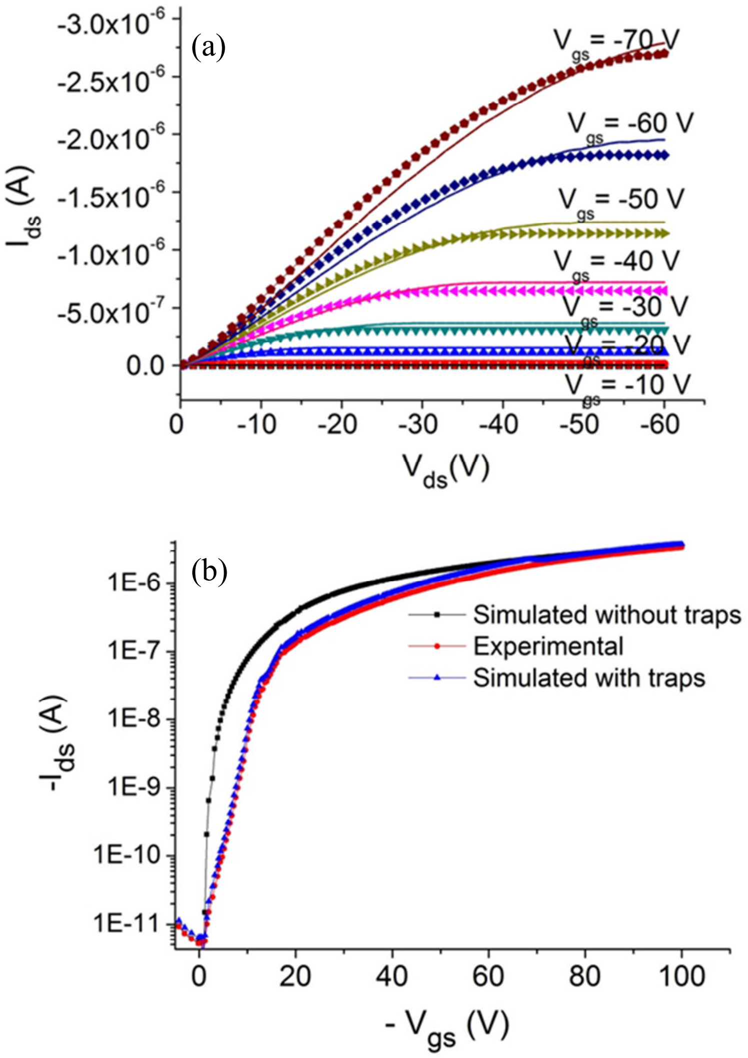

Fig. 5.12: (a) I_{ds}-V_{ds} characteristics of D8, experimental (solid) vs numerical simulation (dashed) with Δ = 0.16 in the entire channel region (all other parameters as given in Table 5.3, without the inclusion of traps) and (b) Experimental and simulated transfer characteristics of D9 at V_{ds}= -50 V.

Table 5.3: Parameters used in the simulation of OTFT with Pd and PANi-PSS electrode.

	D8 (Pd source and drain electrode)		D9 (PANi-PSS source and drain electrode)	
Parameter	Pentacene	10 nm pentacene near Pd contact	Pentacene	10 nm pentacene near PANi-PSS contact
Band gap (E_g) (eV)	2.25	2.25	2.25	2.25
Electron affinity (χ_{pc}) (eV)	2.8	3.0	2.8	2.9
Relative permittivity	4.0	4.0	4.0	4.0
Zero field thermal activation energy (Δ) (eV)	0.16	0.3	0.16	0.3
Zero field mobility (μ_o) (cm^2/Vs)	8.3×10^{-3}	6.8×10^{-4}	2.1×10^{-3}	1.5×10^{-3}
γ $(cm/V)^{1/2}$	4.37×10^{-3}	4.37×10^{-3}	5.72×10^{-3}	5.72×10^{-3}
Exponential trap density (N_{TA}) ($cm^{-3}eV^{-1}$)	10^{16}	10^{18}	10^{16}	10^{18}
Characteristic energy (W_{TA}) (eV)	0.55	0.55	0.55	0.55
Interface charge (N_{ic}) (cm^{-2})	2×10^{11}	2×10^{11}	8×10^{11}	8×10^{11}
Density of states (N_c, N_v) cm^{-3}	10^{21}	10^{21}	10^{21}	10^{21}
Acceptor doping concentration (cm^{-3})	3×10^{16}	3×10^{16}	3×10^{16}	3×10^{16}

It is also seen that at the 10 nm wide interface, where the low mobility layer is considered in the simulation with shifted electron affinity, the charge concentration drops in both cases. But in D9, the concentration again rises beyond ~ 20 nm to almost the initial value, whereas in the case of D8, the concentration which drops at the 10 nm interface continues to be same for ~ 300 nm [Fig. 5.14(b)]. This very low concentration of charge carriers at the interface between source electrode and the semiconductor for considerably large length in the channel in D8, leads to comparatively higher barrier to charge injection, making the contact non-ohmic in nature in the lower bias condition in Fig. 5.8(a), as reflected by the non-linear nature of the curves.

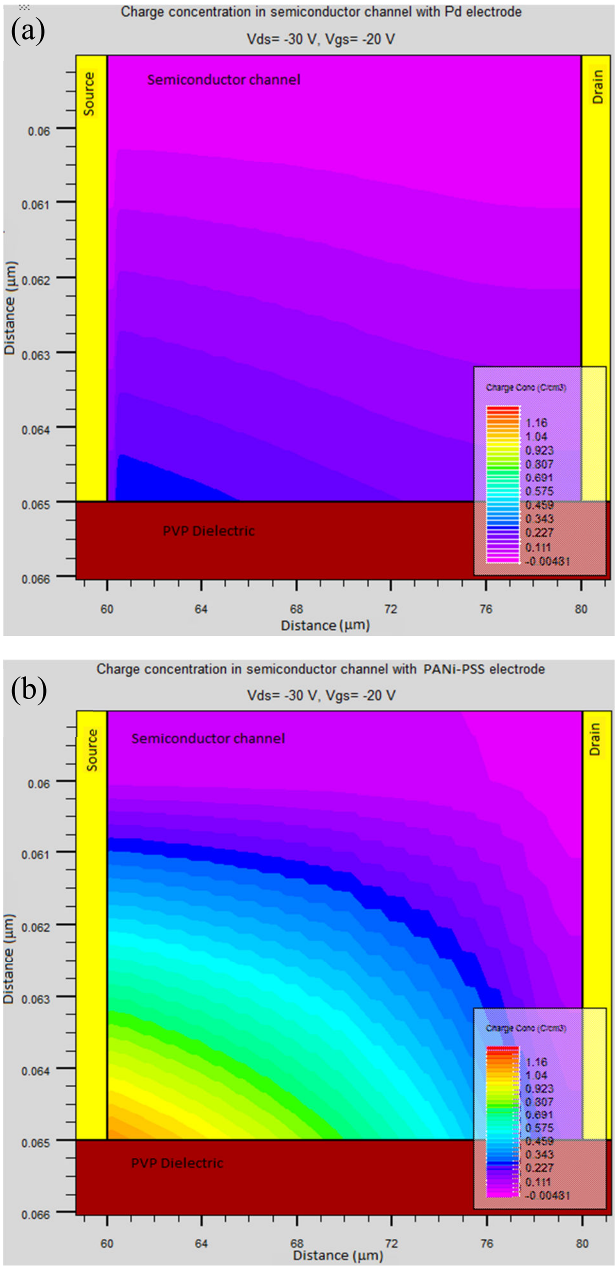

Fig. 5.13: Charge concentration profile in OTFT with 20 µm channel length with (a) Pd electrode and (b) PANi-PSS electrode.

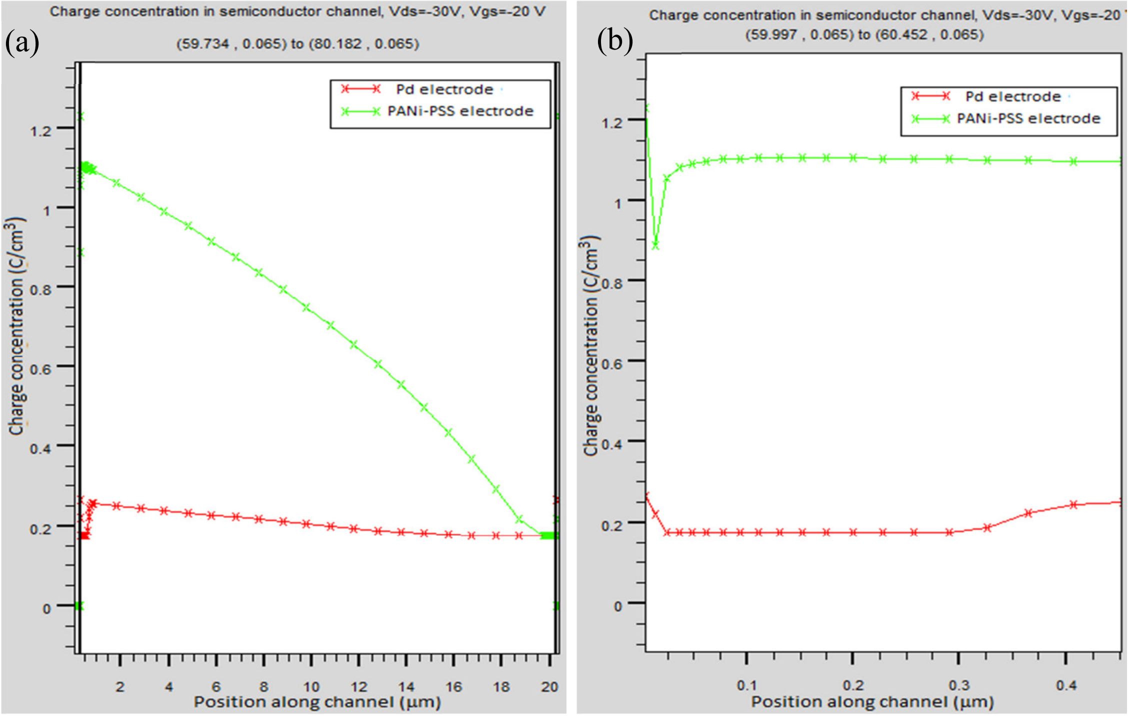

Fig. 5.14: Extracted charge concentration profile of OTFT with Pd and PANi-PSS electrode in (a) 20 µm channel and (b) enlarged view showing the interface at source electrode and semiconductor channel.

PANi-PSS patterned by the parylene lift-off method, hence exhibits lower contact resistance compared to the metal, Pd electrode. The obtained contact resistance values of PANi-PSS in this study and that for other reported conducting polymers are comparable or lower than that for high work function metal such as gold, which is the most commonly used electrode material in OTFTs [29, 145, 204, 227]. Therefore, PANi-PSS is a suitable, patternable conducting polymer electrode that can be used in place of the commonly used metals in OTFTs.

The potential profiles in D8 and D9, are shown in Figs. 5.15 (a) and 5.15(b) at $V_{ds}= -30$ V and $V_{gs}= -20$ V (V_{ds} is increased from 0 to 30 V at steps of – 1.0 V and constant $V_{gs}= -20$ V). At the 10 nm wide interface region, the potential shows a sharp drop in D8, reflecting a higher barrier to charge injection. Whereas in D9, the potential drops gradually with applied bias, which is indicative of an ohmic contact between the source and the semiconductor. The extracted charge concentration and potential profile hence, explain the cause of the observed non-linearity in the lower I_{ds}-V_{ds} curve in the case of D8.

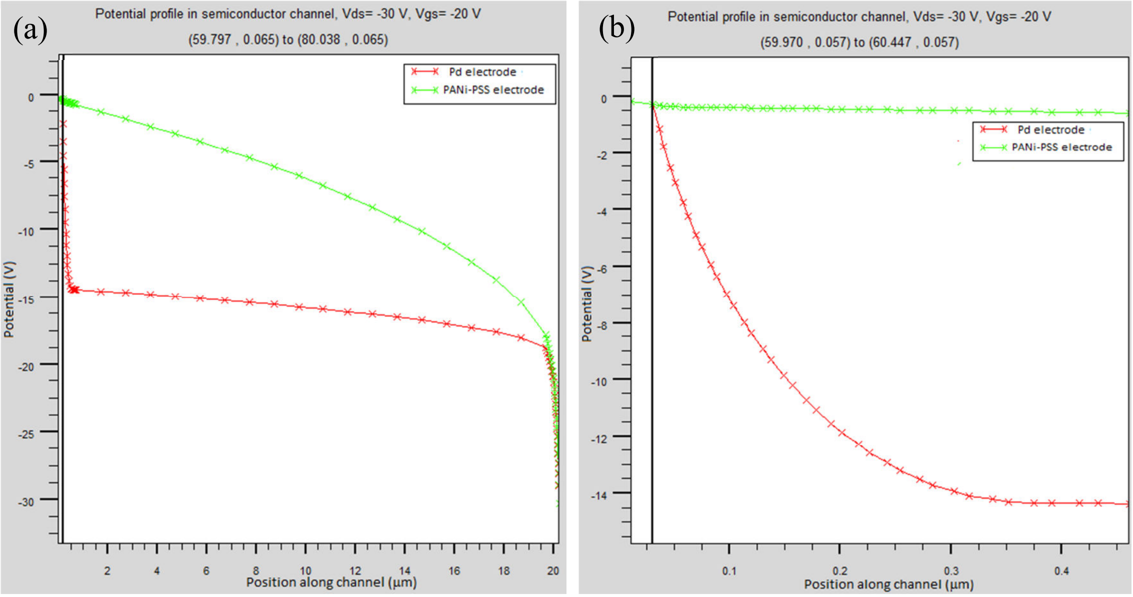

Fig. 5.15: Extracted potential profile of OTFT with Pd and PANi-PSS electrode in (a) 20 µm channel and (b) enlarged view showing the interface at source electrode and semiconductor channel.

Physical mechanisms that contribute to shift in electron affinity, thermal activation energy and low mobility layers due to difference in grain size of the semiconductor at the electrode-semiconductor interface contribute in controlling the charge injection to the channel. Experimental techniques such as Kelvin probe force microscopy (KPFM) or atomic force microscope potentiometry (AFMP) have been reported to be used simultaneously to map the potential and record the topographic profile along metal-semiconductor boundaries of working TFTs [228]. The potential drop in such cases was attributed to the difference in grain size of the semiconductor at the electrode-semiconductor boundary compared to that in bulk [229].

Existence of interfacial electrical dipole is reported to be the major cause of the limited carrier injection from metal contacts to semiconductors [216, 230]. The reasons for the formation of this interfacial dipole are often debatable. Assuming a relative change in the value of δ at the interface and in the bulk [Fig. 5.11] due to the morphological difference of the pentacene grains in these regions, contributed in determining the parameters required for the 2D simulation in the present study. The parameters for the simulation were arrived at after investigations on several combinations and the optimum set of values in Table 5.3 are within the ranges of theoretically calculated and experimentally measured values reported in the literature [208, 224]. The simulation with these parameters could reproduce the whole output characteristics of the devices, D8 and D9 in subthreshold, linear and saturation regime with good agreement to experimental characteristics. The 2D simulation tool can hence be employed in the design of organic transistors with new combinations of semiconductor and conducting polymer electrodes.

5.4 Conclusions

A computer-aided methodology for modelling of OTFTs using SILVACO's ATLAS software was investigated. As the primitive, drift diffusion model could not fully explain the observed properties of fabricated OTFTs, the electric field and temperature dependent, Poole-Frenkel model was employed for the 2D numerical simulation. Electrical characteristics of pentacene TFT with conducting polymer, PANi-PSS as electrodes and metal, Pd electrode were studied by this method. Effect of contact barrier, morphology dependent mobility and interface traps were step-wise incorporated to model the electrical characteristics of the device accurately and match the experimental data. Existence of higher interfacial electrical dipole as a result of difference in morphology at electrode-semiconductor interface was found to be the major cause of the limited carrier injection from metal contact to semiconductor. The microscopic and physical mechanisms determined from the 2D numerical simulation, which control the electrical characteristics of the devices, could explain the difference in contact resistance in the two types of devices with metal and conducting polymer electrodes.

Chapter 6

ORGANIC THIN FILM TRANSISTOR AMPLIFIER FOR ACOUSTIC SENSOR

6.1 Introduction

Organic TFTs are the primary building blocks of numerous devices including organic amplifiers [48, 231]. The performance of OTFT based amplifiers rely on the functional materials employed: OSCs, insulators, conducting and passivating materials. From a fundamental viewpoint, signal amplification is the simplest form of signal processing. In ideal cases, no information contained in the signal should be lost and no extra information introduced during amplification. Any change in the original waveform is considered undesirable. Sensing and signal processing of various signals using conformable flexible organic integrated circuits have been actively researched to enable real time sensing on curvilinear surfaces [45, 232]. Within this scope, ultrathin flexible organic amplifier is the most important building block for large-area signal recording and stabilization in close proximity to the site of interest.

Organic amplifiers have been developed in different layouts on flexible substrates to achieve good frequency response and high gain. To harvest the response of certain materials to pressure/force/strain or temperature stimuli, the sensors often are coupled to TFTs that convert the response generated by the material to an amplified voltage signal, suitable for subsequent interfacing with readout electronics [56, 233-236]. The present study aims at fabrication of a flexible OTFT based amplifier that can amplify acoustic signals on any curved surface. A flexible amplifier of this kind can be integrated in close proximity to the acoustic sensor. The proximity between sensor and electronics minimizes signal loss by avoiding large lengths of cable used for signal transfer. For fabrication of such a flexible amplifier that can be an integral part of acoustic sensing system, optimized materials and processes have to be utilized that yield maximum performance for the OTFTs. An effective passivation of OTFTs with a compatible material such as parylene is also mandatory to ensure consistent and reliable performance of the flexible amplifier.

Differential amplifiers form the building blocks of analog integrated circuits. A differential amplifier can accept two input voltages and amplifies the difference between these inputs, but ideally suppresses identical input signals [50]. The output signal which is produced by the device is multiplied by some constant, called the gain of the device. Among its advantages, first is, differential circuits are less sensitive to noise and interference than single-ended circuits, since noise and interference are often identical at the two input terminals and hence, it can be suppressed. Second, the differential design enables coupled amplifier stages without coupling and bypass capacitors, which is practically helpful because large capacitors are always difficult to realize in standard IC processes.

The amplifier is characterized by certain parameters. The magnitude of gain of an amplifier is an important parameter. The waveform transformation can be described as in Eqn. 6.1.

$$V_o\,(\mathrm{t}) = A\ V_i\,(\mathrm{t}) \tag{6.1}$$

where V_i and V_o are the input and output signals, respectively and A is the constant voltage gain, characterizing the amplification. The amplitude of the amplifier gain in dB (A_{dB}) is given by Eqn. 6.2.

$$A_{dB} = 20.\log_{10}.\frac{V_o}{V_i} \tag{6.2}$$

Another important parameter, bandwidth (BW), is defined as the frequency range in which the gain remains constant. Input signal frequencies outside the design bandwidth will be amplified differently. Therefore, the bandwidth of amplifiers is designed to match the expected signal frequency range. The cutoff frequency (f_c) is the frequency at which A_{dB} drops by 3 dB (– 30%) and the gain bandwidth product (GBWP) is the product of the amplifier's bandwidth and the gain at which the bandwidth is measured [237]. Due to the limitations of the inherent mobility of organic semiconductors, the achievable gain and gain bandwidth are comparatively lower than their inorganic counterparts. The highest open-loop gain and the highest gain bandwidth reported with organic amplifiers is 36 dB [238] and 18 kHz [239], respectively, which are but, adequate for application that do not demand very high speed and very high frequencies. The schematic of an amplifier and single stage differential amplifier are shown in Figs. 6.1(a) and 6.1(b), respectively.

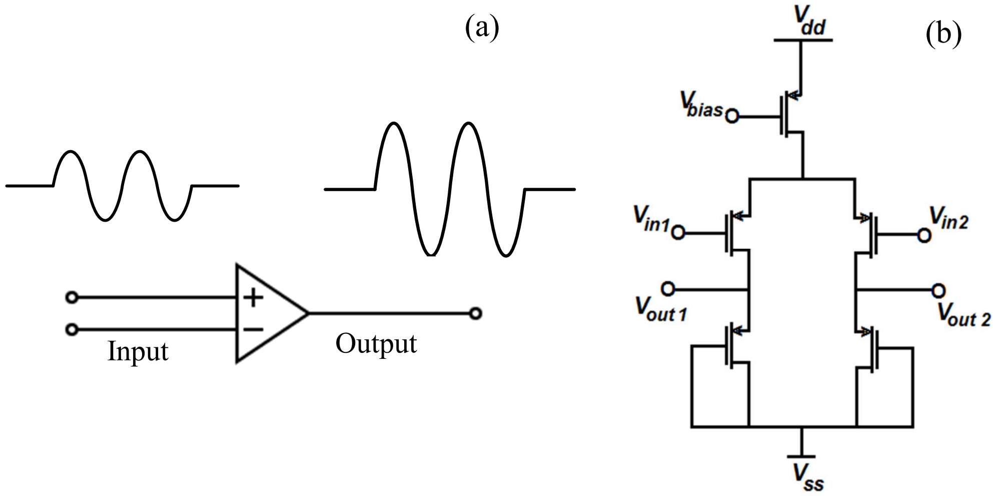

Fig. 6.1: Schematic of (a) an amplifier and (b) single stage differential amplifier (V_{dd} denotes drain supply, V_{ss} is source supply, V_{bias} is bias voltage, V_{in1}, V_{in2} denote the two input voltages, respectively and V_{out1}, V_{out2} denote two output voltages, respectively).

SONARs detect and locate objects by means of acoustic waves, sent out to be reflected by the objects; or detect the presence of a vessel (such as a submarine) by the sound it emits in water. Commonly, the signal from underwater acoustic sensors is relatively weak, i.e. µV to mV. This level of signal is too small for further processing and signal amplification is required. The acoustic frequencies used in sonar systems vary from very low (infrasonic) to extremely high (ultrasonic). Very low frequency sound (100-1000 Hz) can travel great distances and facilitate detection of quiet submarines. For such applications, large arrays of flexible piezoelectric, polyvinylidene fluoride based sensors are employed. The signal from the flexible sensor needs to be buffered and further conditioned by remote electronics conventionally. The inherent low capacitance of polymeric piezoelectrics and the parasitics in the cable, linking the sensor and remote electronics attenuate the input signal. To overcome the above limitations of polymeric piezoelectric sensors, front end electronics in close proximity to the sensor is highly essential. Flexible organic TFT based amplifiers are ideal candidates for real time and on-site amplification of low frequency acoustic signal. Since the frequency range of interest is less than 1 kHz in such application, the upper limits of achievable frequency bandwidth with organic amplifiers is not of much concern. For applications like acoustic sensor, amplifier gain that is much higher than that of a single stage differential amplifier is required. This high performance can be approached by applying additional circuit techniques, including cascade transistors and gain boosting. The applications of these techniques in organic electronics, though achievable, are still challenging.

6.2 Design and Experimental Setup

6.2.1 Mask Layout and TFT Fabrication

The mask design with 37 numbers of TFT was designed so as to realize devices with different aspect ratio, to be suitably employed as load or input devices in the amplifier. The mask design is shown in Fig. 6.2. The length of all the devices was 5 µm and widths of 1700, 1000 and 300 µm were used. 5 µm is the minimum achievable resolution with the parylene lift-off process and hence was chosen as the channel length in the OTFTs to obtain the benefit of shortest possible channel length. The gain of the load TFTs in the amplifiers need not be as high as that of the input TFTs. Hence, the width of the transistors were chosen with two extreme values of 1700 and 300 µm and a mid value of 1000 µm, yielding three ranges of *W/L* ratio (a high *W/L* is required for high gain). The TFTs were fabricated on 3″ wafer on PEN substrate, employing Pd metal as gate electrode; PVP as gate dielectric; pentacene as semiconducting layer; PANi-PSS, patterned by parylene lift-off method, as source and drain electrode and parylene as passivating layer, as explained in section 4.4.2.1. The yield of the devices fabricated was ~ 85%, with almost equal number of TFTs with different aspect ratio. For the convenience of testing, the support wafer beneath the flexible substrate was removed only after the characterization of all the devices and the amplifier circuit.

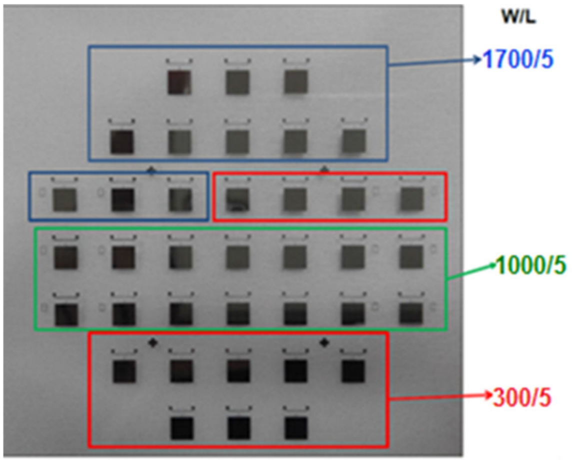

Fig. 6.2: Mask design of OTFTs employed as load or input devices in the amplifier.

6.2.2 Design and Fabrication of Wafer Probing Test Jig for Testing of OTFT Amplifier

The test jig was designed and fabricated to meet two main objectives. First, was to probe all 37 device terminals simultaneously on the 3″ substrate (PEN film supported on wafer). The terminals of each TFT on the wafer were connected to an array of LED to test the connectivity. Second objective was to test the devices in a single and multi-stage amplifier configuration by connecting the TFTs to a matrix of configurable jumpers. Connection between the TFTs on wafer and test jig was established through spring loaded POGO pins on the jig, with the aid of a guide guard with through-holes. The through-holes were made on the guide card as per the position of the probe pads in the mask design to achieve exact alignment of guide card, the pins on the jig and the fabricated devices on the PEN supported wafer. Five stages of amplifier design had been included in the design, with each single stage utilizing five TFTs. Through the matrix of configurable jumpers each TFT could be connected in place of any other TFT location in any amplifier stage. The detailed description of the wafer probing test jig is given in section 2.11.2.

A simple design of a single stage differential amplifier was adopted for testing the achievable gain with the fabricated TFT based amplifier. The gate terminal of the load of *p*-type OTFT was connected to the drain terminal. This resulted in a diode load with the load OTFT biased in saturation region. For higher BW, the diode-connected load performs better and is relatively less sensitive to shift in V_T over time. The schematic of the design of single stage differential amplifier used in the study is shown in Fig. 6.3.

In amplifier with diode connected loads, the voltage gain is represented by Eqn. 6.3.

$$\text{Voltage gain} = g_{mI} / \{g_{mL} + g_{dsI} + g_{dsL}\} \tag{6.3}$$

where, g_m is the transconductance and g_{ds} is the conductance parameter, defined by

$$g_m = \frac{\partial I_{ds}}{\partial V_{gs}} \tag{6.4}$$

$$g_{ds} = \frac{\partial I_{ds}}{\partial V_{ds}} \tag{6.5}$$

the suffix ‘I’ and ‘L’, represent the input and load, respectively.

The transconductance, g_m is proportional to μ and V_T of the transistors. For the voltage gain to have less dependence on μ and V_T, the g_m factor of the devices should be much larger than the g_{ds}. In such cases, voltage gain being a ratio of two g_m factors, will be a weak function of μ and V_T of the TFTs. The voltage gain then will be the ratio of transconductance of input pair of transistors and that of the transistors acting as load devices.

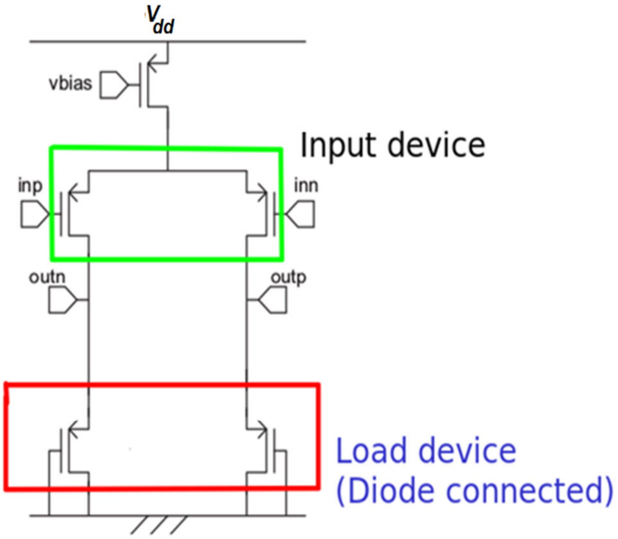

Fig. 6.3: Schematic of the design of single stage differential amplifier used in the study.

6.2.3 Testing of TFTs on Test Jig

6.2.3.1 Placement and alignment of TFTs on test jig

For positioning the wafer with fabricated 37 devices on the test jig, the split microscope and micropositioners of mask aligner stage was utilized. The contact pads on the wafer were aligned with the guide card with through-holes (designed as per the TFT layout in the wafer). The wafer was temporarily stuck with a double side tape to the guide card after alignment. The wafer along with guide card was then placed over the test jig with POGO pins touching the contact pads of the wafer through the through-holes. The photographs of the process of aligning the TFT contact pads with the holes on the guide card using the mask aligner is shown in Figs. 6.4(a)-6.4(c). The schematic of side and top view of the wafer aligned on test jig is shown in Figs. 6.5(a) and 6.5(b).

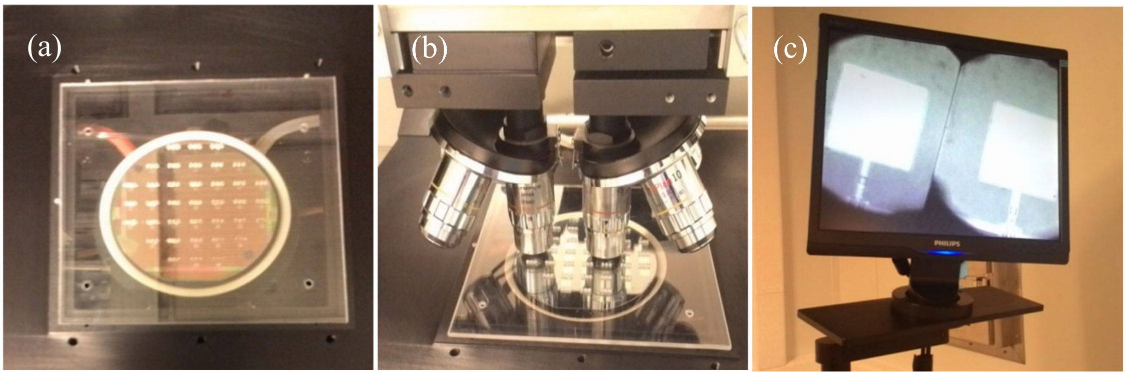

Fig. 6.4: (a)-(c) Photographs of the process of aligning the TFT contact pads with the holes on the guide card using the mask aligner.

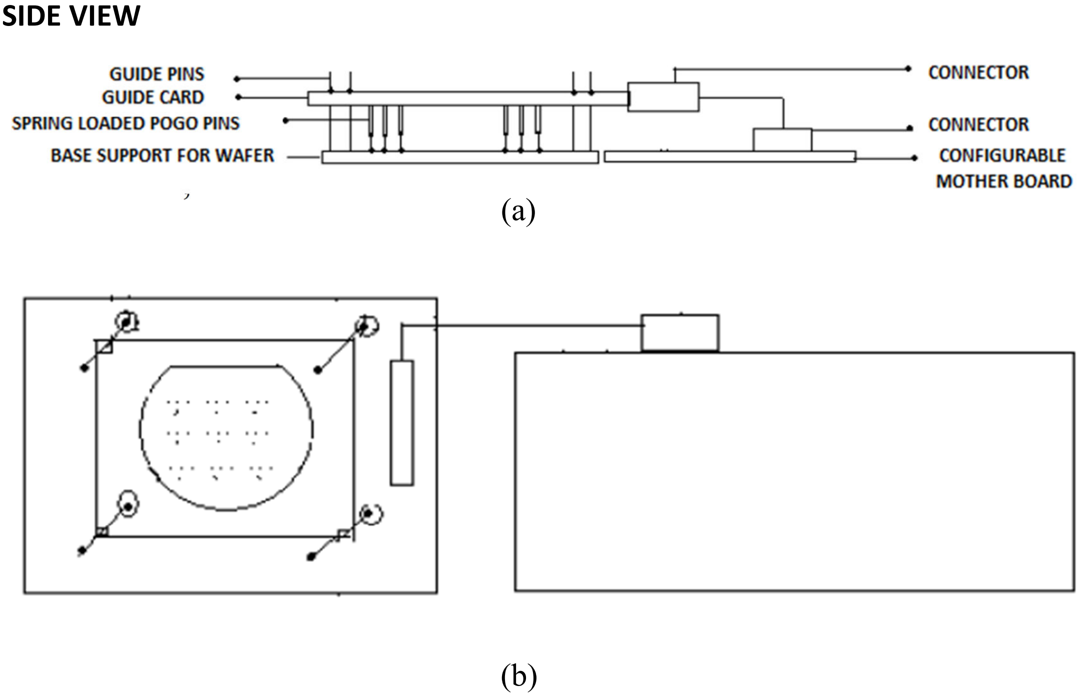

Fig. 6.5: Schematic of (a) side and (b) top view of the test wafer aligned on test jig.

6.2.3.2 Connectivity test for wafer probing test jig

The test is aimed to ensure that all the probe pins make electrical contact with the pad locations on the TFTs (gate, source and drain terminals). For this purpose, only the contact pads of the TFTs were fabricated on a dummy wafer, with positions exactly similar to the pad terminals of OTFTs. All the three pads of each structure were shorted during fabrication. Test was aimed at feeding a voltage to gate terminal with respect to the ground. Since the drain and source pad terminals were shorted to gate pad, voltage would be available at the source and drain terminals also, which could be confirmed by the glowing of a LED connected to the source and drain. For the purpose of testing, all the gate terminals of 37 devices were shorted to a common point. A voltage of – 5 V was applied to the common terminal. Since the source and drain terminals were shorted with the gate and connected to LEDs, on probing all the terminals with the test jig, all the 37 LEDs were glowing. The test proved that all the 37 contact pads were probed with the test jig. The test is important to confirm the availability and probing of all 37 devices with the test jig, during the process of configuring the amplifier. The schematic of the connectivity test with the test jig is shown in Fig. 6.6(a) and the corresponding photograph of the testing is shown in Fig. 6.6(b). An Elnova Model E-DC power supply was used to give the voltage and Keysight 34450A digital multimeter was used to measure the voltages.

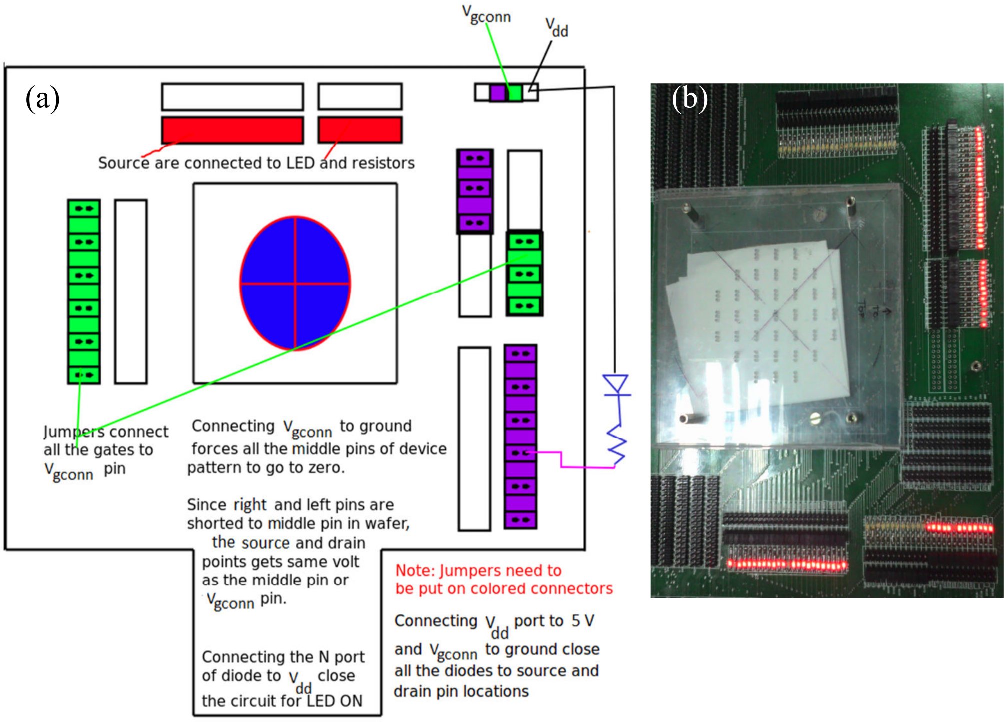

Fig. 6.6: (a) Schematic of the connectivity test with the wafer probing test jig for the 37 devices in a 3″ substrate and (b) photograph showing the devices tested for connectivity on the wafer probing test jig, indicated by the glowing of LED for the properly connected OTFTs.

6.2.3.3 Testing of OTFTs as switches

For simultaneously checking the ‘on’ condition of all the 37 TFTs fabricated on the 3″ substrate, all the gate terminals of devices were connected to a single pin, V_{gconn}. Jumper positions were as shown by coloured locations in Fig. 6.7. V_{dd} of 5 V was applied, with V_{gs} sufficiently low than V_T, enabling the devices to turn on. Since, for each TFT there is a separate diode string, all the 37 TFTs turn on, which is indicated by the glowing of LEDs. For the testing of the ‘off’ condition of the TFTs, $V_{gs} > 0$ V was applied, the condition in which all the devices are expected to be ‘off’. In the test on different sample wafers, an average of 3 devices did not turn off, indicating a low I_{on}/I_{off} ratio. Such TFTs were marked and not used for configuring the amplifier.

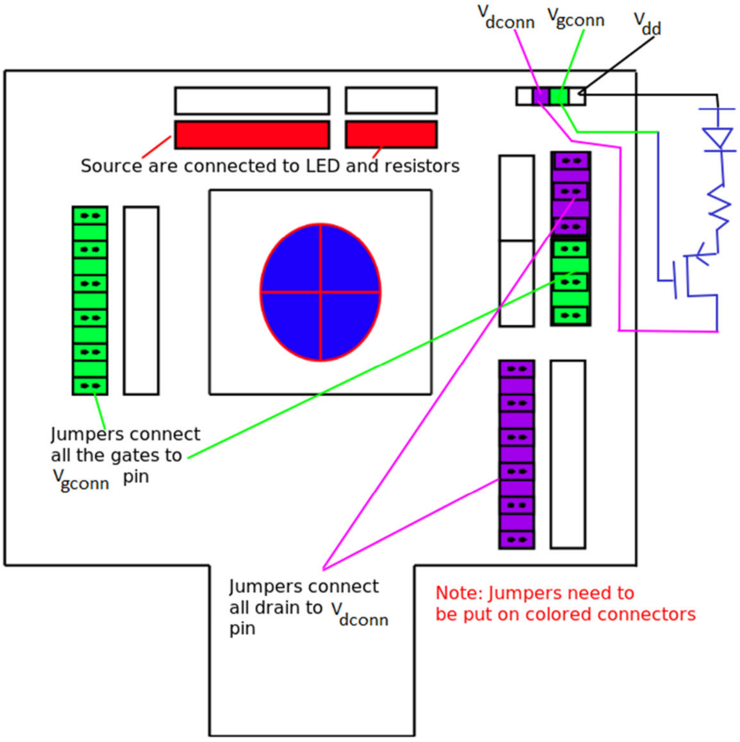

Fig. 6.7: Schematic representing the testing of 37 OTFTs in a 3″ substrate as switches, with the wafer probing test jig.

6.2.4 Configuring and Testing of TFTs as Amplifier for Acoustic Sensor

To determine the achievable gain and bandwidth with the organic transistor based amplifier circuit, simulated signal from a function generator was used. AC signal was generated using Tektronix AFG 3102 dual channel function generator. The output was recorded using Tektronix TPS 2024 four channel digital storage oscilloscope. The gate of the TFTs were protected with transorbs externally, to avoid damage to the circuit due to voltage spike from any other source. Connections were established using the wafer probing test jig as per the schematic shown in Fig. 6.3. Negative input terminal of the amplifier was set to a DC voltage bias. A sinusoid signal of programmable amplitude was added to the DC voltage and given to the positive input terminal. The input conditions were common mode input voltage of 2.5 V and differential input of sine wave of amplitude less than 1 V. Being a differential amplifier, the sinusoid signal only got amplified and the constant DC voltage bias was discarded by virtue of common mode rejection. Few input transistors were connected in parallel to emulate the effect of multiple fingers. Various load configurations for gain enhancement were also implemented through the jig to achieve the required gain. The schematic of circuit for testing the amplifier is shown in Fig. 6.8. The amplifier was characterized for different input voltages (from 10 mV to 500 mV). Five numbers of single stage amplifiers were tested and checked for the voltage gain. The experimental set up used for measuring the amplification of the signal using OTFT based differential amplifier is shown in Fig. 6.9. The amplification of the signal was tested from 100 Hz to 2 kHz.

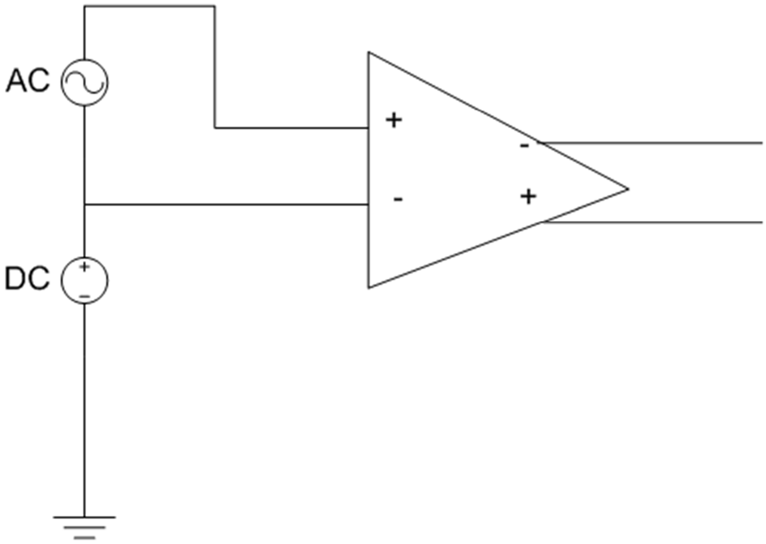

Fig. 6.8: The schematic for testing the amplifier configured using OTFTs on 3″ wafer, mounted on the wafer probing test jig.

The amplification of the acoustic signal was tested with a 10 cm x 10 cm electroded piezoelectric sensor. The schematic of the test set up is shown in Fig. 6.10

(a). A tone burst was fed to a projector (speaker) through an audio power amplifier. The sensor placed in front of the projector senses the acoustic signal. The schematic of circuit representing the amplification of signal from the acoustic sensor is shown in Fig. 6.10(b). The top plate of sensor electrode was connected to a constant DC bias voltage. A resistor of 100 kohm was connected across the electrodes of sensor. The charge in the piezoelectric sensor, upon receiving the acoustic signal varies and flows through the resistor and created a voltage. This voltage is the equivalent of the sensor generated voltage. The bottom plate of the piezoelectric sensor would be at a voltage equal to fixed DC bias +/- the sensor generated voltage. The amplifier amplified the difference in voltage between the input terminals (fixed DC bias being common in both the nodes, gets cancelled) and only the voltage generated by the sensor is amplified. The output voltage from the sensor and the voltage amplified by the OTFT based test amplifier were received at two different channels of the digital storage oscilloscope, through a precision conditioning amplifier [Fig. 6.10(a)]. The ratio of the voltage at channel-II to voltage at channel-I gave the gain of the OTFT amplifier.

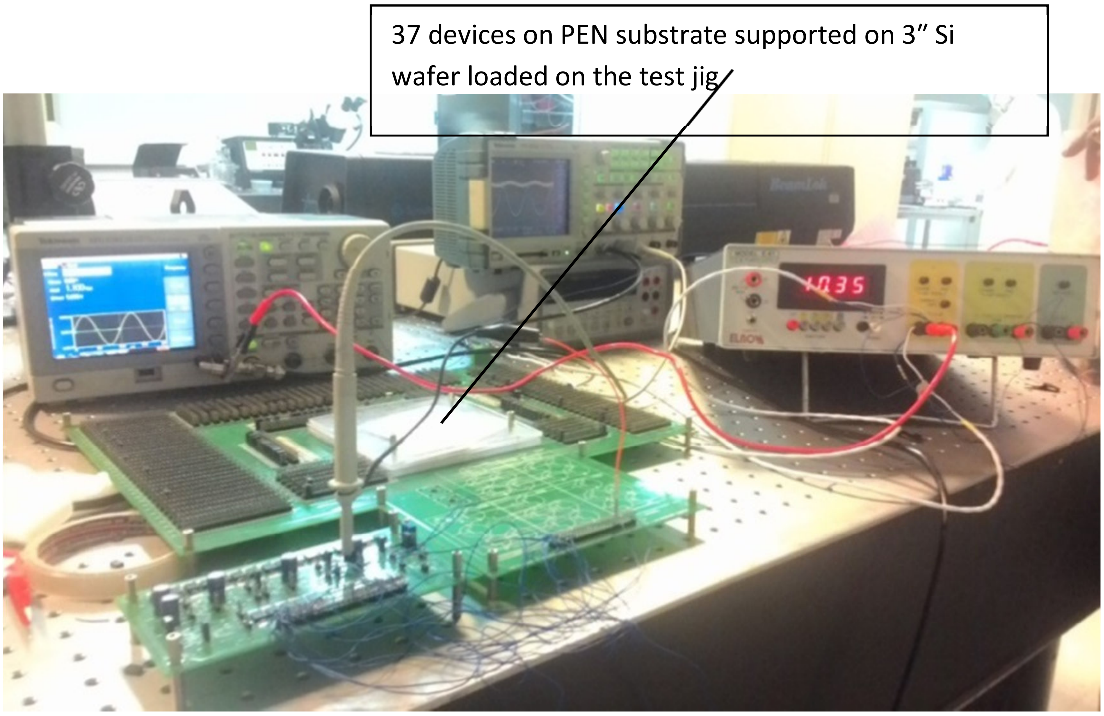

37 devices on PEN substrate supported on 3" Si wafer loaded on the test jig

Fig. 6.9: Experimental set up used for measuring the amplification of the signal using OTFT based differential amplifier (the wafer with the devices is mounted on the centre of the test jig and aligned with the pogo pins of the test jig through the guide card).

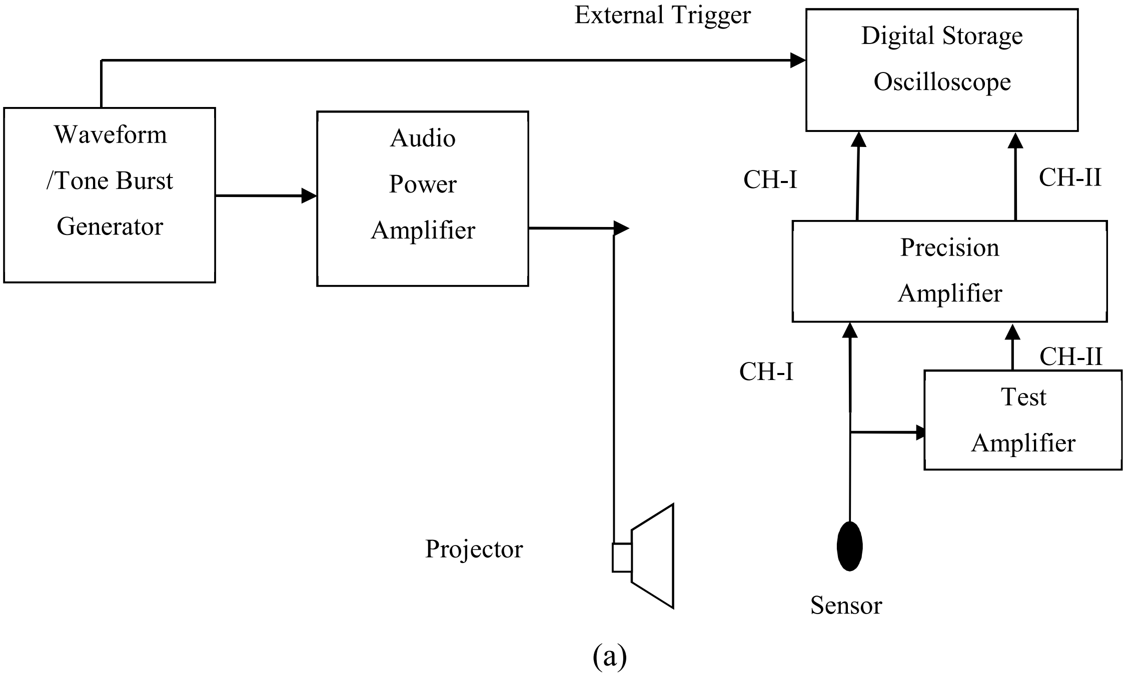

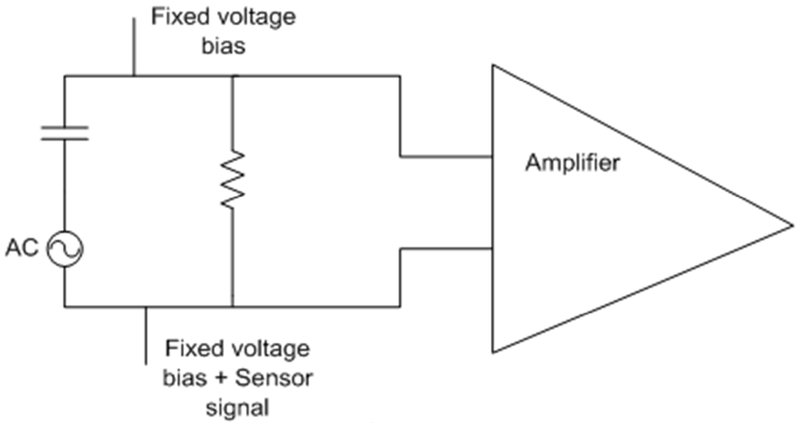

(b)

Fig. 6.10: Schematic of (a) the test set up used for the testing of amplification of acoustic signal generated from a piezoelectric sensor and (b) circuit representing the amplification of signal from the acoustic sensor.

6.3 Discussion on the Results

6.3.1 Importance of Using Wafer Probing Test Jig for Configuring the Amplifier

In this study an in-house designed wafer probing test jig was employed to select the required OTFTs from a group of 37 Nos. of discrete transistors and connect them to form a single stage differential amplifier. The connection between the test jig and the

OTFT was established using POGO pins provided on the jig. Screening of the OTFTs as switch and for their functioning at the start of the experiment, enabled to discard the devices that were non-functional or had low I_{on}/I_{off} ratio. Such devices were not included in the amplifier circuit. As independent jumpers were provided on the test jig to connect to any of the OTFTs on the 3″ wafer, they could be selected irrespective of their position on the wafer. The conventional method of taking connections from such circuits is through wire bonding. Wire bonding is a permanent process and hence, there is no possibility of discarding any non–functional TFT from a circuit. In such cases, due to the improper functioning of any one device, a whole set of 5 or more OTFTs, configured as an amplifier, would have to be discarded.

Measuring the circuit characteristics using a test jig is easier when a new set of materials have to be proven for their utility in analog or digital circuits. Establishing electrical connection through manual wire bonding is tedious and also a time consuming process. Noise characteristics of the circuit will essentially be higher when using a test jig, as the connections are established externally and the discrete OTFTs are placed far apart (≈ 1 cm) on the wafer. But, after proving the feasibility of realizing functional circuits, complete design can be made on wafer itself with connections established by wire bonding, thus minimizing the noise levels, improving the amplifier gain and bandwidth.

6.3.2 Amplifier characteristics

The response of the amplifier was studied from 100 Hz to 2 kHz. The representative response at 1 kHz and 2 kHz is shown in Figs. 6.11(a) and 6.11(b), respectively. The single stage amplifier realized with the organic TFTs exhibited a constant gain of 10 dB from 100 Hz to 1 kHz, which is the frequency band of interest for large area flexible acoustic sensors. The cut off frequency (f_c) was 1.2 kHz, where the gain dropped by 30%. Bode plot representing the voltage gain of the amplifier as a function of frequency is shown in Fig. 6.12. The gain of the amplifier was unity at 2 kHz and hence the response was not measured at further higher frequencies. Similar output was observed on feeding differential input from a piezoelectric sensor to the organic TFT based front end electronics. A flexible amplifier realized on PEN substrate, consisting of OTFTs with solution processable conducting polymer electrode, patterned by the novel parylene lift-off method is reported for the first time.

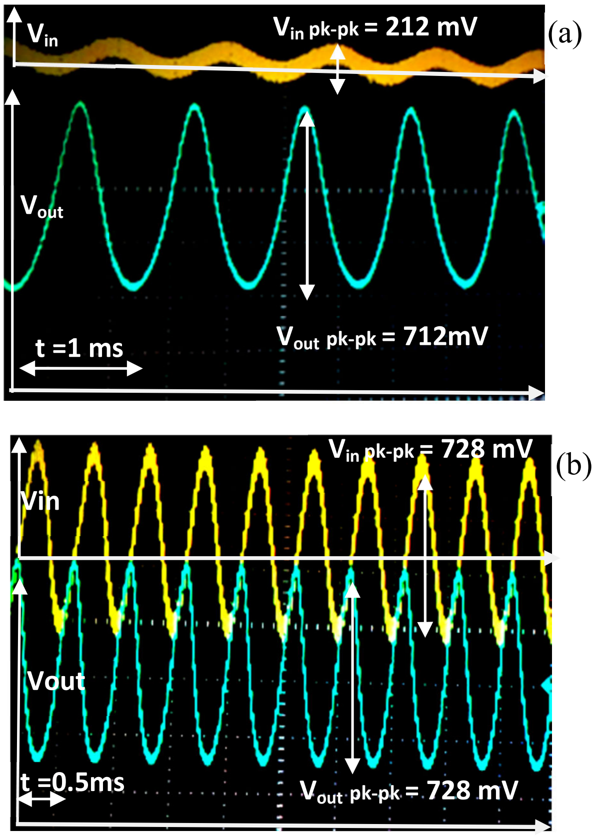

Fig. 6.11: Photograph of the input and output signal, revealing the amplification of signal at (a) 1 kHz and (b) 2 kHz.

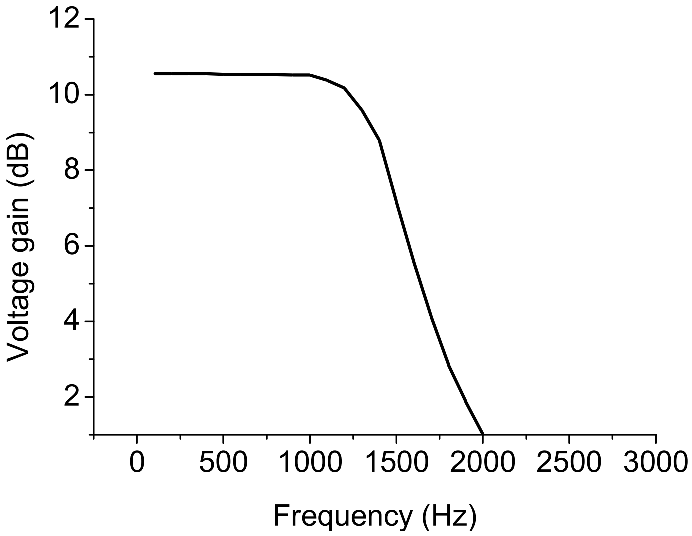

Fig. 6.12: Bode plot showing the voltage gain of the flexible OTFT amplifier as a function of frequency.

Single stage voltage gain of 10 dB and frequency bandwidth of 1 kHz has been achieved as a result of employing conducting polymer electrode, PANi-PSS with lower contact resistance and an effective passivation technique with photopatterned parylene C. PANi-PSS electrode aided in reducing the charge injection barrier in TFTs and parylene passivation protected the active semiconductor layer, pentacene from degrading and in giving a consistent amplifier response. The frequency response and the voltage gain of the amplifier remained almost constant for a period of four months, the period for which the response was monitored. The biasing circuit and interconnections have been realized in the present study with the help of an external jig. The observed voltage gain is comparatively lower than that reported with novel semiconducting materials [49]. However, the gain and bandwidth can further be increased by miniaturizing the circuit design at wafer level, fabricating the interconnections on the wafer and applying additional circuit techniques such as cascading the transistors. Reducing the size of the crossing lines thereby decreasing the parasitic capacitances and noise within the circuit can also improve the achievable single stage gain. By applying techniques to reduce the overlap capacitances between gate and drain & gate and source, the frequency response of the amplifier can be improved. The amplifiers optimized for high gain and minimum chip area are important step towards the realization of flexible electronic systems. Sensor signal amplification and analog-to-digital conversion on a flexible substrate, coupled to a flexible sensor such as acoustic sensor is highly essential for flexible electronic applications. Fabrication of flexible acoustic sensor in close proximity to the amplification circuit, enabling monolithic integration can reduce parasitics to a great extent for large area flexible sensors.

6.4 Conclusions

The method adopted for configuring the discrete TFTs fabricated on a 3″ flexible substrate as a single stage differntial amplifier has been discussed. An in-house developed wafer probing test jig was used for measuring the amplifier response of single stage differential amplifiers. Feasibility of real time sensing of acoustic signal generated by a standard piezoelectric sensor was tested with the fabricated single stage flexible differential amplifier. The flexible amplifier consisting of OTFTs with solution processable conducting polymer electrode, patterned by the novel parylene lift-off method exhibited a gain of 10 dB in a frequency bandwidth of 1 kHz. It is proposed that the gain can be further increased by miniaturizing the circuit design at wafer level and applying additional circuit techniques, including cascading the transistors.

Chapter 7

SUMMARY AND FUTURE PROSPECTS

7.1 Summary and Conclusions

High performance OTFTs are vital in major applications of organic electronics where they are utilized as flexible interface circuits in sensors. Acoustic sensing is one such application where low frequency domains are important as in the underwater sensors. The inherent challenges faced with the organic electronic circuits where operation at high frequencies is limited, is not of much concern for low frequency acoustic applications. Large area flexible piezoelectric sensors, such as the polyvinyledene fluoride based, employed for sensing acoustic signals, are characterized by low capacitance, that attenuate the input signal. The front end electronics, for buffering and amplifying the signal, if located at a remote location from the sensor, will further attenuate the signal due to the large length of the cables employed. In order to overcome the limitations of polymeric piezosensors, the interface front end electronics should be in close proximity to the sensor or be an integral part of the sensor. The thesis investigates the materials and processes for the fabrication of high performance OTFTs. The microscopic mechanism of charge transport in OTFTs has been modelled by two dimensional numerical simulations. Feasibility of employing fabricated flexible OTFTs as building blocks of interface electronics of acoustic sensors for application at low frequencies has also been studied.

The performance of OTFTs can be enhanced by judicious selection of materials and processes employed in their fabrication. An understanding of the physical mechanism of the charge transport by way of two dimensional simulations also can guide in making suitable changes in the conventional materials and processes. The field has become intriguing with the possibility of tailoring conjugated polymers and semiconductors for specific patterning methods to meet the requirements of the intended applications. The search for newer, processable materials and substrate compatible patterning methods continues with the vision of overcoming the challenges associated with the device performance and efficiency. It is imperative that a combination of vacuum processes, photolithography and solution processable patterning methods have to be suitably designed to realize OTFTs that form the components of interface electronics for acoustic sensors. Conjugated organic polymers that function as the semiconducting or conducting layer in an OTFT should be processable to be patterned as a thin film and possess optimum electrical characteristics.

Chapter 1 of the thesis gives an introduction on the recent developments in the field of organic electronics. A description on the conjugated semiconducting and conducting polymers and their performance in OTFTs is given. Operating principle of OTFTs, charge transport in organic semiconductors, application of OTFTs in sensors, patterning in conducting polymers and a brief account of importance of polyaniline is also highlighted.

PANi is a conducting polymer whose redox state can be tuned by controlling the doping level to meet the specific application requirements. The enormous number of published research papers and patents related to PANi and its composites reflect the technological significance of this conducting polymer in various fields of research and industry. In the area of organic electronics this polymer has not been explored to a large extent, owing to its limited solubility in common solvents. Solubility and porocessability of the conducting material are prerequisites for the formation of thin film in the fabrication of transistors. The subsequent patterning of the material as required by the transistor design demands dedicated fabrication processes that do not affect the other layers of the device. With the objective of increasing the processability of PANi, it was synthesized in nanostructured forms by both chemical and electrochemical methods, detailed experimental procedures of which is given in **Chapter 2**.

The conductivity, solution processability, quality of thin film and patternability were the criteria considered for choosing the most appropriate method of synthesis of PANi. Initially PANi was synthesized by the method of conventional chemical oxidative polymerization. Though the method resulted in nanostructured PANi, at the initial stages of synthesis, but as the reaction progressed, the polymer nanofibers became scaffolds for secondary growth of polyaniline and finally turned into irregularly shaped agglomerates containing nanofibers and particulates. Other chemical methods such as dilute polymerization by reducing the ratio of monomer to dopant acid and interfacial polymerization allowing the polymerization to be initiated at the interface between aqueous and organic phase, were also adopted to synthesize nanostructured PANi. In the electrochemical methods, template polymerization inside the pores of gold coated polycarbonate track etched membrane and step galvanostatic method (SGM) were employed to control the morphology of synthesized PANi. Dilute polymerization and the interfacial method resulted in nannofiber growth, but the uniformity and prevention of agglomeration could not be controlled. Electrochemical template polymerization resulted in uniform nanofibers but the retrieval of the synthesized polymer was difficult after the separation of gold of the membrane. Water dispersible nanostructured conducting PANi-PSS composite for patterning as electrodes of OTFT was synthesized by bulk polymerization of aniline templated with polystyrene sulphonic acid. The PANi:PSS ratio and concentration of precursor acid during the synthesis were controlled so as to obtain conducting polymer samples with optimum conductivity and dispersibility. Regioregular poly(3-alkylthiophene) in copolymer structure, PHT-b-PBA, was synthesized to improve its mechanical properties when casted as thin film of semiconductor in the fabrication of OTFT.

Chapter 3 discusses the analysis of synthesized polymers with respect to structure, morphology, conductivity and electrochemical properties. The synthesized PANi based conducting polymers and the semiconducting polymer, PHT-b-PBA were characterized for their suitability to be employed as the conducting and semiconducting channel layer, respectively, of OTFT. To summarize the results, controlling the structure of the nanofibers could be possible with the SGM. At a reduced concentration of both monomer and dopant acid, the sample NP4, with diameter less than 80 nm could be synthesized. CSA doped NP4 also resulted in smooth film when casted from the secondary dopant and solvent, m-cresol. One of the samples of PANi-PSS (PSN3-3), with an average particle size of 20 nm was found optimum for device fabrication as it formed very stable dispersion (stability maintained even after storing for months) and had a conductivity of 0.62 ± 0.05 S/cm, which was further increased to 54 ± 6.0 S/cm on secondary doping with DCA. The observed conductivity is one of the highest reported for a processable conducting polymer. NP4 and PSN3-3 were selected from the synthesized conducting polymers to be patterned as the source and drain electrodes of OTFT.

Chapter 4 elaborates the methodologies adopted in the fabrication of OTFTs. The commercially available small molecule, pentacene and synthesized PHT-b-PBA were employed as semiconducting layer in the OTFTs in this study. Pentacene deposited by low temperature thermal evaporation at high vacuum, was found to give a better performance as compared to the spin coated, polymeric semiconductor. An effective fabrication process was developed for the simultaneous passivation and patterning of the semiconducting channel with parylene C, that increased the operational life time of the fabricated TFTs. Photopatterned layer of parylene could effectively protect the organic device and offer superior barrier properties when compared to the conventional passivation techniques with the use of water based PVA. Thus, the off current was reduced by about two orders of magnitude in the parylene C passivated devices thereby increasing the I_{on}/I_{off} ratio. In this method, effective patterning of the semiconductor layer and hence, isolation of transistors on the substrate could also be achieved, which is critical for circuit implementation.

Of the various conducting polymers studied, the composite, PANi-PSS was found to overcome the shortcomings with non-ohmic nature of metal electrode. PANi-PSS composite and metal electrode, Pd were studied as the conducting source and drain electrode of the OTFT. With PANi-PSS, the electrodes were fabricated by a modified parylene lift-off process and a resolution of 5 μm could be achieved by this method. Non-linearity, which is a direct consequence of the higher contact resistance, was absent in the case of devices with PAN-PSS electrodes employed for hole injection. The determined field effect mobility with PANi-PSS electrode is 0.5 cm^2/Vs and threshold voltage of 3.2 V, whereas with Pd electrode, the calculated mobility is 0.9 cm^2/Vs and threshold voltage of 7.4 V. The contact resistance of the fabricated devices were extracted by Transfer Line Method (TLM). The shortcomings with non-ohmic nature of Pd metal electrode that leads to higher contact resistance were overcome by the use of PANi-PSS conducting polymer electrode. Electrical characteristics of OTFT fabricated with solution processable PHT-b-PBA, semiconductor and PANi-PSS conducting polymer was also studied. Saturation field effect mobility of 4.82×10^{-2} cm^2/Vs is achieved with the solution processable semiconductor, which is one order less than that achieved with vacuum evaporated pentacene.

The electrical characteristics of OTFTs have been modelled by physics based two dimensional numerical simulation and the results presented in **Chapter 5**. The lower contact resistance (two order less) with the conducting polymer electrode was found to be as a result of higher charge concentration and lower charge injection barrier at the conducting polymer–semiconductor interface when compared to a metal–semiconductor interface. The simulation was performed by incorporating parameters for low mobility layer, shifted electron affinity, increased thermal activation energy at electrode–semiconductor interface, trap density and fixed charge density at the semiconductor–insulator interface. The modelling could reproduce the whole output characteristics of the devices with both metal and PANi-PSS electrodes, in subthreshold, linear and saturation regime with good agreement to experimental characteristics. The 2D simulation tool can hence, be employed in the design of organic transistors with new combinations of semiconductor and conducting polymer electrodes.

The OTFTs with the optimum field effect characteristics on a 3″ flexible substrate were configured as a differential amplifier to study the achievable voltage gain for application in sensing of acoustic signals at low frequencies, and the results elaborated in **Chapter 6**. The testing of OTFT based amplifier was performed using an in house fabricated wafer probing test jig. A single stage flexible differential amplifier consisting of OTFTs with different aspect ratio exhibited a gain of 10 dB in a frequency bandwidth of 1 kHz. The capability of sensing low frequency acoustic signals by OTFT based amplifier was thus proven. Hence, the studies in the thesis conclude that an intelligent choice of materials and processes for the fabrication of OTFTs can lead to the realization of consistent organic electronic circuits.

In conclusion, the developed method for synthesizing nanostructured PANi-PSS composite and patterning it as electrodes in an OTFT with such a high resolution is a technological advancement in the field of organic electronics. Hence, the choice of materials and processes in the fabrication of OTFTs, should consider the application it is intended for and best possible combination of vacuum and solution processes should be employed in order to achieve maximum possible performance. OTFTs fabricated with solution processable conducting polymer electrode, PANi-PSS, parylene C passivated semiconducting channel, processes such as parylene lift-off method and an insight into the physical mechanism of charge transport by way of two dimensional numerical simulation have contributed in achieving OTFTs for organic electronic circuits for application in sensing of acoustic signals.

7.2 Future Prospects

The present study affords scope for further investigations, suitable improvements and futuristic developments to realize high performance organic electronic devices. Scope of future work in this area may pertain to advancements in materials, processes and end products. To further improve the electrical characteristics of the OTFT, semiconducting polymers with enhanced crystallinity can be utilized. Such emerging polymeric semiconductors can be deposited by a solution processable method, which will be advantageous for fabrication of large area organic electronic circuits and sensors. To enhance the performance of the conducting polymers, new conducting polymer-secondary dopant system with high solution processability, could be researched. The parylene lift-off method, established in the present study can be utilized for patterning such conducting polymer systems, as electrodes in OTFTs and shall further reduce the charge injection barrier and contact resistance in devices. Attempts could be made for monolithic integration of acoustic sensors and high performance organic electronic circuits for realizing ‘on-chip signal transduction and amplification’. A combination of *p* and *n*-type semiconducting materials is required to make CMOS like electronic circuits for the purpose. However, concurrent fabrication of *p* and *n*-type semiconductor based OTFT is highly challenging and process intensive. Semiconducting materials that exhibit both *p* and *n*- type characteristics can also be researched and utilized for the realization of CMOS like circuits. The fabrication processes involved with such ambipolar molecules will be less complicated than with different kinds of semiconducting materials on same substrate. The achievable amplification in sensor applications with such devices would be immensely high.

REFERENCES

[1]. S. R. Forrest, The path to ubiquitous and low-cost organic electronic appliances on plastic, Nature 428 (2004) 911–918.

[2]. H. Sirringhaus, 25th anniversary article: Organic field-effect transistors: The path beyond amorphous silicon, Adv. Mater. 26 (2014) 1319–1335.

[3]. C. W. Tang, S. A. Van Slyke, Organic electroluminescent diodes, Appl. Phys. Lett. 51 (1987) 913–915.

[4]. J. H. Burroughes, D. D. C. Bradley, A. R. Brown, R. N. Marks, K. Mackay, R. H. Friend, P. L. Burn, A. B. Holmes, Light-emitting diodes based on conjugated polymers, Nature 347 (1990) 539–541.

[5]. M. –H. Park, T. –H. Han, Y. –H. Kim, S. –H. Jeong, Y. Lee, H. –K. Seo, H. Cho, T. –W. Lee, Flexible organic light-emitting diodes for solid-state lighting, J. Photon. Energy 5 (2015) 053599 (21 pp).

[6]. K. Müllen, U. Scherf, Organic light emitting devices: Synthesis, properties and applications, Wiley-VCH, Weinheim, (2006) pp 35–94.

[7]. R. –P. Xu, Y. –Q. Li, J. –X. Tang, Recent advances in flexible organic light-emitting diodes, J. Mater. Chem. C 4 (2016) 9116–9142.

[8]. A. Goetzberger, C. Hebling, H. –W. Schock, Photovoltaic materials, history, status and outlook, Mater. Sci. Eng. R Rep. 40 (2003) 1–46.

[9]. T. M. Tong, J. Asare, E. R. Rwenyagila, V. Anye, O. K. Oyewole, A. A. Fashina, W. O. Soboyejo, A study of factors that influence the adoption of solar powered lanterns in a rural village in Kenya, Perspectives on Global Development and Technology 14 (2015) 448–491.

[10]. C. Lu, Z. Ji, G. Xu, W. Wang, L. Wang, Z. Han, L. Li, M. Liu, Progress in flexible organic thin-film transistors and integrated circuits, Sci. Bull. 61 (2016) 1081–1096.

[11]. C. R. Newman, C. D. Frisbie, D. A. d. S. Filho, J. –L. Bredas, P. C. Ewbank, K. R. Mann, Introduction to organic thin film transistors and design of n-channel organic semiconductors, Chem. Mater. 16 (2004) 4436–4451.

[12]. A. S. Sedra, K. C. Smith, Microelectronic circuits (Fifth Ed.), Oxford University Press, New York, (2004) pp 235–274.

[13]. A. Tsumura, H. Koezuka, T. Ando, Macromolecular electronic device: Field-effect transistor with a polythiophene thin film, Appl. Phys. Lett. 49 (1986) 1210–1212.

[14]. H. Klauk, Organic thin-film transistors, Chem. Soc. Rev. 39 (2010) 2643–2666.

[15]. C. D. Dimitrakopoulos, D. J. Mascaro, Organic thin-film transistors: A review of recent advances, IBM J. Res. Dev. 45 (2001) 11–27.

[16]. X. Guo, Y. Xu, S. Ogier, T. N. Ng, M. Caironi, A. Perinot, L. Li, J. Zhao, W. Tang, R. A. Sporea, A. Nejim, J. Carrabina, P. Cain, F. Yan, Current status and opportunities of organic thin film transistor technologies, IEEE Trans. Electron Devices 64 (2017) 1906–1921.

[17]. U. Zschieschang, H. Klauk, Low-voltage organic transistors with steep subthreshold slope fabricated on commercially available paper, Org. Electron. 25 (2015) 340–344.

[18]. Y. –Y. Lin, D. J. Gundlach, S. Nelson, T. N. Jackson, Pentacene-based organic thin-film transistors, IEEE Trans. Electron Devices 44 (1997) 1325–1331.

[19]. F. Garnier, A. Yassar, R. Hajlaoui, G. Horowitz, F. Dellofre, B. Servet, S. Ries, P. Alnot, Molecular engineering of organic semiconductors: Design of self-assembly properties in conjugated thiophene oligomers, J. Am. Chem. Soc. 115 (1993) 8716–8721.

[20]. M. Yamagishi, J. Takeya, Y. Tominari, Y. Nakazawa, T. Kuroda, S. Ikehata, M. Uno, T. Nishikawa, T. Kawase, High-mobility double-gate organic single-crystal transistors with organic crystal gate insulators, Appl. Phys. Lett. 90 (2007) 182117 (3 pp).

[21]. Z. Bao, A. Dodabalapur, A. J. Lovinger, Soluble and processable regioregular poly(3-hexylthiophene) for thin film field-effect transistor applications with high mobility, Appl. Phys. Lett. 69 (1996) 4108–4110.

[22]. J. Li, Y. Zhao, H. S. Tan, Y. Guo, C. –A. Di, G. Yu, Y. Liu, M. Lin, S. H. Lim, Y. Zhou, H. Su, B. S. Ong, A stable solution-processed polymer semiconductor with record high-mobility for printed transistors, Sci. Rep. 2 (2012) 754 (9 pp).

[23]. J. Choi, H. Song, N. Kim, F. S. Kim, Development of *n*-type polymer semiconductors for organic field-effect transistors, Semicond. Sci. Technol. 30 (2015) 064002 (16 pp).

[24]. M. J. Malachowsk, J. Zmija, Organic field effect transistors, Opto-Electron. Rev. 18 (2010) 121–136.

[25]. J. Puigdollers, C. Voz, I. Martin, A. Orpella, M. Vetter, R. Alcubilla, Pentacene thin film transistors on polymeric gate dielectric: Device fabrication and electrical characterization, J. Non-Cryst. Solids 338–340 (2004) 617–621.

[26]. R. P. Ortiz, A. Facchetti, T. J. Marks, High-k organic, inorganic and hybrid dielectrics for low-voltage organic field-effect transistors, Chem. Rev. 110 (2010) 205–239.

[27]. S. –W. Rhee D. –J. Yun, Metal-semiconductor contact in organic thin film transistors, J. Mater. Chem. 18 (2008) 5437–5444.

[28]. J. A. Nichols, D. J. Gundlach, T. N. Jackson, Potential imaging of pentacene organic thin-film transistors, Appl. Phys. Lett. 83 (2003) 2366–2368.

[29]. N. Koch, A. Kahn, J. Ghijsen, J. J. Pireaux, J. Schwartz, R. L. Johnson, A. Elschner, Conjugated organic molecules on metal versus polymer electrodes: Demonstration of a key energy level alignment mechanism, Appl. Phys. Lett. 82 (2003) 70–72.

[30]. H. W. Zan, K. H Yen, Vertical-channel organic thin-film transistors with meshed electrode and low leakage current, Jpn. J. Appl. Phys. 46 (2007) 3315–3318.

[31]. M. Y. Lee, H. J. Kim, G. Y. Jung, A. R. Han, S. K. Kwak, B. J. Kim, J. H. Oh, Highly sensitive and selective liquid-phase sensors based on a solvent-resistant organic-transistor platform, Adv. Mater. 27 (2015) 1540–1546.

[32]. C. Zhang, P. Chen, W. Hu, Organic field-effect transistor-based gas sensors, Chem. Soc. Rev. 44 (2015) 2087–2107.

[33]. P. Lin, F. Yan, Organic thin-film transistors for chemical and biological sensing, Adv. Mater. 24 (2012) 34–51.

[34]. S. C. B. Mannsfeld, B. C. –K. Tee, R. M. Stoltenberg, C. V. H. –H. Chen, S. Barman, B. V. O. Muir, A. N. Sokolov, C. Reese, Z. Bao, Highly sensitive flexible pressure sensors with microstructured rubber dielectric layers, Nat. Mater. 9 (2010) 859–864.

[35]. J. Kim, T. N. Ng, W. S. Kim, Highly sensitive tactile sensors integrated with organic transistors, Appl. Phys. Lett. 101 (2012) 103308 (5 pp).

[36]. T. Sekitani, Y. Kato, S. Iba, H. Shinaoka, T. Someya, T. Sakurai, S. Takagi, Bending experiment on pentacene field-effect transistors on plastic films, Appl. Phys. Lett. 86 (2005) 073511 (3 pp).

[37]. P. Cosseddu, G. Tiddia, S. Milita, A. Bonfiglio, Continuous tuning of the mechanical sensitivity of pentacene OTFTs on flexible substrates: From strain sensors to deformable transistors, Org. Electron. 14 (2013) 206–211.

[38]. T. Someya, Y. Kato, T. Sekitani, S. Iba, Y. Noguchi, Y. Murase, H. Kawaguchi, T. Sakurai, Conformable, flexible, large-area networks of pressure and thermal sensors with organic transistor active matrixes, Proc. Nat. Acad. Sci. 102 (2005) 12321–12325.

[39]. Y. Zhao, Y. Guo, Y. Liu, 25th anniversary article: Recent advances in *n*-type and ambipolar organic field-effect transistors, Adv. Mater. 25 (2013) 5372–5391.

[40]. W. Smaal, C. Kjellander, Y. Jeong, A. Tripathi, B. V. D. Putten, A. Facchetti, H. Yan, J. Quinn, J. Anthony, K. Myny, W. Dehaene, G. Gelinck, Complementary integrated circuits on plastic foil using inkjet printed *n*- and *p*-type organic semiconductors: Fabrication, characterization, and circuit analysis, Org. Electron. 13 (2012) 1686–1692.

[41]. U. Zschieschang, R. Hofmockel, R. Rödel, U. Kraft, M. J. Kang, K. Takimiya, T. Zaki, F. Letzkus, J. Butschke, H. Richter, J. N. Burghartz, H. Klauk, Megahertz operation of flexible low-voltage organic thin-film transistors, Org. Electron. 14 (2013) 1516–1520.

[42]. A. R. Brown, A. Pomp, C. M. Hart, D. M. de Leeuw, Logic gates made from polymer transistors and their use in ring oscillators, Science 270 (1995) 972–974.

[43]. C. J. Drury, C. M. J. Mutsaers, C. M. Hart, M. Matters, D. M. de Leeuw, Low-cost all polymer integrated circuits, Appl. Phys. Lett. 73 (1998) 108–110.

[44]. U. Zschieschang, M. J. Kang, K. Takimiya, T. Sekitani, T. Someya, T. W. Canzler, A. Werner, J. B. –Nimoth, H. Klauk, Flexible low-voltage organic thin-film transistors and circuits based on C_{10}-DNTT, J. Mater. Chem. 22 (2012) 4273–4277.

[45]. G. Maiellaro, E. Ragonese, A. Castorina, S. Jacob, M. Benwadih, R. Coppard, E. Cantatore, G. Palmisano, High-gain operational transconductance amplifiers in a printed complementary organic TFT technology on flexible foil, IEEE Trans. Circuits Syst. I, Reg. Papers 60 (2013) 3117–3125.

[46]. H. Marien, M. Steyaert, E. van Veenendaal, P. Heremans, DC-DC converter assisted two-stage amplifier in organic thin-film transistor technology on foil, in Proc. of the 37th European Solid-State Circuits Conference, Finland, Sep 2011, 411– 414.

[47]. D. M. Binkley, N. Verma, R. L. Crawford, E. Brandon, T. N. Jackson, Design of an autozeroed, organic thin-film field-effect transistor amplifier for sensor applications, in Proc. of SPIE – The Int. Soc. for Opt. Eng. Colorado, 5522 (2004) 41–52.

[48]. J. Chang, X. Zhang, T. Ge, J. Zhou, Fully printed electronics on flexible substrates: High gain amplifiers and DAC, Org. Electron. 15 (2014) 701–710.

[49]. A. Reuveny, S. Lee, T. Yokota, H. Fuketa, C. M. Siket, S. Lee, T. Sekitani, T. Sakurai, S. Bauer, T. Someya, High-frequency, conformable organic amplifiers, Adv. Mater. 28 (2016) 3298–3304.

[50]. H. Marien, M. Steyaert, E. van Veenendaal, P. Heremans, Analog techniques for reliable organic circuit design on foil applied to an 18 dB single-stage differential amplifier, Org. Electron. 11 (2010) 1357–1362.

[51]. T. Someya, T. Sekitani, S. Iba, Y. Kato, H. Kawaguchi, T. Sakurai, A large-area, flexible pressure sensor matrix with organic field-effect transistors for artificial skin applications, Proc. Natl. Acad. Sci. U.S.A. 101 (2004) 9966–9970.

[52]. W. Olthuis, Chemical and physical FET-based sensors or variations on an equation, Sens. Actuat. B 105 (2005) 96–103.

[53]. G. Schwartz, B. C. –K. Tee, J. Mei, A. L. Appleton, D. H. Kim, H. Wang, Z. Bao, Flexible polymer transistors with high pressure sensitivity for application in electronic skin and health monitoring, Nat. Commun. 4 (2013) 1859–1859.

[54]. M. E. Roberts, S. C. B. Mannsfeld, N. Queraltó, C. Reese, J. Locklin, W. Knoll, Z. Bao, Water-stable organic transistors and their application in chemical and biological sensors, Proc. Natl. Acad. Sci. U.S.A. 105 (2008) 12134–12139.

[55]. Y. Zang, F. Zhang, D. Huang, X. Gao, C. Di, D. Zhu, Flexible suspended gate organic thin-film transistors for ultra-sensitive pressure detection, Nat. Commun. 6 (2015) 6269 (9 pp).

[56]. I. Graz, M. Kaltenbrunner, C. Keplinger, R. Schwödiauer, S. Bauer, S. P. Lacour, S. Wagner, Flexible ferroelectret field-effect transistor for large-area sensor skins and microphones, Appl. Phys. Lett. 89 (2006) 073501 (3 pp).

[57]. I. Graz , M. Krause, S. B. Gogonea, S. Bauer, S. P Lacour, B. Ploss, M. Zirkl, B. Stadlober, S. Wagner, Flexible active-matrix cells with selectively poled bifunctional polymer-ceramic nanocomposite for pressure and temperature sensing skin, J. Appl. Phys. 106 (2009) 034503 (5 pp).

[58]. T. Ji, M. Kathiresan, S. Nair, S. Jung, V. Natarajan, R. M. R. Vishnubhatla, V. K. Varadan, Design and fabrication of OTFT based flexible piezoelectric sensor, in Proc. SPIE—Nanosensors, Microsensors, and Biosensors and Systems, San Diego, CA, 6528 (2007) 65281P-6.

[59]. Y. –J. Hsu, Z. Jia, I. Kymissis, A locally amplified strain sensor based on a piezoelectric polymer and organic field-effect transistors, IEEE Trans. Electron Devices 58 (2011) 910-917.

[60]. H. Shirakawa, E. J. Louis, A. G. Macdiarmid, C. K. Chiang, A. J. Heeger, Synthesis of electrically conducting organic polymers: Halogen derivatives of polyacetylene, $(CH)_x$, J. Chem. Soc. Chem. Commun. 0 (1977) 578–580.

[61]. R. Farchioni, G. Grosso, Organic electronic materials: Conjugated polymers and low molecular weight organic solids, Springer, Berlin, (2001) pp 39–87.

[62]. L. S. Miller, J. B. Mullin, Electronic Materials: From silicon to organics, Plenum Press, New York, (1991) pp 143–154.

[63]. J. H. Schön, C. Kloc, B. Batlogg, On the intrinsic limits of pentacene field-effect transistors, Org. Electron. 1 (2000) 57–64.

[64]. M. Bronner, A. Opitz, W. Brütting, Ambipolar charge carrier transport in organic semiconductor blends of phthalocyanine and fullerene, Phys. Stat. Sol. A 205 (2008) 549–563.

[65]. H. Klauk, M. Halik, U. Zschieschang, G. Schmid, W. Radlik, W. Weber, High-mobility polymer gate dielectric pentacene thin film transistors, J. Appl. Phys. 92 (2002) 5259–5263.

[66]. S. K. Park, T. N. Jackson, J. E. Anthony, D. A. Mourey, High mobility solution processed 6,13-bis(triisopropyl-silylethynyl) pentacene organic thin film transistors, Appl. Phys. Lett. 91 (2007) 063514 (3 pp).

[67]. G. Giri, E. Verploegen, S. C. B. Mannsfeld, S. A. –Evrenk, D. H. Kim, S. Y. Lee, H. A. Becerril, A. A. –Guzik, M. F. Toney, Z. Bao, Tuning charge transport in solution-sheared organic semiconductors using lattice strain, Nature 480 (2011) 504–508.

[68]. Y. Yuan, G. Giri, A. L. Ayzner, A. P. Zoombelt, S. C. B. Mannsfeld, J. Chen, D. Nordlund, M. F. Toney, J. Huang, Z. Bao, Ultra-high mobility transparent organic thin film transistors grown by an off-centre spin-coating method, Nat. Commun. 5 (2014) 3005 (9 pp).

[69]. Z. Bao, A. J. Lovinger, J. Brown, New air-stable *n*-channel organic thin film transistors, J. Amer. Chem. Soc. 120 (1998) 207–208.

[70]. S. Tatemichi, M. Ichikawa, T. Koyama, Y. Taniguchi., High mobility *n*-type thin-film transistors based on N, N′-ditridecyl perylene diimide with thermal treatments, Appl. Phys. Lett. 89 (2006) 112108 (3 pp).

[71]. A. Assadi, C. Svensson, M. Willander, O. Inganäs, Field-effect mobility of poly(3-hexylthiophene), Appl. Phys. Lett. 53 (1988) 195–197.

[72]. S. R. Mane, S. Sarkar, V. N. Rao, A. Sathyan, R. Shunmugam, Efficient method to prepare a new class of regioregular graft copolymer via click chemistry approach, RSC Adv. 5 (2015) 74159–741561.

[73]. B. H. Hamadani, D. J. Gundlach, I. McCulloch, M. Heeney, Undoped polythiophene field-effect transistors with mobility of 1 cm^2/Vs, Appl. Phys. Lett. 91 (2007) 243512 (3 pp).

[74]. Z. Chen, M. J. Lee, S. R. Ashraf, Y. Gu, S. A. –Seifried, M. M. Nielsen, B. Schroeder, T. D. Anthopoulos, M. Heeney, I. McCulloch, H. Sirringhaus, High-performance ambipolar diketopyrrolopyrrole thieno 3,2-b]thiophene copolymer field-effect transistors with balanced hole and electron mobilities, Adv. Mater. 24 (2012) 647–652.

[75]. J. Zaumseil, H. Sirringhaus, Electron and ambipolar transport in organic field-effect transistors, Chem. Rev. 107 (2007) 1296–1323.

[76]. D. Venkateshvaran, M. Nikolka, A. Sadhanala, V. Lemaur, M. Zelazny, M. Kepa, M. Hurhangee, A. J. Kronemeijer, V. Pecunia, I. Nasrallah, I. Romanov, K. Broch, I. McCulloch, D. Emin, Y. Olivier, J. Cornil, D. Beljonne, H. Sirringhaus, Approaching disorder-free transport in high mobility conjugated polymers, Nature 515 (2014) 384–388.

[77]. G. Horowitz, Organic thin film transistors: From theory to real devices, J. Mater. Res. 19 (2004) 1946–1962.

[78]. A. Troisi, Charge transport in high mobility molecular semiconductors: Classical models and new theories, Chem. Soc. Rev. 40 (2011) 2347–2358.

[79]. H. J. Ding, C. Reese, A. J. Makinen, Z. A. Bao, Y. L. Gao, Band structure measurement of organic single crystal with angle-resolved photoemission, Appl. Phys. Lett. 96 (2010) 222106 (3 pp).

[80]. S. Ciuchi, R. C. Hatch, H. Höchst, C. Faber, X. Blasé, S. Fratini, Molecular fingerprints in the electronic properties of crystalline organic semiconductors: From experiment to theory, Phys. Rev. Lett. 108 (2012) 256401 (5 pp).

[81]. C. D. Dimitrakopoulos, P. R. L. Malenfant, Organic thin film transistors for large area electronics, Adv. Mater. 14 (2002) 99–117.

[82]. P. Servati, A. Nathan, G. A. J. Amaratunga, Generalized transport-band field-effect mobility in disordered organic and inorganic semiconductors, Phys. Rev. B. 74 (2006) 245210 (7 pp).

[83]. M. C. J. M. Vissenberg, M. Matters, Theory of the field-effect mobility in amorphous organic transistors, Phys. Rev. B 57 (1998) 12964–12967.

[84]. V. Coropceanu, J. Cornil, D. A. da Silva Filho, Y. Olivier, R. Silbey, J. –L. Brédas, Charge Transport in Organic Semiconductors, Chem. Rev. 107 (2007) 926–952.

[85]. A. Facchetti, π-Conjugated polymers for organic electronics and photovoltaic cell applications, Chem. Mater. 23 (2011) 733–758.

[86]. J. Deng, X. Wang, J. Guo, P. Liu, Effect of the oxidant/monomer ratio and the washing post-treatment on electrochemical properties of conductive polymers, Ind. Eng. Chem. Res. 53 (2014) 13680–13689.

[87]. W. Feng, A. S. Wan, E. Garfunkel, Interfacial bonding and morphological control of electropolymerized polythiophene films on ZnO, J. Phys. Chem. C 117 (2013) 9852–9863.

[88]. C. Janáky, W. Chanmanee, K. Rajeshwar, Mechanistic aspects of photoelectrochemical polymerization of polypyrrole on a TiO_2 nanotube array, Electrochim. Acta 122 (2014) 303–309.

[89]. E. Mazzotta, S. Surdo, C. Malitesta, G. Barillaro, High-aspect-ratio conducting polymer microtube synthesis by light-activated electropolymerization on microstructured silicon, Electrochem. Commun. 35 (2013) 12–16.

[90]. A. G. MacDiarmid, Synthetic metals: A novel role for organic polymers, Curr. Appl. Phys. 1 (2001) 269–279.

[91]. G. G. Wallace, P. R Teasdale, G. M. Spinks, A. P. K. –Maguire, Conductive electroactive polymers, intelligent materials systems (Second Ed.), CRC Press, London, (2002) pp 161–175.

[92]. S. –I. Na, S. –S. Kim, J. Jo, D. –Y. Kim, Efficient and flexible ITO-free organic solar cells using highly conductive polymer anodes, Adv. Mater. 20 (2008) 4061–4067.

[93]. W. H. Kim, A. J. Makinen, N. Nikolov, R. Shashidhar, H. Kim, Z. H. Kafaf, Molecular organic light-emitting diodes using highly conducting polymers as anodes, Appl. Phys. Lett. 80 (2002) 3844–3846.

[94]. J. Ouyang, Q. Xua , C. –W. Chua, Y. Yang, G. Li , J. Shinar, On the mechanism of conductivity enhancement in poly(3,4-ethylenedioxythiophene):poly(styrene sulfonate) film through solvent treatment, Polymer 45 (2004) 8443–8450.

[95]. M. Angelopoulos, N. Patel, J. M. Shaw, N. C. Labianca, S. A. J. Rishton, Water soluble conducting polyanilines: Applications in lithography, J. Vac. Sci. Technol. B 11 (1993) 2794–2797.

[96]. M. Halik, H. Klauk, U. Zschieschang, G. Schmid, W. Radlik, W. Weber, Polymer gate dielectrics and conducting-polymer contacts for high-performance organic thin-film transistors. Adv. Mater. 14 (2002) 1717–1722.

[97]. G. H. Gelinck, T. C. T. Geuns, D. M. de Leeuw, High-performance all-polymer integrated circuits. Appl. Phys. Lett. 77 (2000) 1487–1489.

[98]. F. Garnier, R. Hajlaoui, A. Yassar, P. Srivastava, All-polymer field-effect transistor realized by printing techniques, Science 265 (1994) 1684–1686.

[99]. W. J. Hyun, E. B. Secor, M. C. Hersam, C. D. Frisbie, L. F. Francis, High-resolution patterning of graphene by screen printing with a silicon stencil for highly flexible printed electronics, Adv. Mater. 27 (2014) 109–115.

[100]. R. Parashkov, E. Becker, T. Riedl, H. –H. Johannes, W. Kowalsky, Microcontact printing as a versatile tool for patterning organic field-effect transistors, Adv. Mater. 17 (2005) 1523–1527.

[101]. J. Z. Wang, Z. H. Zheng, H. W. Li, W. T. S. Huck, H. Sirringhaus, Dewetting of conducting polymer inkjet droplets on patterned surfaces, Nat. Mater. 3 (2004) 171–176.

[102]. C. W. Sele, T. von Werne, R. H. Friend, H. Sirringhaus, Lithography-free, self-aligned inkjet printing with sub-hundred- nanometer resolution, Adv. Mater. 17 (2005) 997–1001.

[103]. W. Xu, Z. Hu, H. Liu, L. Lan, J. Peng, J. Wang, Y. Cao, Flexible all-organic, all-solution processed thin film transistor array with ultrashort channel, Sci. Rep. 6 (2016) 29055 (7 pp).

[104]. S. Takamatsu, T. Takahata, K. Matsumoto, I. Shimoyama, Micro-patterning of a conductive polymer and an insulation polymer using the parylene lift-off method for electrochromic displays, J. Micromech. Microeng. 21 (2011) 075021 (6 pp).

[105]. S. Nair, M. Kathiresan, T. Mukundan, Patterned water dispersible conducting polymer electrode in organic thin film transistor through a parylene lift-off process, Synth. Met. 234 (2017) 29–37.

[106]. J. Stejskal, Polyaniline: Preparation of a conducting polymer, Pure Appl. Chem. 74 (2002) 857–867.

[107]. K. Molapo, P. M. Ndangili, R. F. Ajayi, G. Mbambisa, S. M. Mailu, N. Njomo, M. Masikini, P. Baker, E. I. Iwuoha, Electronics of Conjugated Polymers (I): Polyaniline, Int. J. Electrochem. Sci. 7 (2012) 11859–11875.

[108]. Z. Boeva, V. G. Sergeyev, Polyaniline: Synthesis, properties, and application, Polym. Sci. Ser. C 56 (2014) 144–153.

[109]. S. H. Lee, D. H. Lee, K. Lee, C. W. Lee, High-performance polyaniline prepared via polymerization in a self-stabilized dispersion, Adv. Funct. Mater. 15 (2005) 1495–1500.

[110]. A. G. MacDiarmid, A. J. Epstein, Polyanilines: A novel class of conducting polymers, Faraday Discuss. Chem. Soc. 88 (1989) 317–332.

[111]. G. Wang, R. Vivek, J. –Y. Wang, Polyaniline nanoparticles: Synthesis, dispersion and biomedical applications, Mini Rev. Org. Chem. 14 (2017) 56–64.

[112]. O. Abdulrazzaq, S. E. Bourdo, V. Saini, F. Watanabe, B. Barnes, A. Ghosh, A. S. Birisa, Tuning the work function of polyaniline via camphorsulfonic acid: An x-ray photoelectron spectroscopy investigation, RSC Adv. 5 (2015) 33–40.

[113]. S. Nair, R. Rajeswari, V. Natarajan, T. Mukundan, Concentration-dependent growth and morphology of doped polyaniline nanowires, J. Exp. Nanosci. 9 (2014) 982–993.

[114]. M. C. Iovu, R. Zhang, J. R. Cooper, D. M. Smilgies, A. E. Javier, E. E. Sheina, T. Kowalewski, R. D. McCullough, Conducting block copolymers of regioregular poly(3-hexylthiophene) and poly(methacrylates): Electronic materials with variable conductivities and degrees of interfibrillar order, Macromol. Rapid Commun. 28 (2007) 1816–1824.

[115]. M. C. Iovu, M. Jeffries-EL, E. E. Sheina, J. R. Cooper, R. D. McCullough, Regioregular poly(3-alkylthiophene) conducting block copolymers, Polymer 46 (2005) 8582–8586.

[116]. P. R. Griffiths, J. A. de Haseth, J. D. Winefordner, Fourier transform infrared spectrometry (Second Ed.), Wiley, New York, (2007) pp 19–55.

[117]. R. S. Mulliken, Intensities of electronic transitions in molecular spectra VII. Conjugated polyenes and carotenoids, J. Chem. Phy. 7 (1939) 364–373.

[118]. A. O. Patil, A. J. Heeger, F. Wudl, Optical properties of conducting polymers, Chem. Rev. 88 (1988) 183–200.

[119]. R. K. Harris, Nuclear magnetic resonance spectroscopy, Longman Publishing Group, London, (1983).

[120]. B. D. Cullity, Elements of X-ray diffraction (Second Ed.), Addison-Wesley Publishing Company, Inc., Massachusetts, (1978) pp 297-320.

[121]. N. S. Murthy, Recent developments in polymer characterization using x-ray diffraction, Rigaku J. 21 (2004) 15–24.

[122]. A. W. Coats, J. P. Redfern, Thermogravimetric analysis: A review, Analyst 88 (1963) 906–924.

[123]. D. A. Skoog, F. J. Holler, S. R. Crouch, Principles of instrumental analysis (Sixth Ed.), Brooks Cole, New York, (1998) pp 900–904.

[124]. J. D. Menczel, R. B. Prime, Thermal analysis of polymers: Fundamentals and applications (First Ed.), Wiley, New Jersey, (2009) pp 18–57.

[125]. D. McMullan, Scanning electron microscopy 1928–1965, Scanning 17 (1995) 175–185.

[126]. L. Reimer, H. Kohl, Transmission Electron Microscopy: Physics of image formation, Springer-Verlag, New York, (2008) pp 139–192.

[127]. G. Binnig, C. F. Quate, C. Gerber, Atomic Force Microscope, Phys. Rev. Lett. 56 (1986) 930–933.

[128]. T. Young, An essay on the cohesion of fluids, Philos. Trans. R. Soc. Lond. 95 (1805) 65–87.

[129]. A. J. Bard, L. A. Faulkner, Electrochemical methods- Fundamentals and applications (Second Ed.), Wiley, New York, (1984) pp 62–63.

[130]. A. Baba, K. Onishi, W. Knoll, R. C. Advincula, Investigating work function tunable hole-injection/transport layers of electrodeposited polycarbazole network thin films, J. Phys. Chem. B 108 (2004) 18949–18955.

[131]. M. Gross, D. C. Muller, H. –G. Nothofer, U. Scherf, D. Neher, C. Brauchle, K. Meerholz, Improving the performance of doped pi-conjugated polymers for use in organic light-emitting diodes, Nature 405 (2000) 661–665.

[132]. L. B. Valdes, Resistivity measurements on germanium for transistors, in Proc. of the IRE, 42 (1954) 420–427.

[133]. T. Q. Hurd, P. W. Mertens, L. H. Hall, M. M. Heyns, Ultra-clean processing of silicon surfaces-II, Acco, Leuven, Belgium, (1994) pp 143.

[134]. http://www.optek.net.

[135]. S. Middleman, A. K. Hochberg, Process engineering analysis in semiconductor device fabrication, McGraw-Hill, New York, (1993) pp 313.

[136]. M. J. Madou, Fundamentals of microfabrication: The science of miniaturization (Second Ed.), CRC Press USA, (2002) pp 135–136.

[137]. B. J. Lin, Optical Lithography, SPIE Press, Bellingham, WA, (2009) pp 136.

[138]. R. C. Jaeger, Introduction to microelectronic fabrication (Second Ed.), Auburn, Upper Saddle River - Prentice Hall, New Jersey, (2002) pp 277–278.

[139]. M. Sarkar, A. Vijayakumar, D. Sarkar, Development and optimisation of a metal lift-off process, Microelectron. J. 17 (1986) 5–13.

[140]. A. Piegari, Thin film thickness measurement: A comparison of various techniques, Thin Solid Films 124 (1985) 249–257.

[141]. S. Tachi, K. Tsujimoto, S. Okudaira, Low-temperature reactive ion etching and microwave plasma etching of silicon, Appl. Phys. Lett. 52 (1988) 616–618.

[142]. F. Gaynor, J. J. Senkevich, S. B. Desu, A new method for fabricating high performance polymeric thin films by chemical vapour polymerization, J. Mater. Res. 11 (1996) 1842–1850.

[143]. P. V. Necliudov, M. S. Shur, D. J. Gundlach, T. N. Jackson, Contact resistance extraction in pentacene thin film transistors, Solid-State Electron. 47 (2003) 259–262.

[144]. K. Hong, S. H. Kim, C. Yang, T. K. An, H. Cha, C. Park, C. E. Park, Photopatternable highly conductive and low work function polymer electrodes for high-performance *n*-type bottom contact organic transistors, Org. Electron. 12 (2011) 516–519.

[145]. H. S. Kang, J. W. Lee, M. K. Kim, J. Jooa, J. M. Ko, J. Y. Lee, Electrical characteristics of pentacene-based thin film transistor with conducting poly(3, 4-ethylenedioxythiophene) electrodes, J. Appl. Phys. 100 (2006) 064508 (5 pp).

[146]. N. Koch, A. Elschner, J. P. Rabe, R. L. Johnson, Work function independent hole injection barriers between pentacene and conducting polymers, Adv. Mater. 17 (2005) 330–335.

[147]. M. –R. Choi, S. –H. Woo, T. –H. Han, K. –G. Lim, S. –Y. Min, W. M. Yun, O. K. Kwon, C. E. Park, K. –D. Kim, H. –K. Shin, M. –S. Kim, T. Noh, J. H. Park, K. –H. Shin, J. Jang, T. –W. Lee, Polyaniline-based conducting polymer compositions with high work function for hole-injection layers in organic light-emitting diodes, formation of ohmic contacts, ChemSusChem 4 (2011) 363– 368.

[148]. L. Ying, F. Huang, G. C. Bazan, Regioregular narrow-bandgap-conjugated polymers for plastic electronics, Nat. Commun. 8 (2017) 14047 (13 pp).

[149]. J. Liu, E. Sheina, T. Kowalewski, R. D. McCullough, Tuning the electrical conductivity and self-assembly of regioregular polythiophene by blockcopolymerization: Nanowire morphologies in new di- and triblock copolymers, Angew. Chem. 114 (2002) 339–342.

[150]. E. Song, J. –W. Choi, Conducting polyaniline nanowire and its applications in chemiresistive sensing, Nanomaterials 3 (2013) 498–523.

[151]. H. D. Tran, Y. Wang, J. M. D'Arcy, R. B. Kaner, Toward an understanding of the formation of conducting polymer nanofibers, ACS Nano 2 (2008) 1841–1848.

[152]. C. Yang, Z. Fang, P. Zhang, UV-Vis spectra of polyaniline doped with camphor sulfonic acid in different organic solvents, J Cent. South Univ. Technol. 6 (1999) 127–129.

[153]. S. –A. Chen, H. –T. Lee, Structure and properties of poly(acry1ic acid)-doped polyaniline, Macromolecules 28 (1995) 2858–2866.

[154]. A. G. MacDiarmid, A. J. Epstein, Secondary doping in polyaniline, Synth. Met. 69 (1995) 85–92.

[155]. W. R. Salaneck, I. Lundstrom, A two-dimensional-surface 'state diagram' for polyaniline, Synth. Met. 13 (1986) 291–297.

[156]. D. W. Hatchett, M. Josowicz, J. Janata, Acid doping of polyaniline: Spectroscopic and electrochemical studies, J. Phys. Chem. B 103 (1999) 10992–10998.

[157]. S. Quillard, G. Louarn, S. Lefrant, A. G. MacDiarmid, Vibrational analysis of polyaniline: A comparative study of leucoemeraldine, emeraldine and pernigraniline bases, Phys. Rev. B, 50 (1994) 12496–12508.

[158]. J. Huang, R. B. Kaner, A general chemical route to polyaniline nanofibers, Am. Chem. Soc. 126 (2004) 851–855.

[159]. N. T. Kemp, J. W. Cohrane, R. Newbury, Characteristics of the nucleation and growth of template free polyaniline nanowires and fibrils, Synth. Met. 159 (2009) 435–444.

[160]. E. C. Venancio, C. A. R. Costa, S. A. S. Machado, A. J. Motheo, AFM study of the initial stages of polyaniline growth on ITO electrode, Electrochem. Commun. 3 (2001) 229–233.

[161]. S. –J. Tang, A. –T. Wang, S. –Y. Lin, K. –Y Huang, C. –C. Yang, J. –M. Yeh, K. –C. Chiu, Polymerization of aniline under various concentrations of APS and HCl, Polym. J. 43 (2011) 667–675.

[162]. R. Sfez, L. De-Zhong, I. Turyan, D. Mandler, S. Yitzchaik, Polyaniline monolayer self-assembled on hydroxyl-terminated surfaces, Langmuir 17 (2000) 2556–2559.

[163]. M. S. Cho, S. Y. Park, J. Y. Hwang, H. J. Choi, Synthesis and electrical properties of polymer composites with polyaniline nanoparticles, Mater. Sci. Eng. C. 24 (2004) 15–18.

[164]. E. Ruckenstein, Z. F. Li, Surface modification and functionalization through the self-assembled monolayer and graft polymerization, Adv. Colloid Interface Sci. 113 (2005) 43–63.

[165]. M. Mazur, P. Predeep, Surface selective chemical deposition of polyanilines, Polymer 46 (2005) 1724–1730.

[166]. P. Yang, J. Xie, W. Yang, A simple method to fabricate a conductive polymer micropattern on an organic polymer substrate, Macromol. Rapid Commun. 27 (2006) 418–423.

[167]. Z. F. Li, E. Ruckenstein, Patterned conductive polyaniline on Si (100) surface via self-assembly and graft polymerization, Macromolecules 35 (2002) 9506–9512.

[168]. B. S. Flavel, J. Yu, J. G. Shapter, J. S. Quinton, Patterned polyaniline and carbon nanotube–polyaniline composites on silicon, Soft Matter 5 (2009) 164–172.

[169]. Y. Cao, A. Andreatta, A. J. Heeger, P. Smith, Influence of chemical polymerization conditions on the properties of polyaniline, Polymer 30 (1989) 2305–2311.

[170]. L. A. Samuelson, A. Anagnostopoulos, K. S. Alva, J. Kumar, S. K. Tripathy, Biologically derived conducting and water soluble polyaniline, Macromolecules 31 (1998) 4376–4378.

[171]. H. S. Moon, J. K. Park, Structural effect of polymeric acid dopants on the characteristics of doped polyaniline composites: Effect of hydrogen bonding, J. Polym. Sci., Part A Polym. Chem. 36 (1998) 1431–1439.

[172]. J. Stejskal, P. Kratochvil, A. D. Jenkins, The formation of polyaniline and the nature of its structures, Polymer 37 (1996) 367–369.

[173]. Y. M. Y. Xia, A. G. MacDiarmid, A. J. Epstein, Vapour phase "secondary doping" of polyaniline, Synth. Met. 69 (1995) 159–160.

[174]. H. Yan, T. Ohta, N. Toshima, Stretched polyaniline films doped by (±)-10-camphorsulfonic acid anisotropy and improvement of thermoelectric properties, Macromol. Mater. Eng. 286 (2001) 139–142.

[175]. K. Lee, S. Cho, S. H. Park, A. J. Heeger, C. W. Lee, S. H. Lee, Metallic transport in polyaniline, Nature 441 (2006) 65–68.

[176]. J. B. Doyeon, J. Kuewhan, H. Seungjoo, Y. Jaemoon, N. Sungsoo, The work function of doped polyaniline nanoparticles observed by Kelvin probe force microscopy, Nanotechnology 23 (2012) 365705 (7 pp).

[177]. B. J. Polk, K. P. –Kamloth, M. Josowicz, J. Janata, Role of protonic and charge transfer doping in solid-state polyaniline, J. Phys. Chem. B 106 (2002) 11457–11462.

[178]. R. S. Loewe, S. M. Khersonsky, R. D. McCullough, A simple method to prepare head-to-tail coupled, regioregular poly(3-alkylthiophenes) using Grignard metathesis, Adv. Mater. 11 (1999) 250–253.

[179]. A. Sou, S. Jung, E. Gili, V. Pecunia, J. Joimel, G. Fichet, H. Sirringhaus, Programmable logic circuits for functional integrated smart plastic systems, Org. Electron. 15 (2014) 3111–3119.

[180]. B. K. C. Kjellander, W. T. T. Smaal, K. Myny, J. Genoe, W. Dehaene, P. Heremans, G. H. Gelinck, Optimized circuit design for flexible 8 bit RFID transponders with active layer of ink-jet printed small molecule semiconductors, Org. Electron. 14 (2013) 768–774.

[181]. C. A. Bishop, Vacuum deposition onto webs, films and foils (Second Ed.), William Andrew Publishing, New York, (2011) pp 197–212.

[182]. H. Y. Noh, Y. G. Seol, N. E. Lee, Improved electrical stability in cyclically bent organic thin film transistors with nanocomposite gate dielectrics and surface passivation, Appl. Phys. Lett. 95 (2009) 113302 (3 pp).

[183]. H. E. Katz, Z. Bao, The physical chemistry of organic field-effect transistors, J. Phys. Chem. B 104 (2000) 671–678.

[184]. K. Fukuda, T. Sekitani, T. Someya, Effects of annealing on electronic and structural characteristics of pentacene thin-film transistors on polyimide gate dielectrics, Appl. Phys. Lett. 95 (2009) 023302 (3 pp).

[185]. C. Kim, A. Facchetti, T. J. Marks, Polymer gate dielectric surface viscoelasticity modulates pentacene transistor performance, Science 318 (2007) 76–80.

[186]. I. Kymissis, C. D. Dimitrakopoulos, S. Purushothaman, Patterning pentacene organic thin film transistors, J. Vac. Sci. Technol. B 20 (2002) 956–959.

[187]. L. H. Kim, K. Kim, S. Park, Y. J. Jeong, H. Kim, D. S. Chung. S. H. Kim, C. E. Park, Al_2O_3/TiO_2 nanolaminate thin film encapsulation for organic thin film transistors via plasma-enhanced atomic layer deposition, Appl. Mater. Interfaces 6 (2014) 6731– 6738.

[188]. K. C. Dickey, S. Subramanian, J. E. Anthony, L. H. Han, S. Chen, Y. L. Loo, Large-area patterning of a solution-processable organic semiconductor to reduce parasitic leakage and off currents in thin-film transistors, Appl. Phys. Lett. 90 (2007) 244103 (3 pp).

[189]. C. L. Fan, M. C. Shang, B. J. Li, Y. Z. Lin, S. J. Wang, W. D. Lee, B. R. Hung, Teflon/SiO_2 bilayer passivation for improving the electrical reliability of oxide TFTs fabricated using a new two-photomask self-alignment process, Materials 8 (2015) 1704–1713.

[190]. D. M. Taylor, E. R. Patchett, A. Williams, Z. Ding, H. E. Assender, J. J. Morrison, S. G. Yeates, Fabrication and simulation of organic transistors and functional circuits, Chem. Phys. 456 (2015) 85–92.

[191]. J. H. Lee, G. H. Kim, S. H. Kim, S. C Lim, Y. S. Yang, J. H Youk, J. Jang, T. Zyung, Longevity enhancement of organic thin film transistors by using a facile laminating passivation method, Synth. Met. 143 (2004) 21–23.

[192]. J. E. Northrup, M. L. Chabinyc, Gap states in organic semiconductors: Hydrogen and oxygen-induced states in pentacene, Phys. Rev. B 68 (2003) 041202(R) (4 pp).

[193]. D. J. Yun, W. Rhee, Plasma damage on the OTS treated SiO_2 substrate in the source/drain electrode deposition process, J. Electrochem. Soc. 157 (2010) H349–H354.

[194]. H. Yang, L. Yang, M. M. Ling, S. Lastella, D. D. Gandhi, G. Ramanath, Z. Bao, C. Y. Ryu, Aging susceptibility of terrace-like pentacene films, J. Phys. Chem. C 112 (2008) 16161–16165.

[195]. S. H. Han, J. H. Kim, J. Jang, S. M. Cho, M. H. Oh, S. H. Lee, D. J. Choo, Lifetime of organic thin-film transistors with organic passivation layers, Appl. Phys. Lett. 88 (2006) 073519 (3 pp).

[196]. A. Maliakal, K. Raghavachari, H. Katz, E. Chandross, T. Siegrist, Photochemical stability of pentacene and a substituted pentacene in solution and in thin films, Chem. Mater. 16 (2004) 4980–4986.

[197]. P. E. Burrows, G. L. Graff, M. E. Gross, P. M. Martin, M. Hall, E. Mast, C. C. Bonham, W. D. Bennett, L. A. Michalski, M. S. Weaver, J. J. Brown, D. Fogarty, L. S. Sapochak, Gas permeation and lifetime tests on polymer-based barrier coatings, in Proc. SPIE, Organic Light-Emitting Materials and Devices IV, San Diego, CA, 4105 (2001) 75–83.

[198]. A. A. Dameron, S. D. Davidson, B. B. Burton, P. F. Carcia, R. S. McLean, S. M. George, Gas diffusion barriers on polymers using multilayers fabricated by Al_2O_3 and rapid SiO_2 atomic layer deposition, J. Phys. Chem. C 112 (2008) 4573–4580.

[199]. L. Fumagalli, M. Binda, I. Suarez, D. Natali, M. Sampietro, S. Ferrari, L. Lamagna, M. Fanciulli, Multilayer structure for encapsulation of organic transistors, Org. Electron. 10 (2009) 692–695.

[200]. K. Norrman, M. Madsen, S. Gevorgyan, F. Krebs, Degradation patterns in water and oxygen of an inverted polymer solar cell, J. Am. Chem. Soc. 132 (2010) 16883–16892.

[201]. K. Atsuta, H. Suzuki, S. Takeuchi, A parylene lift-off process with microfluidic channels for selective protein patterning, J. Micromech. Microeng. 17 (2007) 496–500.

[202]. C. P. Tan, H. G. Craighead, Surface engineering and patterning using parylene for biological applications, Materials 3 (2010) 1803–1832.

[203]. T. Minari, T. Miyadera, K. Tsukagoshi, Y. Aoyagi, H. Ito, Charge injection process in organic field-effect transistors, Appl. Phys. Lett. 91 (2007) 053508 (3 pp).

[204]. G. B. Blanchet, C. R. Fincher, M. Lefenfeld, J. A. Rogers, Contact resistance in organic thin film transistors, Appl. Phys. Lett. 84 (2004) 296–298.

[205]. J. Dong, P. Yu, S. A. Arabi, J. Wang, J. He, C. Jiang, Enhanced mobility in organic field-effect transistors due to semiconductor/dielectric interface control and very thin single crystal, Nanotechnlogy 27 (2016) 275202 (8 pp).

[206]. D. Gupta, Y. Hong, Understanding the effect of semiconductor thickness on device characteristics in organic thin film transistors by way of two dimensional simulations, Org. Electron. 11 (2010) 127–136.

[207]. W. T. Wondmagegn, N. T. Satyala, R. J. Pieper, M. A. Q. –Lopez, S. Gowrisanker, H. N. Alshareef, H. J. Stiegler, B. E. Gnade, Impact of semiconductor/metal interfaces on contact resistance and operating speed of organic thin film transistors, J. Comput. Electron. 10 (2011) 144–153.

[208]. H. Qiu, B. Wilke, H. Gobel, Device simulation of pentacene based organic field effect transistors, in Proc. Portable Polyelectronic 2008 Conference, Germany, 17-20 Aug 2008.

[209]. http://www.silvaco.com.

[210]. S. Schienert, G. Paasch, T. Lindler, Relevance of organic field effect transistor models: Simulation vs. experiment, Synth. Met. 137 (2003) 1451–1452.

[211]. S. Cherian, C. Donley, D. Mathine, L. LaRussa, W. Xia, N. Armstrong, Effects of field dependent mobility and contact barriers on liquid crystalline phthalocyanine organic transistors, J. Appl. Phys. 96 (2004) 5638–5643.

[212]. V. Capek, E. A. Silinish, Dynamics of electronic polarization in molecular crystals, Chem. Phys. 200 (1995) 309–318.

[213]. D. Gupta, M. Katiyar, D. Gupta, An analysis of the difference in behaviour of top and bottom contact organic thin film transistors using device simulation, Org. Electron. 10 (2009) 775–784.

[214]. K. Hummer, C. A. –Draxl, Electronic properties of oligoacenes from first principles, Phys. Rev. B. 72 (2005) 205205 (10 pp).

[215]. G. Horowitz, F. Dellofre, F. Garnier, R. Hajlaoui, M. Hmyene, A. Yassar, All-organic field-effect transistors made of π-conjugated oligomers and polymeric insulators, Synth. Met. 54 (1993) 435–445.

[216]. A. Kahn, N. Koch, W. J. Gao, Electronic structure and electrical properties of interfaces between metals and π-conjugated molecular films, J. Polym. Sci. B Polym. Phys. 41 (2003) 2529–2548.

[217]. H. Li, Y. Duan, V. Coropceanu, J. L. Bredas, Electronic structure of the pentacene-gold interface: A density-functional theory study, Org. Electron. 10 (2009) 1571–1578.

[218]. http://www.eesemi.com.

[219]. D. J. Perello, S. H. Chae, S. Song, Y. H. Lee, High-performance *n*-type black phosphorus transistors with type control via thickness and contact-metal engineering, Nat. Commun. 6 (2015) 7809 (8 pp).

[220]. J. Frenkel, On pre-breakdown phenomena in insulator and electronic semiconductors, Phys. Rev. 54 (1938) 647–648.

[221]. Y. Jang, D. H. Kim, Y. D. Park, J. H. Cho, M. Hwang, K. Cho, Influence of the dielectric constant of a polyvinyl phenol insulator on the field effect mobility of a pentacene based thin film transistor, Appl. Phys. Lett. 87 (2005) 152105 (3 pp).

[222]. S. Locci, M. Morana, E. Orgiu, A. Bonfiglio, P. Lugli, Modeling of short channel effects in organic thin-film transistors, IEEE Trans. Electron Devices 55 (2008) 2561–2567.

[223]. ATLAS User's Manual: Device simulation software, Silvaco International, Santa Clara, California (2007).

[224]. A. Bolognesi, A. D. Carlo, P. Lugli, Influence of carrier mobility and contact barrier height on the electrical characteristics of organic transistors, Appl. Phys. Lett. 81 (2002) 4646–4648.

[225]. Y. S. Yang, T. Zyung, Preparation and electronic defect characteristics of pentacene organic field effect transistors, Macromol. Res. 10 (2002) 75–79.

[226]. A. Benor, A. Hoppe, V. Wagner, D. Knipp, Electrical stability of pentacene thin film transistors, Org. Electron. 8 (2007) 749–758.

[227]. D. Li, L. J. Guo, Micron-scale organic thin film transistors with conducting polymer electrodes patterned by polymer inking and stamping, Appl. Phys. Lett. 88 (2006) 063513 (3 pp).

[228]. M. Nakamura, N. Goto, N. Ohashi, M. Sakai, K. Kudo, Potential mapping of pentacene thin-film transistors using purely electric atomic-force-microscope potentiometry, Appl. Phys. Lett. 86 (2005) 122112 (3 pp).

[229]. C. Liu, Y. Xu, Y. –Y. Noh, Contact engineering in organic field-effect transistors, Mater. Today 18 (2015) 79–96.

[230]. H. Ishii, K. Sugiyama, E. Ito, K. Seki, Energy level alignment and interfacial electronic structures at organic metal and organic interfaces, Adv. Mater. 11 (1999) 605–625.

[231]. S. Mandal, Y. –Y. Noh, Printed organic thin-film transistor based integrated circuits, Semicond. Sci. Technol. 30 (2015) 064003 (20 pp).

[232]. M. Guerin, A. Daami, S. Jacob, E. Bergeret, E. Benevent, P. Pannier, R. Coppard, High-gain fully printed organic complementary circuits on flexible plastic foils, IEEE Trans. Electron Devices 58 (2011) 3587–3593.

[233]. D. Thuau, M. Abbas, S. Chambon, P. Tardy, C. Ayela, Sensitivity enhancement of a flexible MEMS strain sensor by a field effect transistor in an all organic approach, Org. Electron. 15 (2014) 3096–3100.

[234]. A. Spanu, L. Pinna, F. Viola, L. Seminara, P. Cosseddu, A high-sensitivity tactile sensor based on piezoelectric polymer PVDF coupled to an ultra-low voltage organic transistor, Org. Electron. 36 (2016) 57–60.

[235]. T. Q. Trung, N. T. Tien, Y. G. Seol, D. I. Kim, N. –E. Lee, Transparent and flexible organic field-effect transistor for multi-modal sensing, Org. Electron. 13 (2012) 533–540.

[236]. P. Cosseddu, F. Viola, S. Lai, L. Raffo, A. Bonfiglio, A temperature transducer based on a low-voltage organic thin-film transistor detecting pyroelectric effect, IEEE Electron Dev. Lett. 35 (2014) 1296–1298.

[237]. P. A. Laplante, Comprehensive dictionary of electrical engineering (Second Ed.), CRC Press, London, (2005) pp 190.

[238]. I. Nausieda, K. K. Ryu, D. D. He, A. I. Akinwande, V. Bulovic, C. G. Sodini, Mixed-signal organic integrated circuits in a fully photolithographic dual threshold voltage technology, IEEE Trans. Electron Devices 58 (2011) 865–873.

[239]. B. K. –Boroujeni, G. C. Schmidt, D. Höft, M. Bellmann, K. Haase, K. Ishida, A fully-printed self-biased polymeric audio amplifier for driving fully-printed piezoelectric loudspeakers, IEEE Trans. Circuits Syst. 1, Reg. Papers 63 (2016) 785–794.

List of Publications

In peer-reviewed journals

1. **Shiny Nair**, M. Kathiresan, T. Mukundan, Two dimensional simulation of patternable conducting polymer electrode based organic thin film transistor, Semicond. Sci. Technol. 33 (2018) 025006 (10pp).
2. **Shiny Nair**, M. Kathiresan, T. Mukundan, Patterned water dispersible conducting polymer electrode in organic thin film transistor through a parylene lift-off process, Synth. Met. 234 (2017) 29–37.
3. **Shiny Nair**, M. Kathiresan, T. Mukundan, V. Natarajan, Passivation of organic field effect transistor with photopatterned parylene to improve environmental stability, Microelectron. Eng. 163 (2016) 36–42.
4. **Shiny Nair**, R. Rajeswari, V. Natarajan, T. Mukundan, Concentration-dependent growth and morphology of doped polyaniline nanowires, J. Exp. Nanosci. 9 (2014) 982–993.
5. G. Saranya, **Shiny Nair**, V. Natarajan, K. Senthilkumar, Adsorption of perfluoropentacene on aluminum (100) surface: Structural and electronic properties from first principle study, Comput. Mater. Sci. 89 (2014) 216–223.

In International/National Conferences

6. **Shiny Nair,** T. Mukundan, Nanostructured conducting polyaniline for organic field effect transistors: Novel synthesis and patterning method, ICNAN-16, 19-21 Oct 2016, VIT University, Vellore.
7. **Shiny Nair**, Mahesh V. Kumar, M. Kathiresan, T. Mukundan, V. Natarajan, Patterning of conducting polyaniline by parylene lift-off method for organic field effect transistors, ISSS NC-8, 23-26 Sep 2016, IIT Kanpur.
8. **Shiny Nair**, M. Kathiresan, T. Mukundan, V. Natarajan, Passivation of organic field effect transistor with photopatterned parylene to improve environmental stability, APT-16, 25-26 Feb 2016, CUSAT, Kochi.
9. **Shiny Nair**, M. Kathiresan, T. Mukundan, V .Natarajan, Design and fabrication of amplification circuit with organic field effect transistor, ISSS 2015, 23-25 Sep 2015, CUSAT, Kochi.

10. **Shiny Nair**, M. Kathiresan, V. Natarajan, T. Mukundan, Novel water dispersible polyaniline based electrode for organic field effect transistor, MACRO 2015, 23-26 January 2015, Jadavpur University, Kolkata.
11. **Shiny Nair**, M. Kathiresan, V. Natarajan, Organic transistor active matrix for conformal large area networks of acoustic sensors, Workshop on Women Innovators for Excellence in Research and Science, WINNERS 2015, 8-9 March 2015, CFEES, Delhi **(Best paper award).**
12. **Shiny Nair**, M. Kathiresan, Raja Shunmugam, V. Natarajan, T. Mukundan, Synthesis of diblock copolymers of poly(3-hexylthiophene) and poly(butyl acrylate) for organic field effect transistor, MACRO 2013, 15-18 May 2013, IISc, Bengaluru.
13. **Shiny Nair**, M. Kathiresan, V. Natarajan, OFET flexible sensors for defence applications, DRDO Science Spectrum, (2013) 254-260.